Magnetotelluric study of the Mérida Andes and surrounding basins, Venezuela

Dissertation

zur Erlangung des akademischen Grades

doctor rerum naturalium (Dr. rer. nat.)

im Fachbereich Geowissenschaften

der Freien Universität Berlin

vorgelegt von

José Alejandro Cruces Zabala

Berlin, 2021

Gutachter:
Betreuer: Prof. Dr Oliver Ritter
Freie Universität Berlin, Deutsches GeoForschungsZentrum Potsdam
Zweitgutachter: Prof. Dr. Michael Becken
Westfälische Wilhelms-Universität Münster
Tag der Disputation: 23.04.2021

Eidesstattliche Erklärung

Hiermit versichere ich, dass ich die vorliegende Dissertation selbständig ohne Hilfe Dritter verfasst habe. Andere als die angegebenen Quellen und Hilfsmittel wurden nicht verwendet. Die den benutzten Quellen wörtlich oder dem Sinn nach entnommen Abschnitte sind als solche kenntlich gemacht. Dies gilt auch für Zeichnungen, Skizzen, bildliche Darstellungen und dergleichen, sowie für Quellen aus dem Internet. Die Dissertation hat in dieser oder ähnlicher Form weder ganz noch in Teilen einer in- oder ausländischen Hochschule zum Zwecke der Promotion vorgelegen.

- Teile von Kapitel 1, 2 und 4 sind veröffentlicht in: Cruces-Zabala, J., Ritter, O., Weckmann, W., Tietze, K., and Schmitz, M. (2020). "Magnetotelluric imaging of the Mérida Andes and surrounding areas in Venezuela", Geophysical Journal International 222, 3, pp. 1570--1589. doi: https://doi.org/10.1093/gji/ggaa266
- Teile von Kapitel 4 und 5 wurden bei Journal of South American Earth Sciences eingereicht.

Berlin den 11.05.2021

José Alejandro Cruces-Zabla

Abstract

The Caribbean and South American tectonic plates bound the north-eastwards expulsion of the North Andean Block in western Venezuela. This complicated geodynamic setting resulted in the formation of major strike-slip fault systems and sizeable mountain chains. The 100 km wide Mérida Andes extend from the Colombian/Venezuelan border to the Coastal Cordillera. To the north and south, the Mérida Andes are bound by hydrocarbon-rich sedimentary basins. Knowledge of lithospheric structures, related to the formation of the Mérida Andes, is limited though, due to a lack of deep geophysical data.

This thesis presents the results of the first broadband magnetotelluric profile crossing the Mérida Andes and the Maracaibo and Barinas-Apure foreland basins spanning a distance of 240 km. The MT dataset consists of 72 stations installed during March and April 2015 with a minimum recording period of 3 days per station. Geoelectrical strike and dimensionality analyses are consistent with one- or two- dimensional subsurface structures for the sedimentary basins yet also indicate a strong three- dimensional setting for the Mérida Andes. Even more significantly, these analyses showed the presence of off-profile features that influenced the data considerably, particularly at long periods. Therefore, a combination of 2D and 3D modelling was necessary for analysing the geoelectrical structures associated with this dataset.

Off-profile structures can significantly affect the outcome of a 2D inversion. Thus, the systematic examination of the influence of 3D structures on 2D inversions was necessary to support the obtained result. Synthetic data sets derived from 3D modelling allowed identification and quantification of spurious off-profile features as well as smoothing artefacts due to limited areal station coverage of data collected along a profile. In general, structures in the 2D inversion are affected by the projection and rotation of the data resulting in sub-horizontal anomalies to reproduce the oblique extent of the fault systems and sedimentary basins.

Moreover, a profile distributed dataset can limit the lateral resolution of a 3D inversion considerably. Hence, the effect of data distribution on a 3D inversion was carefully studied to determine the areas of the models that can be confidently explained by the data. To this end, several synthetic datasets were derived from 3D models with varying levels of complexity. The analysis of the synthetic datasets allows determination of the lateral resolution of the 3D models and identification of spurious shallow and deep features considered artefacts related to off-profile features.

Furthermore, the inversion of synthetic models provided support to the geological interpretation of the recovered anomalies for the 2D and 3D modelling.

The 2D and 3D inversion models were similar above the sedimentary basins and showed marked differences above the Mérida Andes, due to the 3D nature of this section. The inversion models show electrically conductive basins with depths of 2 to 5 km for the Barinas-Apure and 2 to 9 km for the Maracaibo basins. Many resistive bodies within the Maracaibo basin could be related to active deformation causing juxtaposition of older geological formations and younger basin sediments. A conductive zone under the Maracaibo Basin correlates spatially with the location of a Bouguer anomaly low and seem to describe the SE tilt of the Maracaibo Triangular Block under the Mérida Andes. This conductive zone is limited towards the mountain by the north-western thrust system, whose fault plane may function as a detachment surface reaching depth larger than 30 km in the 3D inversion models.

The most prominent fault systems of the area, the Boconó and Valera Faults, cross-cut the Mérida Andes in NE-SW direction along its strike with a length 400 km and N-S direction at its centre with a length 60 km, respectively. Both faults are associated with sub-vertical zones of high electrical conductivity and sensitivity tests suggest that the Valera fault reach depths of up to 12 km. The Boconó fault can be considered a crustal structure with a depth up to 35 km. The observed anomalies seem to show a deep connection of the fault planes, possibly related to the formation of the fault systems in a transpressive regime. Conductive anomalies to the south of the Boconó Fault seem to represent a considerable back thrust structure well constrained between 3 and 10 km depth. The high conductivity of these structures is possibly related to weathering water from the surface and the accumulation of clay minerals in the fault gauges. However, fluids related to the flat and shallow subduction of the Caribbean Plate in north-western Venezuela could better explain the low resistivity of the deep structures (> 15 km).

A sizeable conductor at 50 km depth, which appears consistently in the 2D sections, could be identified as an inversion artefact caused by a conductor east of the profile. The 3D inversion places this structure 10 km to the east at 15 km deep. This model also shows depth connection (12 km depth) of the anomalies related to the Valera and Boconó faults with the off-profile conductor. The observed anomalies in the 2D and 3D inversion related to these conductors were tested and reproduced employing synthetic datasets, leading to the speculation that the high conductivity associated with the off-profile conductor may be related to the detachment of the Trujillo Block.

The models obtained confirm the shape and distribution of the known geological structures related to the complicated geodynamic settings responsible for the formation of the Mérida Andes. These results partially support the "floating orogen hypothesis" developed to explain the geodynamic evolution of western Venezuela, and they highlight the relevance of the Trujillo Block in this process. However, they also show that features of known structures such as the Boconó fault system maximum depth, the back-thrusting in the Mérida Andes, and the relevance of the escape of the Trujillo Block in the tectonic processes need to be adjusted to the current knowledge.

Kurzzusammenfassung

Die Karibische und Südamerikanische tektonischen Platten begrenzten die nordöstliche Abschiebung des Nord-Anden-Blocks im Westen Venezuelas. Diese komplizierte geodynamische Umgebung führte zur Bildung großer Blattverschiebungen-Verwerfungssysteme und beträchtlicher Gebirgsketten. Die 100 km breiten Mérida-Andes erstrecken sich von der Grenze zwischen Kolumbien und Venezuela bis zum Coastal Cordillera. Im Norden und Süden sind die Mérida-Anden von kohlenwasserstoffreichen Sedimentbecken umgeben. Das Wissen über lithosphärische Strukturen im Zusammenhang mit der Bildung der Mérida-Anden ist jedoch aufgrund des Mangels an tiefen geophysikalischen Daten begrenzt.

Diese Arbeit präsentiert die Ergebnisse des ersten breitbandigen magnetotellurischen Profils, das die Mérida-Anden und die Vorlandbecken Maracaibo und Barinas-Apure über eine Entfernung von 240 km quert. Der MT-Datensatz besteht aus 72 Stationen, die im März und April 2015 mit einer Mindestaufzeichnungsdauer von 3 Tagen pro Station installiert wurden. Geoelektrische Streich- und Dimensionalitätsanalysen stimmen mit ein- oder zweidimensionalen Untergrundstrukturen für die Sedimentbecken überein, weisen jedoch auch auf eine starke dreidimensionale Strukturen in der Umgebung der Mérida-Andes hin.. Noch wichtiger ist, dass diese Analysen das Vorhandensein von Merkmalen außerhalb des Profils zeigten, die die Daten insbesondere für lange Perioden erheblich beeinflussen. Daher war eine Kombination aus 2D- und 3D-Modellierung erforderlich, um Störungssysteme und Sedimentbecken quer zum Profil zu reproduzieren.

Off-Profile-Strukturen können das Ergebnis einer 2D-Inversion erheblich beeinflussen. Daher war die systematische Untersuchung des Einflusses von 3D-Strukturen auf 2D-Inversionen erforderlich, um das erhaltene Ergebnis zu verifizieren. Synthetische Datensätze, die aus der 3D-Modellierung abgeleitet wurden, ermöglichten die Identifizierung und Quantifizierung von störenden Strukturen außerhalb des Profils sowie die Glättung von Artefakten aufgrund der begrenzten Stationsüberdeckung der entlang eines Profils gesammelten Daten. Im Allgemeinen werden Strukturen in der 2D-Inversion durch die Projektion und Rotation der Daten beeinflusst, was zu flach stehenden Anomalien führt, um die schräge Ausdehnung der Verwerfungssysteme und Sedimentbecken zu reproduzieren.

Darüber hinaus kann ein Datensatz entlang eines Profils die laterale Auflösung einer 3D-Inversion erheblich einschränken. Daher wurde die Auswirkung der Datenverteilung auf eine 3D-Inversion sorgfältig untersucht, um die Bereiche der Modelle zu bestimmen, die durch die Daten sicher erklärt werden können. Zu diesem Zweck wurden mehrere synthetische Datensätze aus 3D-Modellen mit unterschiedlicher Komplexität abgeleitet. Die Analyse der synthetischen Datensätze ermöglicht die Bestimmung der lateralen Auflösung der 3D-Modelle und die Identifizierung von störenden oberflächennahen und tiefen Merkmalen, die als Artefakte im Zusammenhang mit Strukturen außerhalb des Profils betrachtet werden.

Darüber hinaus unterstützte die Inversion synthetischer Modelle die geologische Interpretation der reproduzierten Anomalien für die 2D- und 3D-Modellierung.

Die 2D- und 3D-Inversionsmodelle stimmen über den Sedimentbecken überein. Aufgrund der 3D Strukturen über den MA ergaben sich jedoch deutliche unterschiede. Die Inversionsmodelle zeigen elektrisch leitende Becken mit Tiefen von 2 bis 5 km für das Barinas-Apure und 2 bis 9 km für das Maracaibo-Becken. Viele Gebiete höheren Widerstands im Maracaibo-Becken könnten mit einer aktiven Deformation zusammenhängen, die ein Nebeneinander älterer geologischer Formationen und jüngerer Beckensedimente verursacht. Eine besserleitende Zone unter dem Maracaibo-Becken korreliert räumlich mit der Lage einer Bouguer-Anomalie und scheint die SE-Neigung des Maracaibo-Dreiecksblocks unter den Mérida-Anden zu markieren. Diese leitende Zone ist in Richtung des Gebirges durch das nordwestliche Schubsystem begrenzt, dessen Störungsebene als Ablösefläche fungieren kann, die in den 3D-Inversionsmodellen eine Tiefe von mehr als 30 km erreicht.

Die bekanntesten Störungssysteme des Gebiets, die Verwerfungen Boconó und Valera, kreuzen die Mérida-Anden in Nordost-Südwest-Richtung entlang ihres Streichens mit einer Länge von 400 km und die N-S-Richtung in ihrer Mitte mit einer Länge von 60 km. Beide Störungen sind durch steil stehende Zonen hoher elektrischer Leitfähigkeit verbunden. Sensitivitätsstudien legen nahe, dass die Valera-Störung Tiefen von bis zu 12 km erreicht. Die Boconó-Verwerfung kann als Krustenstruktur mit einer Tiefe von bis zu 35 km angesehen werden. Die beobachteten Anomalien scheinen eine tiefe Verbindung der Verwerfungsebenen zu zeigen, möglicherweise im Zusammenhang mit der Bildung der Verwerfungssysteme in einem transpressiven Regime. Leitfähige Anomalien südlich der Boconó-Verwerfung scheinen eine beträchtliche Rückschubstruktur darzustellen, die zwischen 3 und 10 km Tiefe gut lokalisiert ist. Die hohe Leitfähigkeit dieser Strukturen hängt möglicherweise mitWasser aus Verwitterungsprozessen nahe der Erdoberfläche und der Ansammlung von Tonmineralien in den Störungszonen zusammen. Alte Fluide im Zusammenhang mit flach stehenden und oberflächenahen Subduktion der Karibikplatte im Nordwesten Venezuelas könnten jedoch den geringen spezifischen Widerstand der tiefen Strukturen (> 15 km) besser erklären.

Ein beträchtlicher Leiter in einer Tiefe von 50 km, der in den 2D-Schnitten konsistent erscheint, konnte als Inversionsartefakt identifiziert werden, der durch einen Leiter östlich des Profils verursacht wird. Durch die 3D-Inversion wird diese Struktur 10 km östlich in 15 km Tiefe platziert. Dieses Modell zeigt auch die Tiefenverbindung (12 km Tiefe) der Anomalien im Zusammenhang mit den Störungen von Valera und Boconó mit dem Leiter außerhalb des Profils. Die beobachteten Anomalien in der 2D- und 3D-Inversion in Bezug auf diese Leiter wurden unter Verwendung synthetischer Datensätze getestet und reproduziert. Daher kann man annehmen das die mit dem Leiter abseits des Profils verbundene Leitfähigkeit mit der Ablösung des Trujilo Blocks zusammenhängt.

Die erhaltenen Modelle bestätigen die Form und Verteilung der bekannten geologischen Strukturen im Zusammenhang mit dem komplizierten geodynamischen Millieu, welches für die Bildung der Mérida-Andes verantwortlich ist. Diese Ergebnisse stützen teilweise die "schwimmende Orogenhypothese", die entwickelt wurde, um die geodynamische Entwicklung West-Venezuelas zu erklären, und sie unterstreichen die Relevanz des Trujillo-Blocks in diesem Prozess. Sie zeigen jedoch auch, dass Merkmale bekannter Strukturen wie die maximale Tiefe des Boconó-Verwerfungssystems, das Zurückschieben in den Mérida-Anden und die Relevanz des Entweichens des Trujillo-Blocks in den tektonischen Prozessen an den aktuellen Kenntnisstand angepasst werden müssen.

Resumen

Las Placas del Caribe y Sudamérica limitan la expulsión con dirección nor-este del Bloque Norandino en el occidente de Venezuela. Este complicado escenario geodinámico resultó en la formación de mayores sistemas de falla de deslizamiento lateral y sistemas montañosos de tamaño considerable. Los Andes de Mérida con un ancho de 100 km se extienden desde la frontera colombo-venezolana hasta la Cordillera de la Costa. Hacia el norte y el sur, los Andes de Mérida están limitados por cuencas sedimentarias ricas en hidrocarburos. Sin embargo, el conocimiento de las estructuras litosféricas relacionadas con la formación de los Andes de Mérida es limitada, dado la falta de datos geofísicos profundos.

Esta tesis presenta los resultados del primer perfil de datos magnetotelúricos cruzando los Andes de Mérida y las cuencas de ante-país de Maracaibo y Barinas-Apure a lo largo de 240 km. El set de datos magnetotelúricos consiste de 72 estaciones instaladas entre Marzo y Abril de 2015 con un período mínimo de 3 días por estación. Análisis de strike geoeléctrico y de dimensionalidad son consistentes con dimensionalidad 1D y 2D para las cuencas sedimentarias, y dimensionalidad 3D para los Andes de Mérida. Aún más significativo, estos análisis muestran una influencia considerable en los datos de estructuras fuera del perfil, particularmente en los periodos largos. Por lo tanto, una combinación de modelados 2D y 3D fue necesaria para el análisis de las estructuras geoeléctricas asociadas a este set de datos.

Estructuras fuera del perfil pueden afectar significativamente los resultados de una inversión 2D. Por lo tanto, para confirmar los resultados obtenidos fue necesario el estudio sistemático de la influencia de estructuras 3D en una inversión 2D. Sets de datos sintéticos derivados del modelado 3D permitieron la identificación y cuantificación de características espurias fuera del perfil así como artefactos de suavizado debidos a la limitada cobertura areal de estaciones colectadas a lo largo de un perfil. En general, las estructuras modeladas en una inversión 2D son afectadas por la proyección y rotación de los datos resultando en anomalías sub-horizontales para reproducir la extensión oblicua de las cuencas sedimentarias y sistemas de fallas.

La distribución de las estaciones a lo largo de un perfil puede limitar considerablemente la resolución lateral de una inversión 3D. Por consiguiente, el efecto de la distribución de los datos en una inversión 3D fue cuidadosamente estudiado para determinar las áreas del modelo que pueden ser explicadas con un alto grado de confianza. Con esta finalidad, varios set de datos sintéticos fueron derivados de modelos 3D con grados variables de complejidad. El análisis de los datos sintéticos permitió la determinación de la resolución lateral de los modelos 3D y la identificación de características espurias superficiales y profundas consideradas artefactos relacionados a estructuras fuera del perfil.

Además, la inversión de modelos sintéticos complementó las interpretaciones geológicas de las anomalías recobradas en el modelado 2D y 3D.

Los modelos de inversión 2D y 3D son similares en las cuencas sedimentarias y mostraron marcadas diferencias en de los Andes de Mérida, debido a la naturaleza 3D de esta sección. Los modelos de inversión muestran cuencas eléctricamente conductivas con profundidades entre 2 y 5 km para la cuenca Barinas-Apure y 2 a 9 km para la de Maracaibo. Cuerpos resistivos dentro de la cuenca de Maracaibo podrían estar relacionados a procesos activos de deformación que causan la yuxtaposición de estructuras geológicas antiguas con sedimentos mas jóvenes de la cuenca. Una zona conductiva debajo de la cuenca de Maracaibo se correlaciona espacialmente con la posición de un bajo en la anomalía de Bouguer y parece describir la inclinación SE del Bloque Triangular de Maracaibo por debajo de los Andes de Mérida. Esta zona conductiva esta limitada en dirección a la montaña por el sistema de empuje occidental, cuyo plano de falla podría funcionar como una superficie de despeje alcanzando profundidades mayores a los 30 km en los modelos de inversión 3D.

Los sistemas de fallas más prominentes en el área, las fallas de Boconó y Valera, cruzan los Andes de Mérida en dirección NE-SO a lo largo de su strike con una extensión de 400 km y N-S en su centro con una extensión de 60 km, respectivamente. Ambas fallas están asociadas con zonas sub-verticales de alta conductividad eléctrica y los estudios de sensitividad siguieren que la falla de Valera alcanza profundidades de hasta 12 km. La falla de Boconó es considerada una estructura cortical con una profundidad mayor a 35 km. Las anomalías observadas parecen mostrar una conexión profunda de los planos de falla, posiblemente relacionada a la formación de los sistemas de fallas en un régimen transpresivo. La alta conductividad de estas estructuras esta posiblemente relacionada a fluidos de meteorización provenientes de la superficie y a la acumulación de minerales de arcilla los planos de falla. Sin embargo, fluidos relacionados a la subducción somera y plana de la Placa del Caribe en el noreste de Venezuela podría explicar mejor la baja resistividad de las estructuras profundas (> 15 km).

Un conductor de tamaño considerable a 50 km de profundidad, recobrado consistentemente en las secciones 2D, podría ser identificado como un artefacto de la inversión causado por un conductor al este del perfil. La inversión 3D ubica esta estructura 10 km hacia el este a 15 km de profundidad. Éste modelo también muestra un conexión profunda (12 km) de las anomalías relacionas a las fallas de Valera y Boconó con el conductor fuera del perfil. Las anomalías observadas en los modelos de inversión 2D y 3D relacionas a estos conductores fueron probadas y reproducidas con el uso de set de datos sintéticos, llevando a la especulación que la alta conductividad asociada con el conductor fuera del perfil podría estar asociada con la superficie de despeje del Bloque de Trujillo.

Los modelos obtenidos confirman la forma y distribución de las estructuras geológicas conocidas relacionadas con las características geodinámicas complejas responsables por la formación de los Andes de Mérida. Estos resultados parcialmente apoyan la hipótesis del ‘Orogeno Flotante’ desarrollada para explicar la evolución geodinámica de Venezuela Occidental, y realzan la relevancia del Bloque de Trujillo en este proceso. Sin embargo, los resultados también indican que elementos de estructuras conocidas como la profundidad máxima del sistema de fallas de Boconó, el ‘back-thrust’ en los Andes de Mérida y la relevancia del escape del Bloque de Trujillo en los procesos tectónicos deben ser ajustados al conocimiento actual.

Acknowledgements

Through the course of this thesis, I received the help and support of several people to whom I will always be thankful. Here, I give particular mention only to those whose input was pivotal in the completion of this project.

Above all, I want to express my most sincere gratitude to my PhD advisor Prof. Dr. Oliver Ritter, who gave me the opportunity to write my dissertation. Furthermore, he helped me through every single step that led to the development of this project, from my scholarship application to the submission of this work. He masterfully walked the fine line between patiently allow me to learn in my rhythm and pushing me at times when I was lost. Without his invaluable input in data processing, analysis and inversion and the subsequent interpretation of the resulting models, I would not have completed this work. Thank you for your patience and kindness.

This project would have never come to be without the tireless work of Dr. Michael Schmitz. Countless students within the GIAME project and I credit him for allowing us to work in science. He also provided constant support to navigate the nuances of organizing the field campaign, develop the cooperation agreement and getting my scholarship. From a personal point of view, he showed me an enormous level of trust, and I found his resilience a source of inspiration to keep going and aspire to my goals.

Prof. Dr Ute Weckmann and Dr Kristina Tietze showed me infinite levels of patience while teaching me everything from data processing and analysis to data inversion. Reinhard Schmitt and Dr. Gerard Muñoz also helped me through my first experiences with scripting, data processing and filtering.

I want to thank Dr. Nasser Meqbel for sharing with me his knowledge in EM inversion. He has been a great teacher and mentor. I have lost count of the many conversations and interesting discussions about MT data modelling, testing and interpretation.

I was lucky enough to share my time at the GFZ with the fantastic group of section 2.7. Your doors were always open, and you always welcomed a good discussion. Particularly, my gratitude goes to Dr. Anna Platz, Dr. Gerard Muñoz, Dr. Cedric Patzer, who helped me to understand topics related to programming, data processing, inversion and presentation. We were also able to build a space that allowed me to discuss my results and openly share my input on other works.

Thanks go to Abubakar, Anna, Basil, Cedric, Gregor, Jade, Jaime, Roshan and Walja.

I benefited greatly from my visits to the GFZ between 2013 and 2015. These experiences lead to a successful field campaign in Venezuela, where the invaluable work of researchers from the GFZ, FUNVISIS, PDVSA and students from the USB and UCV, combined with the high quality equipment provided by the Geophysical Instrument Pool Potsdam (GIPP) allowed me to gather the data necessary to complete this thesis. In particular thanks to Javier Sánchez, Yuniev Martinez and Luis Yegres for sharing with me the weight of the responsibilities in organizing and overseeing the data acquisition.

My days at the GFZ would have been more challenging to manage without the moral support provided by other doctoral researchers. Among these Milena, Johannes and Peter were incredible support, and we also shared the experience of organizing the NextGen 2018 conference, surely a milestone in our time at GFZ.

Like up to two thirds of the doctoral researchers at all Helmholtz centres, I also struggle with mental health problems. In this sense, I am thankful for my amazing Ultimate Frisbee team, the Goldfingers of Potsdam, who helped me to keep sane and fit on and off the field; for my friends who were always willing to talk about life and distract each other from the world at large; and to Ellen Zwickl, who helped me to balance life/work/sports in general and particularly during the COVID lock-down.

Finally, to my family, the ones that are always there and will always be, the main reason for the path I have followed, to you I dedicate this thesis.

Contents

List of Figures

List of Tables

Introduction

The Venezuelan Andes (Mérida Andes, MA) are the most prominent feature in western Venezuela; they are part of a mountain chain extending from Ecuador, across Colombia, and into western Venezuela (the Eastern Cordillera), which formed due to the NE tectonic escape of the North Andean Block (e.g. Dewey, 1972). The uplift of the Mérida Andes started in the Early Miocene (Audemard, 2014) by the interaction of different tectonic blocks controlled by the eastward movement of the Caribbean Plate relative to the South American Plate. These tectonic settings resulted in a plate boundary along northern Venezuela that is under a stress field characterised by a strike-slip regime responsible for the present kinematics and earthquake activity of five sets of faults within a 100 km wide deformation belt (Audemard *et al.*, 2000). Earthquake occurrence is common in Venezuela, and it is distributed along northern Venezuela, yet western Venezuela is considered the most seismogenically active zone. Historic seismological data (e.g. Audemard *et al.*, 2005; ISC, 2003; U.S. Geological Survey, 2020) show that most earthquakes occur at crustal depths (<50 km) and are related to the main fault systems (Fig. 1), while deeper earthquakes are rare in the Venezuelan Andes and they are mostly localised under the Eastern Cordillera, as a result of the deep subducting slab of the Nazca plate under South America (Bezada *et al.*, 2010). However, due to the lack of geophysical images, the crustal structure of the Mérida Andes, as well as the interactions of the active faults systems and the tectonic related processes in the area are poorly understood.

Therefore, the Integrated Geoscience of the Mérida Andes Project (the GIAME project, from its Spanish acronym) was initiated in 2013. The main objective of the project was to image the Mérida Andes on a lithospheric scale and to develop a dynamic model of their evolution by integrating wide-angle seismic, magnetotelluric and potential field data.

Until recently, the deep structures below the Mérida Andes were studied mainly with regional gravity. Based on gravity profiles, Hospers & VanWijnen (1959) developed a simple one-layer model to describe the gravimetric anomalies of the Maracaibo basin, the Mérida Andes and the Barinas-Apure. In this model, a gravimetric minimum was identified to the north-east of the mountain chain. Folinsbee (1972) confirmed this displacement using Bouger anomaly profiles, and attributed it to the thickness of the Maracaibo basin. Later, Kellogg & Bonini (1982) integrated gravity data, well logs, seismic profiles, radiometric and earthquake data to present tectonic interpretations of the Caribbean-South American plate boundary, including the deformation rate in western Venezuela and the associated processes.

Since then, several authors have presented geophysical studies on the origin, evolution and current configuration of the Mérida Andes (e.g. De Toni & Kellogg, 1993; Audemard *et al.*, 1999; Audemard & Audemard, 2002; Callejón & von der Dick, 2002; Chacín *et al.*, 2005; Duerto *et al.*, 2006; Arnaiz-Rodríguez *et al.*, 2011). However, these studies have focussed on findings for hydrocarbon exploration, which only gives information for the upper 8-10 km.

The current tectonic settings of western Venezuela are often described by floating blocks or orogens, whose deformations are controlled by the relative movement of the Caribbean and South American plates. Monod *et al.* (2010), present an orogenic float model for the Mérida Andes based on the orogenic float concept for transpressional orogens (Oldow *et al.*, 1990). In this model, the Boconó Fault system is considered an upper crustal fault that connects to a mid-crustal detachment level, which allows the orogen to float on the underlying lithosphere. Moreover, based on shear wave splitting analysis, Masy *et al.* (2011) propose the Boconó Fault to cause deformation at lithospheric scale. However, many aspects of the tectonic evolution and the deep lithospheric structures are still disputed.

Fault zones in the upper crust are typically composed of complex fracture networks and geochemically altered rocks (Caine & Forster, 1999). These conditions create channels for fluid circulation. The electrical resistivity of rocks is highly sensitive to the presence of interconnected conductive fluids. Studies in subduction zones have shown that changes in the coupling between tectonic plates correlate with spatial variations in the electrical resistivity structure above the plate interface (e.g. Heise *et al.*, 2013; Wannamaker *et al.*, 2014). Thus, imaging of the electrical conductivity structure is particularly useful in this respect. The magnetotelluric (MT) method, based on electromagnetic induction in the Earth, is the only method capable of imaging the electrical conductivity structure between the shallow crust and upper mantle depths.

MT studies of orogens often reveal complex resistivity structures, typically associated with active deformation (see Unsworth, 2010; Brasse, 2011, and references therein). Particularly zones of high electrical conductivity are often associated with major fault zones or detachment zones in the mid- and lower-crust . High conductivity in active tectonic regimes is often explained with fluids in fault systems and/or fluids derived from remineralization reactions of hydrous minerals (e.g. Jones, 1993; Boerner *et al.*, 1998; Ritter *et al.*, 2005; Becken & Ritter, 2011; Meqbel *et al.*, 2016).

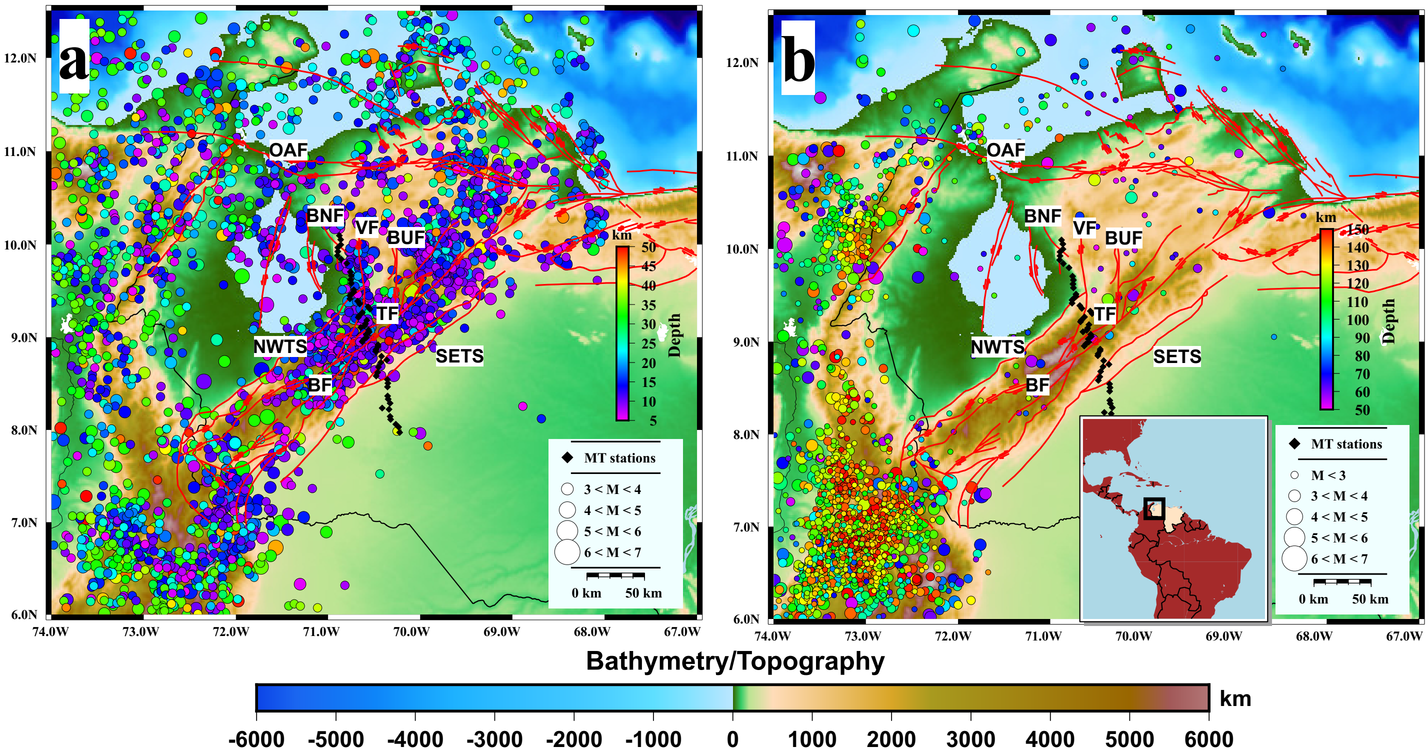

Figure 1.: Map of historical seismicity in north-western Venezuela showing the location of the Mérida Andes and including the Quaternary fault systems (red lines, after Audemard *et al.*, 2000). (a) Shallow earthquakes (< 50 km depth) (b) deep earthquakes (> 50 km depth). Seismological information compiled from Audemard *et al.* (2005); ISC (2003); U.S. Geological Survey (2020); and FUNVISIS historical database (pers. comm.). Topography and bathymetry were taken from Amante & Eakins (2009). Abbreviations: OAF- Ocá - Acón Fault, BF - Boconó Fault, VF - Valera Fault, TF - Tuñame Fault, NWTS - Northwestern Thrust System, SETS - Southwestern Thrust system, BUF - Burbusay Fault.

The basis of this work is a regional MT data set, acquired in the framework of the GIAME project. Data acquisition took place between March and April 2015, with a total of 72 MT stations installed along a 240 km long profile (Fig. 1) oriented ~17°NW across the central part of the Mérida Andes and their foreland basins.

The results presented in this thesis show the first deep geoelectric images of western Venezuela. MT data allow to clearly distinguish between generally more conductive foreland basin structures and resistive domains associated with the MA. They also show evidence for narrow, deep-reaching zones of high electrical conductivity, which appear to be associated with major fault systems of the MA.

An in-depth examination of these zones of high conductivity, their spatial resolution and correlation with tectonic features is the main focus of this work. The analyses suggest that only the northern and southern parts of the dataset are generally consistent with simple (one- or two-dimensional) subsurface structures. Since data coverage is primarily along a single profile, a central component of this work is the two-dimensional inversion of the data and the study of the limitations of the resulting models. Three-dimensional inversion was employed for a better description of the most complicated areas of the data set.

Thesis outline

This thesis is structured into five chapters.

- Chapter 1 Summarizes the tectonic and geodynamic settings of north-western Venezuela, establishing a relationship between the main tectonic structures and the formation of the Mérida Andes and their foreland basins. It also presents a compilation of the dominant theories on the formation of the mountain chains and includes a description of the major fault systems and surface structures.
- Chapter 2 presents the fundamentals of the MT method that are relevant to the analyses carried out in this study. Some parts of this chapter are contained in a manuscript submitted to Journal of Geophysical Research.
- Chapter 3 describes the central aspects of the GIAME MT data set. The data quality is analysed, and the data processing scheme is explained. The data set is characterized in terms of its complexity and preliminary findings about the structures in the subsurface are shown.
- Chapter 4 presents the two- and three-dimensional models of the resistivity structures of the Mérida Andes and their foreland basins. It also describes the inversion schemes used and the limitations of the methodologies. Both models show conductive structures associated with the fault systems and off-profile features related to the active tectonic processes. Some parts of this chapter are contained in a manuscript accepted for publication by the Geophysical Journal International.
- Chapter 5 contains the conclusions of this study and possible areas to expand the investigation.

Related Publications

Peer reviewed article. Cruces-Zabala, J., Ritter, O., Tietze, K., Weckmann, U., Schmitz, M. (2020): Magnetotelluric imaging of the Mérida Andes and surrounding areas in Venezuela. - Geophysical Journal International, 222, 3, 1570-1589. https://doi.org/10.1093/gji/ggaa266

Conference presentation. Cruces-Zabala, J., Ritter, O., Weckmann, U., Tietze, K., Schmitz, M. (2019): Conductive anomalies related to the Mérida Andes derived from a magnetotelluric profile. Haltern am See, 23.-27. September 2019, 28. Schmucker-Weidelt-Kolloquium für Elektromagnetische Tiefenforschung.

Conference Paper. Cruces-Zabala, J., Ritter, O., Weckmann, U., Tietze, K., Schmitz, M. (2017): The Mérida Andes of Venezuela: Magnetotelluric forward modelling and comparison with real data. - In: Becken, M., Hölz, S. (Eds.), - Protokoll über das 27. Schmucker-Weidelt-Kolloquium für Elektromagnetische Tiefenforschung: Breklum, 25.-29. September 2017, 27. Schmucker-Weidelt-Kolloquium für Elektromagnetische Tiefenforschung (Breklum 2017), 104-104.

1. Tectonic evolution and geological settings

The formation of the Mérida Andes (MA) is generally accepted to be the result of oblique convergence of the Caribbean and South American Plates, resulting in strain partitioning along the MA supported by a system of left-lateral strike-slip faults (i.e. González de Juana *et al.*, 1980a; Kellogg & Bonini, 1982; Yrigoyen & Urien, 1988; Audemard, 2003; Duerto *et al.*, 2006; Monod *et al.*, 2010; Arnaiz-Rodríguez *et al.*, 2011; Dhont *et al.*, 2012; Pérez *et al.*, 2018). This regional tectonic process also dominates the geological evolution of the northern part of the South American continent, thus to describe the geodynamic settings that lead to the uplift of the Mérida Andes, it is necessary to describe the settings of the entire region.

1.1. Tectonic evolution of north-western Venezuela

The geodynamic settings that shaped western Venezuela began with the separation of the supercontinent Pangea. Pushing the South American plate initially to the west and then northwestward, forming what came to be the central parts of the *MA* as well as the basement of western Venezuela, which has been dated as Precambrian to early Paleozoic.

A period of extension during the Jurassic is responsible for the formation of grabens and other extension structures and filled them with continental sediments (Duerto, 1998). Approximately 100 Ma ago the development of a passive margin and subsidence fosters the formation of the Proto-Pacific ocean in the northern part of the South American plate. From early Cretaceous to middle Eocene, sediments were deposited in an extensive passive continental margins setting. These Cretaceous formations, mostly marine sandstone, shale, and limestone, are the main source rocks of the sedimentary basins located today in western Venezuela (De Toni & Kellogg, 1993), namely the Maracaibo (MB) and Barinas-Apure Basins (BAB), north and south of the MA, respectively.

The diachronous oblique convergence between Caribbean arc terranes and the South American continental margin from the Late Cretaceous (western area of Colombia) to the present (eastern area of Trinidad) formed a west-east younging pattern of thrusts, lateral ramp faults and foreland basins onshore (Escalona & Mann, 2006a). Also resulting from this convergence, the collision of the Panama Arc with the South American plate in the early Miocene caused uplift of the MA and other major mountain chains, including the Perijá Sierra at the western boundary of the Maracaibo basin. Since the Late Miocene, the escape of the North Andean Block partially controls the deformation rate. The interaction between the Caribbean Plate and the North Andean Block favours the formation of a series of right-lateral strike-slip fault zones reaching its north-east boundary at the triple junction between the Boconó (BF), Morrocoy (MF) and San Sebastian (SF) fault systems (Pérez *et al.*, 2018) (Fig. 1.1).

Uplift of the MA accelerated during the Plio-Quaternary due to transpression related to oblique convergence between two independent blocks belonging to the South American plates: the Maracaibo triangular block to the west, and the Guyana shield to the east (Dhont *et al.*, 2005). This process led to an inversion of a pre-existing Jurassic graben, exposing crystalline and metamorphic rocks of Precambrian to Paleozoic age in the central part of the MA. During this Pliocene - Pleistocene E-W compression the North Andean depocenter was reinforced by approximately 9150 m of sediments (Duerto, 1998).

As a consequence of the relative convergence between the Maracaibo triangular block and the Guyana shield, a strike-slip regime of deformation developed, and it is marked by shearing along the BF, Burbusay (BUF) and Valera (VF) faults, which individualized two triangular wedges in the larger Trujillo Block. This strike-slip faulting-dominated compressional–extensional tectonic regime allowed the crustal Trujillo Block to move towards the NE (Backé *et al.*, 2006). The Trujillo Bock is bounded laterally by both the BF and VF fault systems and is assumed to have a detachment level at mid-crustal depth (~15 km) (Dhont *et al.*, 2012).

According to Backé *et al.* (2006), the last stage of deformation of the MA and western Venezuela is still active today and corresponds to an extension phase. Extension, turning progressively from SE to NE in the central part of the Trujillo Block, is associated with the motion of crustal blocks moving relative to each other, probably above a detachment located at upper-lower crust transition. Such extensional deformation can be understood considering that the crust extends and stretches at the same time as it moves towards the NE. The crustal blocks are escaping towards the Caribbean Plate, which is subducting under South America and is moving laterally towards the east at the same time.

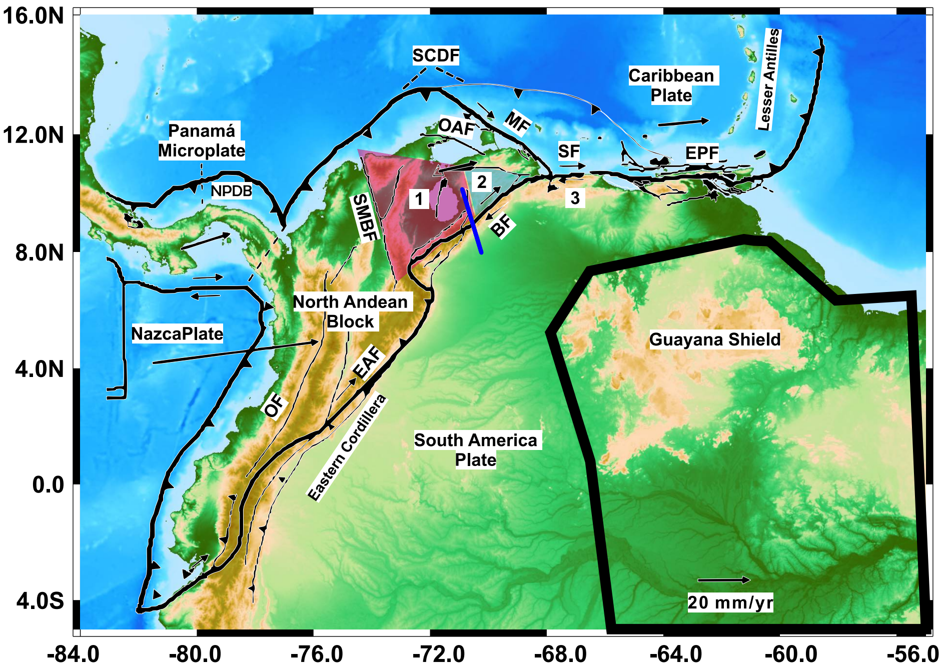

Figure 1.1.: Schematic geodynamic setting of north-western South America (modified from Pérez *et al.*, 2018). The black line indicates the position of the MT profile. Abbreviations: NPDB - Northern Panamá Deformation Belt, OF - Oriente Fault, EAF - East Andean Fault, SCDF - South Caribbean Deformed Belt, MF - Morrocoy Fault, OAF- Ocá - Acón Fault, BF - Boconó Fault, SMBF - Santa Marta - Bucaramanga Fault, SF - Sebastian Fault and EPF - El Pilar Fault. 1 - Maracaibo Triangular Block (MTB, limited by SMBF - BF - OAF) 2 - Trujillo Triangular Block (TTB) and 3 - Coastal Cordillera. Relative motion vectors compiled by Pérez *et al.*, 2018.

Such a unique geodynamic setting not only favours the north-eastward motion of the North Andean Block but also can be considered as a driving force for the escape process. The structural pattern of the Venezuelan Andes is dominated by escape structures, namely strike-slip faults binding escaping wedges and by normal faults accommodating the gravitational collapse of the topographic highs (Backé *et al.*, 2006).

Several authors (e.g. Audemard *et al.*, 1999; Audemard & Audemard, 2002; Backé *et al.*, 2006; Monod *et al.*, 2010; Dhont *et al.*, 2012) agree that the present-day distribution of the deformation in the Mérida Andes is consistent with strain partitioning with compression restricted on both flanks of the mountain belt, and strike-slip and extension occurring in the central part of the mountain range.

1.2. Regional structures

1.2.1. The Caribbean Plate

The Caribbean plate, located between the longitudes 60° and 90° W and latitudes 10° and 20° N, has an area of approximately 3,500,000 km^2. From west to east, it extends from Middle America to the Lesser Antilles and from north to south, from Cuba to the northern limit of the South American plate (Figure 1.2).

Historical seismicity (e.g. Molnar & Sykes, 1969) shows well defined western and eastern boundaries, the Middle American subduction zone and the Lesser Antilles subduction zone, respectively. However, the northern and southern boundaries are not well defined. The northern boundary is dominated by the transcurrent displacement along a fault system extending from the middle of Guatemala to the Lesser Antilles. In comparison, the southern boundary of the Caribbean plate controls northern Venezuela geodynamics.

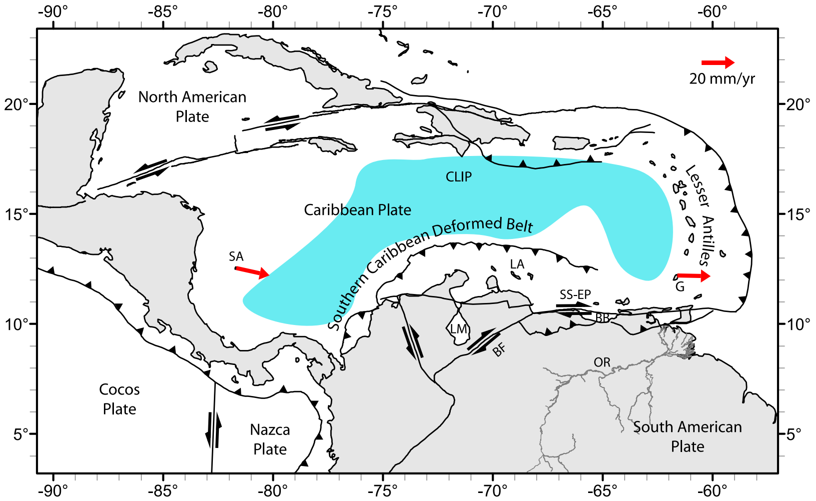

Figure 1.2.: Plate boundaries in the Caribbean from the University of Texas - Institute for Geophysics (UTIG) plates database. SA - San Andrés island; LA - Leeward Antilles; G - Grenada; CLIP - Caribbean Large Igneous Province (light blue shaded area); LM - Lake Maracaibo; SS-EP - San Sebastián-El Pilar fault system; BF - Boconó fault system; BB - Barcelona Bay; OR - Orinoco River. Red arrows show the motion of the Caribbean plate relative to the South American plate (after Calais & Mann, 2009).

The southern boundary is characterized by Pindell & Barrett (1990) as a complex shifting zone with transcurrent movement and rifting, while Audemard & Audemard (2002) define it as an over 100 km wide active transpressional zone. Off the coast of north-western Venezuela, the Caribbean crust is anomalously thick; Burke (1978; 1988) proposed thickness of 15-20 km to explain the central 4 km depth of the Caribbean sea-floor.

The abnormally light Caribbean Plate overrides the South American Plate (James *et al.*, 2009). Thus, the tectonic settings do not conform to a typical oceanic-continental collision. The subduction process varies largely from NW to NE South America. The former is defined by three different slab segments separated by kinks or bends: a north-western shallow and very flat slab segment with a central intermediate-depth and flat slab segment with could have different geometries, thicknesses, and physical properties; a south-eastern deep slab (Taboada *et al.*, 2000; Mora *et al.*, 2017); and a very steep slab segment imaged by Bezada *et al.* (2010). Whereas, towards the NE the boundary between the Caribbean and South American plates is dominated by right-lateral easterly oriented shear motion of $\sim 19.6 \pm 2.8\, mm/yr$, which splits along to easterly striking, right-lateral subparallel fault zones: the San Sebastian fault ($\sim 17 \pm 0.5\, mm/yr$) and the La Victoria fault ($\sim 2.6 \pm 0.4\, mm/yr$) (Pérez *et al.*, 2018).

The steep descent of the Caribbean plate under the Maracaibo block and the Mérida Andes indicate that there should be a tear in the Caribbean Plate (Taboada *et al.*, 2000; Bezada *et al.*, 2010; Masy *et al.*, 2011; Levander *et al.*, 2014), which would be separating the steeper dipping Caribbean slabs, located to the south of the Oca-Acón-El Pilar-San Sebastián dextral fault system (OEPFS), from the shallow Caribbean Plate that has been imaged north of the same fault system. Expanding on this concept Mora *et al.* (2017) explain that the boundary between northern South America and the Caribbean Plate consists of two tears or subduction-transform edge propagators (STEP, i.e. Govers & Wortel, 2005) (see Fig. 1.3). To the east, one STEP is tearing the Atlantic/South American Plates, at the eastern end of the OEPFS in north-eastern Venezuela (Russo *et al.*, 1993). To the west, another STEP would be tearing the Caribbean Plate in an undefined area of the western OEPFS, probably close to the Sierra Nevada de Santa Marta. This suggest that the Oca-San Sebastián-El Pilar dextral fault system is the tear fault that limits the Caribbean and South American/Atlantic Plates at crustal and mantle levels.

The complex interaction of different tectonic settings along the Caribbean plate boundaries resulted in the formation of several micro-plates and tectonic blocks (Byrne *et al.*, 1985; Mann *et al.*, 1990; Jansma *et al.*, 2000). Along the northern border, the Gonave and La Española micro-plates and the Puerto Rico-Virgin Islands block can be found. Along the southern border, there are the Maracaibo, Romeral and Panamá Blocks (Mann *et al.*, 1990).

Origins of the Caribbean Plate

There are two fundamentally different groups of models for the formation and plate tectonic evolution of the Caribbean plate. The first group of models suggests formation of the Caribbean crust in a position between North America and South America plates, known as the in-situ

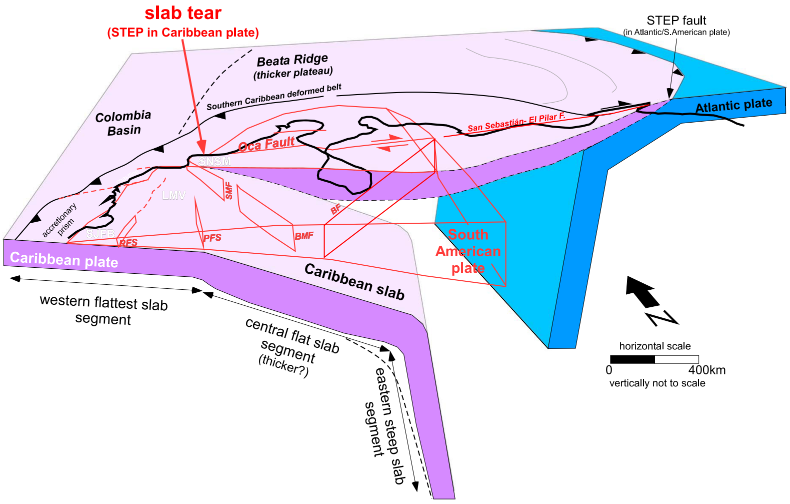

Figure 1.3.: Three-dimensional lithospheric configuration of NW South America, as interpreted from shallow reflection seismic mapping, intermediate-depth seismicity, and deep tomographic imaging (taken from Mora *et al.*, 2017); including a slab tear or STEP fault (Govers & Wortel, 2005) in the Caribbean Plate (see text).

model. Whereas, the second group suggests an origin in the Pacific Ocean and the north-eastwards migration of the Caribbean plate to its current position, known as the pacific model. In the following a summary of the main aspect of each model taken from James (2005b) is presented:

The in-situ model

In this model, the Caribbean Plate is part of the oceanic province that formed when North America drifted NW from Gondwana in the Jurassic-Early Cretaceous (Meschede & Frisch, 1998). Thickening of ocean crust in areas of the present-day Venezuelan, Yucatan and Colombian basins occurred as a result of extension, possibly over triple junctions heralding spreading jumps to the Atlantic and Pacific in the Aptian (James, 2005a), as presented in Figure 1.4a. Interaction between the Caribbean area and the new spreading centres resulted in outward facing island-arcs along the boundaries of the newly identified plate to the east and south-west.

Strike-slip along the northern and southern plate boundaries resulted in thrusting and complementary foreland basins and pull-apart extension, all becoming younger to the east. Continued convergence between the Pacific Cocos Plate and the Atlantic Plate resulted in continued volcanic-arc activity along the south-western and eastern plate boundaries.

This theory has been recently supported by an investigation on magnetic anomalies (Orihuela Guevara *et al.*, 2012). This study shows that, the magnetic striped pattern of the Eastern Caribbean is associated with a low-spreading centre compared to the velocity of the currently active ridges. Velocity estimation suggests that the Caribbean stripes are similar to those of the North Atlantic.

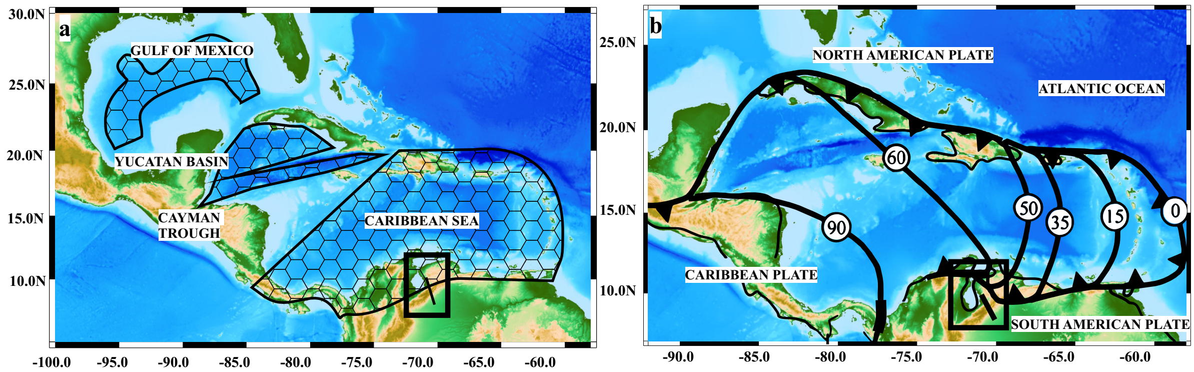

Figure 1.4.: In-situ (a) and Pacific (a) models for the origin of the Caribbean Plate. For simplicity, both are shown in the context of a modern map with topography and bathymetry taken from NOAA database (Amante & Eakins, 2009). (a) shows formation of oceanic areas (cross-hatched) between W-NW, sinistrally diverging North and South America in the Jurassic - Early Cretaceous (taken from James *et al.*, 2009). (b) shows stages of arc migration, at the leading edge of the Caribbean Plate as it migrated from the Pacific (modified from Escalona & Mann, 2006a).

The Pacific model

The "proto-Caribbean" and the Gulf of Mexico formed in the Jurassic to Early Cretaceous as North America drifted away from Pangea. An east-facing island arc ('proto Antilles' or "Caribbean Great Arc") trended NW-SE across the western end of the proto-Caribbean, extending alongside Mexico and NW South America. The Caribbean Plate formed west or south of this, with a west-facing volcanic arc on its west flank. The Caribbean Plate thickened to form a Large Igneous Province/Ocean Plateau, either as it migrated north-eastward across the Galapagos Hot Spot (e.g. Duncan & Hargraves, 1984; Bouysse, 1988) or above a rapidly melting mantle plume head (or both) (Hall *et al.*, 1995; Kerr *et al.*, 1997), or above two plumes, Sala y Gomez and Galapagos. The plate then entered the gap between North and South America, overriding 'proto- Caribbean' oceanic crust (Figure 1.4b), after a reversal of subduction direction below the leading edge of the 'Great Arc'.Volcanic activity ceased along the northern and southern Great Arc segments after they had rotated and collided with North and South America in the Paleocene-Middle Eocene.

The Caribbean Plate assumed an eastward migration direction relative to North and South America from the Oligocene onwards. Sinistral and dextral offset of 1,100 to 1,300 km occurred along the northern and southern plate boundaries since Cayman Trough opening began in the Eocene.

1.2.2. The North Andean Block

The North Andean block is a micro-plate attached to the South American plate formed from the crustal deformation in Central and South America, as a result of the complex interaction of the Nazca, Cocos, Caribbean, and South American plates, as shown in Fig. 1.1. The escape of the North Andes is believed to be a result of increased coupling between the obliquely subducting Nazca plate and the overriding South American Plate due to the subduction of the Carnegie Ridge in the Ecuador–Colombia trench (e.g. Lonsdale, 1978; Freymueller *et al.*, 1993; Gutscher *et al.*, 1999), a process known as slip partitioning. The beginning of this escape is dated at least 1.8 Ma if the subduction of the Carnegie Ridge is the driving mechanism for the north-westward displacement (Egbue & Kellogg, 2010). This deformation process is partitioned along several right-lateral slip fault traces of the N-S-trending eastern cordillera and the NE-trending Boconó fault system.

The North Andean block is bounded by the Colombian–Ecuador trench and the Panama block to the west, the South Caribbean deformed belt to the north, and the Boconó fault and East Andean fault zones to the east (Pennington, 1981; Kellogg & Vega, 1995). Compiled GPS data by Egbue & Kellogg (2010) show that the North Andean block NE movement relative to the South American plate at a rate of 2 to 10 mm/a. Pérez *et al.* (2018), however, define the north-eastern boundary of the North Andean block at a triple junction between the Morrocoy, Boconó and San Sebastian fault systems in northern Venezuela (see Fig. 1.1), and a displacement rate relative to the South American plate of 15 mm/a.

The North Andes block is composed of several continental units that move around relative to their neighbour while at the same time all moving together towards the NE (Backé *et al.*, 2006). The occurrence of a detachment level located at the upper-lower crust transition under the Venezuelan Andes (Chacín *et al.*, 2005; Duerto *et al.*, 2006) favours the lateral displacements of upper crustal sheets (Meissner & Mooney, 1998) like the Trujillo block. However, the tectonic escape of the Trujillo block, as well as the tectonic escape of the North Andes block, necessarily implies the existence of a free boundary away from the collision zone to be effective. The Caribbean plate provides unusual conditions to constitute such a weak boundary (Ego *et al.*, 1996).

The Maracaibo Block

The Maracaibo Block is a fraction of independent continental lithosphere triangularly shaped located in north-western Venezuela as presented in Figure 1.5. The block bounded by the left-lateral Santa Marta-Bucaramanga fault to the west; the right-lateral Boconó fault, to the east, and by the south-Caribbean deformed belt, to the north (Mann & Burke, 1984). This region has been interpreted as an escaping continental block squeezed in an area of intra-continental shortening (Backé *et al.*, 2006) as a consequence of the late-Neogene west to east collision of the Panamá arc with north-western South America (Mann *et al.*, 1990; Audemard & Audemard, 2002). The Maracaibo Block is cut by a series of N–S left-lateral strike-slip faults separating several crustal units (Audemard *et al.*, 2000; Escalona & Mann, 2003; Mann *et al.*, 2006). Among these, the most important is the easternmost Trujillo Block (Hervouët *et al.*, 2001).

The NNE extrusion of the Maracaibo Block with respect to South America caused this block to override the Caribbean plate north of the Leeward Antilles Islands, where a young south-dipping, amagmatic, flat oceanic subduction of low dip in S direction has been forming in the last 5 Ma (Audemard *et al.*, 2000).

The oblique convergence between the Maracaibo Block and the Guyana shield has led to strain partitioning along the Mérida Andes (e.g. Rod, 1956; Colletta *et al.*, 1997; Audemard & Audemard, 2002; Audemard, 2003; Audemard *et al.*, 2006), divided between (1) shortening perpendicular to the belt and which causes uplift and development of the Northern and Southern Thrust Systems, (2) right-lateral strike-slip movement along the Boconó Fault, and (3) the partition and tectonic escape of the Trujillo Block (Backé *et al.*, 2006).

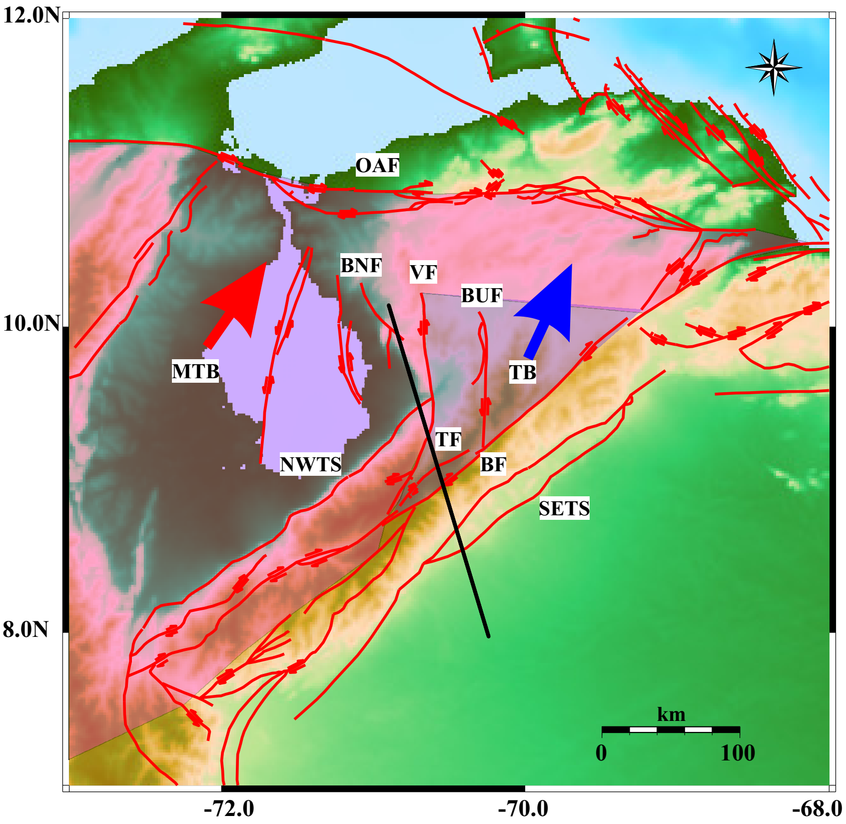

Figure 1.5.: Location of the Maracaibo (MTB) and Trujillo (TB) blocks shown in the context of a modern map with topography and bathymetry taken from NOAA database (Amante & Eakins, 2009) and the Quaternary fault system (red lines after Audemard *et al.*, 2006). The blue and red arrows indicate the orientation of the tectonic escape (see text). Abbreviations: MTB - Maracaibo Triangular Block, TB - Trujillo Block, BNF - Burro Negro Fault, VF - Valera fault, TF - Tuñame Fault, BF - Boconó fault, BUF - Burbusay Fault, NWTS - Northwestern thrust system (also known as Las Virtudes thrust system) and SETS - South-eastern thrust system.

The Trujillo Block

The Trujillo Block is a partition of the Maracaibo Triangular Block formed due to E-W convergence between the Maracaibo Block to the north-west and the Guyana shield to the south-east (Fig. 1.5). As mentioned, this oblique collision resulted in strain partitioning that is partially accommodated by the tectonic escape to the NE of the Trujillo block. According to Hervouët *et al.* (2001) and Dhont *et al.* (2005), the Trujillo Block moves towards the NE as a consequence of conjugate strike slip motions along the Boconó and Valera faults (Fig. 1.6a). Dhont *et al.* (2012) concludes that the Trujillo Block is composed by a series of crustal fault-bounded blocks, that are tilted in agreement with a recent (possibly Plio-Quaternary) extension and/or transtension;

and that the geometry and organisation of the faults at depth indicate that the escape the block might be associated to a general spreading of the upper crust due to extension. Considering that motion of the Trujillo Block is related to such tectonic escape process, it should be subjected to both horizontal lateral flow and large-scale extensional deformation (Backé *et al.*, 2006).

The Trujillo Block is bounded laterally both by the Boconó and Valera - Motatán fault systems and by a detachment level at mid-crustal depth (15 km) (Dhont *et al.*, 2005). Its southern termination is composed of smaller blocks limited by the Motatán, Momboy and Tuñame normal faults (Fig. 1.6b). These faults connect to the Boconó fault at a shallow (8 km) level in the crust and form individual tilted wedge-shaped fault blocks (Dhont *et al.*, 2012).

The Trujillo Block is cut by two main ~ N–S left-lateral strike-slip structures. These are (1) the Burbusay fault, to the west, and (2) the El Tocuyo fault, to the east, which have been interpreted as active structures during the Plio-Quaternary (Backé *et al.*, 2006).

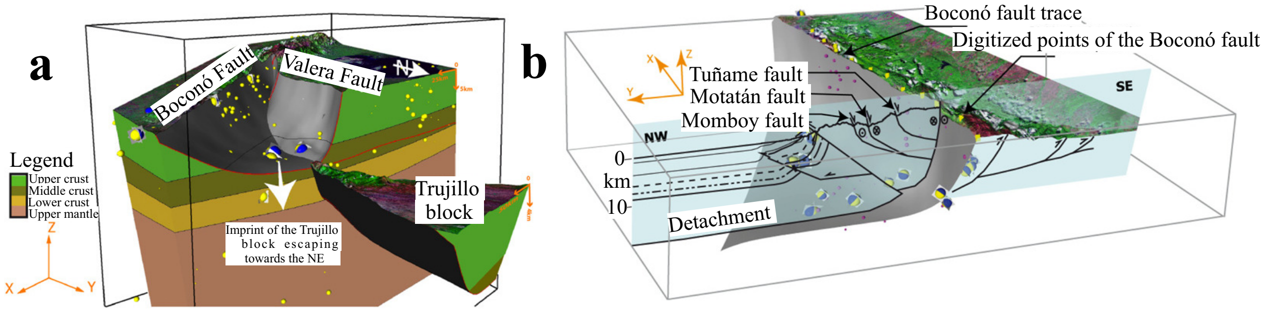

Figure 1.6.: Schematics of the Trujillo Block and its internal subdivisions (taken from Dhont *et al.*, 2012). (a) Block diagram intended to display the shape of the Trujillo Block at depth. The connection between the Boconó and Valera faults at depth forms an intersection line dipping towards the north from the surface until mid-crustal depth (~15 km). (b) A crustal scale cross-section (Monod *et al.*, 2010) used to construct the 3D shape of the Boconó fault at depth (Dhont *et al.*, 2012).

1.3. Crustal models proposed for the Mérida Andes

Over the last 70 years, several models have been proposed to explain the current geometry of the Mérida Andes regarding their geodynamic evolution (e.g. González de Juana, 1972). This mountain chain is related to the complex geodynamic settings resulting from the interaction between the Caribbean, South America and Nazca plates (Audemard *et al.*, 2000). The plate boundary in western Venezuela is up to 600 km wide and comprises a set of discrete tectonic blocks, independently moving among the surrounding larger plates (Audemard *et al.*, 2000).

Audemard & Audemard (2002) explain that in general, two main conceptual currents explain the structural configuration, the geometry and the interaction of the deep structures of the mountain chain. On one hand, some models have conceived the MA as an essentially symmetric chain to a major axial strike-slip fault, with both sides bounded by reverse faults—responsible for chain vertical growth. Consequently, the MA would resemble a positive flower structure. On the other hand, several other models incorporated the asymmetry of the MA revealed by the gravimetric survey of Hospers & VanWijnen (1959); as a matter of fact, gravity anomaly studies (e.g. Bonini, 1978; Chacín *et al.*, 2005) revealed considerable differences in thickness in the fore-deep and foreland basins associated to the MA, which is considered to be directly related to the asymmetry of the mountain chain.

The main problem of the proposed crustal models is that they give little importance to the horizontal shearing, which is responsible for both strain partitioning in the belt and NE-ward motion of the Trujillo Block resulting from a tectonic escape driven by both the Boconó and Valera strike-slip faults (Dhont *et al.*, 2005; Backé *et al.*, 2006). Jácome *et al.* (1995); Audemard & Audemard (2002); Monod *et al.* (2010) proposed an orogenic float model for the *MA* based on the orogenic float concept for transpressional orogens (Oldow *et al.*, 1990). In this model, the Boconó fault (BF) is considered an upper crustal fault and connects to a mid-crustal detachment level, so the orogen "floats" on its underlying lithosphere.

Following the general division of Audemard & Audemard (2002) and including the orogenic float model, Monod *et al.* (2010) compiled a summary of the different crustal models for the formation of the MA noting their advantages and possible problems. These descriptions are reproduced in the following:

1.3.1. Symmetrical orogen

Positive flower structure

According to Rod (1956) and González de Juana (1972), the Mérida Andes formed as a positive flower structure (Fig. 1.7a). Shortening by inversion of an older rift basin is responsible for vertical growth of the belt, which is controlled by the opposite vergent thrust systems on both flanks symmetrically branching the Boconó wrench fault (Taboada *et al.*, 2000). This model accounts for both strain partitioning and inversion of former asymmetric Late Jurassic grabens. It also requires that lateral movement along the Boconó fault and mountain building are coeval. However, the Mérida Andes started to rise in the Miocene with a main orogenic pulse in the Pliocene, whereas initiation of Boconó fault is supposed to be younger than that. Another problem is that the flower structure model does not account for the geometry of the structures at a depth greater than the upper crust.

Laramide style low-angle subduction

Duerto *et al.* (2006)developed a model in which the flat slab subduction of the Caribbean oceanic plate beneath the Maracaibo Block (van der Hilst & Mann, 1994; Taboada *et al.*, 2000; Pindell *et al.*, 2005) extents further south under the Venezuelan Andes (Figure 1.7b). Shallow subduction of the Caribbean Plate creates a broad zone of shearing between the upper and lower plates. Transmission of the strength upwards produced uplift and shortening in the overriding South American plate. Subsequent deformation of the Venezuelan Andes in a pop-up style is related to the inversion of the NE-trending steep dipping normal faults inherited from the Late Jurassic extensional phase into reverse and strike–slip faults. However, the southward extension of the Caribbean slab is not accounted for by the intermediate seismicity (Dewey, 1972; Pérez *et al.*, 1997); and the role played by the Boconó and Valera faults is not explained. Malavé & Suárez (1995) show seismicity related to Maracaibo Block to the south up to Bucaramanga.

1.3.2. Asymmetrical orogen

SE-directed continental subduction

Some authors favour the hypothesis of SE-directed continental subduction of the Maracaibo crust under the Guyana shield (Kellogg & Bonini, 1982; De Toni & Kellogg, 1993; Sánchez *et al.*, 1994) (Figure 1.7c). The model has been further refined by Colletta *et al.* (1997) by taking into account the inversion of the Late Jurassic grabens. The main argument for a SE subduction polarity comes from the sinking of the basement in the Maracaibo basin, which is deeper than the Barinas–Apure basin. The SE polarity model is also consistent with the development of a series of NW-vergent late Neogene imbricated duplexes cut by the SE-dipping Pliocene–Quaternary Las Virtudes thrust in the north-western flank of the belt (Audemard, 1992; Hervouët *et al.*, 2001). Nevertheless, this model gives little importance to the Boconó fault, which is a major structure accommodating the NE-ward motion of the Maracaibo block.

NW-directed continental subduction

Audemard (1992) proposed a model in which the structure of the Venezuelan Andes results from an incipient NW-directed continental subduction presented in Figure 1.7d. The Maracaibo and the Barinas–Apure basins formed as flexural basins loaded by the weight of the belt, the former being deeper because of its smaller lateral dimensions. The main evidence for an NW subduction polarity comes from consideration of difference of crustal thicknesses between the thin crust of the Maracaibo basin (29 km, Padrón & Izarra, 1996), which experienced the Late Jurassic rifting event, and the relatively thick Guyana shield 46 km (Schmitz *et al.*, 2002) and 42 km (Schmitz *et al.*, 2008). Eocene rifting of the Maracaibo basin according toEscalona & Mann (2003) may also account for a thinner crust even if the 0.8 to 2.25 km amount of Eocene extension is small relative to the Jurassic rifting and that it probably did not influence the present-day deep crustal structure of the belt.

As pointed out by Audemard & Audemard (2002), the colder and denser Guyana crust would under-thrust the Maracaibo crust rather than the opposite. Gravity modelling along an NW–SE trans-Andean transect presents a crustal break interpreted as an incipient NW-directed underthrusting of the South American cratonic crust beneath the Barinas–Apure basin and the less rigid Maracaibo transitional crust (Chacín *et al.*, 2005).

1.3.3. Orogenic float model

The model of NW-directed subduction has been improved by Jácome *et al.* (1995); Yoris & Ostos (1997); Audemard & Audemard (2002) and others who proposed a model based on the orogenic float concept for transpressional orogens (Oldow *et al.*, 1990) and presented in Figure 1.7e. Following this model, the Boconó fault and the major thrusts involved in the strain partitioning connect to the mid-crustal décollement level and may, therefore, be considered as upper crustal faults, so that the crustal section of the orogen “floats” on its underlying lithosphere. Within continent–continent and ocean–continent oblique subductions, the orogenic float concept explains asymmetrical orogens undergoing strain partitioning resulting in the development of coeval thrust and strike– slip faults. In this case, convergence between the South Caribbean plate and the Maracaibo block is the driving force for the development of fold-and-thrust belts in the Northern Andes, inducing significant deformation accommodated in the Mérida Andes far from the main S-directed South Caribbean collisional front (Monod *et al.*, 2010). Employing the methodology of balanced cross-sections across the MA, Monod *et al.* (2010) estimated a total shortening of 40 km to the southern part of the MA and 30 km for the northern one. The difference of 10 km of shortening between both cross-sections may be related to the escape of the Trujillo block, which therefore absorbs a quarter of the contractional strain. The orogenic float model not only explains the deep structures of the MA but also the NNE tectonic escape of the Maracaibo block at a larger scale.

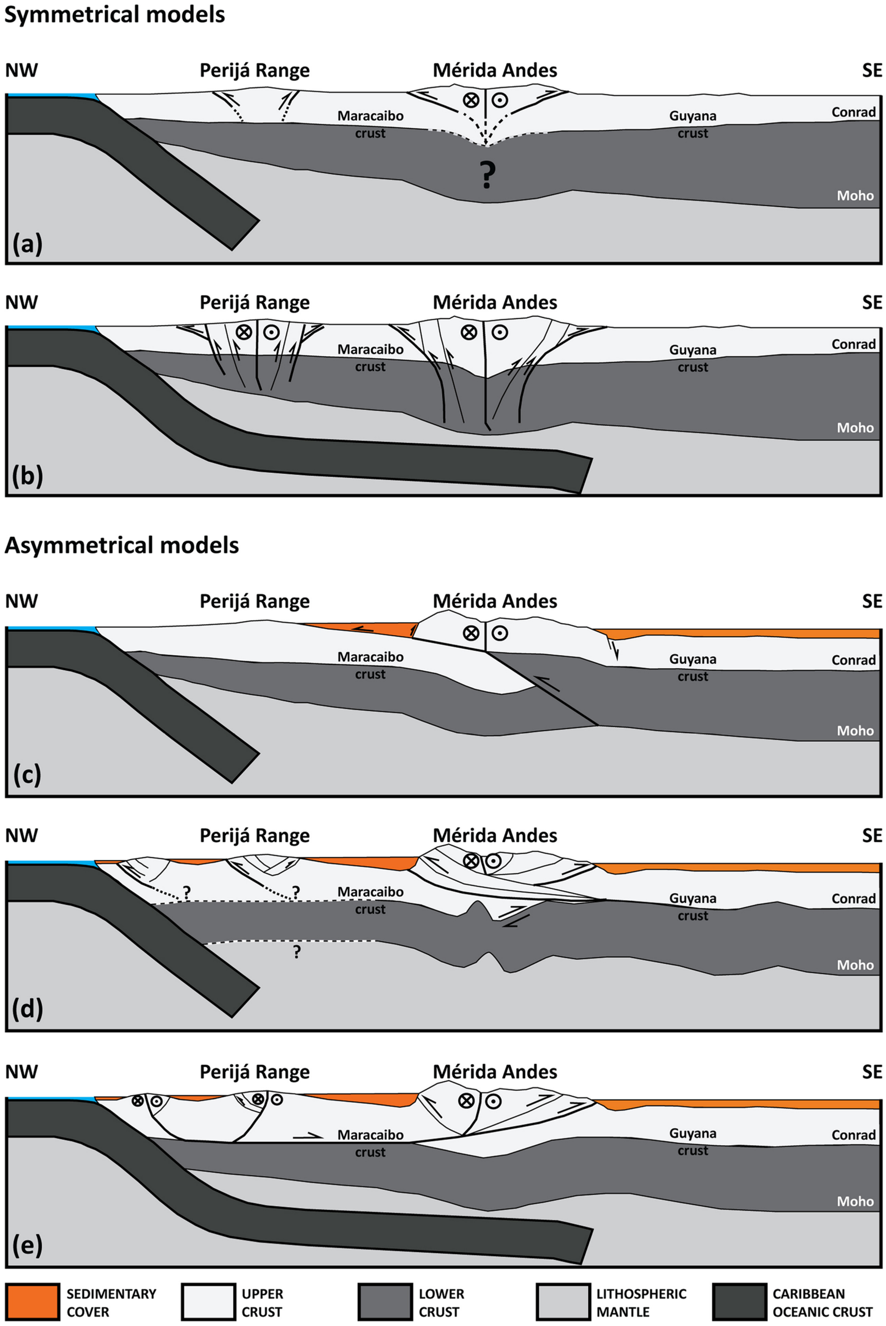

Figure 1.7.: Schematic diagrams (not to scale) showing the proposed models for the deep structures of north-western South America (modified from Monod *et al.*, 2010). Models are differentiated in symmetrical: (a) Positive flower structure; (b) Laramide style low-angle subduction; and asymmetrical; (c) SE-directed continental subduction; (d) NW-directed continental subduction; (e) Orogenic float model. (taken from Mazuera *et al.*, 2019).

1.4. Geological structures

The geology of the study area comprises three main structures, the Maracaibo and Barinas - Apure basins, and the Mérida Andes. Although the formation of the basins is related with the tectonic processes that uplifted the Venezuelan Andes, they present marked differences in terms of depth, extent, and structural development.

1.4.1. The Maracaibo basin

The Maracaibo basin (MB) is a 50,000-km^2 triangular inter-montane depression bounded to the east and west by Mérida Andes and Sierra de Perijá, respectively, and by the Ocá fault to the north as presented in Figure 1.8 (Duerto *et al.*, 2006). It is the most productive hydrocarbon basin in the Caribbean–South America region. The MB is reported to be an asymmetric through that contains up to 12 km of carbonates and shale of late Cretaceous to Eocene age (De Toni & Kellogg, 1993) at its depocenter. Towards its boundaries, the MB is as shallow as depths of about 2 km to 5 km (Escalona & Mann, 2003, 2006b), related to the uplift of the *MA* and the Perijá Range (see Fig. 1.8) and active fault systems to the east (the Burro Negro - *BNF*, and the Valera - *VF* faults).

The geology of the Maracaibo basin is dominated by complex Mesozoic–Cenozoic interactions between North American, South American and Caribbean plates. The basin records an evolution from the separation and rifting between North America and South America during the Jurassic, followed by migration of the Caribbean plate to its present position since the late Paleocene (e.g. Lugo & Mann, 1995). Active tectonic associated with the uplift of the MA exposed Paleozoic basement rocks, Mesozoic–Cenozoic carbonates, and clastic rocks that were folded and thrust by regional shortening in the Paleogene and late Neogene (Duerto *et al.*, 2006). The latter fostered deformation structures like synclines and anticlines and shale diapirism towards the edges of the basin (Escalona & Mann, 2006a).

The Maracaibo basin is actively subsiding and its topography and elongate geologic outcrop patterns of its boundaries are closely controlled by north-west to north-east transpressional strike–slip faults (e.g. Boconó fault) (Escalona & Mann, 2003).

1.4.2. The Mérida Andes

The Mérida Andes (MA) are the most prominent feature of Western Venezuela. They conform a 100 km-wide 425 km-long mountain chain that reaches a maximum elevation of ~5 km above the sea level (Figure 1.1 and 1.8). The MA are the eastern boundary of the North Andean

Block (Fig. 1.1) which moves towards the NNE by approximately 1.5 cm/year with respect to South America (Pérez *et al.*, 2018) since the Late Miocene (Audemard, 2014). Although the MA start as a prolongation of the Eastern Ranges of the Colombian Andes (Figure 1.1), both mountain chains have no genetic relationship, as the MA are not the result of a conventional type B subductive process. Instead, the MA developed as a transpressional orogen related to the complex relationship between the South American, Caribbean and Nazca plates, as the oceanic plates subduct under the continental plate. More specifically they are the result of the E–W low-angle convergence between the Maracaibo triangular block and the Guyana Shield since the late Miocene (Audemard & Audemard, 2002).

The present geodynamic setting is responsible for ongoing strain partitioning along the Mérida Andes where the foothills and the mountain belt have been shortened transversely in a NW–SE direction whereas the Boconó fault, roughly located in the core and along the Mérida Andes axis, accommodates dextral slip. Tectonic inheritance in the Mérida Andes plays a major role, since the chain growth partly results from inversion of Jurassic (half-) grabens, exposing Precambrian and Paleozoic rocks of the South American continental crust along the chain core (Audemard, 2003).

Along both flanks of the chain the uplift of the MA formed synorogenic molassic deposits, deposited in flexural basins, whose thicknesses reach 8 km and 3 km on the north-west and south-east of the Mérida Andes, respectively. These continental deposits of essentially Plio-Quaternary age are arranged in up-dip convergence growth wedges, which are being deformed or destroyed by basin-vergent intracutaneous wedges, triangular zones and/or flat-and-ramp structures rooted under the Mérida Andes (Audemard, 2003).

Moreover, Audemard (2003) reports that the MA core comprises igneous and metamorphic rocks formed at depths of 8–10 km, that are cropping out at its highest summits at about 5000 m elevation, implying a total uplift of the order of 12–15 km in the last 3–5 Ma (average uplift rate of 2–5 mm/a).

Audemard & Audemard (2002) argue that the mountain chain present two conspicuous foothills, that are clearly distinguishable along both flanks, the north-western and south-eastern foothills (Figure 1.8). The north-western foothills are defined by a major NW verging thrust sheet, the Las Virtudes overthrust (or *NWTS* in Fig. 1.8), which brings Precambrian and Paleozoic metamorphic rocks in contact with Tertiary rocks at the mountain front. The south-eastern foothills are defined by a NE-SW-trending flexural scarp facing SE, known as South-eastern thrust system which extends for over 200 km and reaches a maximum height of 300 m above the low topography of the Llanos plains (Audemard, 1999). The thrust system displays active flat-ramp thrust faults, triangular zones and associated piggy back basins filled with Late Miocene-Quaternary molassic deposits (Audemard & Audemard, 2002).

The most prominent tectonic features of the *MA* are the Boconó (*BF*) and Valera (*VF*) fault systems. According to Dhont *et al.* (2005) the *BF* is a NE-trending 500 km-long fault which cross-cuts the belt longitudinally more or less along its axial part. The VF is a ~240 km long left-lateral strike–slip cross-cutting the northern part of the MA.

1.4.3. The Barinas-Apure basin

The Barinas – Apure Basin (BAB) is Venezuela's third largest oil-producing basin. This depression has an area of about 95,000 $km^2$and a maximum depth of about 5000 m (González de Juana *et al.*, 1980b) and it is located in western Venezuela south-east of the Mérida Andes (Figure 1.8). This basin is separated from the Colombian Llanos basin by a gravimetric high reported by Hospers & VanWijnen (1959). The BAB had been described as an asymmetric basin, slightly inclined on its southern flank, following the tilt of the Guayana shield. This foreland basin formed as a result of the uplift of the MA in the Late Miocene. The central part of the BAB present grabens, which are considered as evidence of the opening of the Proto-Caribe associated with the separation of the Americas (Yoris & Ostos, 1997).

The BAB comprises in its stratigraphic section Aptian through Pleistocene sediments (Callejón & von der Dick, 2002). The Cretaceous section consists of sandstone, limestone, and shale. A tertiary section with a major oil-producing interval, characterized by sandstone and the Andean uplift is represented by the molassic sequences of sandstone, shale, and conglomerates. These sediments rest disconformably over a pre-Paleozoic basement of igneous and metamorphic rocks, exposed by the uplift of the *MA* (Callejón & von der Dick, 2002).

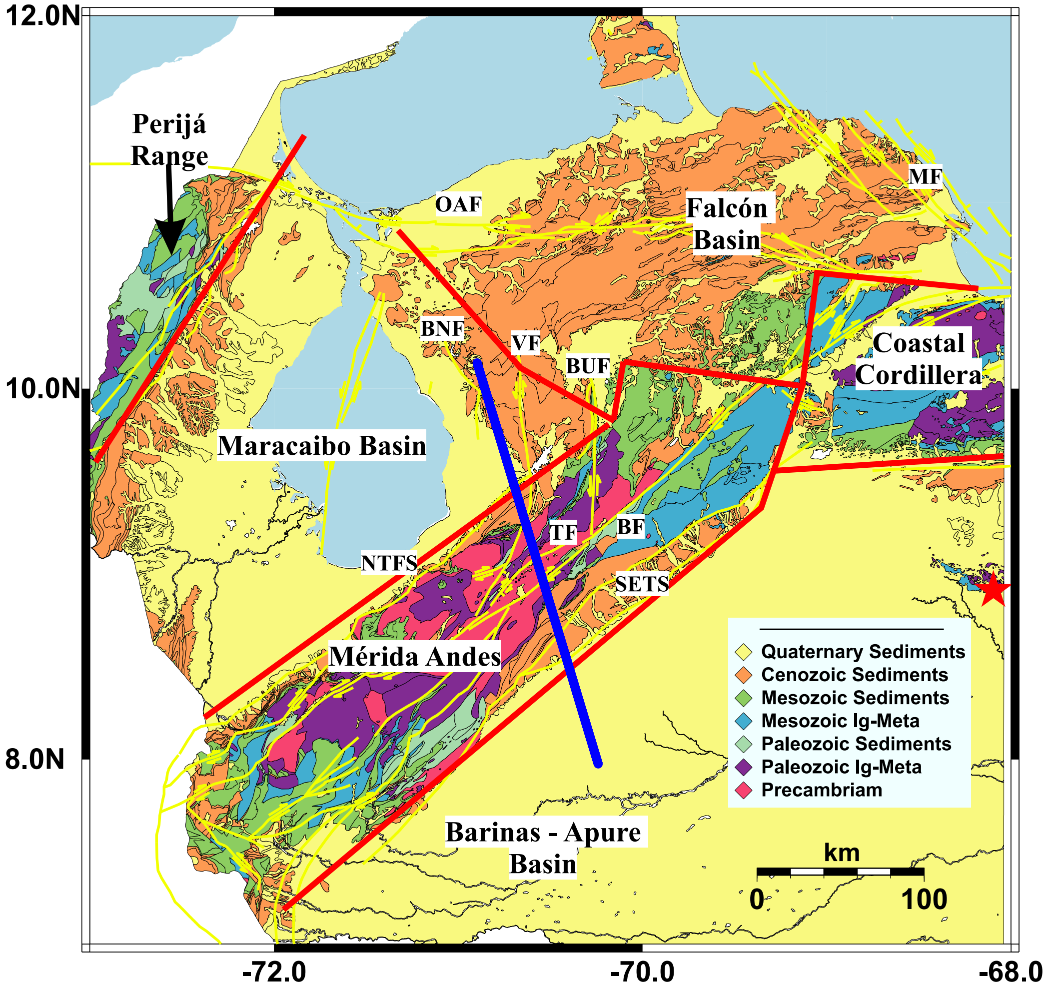

Figure 1.8.: Mayor tectonic units of western Venezuela based on a simplified geology after Hackley *et al.* (2006). Red lines mark the limits of the major surface structures after the classification of Urbani (2017). Quaternary fault systems are marked with yellow lines (after Audemard *et al.*, 2006). The blue line indicates the location of the MT profile. The red star marks the location of the remote reference MT station. Abbreviations see Figure 1.5. (taken from Cruces-Zabala *et al.*, 2020)

1.4.4. Main fault systems in the study area

Oca - Acón fault system

The Oca - Ancón fault system extends eastward from Santa Marta on the Caribbean coast of northern Colombia to the town of Boca de Aroa, located on the eastern coast of Falcón State (north-western Venezuela). According to Audemard *et al.* (1994) the Oca - Acón fault is a

650 km long right-lateral strike-slip fault system with a W-E orientation (Figs. 1.1, 1.5 and 1.8). Audemard *et al.* (2000) summarizes the tectonics of the fault system as: The Oca - Ancón fault system sharply truncates the north ends of the Santa Marta Block (northern Colombia) and the Perijá Range; both units are mainly composed of Mesozoic rocks whereas the remainder of the trace cuts across Quaternary alluvial units in the Maracaibo basin and Tertiary sedimentary rocks of the Falcón Range. Between the middle Miocene and the Pliocene this fault system played a leading role as part of the Caribbean-South America right-lateral strike-slip plate boundary.

Burro Negro fault system

Following the description from Escalona & Mann (2006b), the approximately 100-km-long Burro Negro fault is a right-lateral strike-slip fault separating less deformed, inner- to outer-shelf rocks of the western Maracaibo Basin from highly deformed, deep-marine rocks of the eastern Maracaibo Basin (Figs. 1.5 and 1.8). Seismic lines north-east of the Burro Negro fault zone show elongate, subsurface basins bounded by partially inverted reverse and strike-slip faults filled with about 3 km of Oligocene and Miocene clastic marine sedimentary rocks.

Valera fault system

The 220-240 km long left-lateral strike–slip Valera fault cross-cut the northern part of the Mérida Andes. It has a N30°E orientation south of Valera city and almost N-S north of the city (Figs. 1.5 and 1.8). The Valera fault has been described as a normal synsedimentary fault during the Mio-Pliocene (Kerher, 1925; Garcia & Campos, 1977), and is supposed to have been reactivated as a sinistral strike–slip fault in the Quaternary (Soulas *et al.*, 1985). Soulas & Giraldo (1994), also describe it as sinistral strike–slip fault in its northern strand and sinistral normal in its southern strand.

The Valera fault's Quaternary reactivation is considered complex, possibly as a consequence of its oblique position in respect to the Mérida Andes, and as a result of its change in direction around Valera city. Therefore, its northern and southern sections present different tectonic characteristics, despite of being part of the same fault system and being geographically connected (Soulas & Giraldo, 1994).

The northern segment of the Valera fault has a N-S orientation with a vertical dip. In general, it presents a maximum displacement of 1 mm/yr, which progressively decrease northwards until its value is no longer measurable. The southern segment presents a N30°E orientation and a SE dip, also known as the Momboy fault, its total Quaternary displacement is about 1.4 km, with an average of 0.7 mm/yr (Audemard *et al.*, 2000).

The Valera and associated Río Momboy faults extend roughly north-south through different geographical regions (Ziruma-Trujillo Range, northern Andes Foothills, and Andes Mountains) and geological units (Tertiary sedimentary sequence of the Maracaibo Basin, Mesozoic sedimentary units, and the Precambrian core of the Andes Mountains) (Audemard *et al.*, 2000). The Valera fault system is one of the north-south faults that rupture the Maracaibo Block into smaller discrete blocks that are rotated clockwise by dextral shear (i.e., bookshelf rotation) produced by the Oca - Ancón and Boconó faults on the N and SE, respectively.

Northwestern thrust system (also known as Las Virtudes thrust system)

The Northwestern thrust system is an active fault that represent the limit between the Andean mountain chain and the plains of the Maracaibo lake (Figs. 1.5 and 1.8). It is a reverse fault system extending about 150 km within the city of El Vigia and the town of Agua Viva (see Fig. 1.8), where it presumably joint the Burro Negro NE fault system (Palme de Osechas *et al.*, 2001).

The Northwestern thrust system formed during the Plio-Pleistocene as the Andean units overthrust the fore-deep basin (Hervouët *et al.*, 2001). The Las Virtudes overthrust brings Precambrian and Paleozoic metamorphic rocks, the Andean basement, in contact with Tertiary rocks at the mountain front (Audemard & Audemard, 2002).

Burbusay fault system

The Burbusay fault (BUF) is a N-S left lateral strike-slip structure with an approximate extension of 125 km, limited to the south by the Boconó Fault system (see Fig. 1.8). The BUF represents the most relevant tectonic feature in the Trujillo Block According to Audemard *et al.* (2007a), the BUF presents an active left-lateral horizontal Quaternary slip rate of 2-3 mm/year, with transpressive structures (hills and mountains) associated to its N-S section.

Tuñame fault system

The Tuñame fault is an active 66 km-long normal fault within the central Venezuelan Andes (Figs. 1.5 and 1.8). The kinematics of this fault results from a corner effect (mass deficiency) at the divergence of the Valera fault from the Boconó fault, produced by clockwise rotation induced by bookshelf rotation mechanism that is partly accommodated by the neighbouring left-lateral strike-slip Valera fault. The Tuñame fault used to be a reverse fault that juxtaposed Precambrian and Paleozoic rocks of the Andes core (Audemard *et al.*, 2000). It is formed by two different segments with their own orientation, that were reactivated during the Quaternary.

The northern segment has an extension of 30 km and an orientation of N65°E, it is considered to be an “echelon” fault with a main component normal and a secondary and smaller dextral one. It is dated 0.033 Ma at its bottom (Schubert, 1982) and 0.017 Ma at its top (Soulas & Giraldo, 1994). The southern segment has a N30°E orientation with a length of 20 km. It presents a Quaternary normal vertical component, with a strong dextral horizontal one (Soulas, 1986).

Boconó fault system

The NE–SW trending right-lateral-strike-slip Boconó fault runs slightly oblique to the MA chain axis and its north-eastern tip bounds the Caribbean Coast range of northern Venezuela on the west, thus extending for about 500 km between the Táchira depression at the border between Colombia and Venezuela, and Morón on the Caribbean coast of Venezuela (Audemard & Audemard, 2002) (Figs. 1.1, 1.5 and 1.8). Age estimates for this structure vary from late Miocene (Audemard & Audemard, 2002), Pliocene (Dewey, 1972), or Pleistocene (Schubert & Vivas, 1993). This fault system connects with the EW-trending San Sebastian-El Pilar and the Morrocoy fault system at the triple point that signals the eastern boundary of the North Andean Block (Pérez *et al.*, 2018) (see Fig. 1.1). Important thrusting also occurs subparallel to the Boconó fault on both sides of the Andes chain, which sustains the mountain’s height. Therefore, shear (and slip) partitioning occurs here due to an oblique (east-west) maximum horizontal stress (Audemard *et al.*, 2000).

The Boconó fault has been mapped and characterized by the large number of along-strike geomorphological features, such as: continuous series of aligned 1–5 km-wide valleys and linear depressions, passes, saddles, trenches, sag ponds, scarps and sharp ridges (as noted by Audemard & Audemard, 2002 after Rod, 1956; Giraldo, 1985; Schubert, 1980b,a, 1982; Soulas *et al.*, 1985; Soulas, 1986; Singer & Beltrán, 1996; Audemard *et al.*, 1999). The Boconó fault shows a Quaternary slip rate between 3-11 mm/year (Schubert, 1980a) and 5-9 mm/year (Soulas *et al.*, 1985; Soulas, 1986). These rates are essentially consistent with those predicted by plate motion models of about 1 cm/year, assuming that the Boconó fault is part of the main boundary between the Maracaibo triangular block and South America plate (e.g. Molnar & Sykes, 1969; Minster & Jordan, 1978; Soulas, 1986; Freymueller *et al.*, 1993).

The estimates of total displacement of the Boconó fault range from 9 km (Schubert, 1993), to 30 km estimated from the offset of the Bouger anomaly (Audemard & Audemard, 2002; Audemard *et al.*, 2007b) and to 80 km estimated from the shift of depositional ages of the Caribbean allochthons (Stephan, 1982). The initiation of movement on the Boconó fault is difficult to access mainly because sediments within the fault-bounded transtensional basins are continental formations and thus difficult to date. Because it is the focus of major earthquakes, many studies have dealt on the surface expression, kinematics, and paleoseismic history of the Boconó fault (see Audemard *et al.*, 2008 for a synthesis). Although, the geometry of the fault at depth together with its crustal or lithospheric nature remains unclear (Monod *et al.*, 2010), based on shear splitting wave analysis Masy *et al.* (2011) proposed the Boconó fault to have a deformation at lithospheric scale.

South-eastern thrust system (The Andes Southern Foothills Flexure)

The South-eastern thrust system or Andes Southern Foothills Flexure extends for 373 km, from the south-west of the city of Acarigua - Araure (on the north-east) (see Fig. 1.8)(Audemard *et al.*, 2000). This SE-vergent blind thrust fault is rooted under the Venezuelan Andes, and deforms the Neogene sedimentary (mainly molassic) sequence along the southern foothills of the Andean mountain chain. This structural feature comprises flats and ramps, but does not crop out since it has a blind fault tip that is responsible for flexing Quaternary alluvial terraces that form these foothills. This fault is an outer thrust of the much wider main thrust system, which forms the mountain-foothills boundary closer to the Andes. It is believe to be symmetrically opposed to the NE-vergent thrusts on the NW side of the Mérida Andes (the Northwestern thrust system).

1.5. The electrical resistivity of the Mérida Andes and surrounding structures

The central part of the MA consists mostly of Cenozoic and Mesozoic igneous-metamorphic rocks. Fault traces possibly operate as flow paths for groundwater concentrations, and the fracturing associated with the faults may increase the porosity of the surrounding formations. Drainage and alluvial deposits are reported along strike of the BF by Audemard & Audemard (2002). Another possible explanation for the conductivity contrast related to the BF is the presence of clay minerals on the faults. These minerals are commonly found in fault gouges and may contribute to the weakness of strike-slip faults (Unsworth *et al.*, 1997).

The foreland basins (MB and BAB) have similar sedimentary contents but different depocenter depths and are subjected to different deformation regimes. Nevertheless, their sedimentary content (sandstone, limestone, and shale) ranging from Cretaceous to Quaternary is considered mostly conductive material (low resistivity). High content of hydrocarbons and varying degrees of compactation related to the age of formation and tectonic processes may increase the resistivity of the rocks. These variation on resistivity may be an indication of the geodynamics of the area.

2. The magnetotelluric method

Magnetotellurics (MT) is a passive electromagnetic (EM) exploration method used to derive the electrical resistivity structure within the Earth from depths of a few tens of meters to the upper mantle by simultaneously measuring naturally occurring variations of the magnetic and electric fields at the surface. The electrical resistivity (ρ) is a is a physical property that quantifies the ability of materials to oppose the flow of electric currents. The method was introduced in the 1950s by Tikhonov (1950) and Cagniard (1953) and is based on the physical principle of EM induction, as explained by the Maxwell's equations.

2.1. The electrical resistivity of rocks

The electrical resistivity of geological materials, and its reciprocal the electrical conductivity (σ), depends on a wide range of petrological and physical parameters and it is sensitive to small changes in minor constituents of rocks (Schwarz, 1990). Resistivity values do not allow to unambiguously identify a specific rock; different lithologies and rock types have a similar range of resistivities (i.e. electrical resistivity of crustal rocks range several order of magnitude 0.1-100000 Ωm). The bulk resistivity of rocks is influenced by content of fluids, porosity, permeability, free carbon, presence of conducting minerals and rock-melts.

The conduction of (or resistance to) electrically charged particles through the Earth has been divided into three principal electrical charge propagation mechanisms (Simpson & Bahr, 2005):

- Electronic conduction, which occurs in metallic ore minerals (e.g. magnetite, haematite) that contain free electrons that can transport charge. This is particularly relevant in Earth's core, metallic ore and for graphite studies.
- Semi-conduction occurs in poor conductors containing few free charge carriers, meaning that only a small fraction of the electrons present in the medium contribute to conduction. Semi-conduction is expected to dominate in mantle minerals such as Olivine.
- Electrolytic conduction occurs in a solution containing free ions. This can be related to the content of saline water on a rock or structure, which increase the transmission of electrically charged particles. In active tectonic regions, any partial melt generated by

enhanced temperatures, adiabatic decompression or asthenospheric upwelling will also act as an electrolyte (e.g. Shankland & Waff, 1977).

Another important factor for conductive materials to enhance conductivities is the interconnectivity of the conductive areas within the resistive host medium (Simpson & Bahr, 2005). The porosity and permeability can vary significantly according to rock type and formation, and these two factors bare substantial influence in the value of electrical conductivity.

Figure 2.1 present the electrical resistivities for common Earth materials taking into account their origins, composition and exposition to erosion.

Identifying geological structures by their most common resistivity ranges and recognizing the processes that alter them is one of the purposes of MT data interpretation.

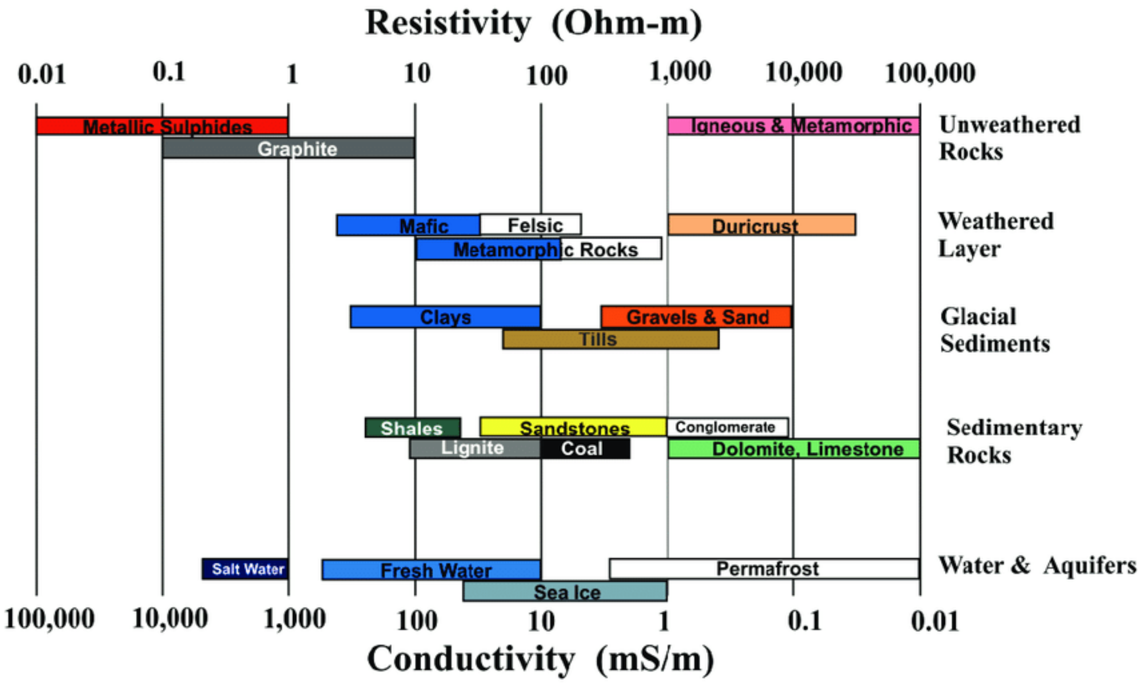

Figure 2.1.: Typical ranges of resistivities of Earth's Materials. After Palacky (1988).

2.2. Magnetotelluric sources

The MT method utilizes a wide period range of naturally generated EM field variations. In this thesis we focused on the period range from 10^{-4} s to 10^{5} s. Which is usually associated to two main sources (see Vozoff, 1991):

- Lightning discharge, and
- interaction of the solar wind with the Earth's magnetosphere

Electromagnetic fields of periods shorter than 1 s to about 10^{-3} s have their origin in lightning discharges occurring in the tropics because irradiation from the sun, which causes a huge upstream of air masses near the equator. The EM fields generated by these discharges can travel around the Earth between the conductive subsurface and the conductive ionosphere. These so-called *sferics* are more important to MT than local lightning discharges, which represent in-homogeneous sources and can lead to an overload in the data acquisition equipment.

Electromagnetic fields of periods longer than about 1 s originate in the EM interaction of charged particles coming from the sun, the solar wind, with the Earth's magnetosphere and ionosphere at heights of more than 60 km. Different processes like the separation of positively (protons) and negatively (electrons) charged particles in the magnetosphere, magnetic storms, trapping of charged particles by the Earth's magnetic field or deformation of the magnetosphere can cause strong and time dependent electric fields and currents.

Between those two period ranges there is an excitation minimum (see e.g. Simpson & Bahr, 2005). This so-called dead band that leads to significantly lower signal to noise ratios in the period range between 0.1 s and 10 s.

2.3. Electromagnetic induction in the Earth

In MT, it is assumed that natural EM field variations penetrate into the Earth and induce secondary EM fields. These secondary fields contain information about the electrical resistivity of the medium in which they propagate.

The phenomenon of EM induction which relates the observed natural fields can be described using Maxwell's equations.These equations describe the relation between the time varying electric and magnetic fields. Presented in their differential form Maxwell's laws are:

$$\nabla \times E = -\frac{\partial B}{\partial t} \tag{2.1}$$

$$\nabla \times H = J + \frac{\partial D}{\partial t} \tag{2.2}$$

$$\nabla \cdot B = 0 \tag{2.3}$$

$$\nabla \cdot D = q \tag{2.4}$$

Here, E is the electric field $[V/m]$, B is the magnetic flux density $[nT]$, H is the magnetic field

$[A/m]$, D is the electric displacement current $[C/m^2]$, and J is the current density $[A/m^2]$.

Equation 2.1 is the Faraday's law of induction, which indicates that the induced electric field is equal to the time rate of change of the magnetic flux. Equation 2.2 is the modified (after Maxwell) Ampère's law which relates the magnetic field with the electric current density and the electric displacement current. The third of Maxwell's laws, Gauss's law for magnetism (eq. 2.3), basically states that magnetic monopoles do not exist. While, the fourth of Maxwell's laws (eq. 2.4) is the Gauss's law for electricity which shows that the electric field is the result of the distribution of electric charge.

Maxwell's equations are complemented by the constitutive relationships for linear, isotropic and homogeneous materials:

$$D = \varepsilon E = \varepsilon_0 E \tag{2.5}$$

$$B = \mu H = \mu_0 H \tag{2.6}$$

where ε_0 and $\mu_0$are the electrical permittivity and magnetic permeability in the vacuum, respectively. Whose within the Earth can be considered as period independent, scalar quantities ($\varepsilon = \varepsilon_0 = 8.85x10^{-12}\,[F/m]$ and $\mu = \mu_0 = 1.2566x10^{-6}\,[H/m]$).

Following Faraday's law of induction (eq. 2.1), time-varying external magnetic fields induce an electric field within the earth's subsurface. This induced electric field drives electric currents, which eventually have an associated magnetic field according to Ampère's law (eq. 2.2). Applying the Ohm's law (eq. 2.7) to equation 2.2 we obtain:

$$J = \sigma E \tag{2.7}$$

$$\nabla \times H = \sigma E + \frac{\partial D}{\partial t} \tag{2.8}$$

Equation 2.8 shows that the magnitude of the induced magnetic field will be proportional to the electrical conductivity (σ) of the medium in which the induced currents flow. Therefore, the amplitude of the induced fields is dependent on the properties of the external fields and on the conductivity of underground materials.

2.4. Assumptions of the MT methods

For the purpose of investigation of the Earth with MT, the following simplifying assumptions are applicable:

1. the electric displacement field within the conductive Earth is quasi-static in MT. Therefore, time-varying displacement currents are negligible compared with the time-varying

conduction currents (i.e. $\frac{\partial D}{\partial t} \ll \sigma E$), hence equation 2.8 can be written as:

$$\nabla \times H = \sigma E \Longrightarrow \nabla \times B = \sigma \mu_0 E \tag{2.9}$$

there is no accumulation of free charges within a layered earth. However, within a multi dimensional earth, charges can accumulate along discontinuities, this is known as galvanic effect (Jiracek, 1990),

2. as the penetration depth of the fields is small compared to the source dimensions (Schmucker, 1987), the electromagnetic fields can be considered a homogeneous plane wave over the induction region (the plane wave assumption). Generally, practitioners assume that the plane wave assumption is valid at mid-latitude regions for periods shorter than 10000 s (e.g. Simpson & Bahr, 2005),
3. electromagnetic waves have harmonic time dependence (i.e. $F = F_0 e^{i\omega t}$, where A represents E or H, $\omega = 2\pi/T$, and T is the period of the wave [s]),

With these constrains, Maxwell's equations can be transformed. Multiplying equation 2.1 and equation 2.2 by $\nabla\times$, substituting B and E by its constitutive relationship and using equation 2.9 and considering that the electromagnetic sources lie outside the Earth ($\nabla \cdot E = 0$), the electric field E satisfy a diffusion equation of the form equation 2.10:

$$\nabla^2 F = \mu_0 \sigma \frac{\partial F}{\partial t} \tag{2.10}$$

With F representing either E or B, the fields can be represented as:

$$\nabla^2 E = i\mu_0 \sigma \omega E = k^2 E \tag{2.11}$$

$$\nabla^2 B = i\mu_0 \sigma \omega B = k^2 B \tag{2.12}$$

where $k = \sqrt{i\mu_0\sigma\omega}$ is the complex wave number, which describes the propagation of electric and magnetic fields as diffusion in a homogeneous medium of conductivity σ. In non-conducting regions, i.e. air layer, where $\sigma = 0$, we get:

$$\nabla^2 E = 0, \nabla^2 B = 0$$

Resolving the square root of the complex wave number yields:

$$k = \sqrt{i\mu_0\sigma\omega} = \sqrt{i}\sqrt{\mu_0\sigma\omega} = \frac{1+i}{\sqrt{2}}\sqrt{\mu_0\sigma\omega} = (1+i)\sqrt{\mu_0\sigma\omega/2} \tag{2.13}$$

Equation 2.13 shows that the wave number has equal real and imaginary parts. The real part is then defined as:

$$Real(k) = \frac{1}{p} \tag{2.14}$$

where $p = \sqrt{2/\mu_0\sigma\omega}$ is known as the *skin depth*. The *skin depth* is usually adopted as a criterion for the penetration of the electromagnetic wave. It describes at which depth the amplitude of the signal is reduced to $1/e$ of its original strength. For resistivity in Ωm and period in s, the skin depth is given in m in is simplified form as:

$$p \approx 500\sqrt{\rho T} \tag{2.15}$$

Taking into account the plane wave assumption and electromagnetic waves harmonic time dependence, equation 2.10 can be solved by the Fourier transform:

$$F = F_0 e^{i\omega t - kz} \tag{2.16}$$

Assuming a homogeneous half-space of resistivity ρ $(= 1/\sigma)$, by considering ratios between measured electromagnetic fields at surface, it is possible to gain information about the subsurface resistivity structure, independently of the intensity of the external fields. For example, the resistivity of the half space can be calculated from the ratio between orthogonal horizontal electric and magnetic fields, and their period, expanding from equation 2.1 and combining with equation 2.16:

$$\frac{\partial E_x}{\partial z} = -\frac{\partial B_y}{\partial t}$$

$$-kE_x = -i\omega B_y$$

$$\frac{E_x}{B_y} = \frac{i\omega}{k} = \sqrt{\frac{i2\pi\rho}{\mu_0 T}}$$

2.5. Magnetotelluric transfer functions

Maxwell equations show that, in the frequency domain, the electric and magnetic field components are linked by linear relationships. Such linear relationships can be described through transfer functions linking an input and an output quantity.

The impedance tensor

The magnetotelluric impedance tensor (Z) is the most common of the transfer function, it describes the linear relationship between the orthogonal horizontal components of the electric and magnetic fields.

Expanded to use all possible magnetic and electric horizontal component, the impedance in its tensorial form is presented as:

$$\begin{pmatrix} E_x \\ E_y \end{pmatrix} = \begin{pmatrix} Z_{xx} & Z_{xy} \\ Z_{yx} & Z_{yy} \end{pmatrix} \cdot \begin{pmatrix} B_x \\ B_y \end{pmatrix}; \, or \, Z_{ij} = \frac{E_i}{B_j} \tag{2.17}$$

with E being the electric field in $[V/m]$, B the magnetic field in $[T]$ and Z_{ij} $(i;j = x;y)$ the components of the impedance tensor Z in units of $[m/s]$. The impedance tensor Z is complex, being composed of both real and imaginary parts $Z = X + iY$. The complex tensor Z carries information about the Earth's electrical conductivity structure and its elements can be presented in magnitude in terms of apparent resistivity ρ_{ij} and phase ϕ_{ij}:

$$\rho_{ij}(\omega) = \frac{\mu_0}{\omega} |Z_{ij}(\omega)|^2 \tag{2.18}$$

$$\phi_{ij}(\omega) = arctan \frac{Imag(Z_{ij}(\omega))}{Real(Z_{ij}(\omega))} \tag{2.19}$$

The apparent resistivity is the average resistivity of the volume that is penetrated by the EM fields for a given period. The phase value expresses the phase lag between the electric and magnetic fields.

The vertical magnetic transfer function

The linear relation between the vertical magnetic component (B_z) and the horizontal magnetic field components (B_x, B_y), is described by the vertical magnetic transfer function (VTF) and can be written as:

$$B_z = \begin{pmatrix} T_x & T_y \end{pmatrix} \begin{pmatrix} B_x \\ B_y \end{pmatrix} \tag{2.20}$$

where T is the vertical magnetic transfer function, which emerges only if a lateral conductivity contrast is nearby. Typically, this transfer function is graphically represented by induction vectors (or arrows), which are composed by real and imaginary parts of T_x and T_y. In Wiese convention (Wiese, 1962), induction vectors of real parts point away from good conductors and are computed as:

$$amplitude = \sqrt{Re(T_x)^2 + Re(T_y)^2} \tag{2.21}$$

$$angle = arctan\left(\frac{Re(T_x)}{Re(T_y)}\right) \tag{2.22}$$

The imaginary part is computed accordingly. Figure 2.2 presents an example of the behaviour of the real component of the induction vector in the Wiese convention.

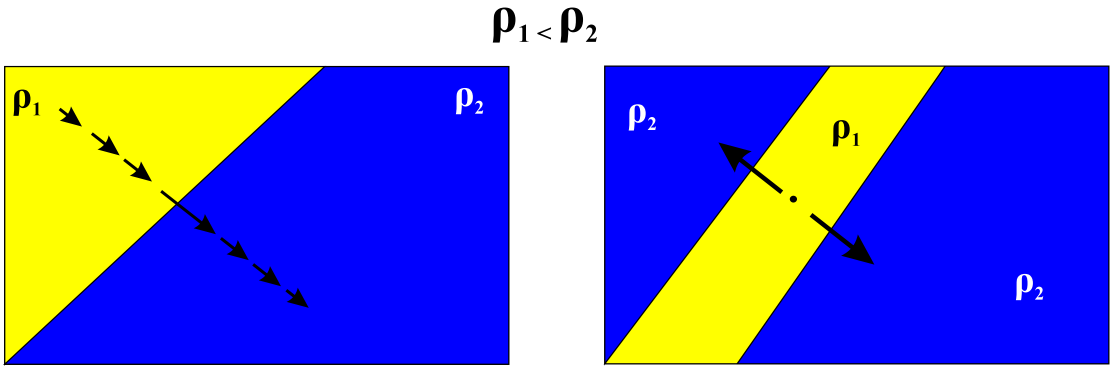

Figure 2.2.: Expected behaviour of the real induction vectors in Wiese convention.

Estimation of the transfer functions

For transfer function estimation, equations 2.17 and 2.20 have to be solved. They can be mathematically treated in the same manner using the simplified term:

$$X = Z_1 Y_1 + Z_2 Y_2 \tag{2.23}$$

This equation present a single output channel X and two input channels Y_1 and Y_2. The output channel X is associated to E_x and E_y or B_z for the row-wise solution of the impedance matrix or the vertical magnetic transfer function. The input channels Y_1 and Y_2 are associated with the horizontal magnetic fields B_x and B_y of the local station. Z_1 and Z_2 are the response functions normally solved using the least squares (LSQ) methods and presented as:

$$Z_1 = \frac{\langle Y_2 Y_2^* \rangle \langle X Y_1^* \rangle - \langle Y_2 Y_1^* \rangle \langle X Y_2^* \rangle}{\langle Y_1 Y_1^* \rangle \langle Y_2 Y_2^* \rangle - \langle Y_1 Y_2^* \rangle \langle Y_2 Y_1^* \rangle} \tag{2.24}$$

$$Z_2 = \frac{\langle Y_1 Y_1^* \rangle \langle X Y_2^* \rangle - \langle Y_1 Y_2^* \rangle \langle X Y_1^* \rangle}{\langle Y_1 Y_1^* \rangle \langle Y_2 Y_2^* \rangle - \langle Y_1 Y_2^* \rangle \langle Y_2 Y_1^* \rangle} \tag{2.25}$$

with $\langle\rangle$ representing the stacked auto- and cross-spectra.

Least squares methods can only product the best results possible if the EM noise is independent and follows a Gaussian distribution. However, as explained by Egbert & Booker (1986), MT data is deemed to have a considerable error due to the failure of basic assumptions in data source and noise distribution. Meaning that data can be populated with outliers and without a proper statistical analysis, it tends to have a bias towards noise.

2.6. Dimensionality of the subsurface

The dimensionality describes the complexity of an area or its deviation from simple structures, such as a homogeneous or layered (1D), a subsurface dominated by a (regional 2D) geoelectrical strike or by more complex (3D) structures without a clear geoelectrical strike, as shown in Figure 2.3. This complexity reflect on the transfer functions (eq. 2.17 and 2.20), which are reduced to specific expressions depending on the spatial distribution of the electrical conductivity being imaged (Fig. 2.3).

For a homogeneous half-space (Fig. 2.3 1D), the apparent resistivity represents the true resistivity of the subsurface and the phases are 45° for all periods. For a 1D layered subsurface, both off-diagonal components of the impedance tensor (Z_{xy} and Z_{yx}) have the same amplitude with opposing signs. Impedance phases higher than 45° indicate decreasing resistivity with depth and phases less than 45° are indicative of increasing resistivity.

For a 2D subsurface, resistivities vary along one horizontal direction and with depth (Fig. 2.3 2D). When the x- and y- directions are aligned with the lateral conductivity interface (ideal 2D case), the impedance tensor assumes the form presented in Figure 2.3 2D, with Z_{xy} parallel to the conductivity interface and Z_{yx} perpendicular to it. The direction of the lateral conductivity interface is also known as the regional geoelectrical strike, which is present in the data when the horizontal dimensions of a conductivity anomaly are comparable with the depth of penetration (Bahr, 1988).

Furthermore, in an ideal 2D case, when the coordinate system is aligned with the strike direction, Maxwell's equations can be decoupled and the MT impedance responses can be divided into two modes. The transverse electric (TE) mode, with the electric field parallel to strike, also known as E-polarization; and the transverse magnetic (TM) mode, with the magnetic field (B) parallel to strike also known as B-polarization (as presented in equation 2.26). The VTF exists only the component perpendicular to the strike direction (Fig. 2.3 2D).

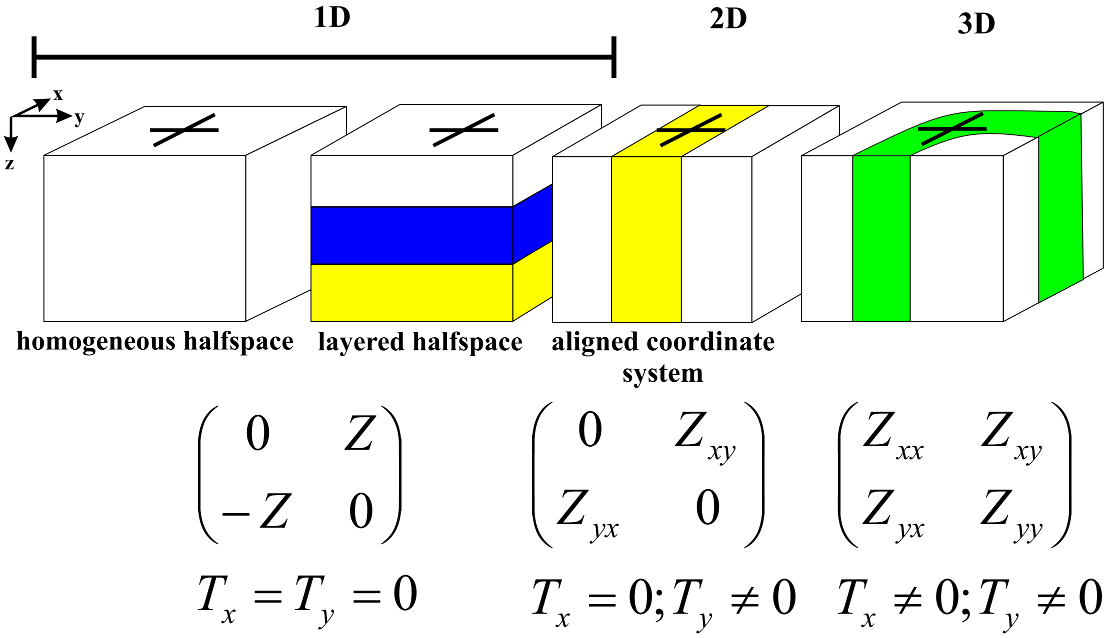

Figure 2.3.: Simplified example of the 1-D, 2-D and 3-D dimensionality of the subsurface including the variations of the transfer function (2.17) for the different cases. The different colours mean different resistivities.

$$\begin{array}{cc}
TE-mode & TM-mode \\
E\left(E_x,0,0\right); B\left(0,B_y,B_z\right) & B\left(B_x,0,0\right); E\left(0,E_y,E_z\right) \\
\frac{\partial B_z}{\partial y} + \frac{\partial B_y}{\partial z} = \mu_0 \sigma E_x & \frac{\partial E_z}{\partial y} + \frac{\partial E_y}{\partial z} = -i\omega B_x \\
-\frac{\partial E_x}{\partial y} = -i\omega B_z & -\frac{\partial B_x}{\partial y} = \mu_0 \sigma E_z \\
\frac{\partial E_x}{\partial z} = -i\omega B_y & \frac{\partial B_x}{\partial z} = \mu_0 \sigma E_y
\end{array} \tag{2.26}$$

For an arbitrary measurement setup that is not align with the strike, no elements of the impedance tensor vanish. However, Z can be mathematically rotated to find an angle in which the measurement's coordinate system can be aligned along the regional geoelectrical strike, as follows:

$$Z_R = RZR^T \tag{2.27}$$

where Z_R is the rotated to strike impedance tensor, R is a clockwise rotation matrix, Z is the impedance tensor in the measured coordinate system, and the superscript T indicate that the matrix R is transposed, R takes the form:

$$R = \begin{pmatrix} cos\theta & sin\theta \\ -sin\theta & cos\theta \end{pmatrix} \tag{2.28}$$

For more complex electrical conductivity structures (Fig. 2.3 3D), charge accumulations at surfaces depends on shape, depth and conductivities of the 3-D bodies. The EM fields do not decouple into TE- and TM-modes Vozoff, 1991. Horizontal electric (E) and magnetic (H) fields are not orthogonal, thus there is no angle in which the diagonal component of Z vanish.

2.6.1. Phase tensors analysis

Phase tensor analysis (PT, Caldwell *et al.*, 2004) was used to investigate the dimensionality of the study area. The PT (Φ) are the ratio between the real (X) and imaginary (Y) parts of the impedance tensor (eq. 2.17), which expanded to all the elements of Z can be written as:

$$\Phi = X^{-1}Y = \frac{1}{det(X)} \begin{bmatrix} X_{yy}Y_{xx} - X_{xy}Y_{yx} & X_{yy}Y_{xy} - X_{xy}Y_{yy} \\ X_{xx}Y_{yx} - X_{yx}Y_{xx} & X_{xx}Y_{yy} - X_{yx}Y_{xy} \end{bmatrix} = \begin{pmatrix} \Phi_{xx} & \Phi_{xy} \\ \Phi_{yx} & \Phi_{yy} \end{pmatrix} \tag{2.29}$$

Phase Tensors are second rank 2-D matrices that can be characterized by its coordinate invariants and represented graphically by an ellipse (e.g. Bibby, 1986). The maximum (Φ_{max}) and minimum (Φ_{min}) tensor values are used to construct the major and minor axes of the ellipses, respectively. The tensor skew angle (β) serves as a measure of the tensor asymmetry, the angle α expresses the dependence of the phase tensor on the coordinate system. While the relationship $(\alpha - \beta)$ angle describes the orientation of the major axis (see Caldwell *et al.*, 2004; Booker, 2013).

$$\beta = \frac{1}{2} arctan \left(\frac{\Phi_{xy} - \Phi_{yx}}{\Phi_{xx} + \Phi_{yy}} \right) \tag{2.30}$$

and

$$\alpha = \frac{1}{2} arctan \left(\frac{\Phi_{xy} + \Phi_{yx}}{\Phi_{xx} - \Phi_{yy}} \right) \tag{2.31}$$

In terms of its invariants the PT can rewritten as:

$$\Phi = R^T(\alpha - \beta) \begin{pmatrix} \Phi_{max} & 0 \\ 0 & \Phi_{min} \end{pmatrix} R(\alpha + \beta) \tag{2.32}$$

where $R(\alpha+\beta)$ is a rotation matrix in the form:

$$R(\alpha+\beta) = \begin{pmatrix} cos(\alpha+\beta) & sin(\alpha+\beta) \\ -sin(\alpha+\beta) & cos(\alpha+\beta) \end{pmatrix} \tag{2.33}$$

The main elements of the PT are presented in graphical form in Figure 2.4. An important characteristic of the PT is that it is preserved in the presence of galvanic distortion independent of the dimensionality of the subsurface structure (Caldwell *et al.*, 2004).

In MT surveys, localized near-surface small-scale heterogeneities in conductivity can impose significant galvanic distortion on the electric field and subsequently bias the impedance response. As galvanic distortions can be represented as a real 2-D tensor (C). Assuming undistorted magnetic fields, the observed impedances can be seen as a combination of the regional impedance and the distortion matrix ($Z_D = CZ$).

$$Z_D = CZ = X_D + iY_D = CX + C(iY) \tag{2.34}$$

Taking a distorted PT (Φ_D), it is easy to prove that since C is real the essential phase relationship between real and imaginary parts of the impedance tensor remain unaffected by the distortion (Caldwell *et al.*, 2004) as:

$$\Phi_D = X_D^{-1} Y_D = X^{-1} C^{-1} C Y = X^{-1} Y = \Phi \tag{2.35}$$

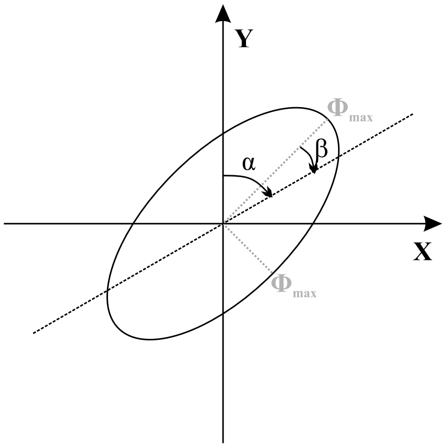

Figure 2.4: Graphical representation of phase tensors. Φ_{max} and Φ_{min} are used to scale major and minor ellipse axis, respectively. The angle gives the orientation of the major axis in the observer's coordinate system. In the general case, the angle represents the rotation of the major axis from an identically shaped ellipse representing a symmetric tensor (black dashed line). Figure drawn after Caldwell *et al.* (2004).

2.6.2. The galvanic effect

Magnetotelluric data is often affected by small scale conductive structures, that change direction and magnitude of the E field (Bahr, 1988). These distortions are caused by charges accumulating at the boundaries of the small scale structures, distorting the pattern of regional current flow in a localized area encompassing the structure (Caldwell *et al.*, 2004). These frequency independent distortions are known as galvanic distortions and can be represented as a real tensor. The physical meaning of this phenomena can be explained as follows:

Taking the divergence of (2.7),

$$\nabla \cdot J = \nabla \cdot (\sigma E) = \sigma \nabla \cdot E + \nabla \sigma \cdot E = 0 \tag{2.36}$$

Combined with (2.4) and the constitutive relation for D, give us:

$$q = -\varepsilon_o \nabla \sigma \cdot \frac{E}{\sigma} \tag{2.37}$$

Equation (2.37) states that a conductivity contrast between two adjacent media with different σ, will generate charge accumulation, which occurs if there is a regional or primary electric field E and a component of this field is in the direction of the conductivity change. This charge accumulation generates a secondary electric field (E_s) which can be quite large and adds to the regional inductive subsurface response E.

Figure 2.5 visualizes the galvanic effect of an anomalous body. The secondary field E_s associated with the boundary charges of the anomaly adds vectorially to the induction-related primary field E (E_p in Fig. 2.5a and b). In summary, if the anomalous body is less resistive than the medium ($\sigma_1 > \sigma_0$ Figs. 2.5a and c) the measured field reduces over the body and if the body is more resistive than the medium ($\sigma_1 < \sigma_0$Figs. 2.5b and d) the measured field increases directly over the body.

The galvanic distortion of the electric field is constant over frequency and persists at low frequencies, where the inductive response is negligible. Mathematically, it can be described as a real 2x2 period independent tensor C, which relates observed (E) and regional or primary (E_r) electric field, which would be measured in absence of the anomaly (e.g. Bahr, 1988):

$$E = C \cdot E_r = \begin{pmatrix} c_{xx} & c_{xy} \\ c_{yx} & c_{yy} \end{pmatrix} \begin{pmatrix} E_x^r \\ E_y^r \end{pmatrix} \tag{2.38}$$

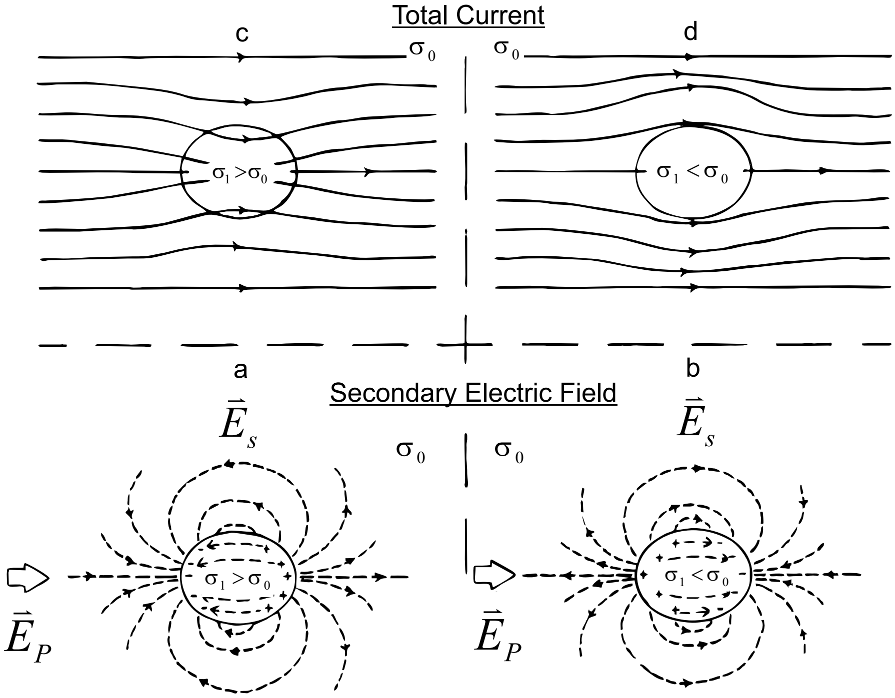

Figure 2.5.: Galvanic effect. Boundary charges form on surface of (a) conductive inclusion and (b) resistive inclusion producing secondary electric fields E_s (dashed). Primary field E_p and secondary fields E_s, add vectorially to produce total electric field E resulting in (c) "current channelling" and (d) "current deflection" (from Jiracek, 1990).

The galvanic distortion of the electric field propagates to the magnetotelluric impedance Z, which describes the amplitude and phase relationship between the horizontal components of the electric and magnetic fields following equation 2.17:

$$E = C \cdot E_r = C \cdot (Z_r \cdot B) = (C \cdot Z_r) \cdot B \rightarrow Z = C \cdot Z_r \tag{2.39}$$

Expanded to all elements of Z takes the form:

$$Z = \begin{pmatrix} c_{xx} & c_{xy} \\ c_{yx} & c_{yy} \end{pmatrix} \cdot \begin{pmatrix} Z_{xx} & Z_{xy} \\ Z_{yx} & Z_{yy} \end{pmatrix} = \begin{pmatrix} c_{xx}Z_{xx} + c_{xy}Z_{yx} & c_{xx}Z_{xy} + c_{xy}Z_{yy} \\ c_{yx}Z_{xx} + c_{yy}Z_{yx} & c_{yx}Z_{xy} + c_{yy}Z_{yy} \end{pmatrix} \tag{2.40}$$

This explains that in the 3D case both apparent resistivity and phases are affected by distortion. Above a 1D or 2D underground where the coordinate system is aligned with the geoelectric strike, the diagonal elements of the impedance tensor tend to zero. The impedance tensor takes the form:

$$Z_{1D/2D} = \begin{pmatrix} c_{xy}Z^r_{yx} & c_{xx}Z^r_{xy} \\ c_{yy}Z^r_{yx} & c_{yx}Z^r_{xy} \end{pmatrix} \tag{2.41}$$

The superscript r means rotated. In this case, the phase relation of the off-diagonal elements is not affected but the apparent resistivities are biased by the distortion. The galvanic distortion effect is observable as a vertical offset in the log apparent resistivities versus period curves, known as the *static shift*.

2.6.3. The topographic effect

Strong topographic gradients have a large influence in the magnetotelluric transfer functions. As in the case with surface inhomogeneities (see Fig. 2.5), the total E field is obtained by a vector sum of the primary and secondary fields, where the total electric field pattern and current flow beneath surface topography (Figure 2.6a), is completely tangential at the surface. This leads to differences in the measured fields at convex or concave surfaces. In other words, electric fields are reduced on topographic hills and are increased in valleys due to the galvanic effect (from Jiracek, 1990). Hence, the apparent resistivity values due to the galvanic effect are highest in valley troughs and lowest on topographic peaks (Figure 2.6b).

At small scale topography, charges can accumulate at the surface, which as galvanic charges, disturb the measured secondary electric field (E_s), leading to galvanic distortion effects. Larger topography structures become effective inductively, e.g. currents can be concentrated in valleys. The inductive effect of the topography on MT data can be modelled and taken into account when determining the conductivity distribution in the inversion of the data.

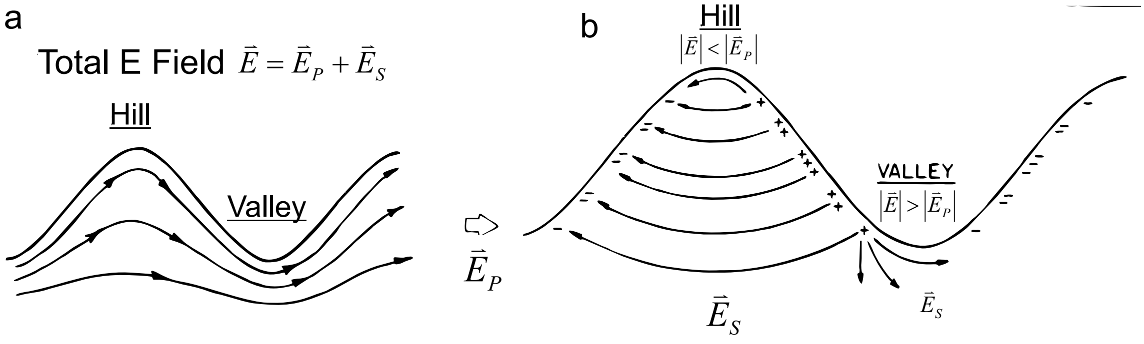

Figure 2.6.: Topographic effect. (a) total electric field E pattern. (b) Galvanic charge distribution (magnitude shown schematically) and resulting secondary fields E_s for a hill-valley sequence (modified from Jiracek, 1990).

2.7. General concepts for MT data inversion

To estimate the spatial distribution of resistivity values which can explain the observed data (transfer functions), forward or inverse modelling can be applied.

2.7.1. Forward modelling

Magnetotelluric forward modelling aims to solve Maxwell's equations (eqs. 2.1, 2.2, 2.3 and 2.4) to simulate the spatial and temporal distribution of electric and magnetic fields in the subsurface for a given conductivity distribution and a range of periods.

In forward modelling, the propagation of EM waves within a model of the Earth are simulated using numerical approximations which depend on the distribution of resistivity within the model. Following this procedure, the spatial distribution of EM fields are calculated, which allow to compute transfer functions (model responses) at any position of the model.

The most popular and widely used methods to solve Maxwell's equations are the differential equation methods. In these methods the entire earth model (not only the anomalous structures) is subdivided (discretized) into cells (2D) or cubes (3D) and each cell/cube is assigned a constant conductivity value Meqbel (2009). For each of these cells/cubes, Maxwell's equations are solved.

In general terms, for solving the MT forward problem, a large number of model parameters $m = (m_1, m_2, ..., m_M)^T$ are required which describe the Earth's electrical resistivity structure. While, the model responses, e.g. transfer functions, are represented by the data vector $d = (d_1, d_2, ..., d_N)^T$. The froward problem is then defined as:

$$d = F(m) \tag{2.42}$$

with F being a non-linear forward operator.

The EM forward operator $F(m)$ generally involves two steps: (1) Maxwell's equations, with conductivity defined by the parameter m are solved numerically with appropriate boundary conditions and sources; (2) the resulting solution is used to compute predicted data (e.g. an electric or magnetic field component, TF or apparent resistivity) at a set of site locations (Egbert & Kelbert, 2012).

Following The non-linear forward operator $F(m)$ can be linearised through the Taylor expansion:

$$F(m + \Delta m) \approx F(m) + \frac{\partial F(m)}{\partial (m)} \Delta m = F(m) + J\Delta m \tag{2.43}$$

where J is the Jacobian Matrix

$$J_{ij} = \frac{\partial F_i(m)}{\partial m_j} \tag{2.44}$$

also known as sensitivity matrix, as it describes the sensitivity of the model response ($F(m)$) to small changes (Δm) in the model parameters.The small model variations Δm associated change in the model response Δd, in relation to the forward problem can be expressed as:

$$\Delta d = F(m + \Delta m) - F(m) = J\Delta m \tag{2.45}$$

2.7.2. Data inversion

Considering a data vector $d = (d_1, d_2, ..., d_N)^T$, e.g. transfer functions, a model parameters vector $m = (m_1, m_2, ..., m_M)^T$and an error vector of model parameters $e = (e_1, e_2, ..., e_M)^T$ a solution have to be found in the form:

$$F(m) = d + e \tag{2.46}$$

In order to solve the MT inversion problem we have to find a model variation Δm, that when compared to the original model m the deviation between measured data d and the model responses $F(m + \Delta m)$ is minimal in between a reasonable error floor. This is usually achieved employing a target function $\Phi(m)$, defined by the residuals of the data $(d - d_m)$ divided by the error e.

$$\Phi(m) = \sum_{i=1}^{N} \left| \frac{d_i - d_{mi}}{e_i} \right|^2 = min \Rightarrow \Phi(m) = ||W[d - d_m]||^2 = ||W[d - F(m)]||^2 \tag{2.47}$$

where is a diagonal matrix in the form $W_{ii} = 1/e_i$. The target function $\Phi(m)$, when evaluated for small model variations can be expressed as:

$$\Phi(m + \Delta m) = [d - F(m) - J\Delta m]^T W^T W [d - F(m) - J\Delta m] \tag{2.48}$$

The first derivative tending to zero ($\partial\Phi/\partial\Delta m = 0$) of $\Phi(m + \Delta m)$ allows to obtain the model variation's vector (Δm eq. 2.49), for a detailed explanation of the solving of this expression see i.e. Chave & Jones (2012). In this case, the data vector d represent the difference between measured data and modelled data.

$$\Delta m = (J^T W^T W J)^{-1} J^T [d - F(m)] \tag{2.49}$$

Equation 2.49 can be iteratively solve using the Gauss-Newton method to obtain the resulting model of each iteration (eq. 2.50). The iterative process is repeated until the objective function reach a defined minimum value or other termination condition is met.

$$m_{n+1} = m_n + (J^T W^T W J)^{-1} J^T [d - F(m_n)] \tag{2.50}$$

The Gauss-Newton method has the disadvantages of presenting a slow convergence rate and a lack of stability when the model parameters are much more numerous than the measured data. These effects are caused by low sensitivity values, forcing the determinants of the matrix $J^T W^T W J$ to tend to zero (0). To avoid this, a diagonal matrix βI (I is a unix matrix) can be add to the operator $J^T W^T W J$, which is known as the Levenberg-Marquardt method.

2.7.3. Model regularization

To stabilize an inversion certain conditions can be define for the model parameters to meet, that restrict the model space. This conditions are known as regularization, and can be related to different characteristics of the model. One possibility is to generate the smoothest model with the smallest conductivity gradient. For example, the Tikhonov regularization expands the target function by adding a "stabilizing functional" Ω:

$$\Psi(m) = \Phi(m) + \lambda\Omega(m) = ||W[d - F(m)]||^2 + \lambda\Omega(m) \tag{2.51}$$

The stabilizing functional $\Omega(m)$ can take very diverse forms, typically a local derivative operator. The λoperator is used to balance the trade-off between the data fit ($\Phi(m)$) and the model smoothness ($\Omega(m)$).

Considering that solving the MT forward problem requires a large number of model cells to avoid an under parametrization of the system (e.g. Newman & Alumbaugh, 1997). The inverse problem is under-determined as a large number of unknown model parameters is opposed by a much smaller number of data points, the regularization term is added to reduce the number of possible models that can explain the data, and to stabilize the inversion process.

3. The Venezuelan magnetotelluric dataset

3.1. The Integrated Geoscience of the Mérida Andes Project

The Andean orogen is one of the most important structures in the geological context of Venezuela, however its formation, geodynamic interactions and deep structures are not yet well studied (e.g. Audemard & Audemard, 2002; Chacín *et al.*, 2005; Monod *et al.*, 2010). Thus, the Integrated Geoscience of the Mérida Andes Project (GIAME Project, Spanish acronym) was proposed in 2013. The GIAME Project is aimed to generate lithosphere scale models and to develop a temporary dynamic model of the Mérida Andes. This multidisciplinary research group is composed of several main tasks, which are executed by different subgroups pertaining to the Venezuelan Foundation for Seismological Research (FUNVISIS, Spanish acronym), University of Los Andes (ULA, Spanish acronym), Central University of Venezuela (UCV, Spanish acronym) and Venezuelan Petroleum State Company (PDVSA, Spanish acronym).

The GIAME project is a basis for the lithospheric investigations of the Mérida Andes, including wide-angle seismic and magnetotellurics profiles crossing the orogen. The project also provides information of absolute gravity, gravity and magnetic anomalies at different scales in order to determine the internal structure and the relationship to the gravimetric root of the orogen.

Another principle task involves the study of the Quaternary deformations by means of structural geology and morphotectonics applied to active structural features, such as neotectonics and paleoseismology, georadar, cinematic GPS, SAR interferometry, thermocronology, cosmogenic timing, re-evaluation of historical seismicity, paleolimnology, among others.

Finally, as one of the main objectives is to contribute to the determination of the seismic hazard in the region, the local seismological network will be densified and integrated into the local network. This will allow the development of detailed studies of focal mechanisms and surface wave inversion, which together with the evaluation of the historic earthquake dataset, neotectonic and paleoseismic investigations, will improve and update the knowledge of the regional seismic hazards.

3.2. GIAME magnetotelluric data set

The magnetotelluric (MT) data of this study were acquired between March and April 2015. A total of 72 MT stations were installed along a 240 km long profile oriented in NNW-SSE direction (~17°NW) across the central part of the Mérida Andes (MA) (Figure 3.1). The profile was initially planned to be perpendicular to the MA and its major fault systems, however its final position resulted from a combination of accessibility and the locations of the profiles of other geophysical methods acquired in the framework of the GIAME project.

The final design of the profile considered the major tectonic-geological targets and access in mountainous areas. The general idea was to have denser station spacing whenever the geological conditions suggested interesting or complex situations. Hence, station spacing varied between 3 km and 5 km (Table 3.1). Site distances in the MA were smaller to account for topography and to achieve a better coverage of fault system and active deformation structures. Site distances were larger at both profile ends, along the Maracaibo and Barinas-Apure basins.

A station was installed approximately 300 km to the East of the profile in Cojedes state as shown in Figure 3.1 (red star in the bottom left panel) to be used as a remote reference and was recording for the entire duration of the study. This distance ensured that any noise source would be at least different between the remote and the profile stations (Gamble *et al.*, 1979; Egbert & Booker, 1986; Ritter *et al.*, 1998).

Table 3.1.: Station spacing with respect to the main geological structures underneath (see Fig. 3.1).

Stations	Spacing	Main Structures
0042 - 0061	5 km	Barinas-Apure Basin
0016-0041	3 km	Mérida Andes
0015 - 0001	5 km	Maracaibo Basin

Although electromagnetic (EM) man-made noise (e.g. power lines and fences, populated areas, power plants) and availability of construction space shaped final set up of the profile, spacing between stations was kept mostly as planned. From 79 stations originally proposed, 72 were finally recorded.

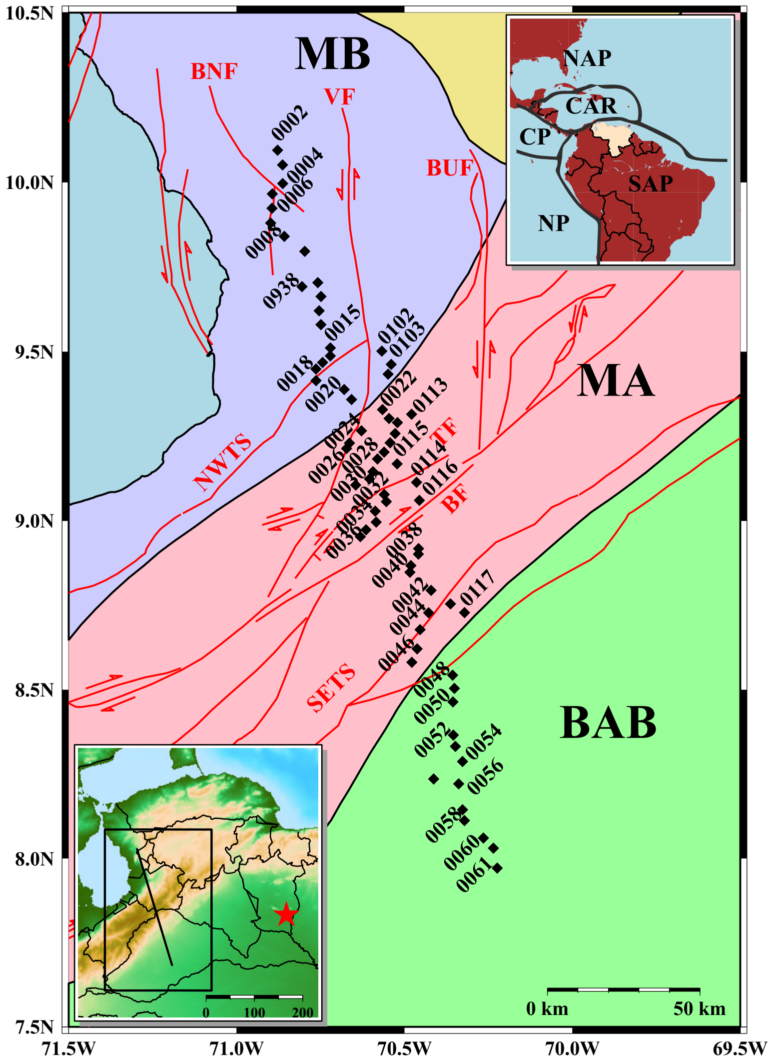

Figure 3.1.: Study area and station distribution. Main map shows the location of the MT stations (black squares) and the main surface structures (colour shaded) with the red lines indicating the Quaternary fault system (after Audemard *et al.*, 2006). For clarity most odd numbered station labels were omitted. Abbreviations: MB - Maracaibo Basin, MA - Mérida Andes, BAB - Barinas-Apure Basin, BNF - Burro Negro Fault, VF - Valera fault, TF - Tuñame Fault, BF - Boconó fault, BUF - Burbusay Fault, NWTS - Northwestern thrust system (also known as Las Virtudes thrust system) and SETS - South-eastern thrust system. Top right: Venezuela location in reference to the American continent. Black lines indicate the limits of the tectonic plates. Abbreviations: NAP - North American Plate, CAR - Caribbean Plate, CP - Cocos Plate, NP-Nazca Plate, SAP - South American Plate. Bottom left: topographic map of western Venezuela highlighting the profile position and the location of the remote reference station (red star).

3.2.1. Data acquisition

Field measurements began on March 3rd and were finished on April 5th 2015. On the first day the remote reference station was installed, and it was left recording until the end of the project, so that it could be used as a reference for all stations on the profile.

MT data were collected in a broadband configuration, in the period range of 10^{-5} s to more than 1000 s. Magnetic fields were recorded with Metronix MFS06/07/10 induction coils magnetometers and the electric fields with non-polarizing silver - silver chloride (Ag-AgCl) electrodes, supplied by the Geophysical Instrument Pool Potsdam (*GIPP*). The three coils were oriented N-S, E-W and vertically, and placed in a 5 meters radius from the centre of the station. The electrodes formed two 60 m long orthogonal dipoles, oriented N-S and E-W. The main elements of a standard MT station are presented in Figure 3.2. The x-axis was oriented to the magnetic North and the magnetic declination was -9.2°, which was corrected during processing.

All measuring instruments were connected to a sensor box, which pre-amplify the analogue signals, and then connected to a S.P.A.M Mk IV data logger that translates the recorded signal from analogue to digital and stores the measured fields. Three different sampling rates were used in order to guarantee a good coverage of short and long period data. Short period (high frequency) data were recorded in intervals: once a day for 10 min with a sampling rate of $4\text{x}10^{-5}$ s^{-1}(25 kHz), and for 10 min every 2 hours with a sampling rate of $8\text{x}10^{-4}$ s^{-1}(1250 Hz). Longer period (lower frequency) data were recorded continuously with a sampling rate of 0.02 s^{-1}(50 Hz).

Data acquisition was accomplished by four teams that worked independently installing new sites and servicing those already installed. Each station had a minimum of 3 days of recording, exemplary good quality sites were active up to two weeks to serve as local references. The remote reference was serviced once a week. All stations were time stamped using a GPS system. Data were stored internally and retrieved when stations were serviced.

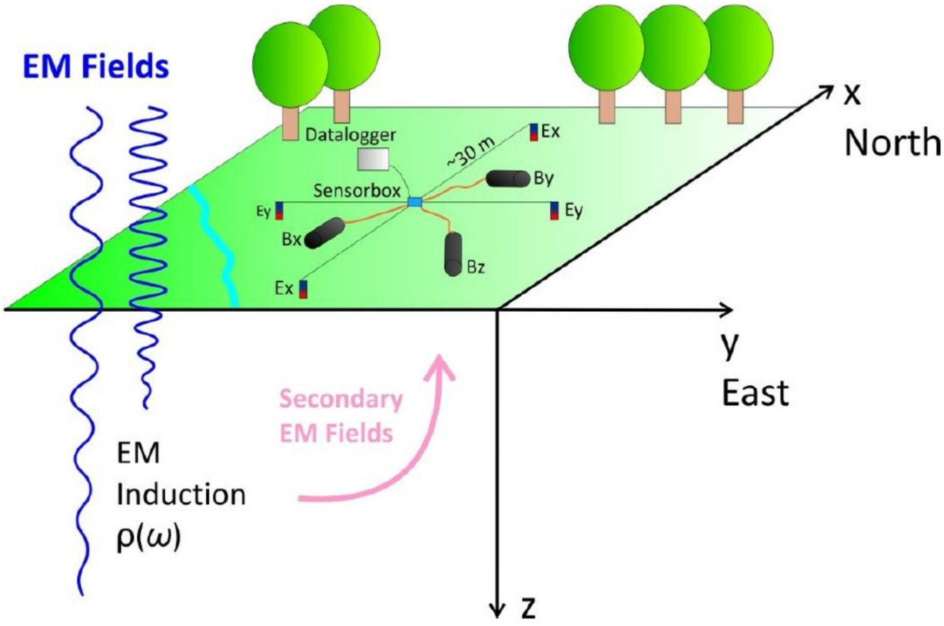

Figure 3.2.: Main elements of a MT station. Source EM fields (blue) diffuse into the soil and induce currents in the surface. The induced secondary fields (pink) of these current system contain information about the conductivity distribution of the underground and are recorded along with the primary field at the earth's surface with a MT station. Two perpendicular 50 - 60 m long dipoles measure the horizontal electric field in the S-N (E_x) and W-E (E_y) directions. The magnetic fields are measured in all three directions (B_x, B_y and B_z) with induction coils. Figure taken from Adao (2015).

3.2.2. Data quality

The reliability of any EM method depends on the signal-to-noise ratio at the receiver (Szarka, 1988). Data acquired in urban and suburban areas is usually saturated with EM man-made noise that often deteriorates the recorded time-series by overprinting the derived natural field variations. It is important then to identify the effects of noise on the data and to determine the best ways to eliminate or reduce its influence.

The MT data of this study are heavily affected by EM noise at different frequencies. Sources ranged from electric fences to the power grid, a hydroelectric plant and a number of small communities and cities. As security measure, stations were installed in between the limits of farming and cattle areas, which also influenced the data quality, even with the collaboration of local land owners (e.g. switching off local power grids). Stations on the southern and northern flanks of the Mérida Andes were noisier than those located on the mountain (see Figure 3.7 for reference on location), given that these zones are more densely populated and stations were mostly located in agricultural and livestock zones. Nevertheless, the time series responded well to filtering and processing techniques. In total only 4 stations out of the 72 recorded could not be used. Two of them due to proximity to power lines and active roads; one due to the influence of electric fences and the one due to its proximity to a city.

Man-made EM noise can be distinguished from natural sources, as it is usually coherent and monotone and its amplitude is above the natural signals. In raw time series such noise can be identified as evenly spaced peaks, similar in amplitude and wavelength. In the frequency domain, provided that enough samples are stacked, a dominant frequency of the EM noise source can be identified as a peak above the rest of the signal.

Figure 3.3 shows a comparison of the recorded magnetic (B_x, B_y and B_z) and electric (E_x and E_y) fields of stations 40 (a and c) and 36 (b and d) in time (top) and frequency (bottom) domain. Station 40 was located at approximately 4 km away from a hydro-power plant and it is a clear example of a station heavily affected by man made EM noise. In the time domain there are several evenly space peaks considerably larger than the signal (see red arrows), and in the frequency domain we can clearly see two peaks at 3.54 s and 2 Hz (black and red arrow respectively) and their harmonics. The time series at the station 36 (Fig. 3.3b) show correlated groups of peaks throughout the channels (highlighted with black arrows). However, in this case there is no equidistant repetitions, an indication of these could be related to natural sources or to non-constant noise sources. Along with the absence of strong peaks in the frequency domain, these are indicators of the good quality at this station. Nonetheless, there is one peak marked with a black arrow in the frequency domain at 3.57 s which harmonics extend to approximately 5.92 Hz, possibly related to the data logger.

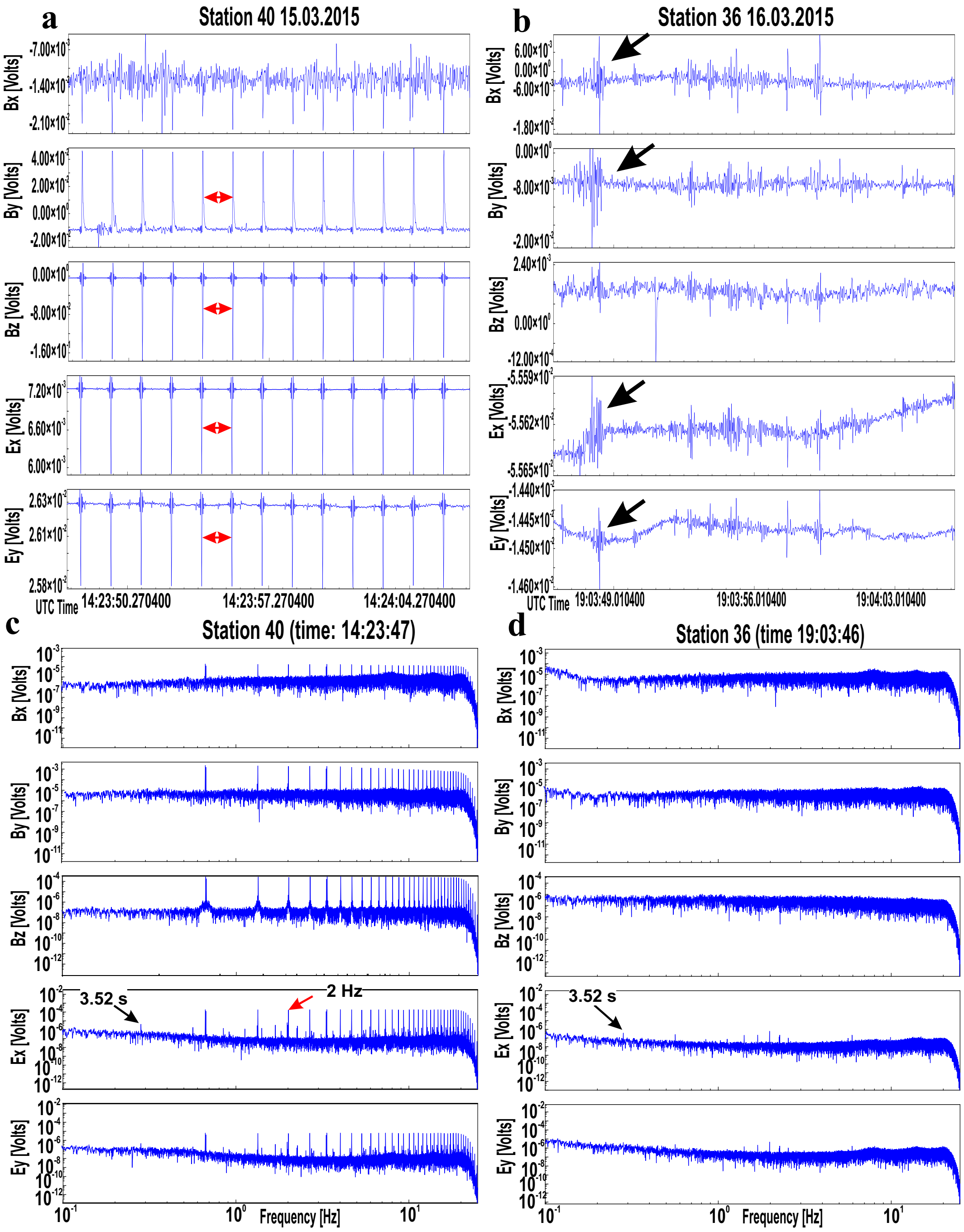

Figure 3.3.: Time series for around 40 seconds of data on the 50 Hz recording band (long period) low passed at 20 Hz of stations 40 and 36, left and right respectively, showing data in time domain (a and b) and frequency domain (c and d). Recording channels per subset from top to bottom are B_x, B_y, B_z, E_x and E_y, for reference on channels directions see Figure 3.2. Time domain consist of 2000 stacked samples, while frequency domain data stacked 20000 samples.

3.2.3. Data filtering

The analysis of the time series of all the stations in the profile showed two main sources of coherent noise at ∼2 Hz to ∼60 Hz and its harmonics. These are related to electric fences and the frequency of the power grid in Venezuela, respectively. In most of the dataset the odd harmonics showed higher peaks than the even ones, an indication that the power system is not perfectly balanced (Szarka, 1988). Other frequencies identified as common EM noise affecting sections of the data were 30 Hz, 90 Hz, 116 Hz.

To remove or at least decrease the influence of the EM noise a Notch filter was applied (Hanstein *et al.*, 1986). The Notch filter is a band stop filter, rejecting the parts of the signal that lay between the cut-off frequency. It can be applied to a single frequency and extended to all of its harmonics. EM noise sources are often unstable, meaning that their peaks or spikes are not fixed to well define frequency but rather vary in a range. A common practice to address this issue is to filter a bandwidth, for this dataset a default setting of 3 dB was set.

Figure 3.4 provides an example of station 02 before and after the notch filter was applied on 60 Hz and its harmonics (120 Hz, 180 Hz, 240 Hz and 300 Hz). In Figure 3.4A, can be seen that the unfiltered time series is populated by a monotonous signal masking the natural measured EM fields. In frequency domain at 60 Hz and its harmonics are visible (marked with a black arrow in Figure 3.4C). After filtering (Figures 3.4B and D), a group of spikes can be seen throughout all the channels in the time series (marked with black circles in Figure 3.4B). Furthermore, in the frequency domain (Figure 3.4D) after filtering the peaks in 60 Hz are no longer visible, a clear indication that the filter has decreased the effect of the EM noise in the dataset.

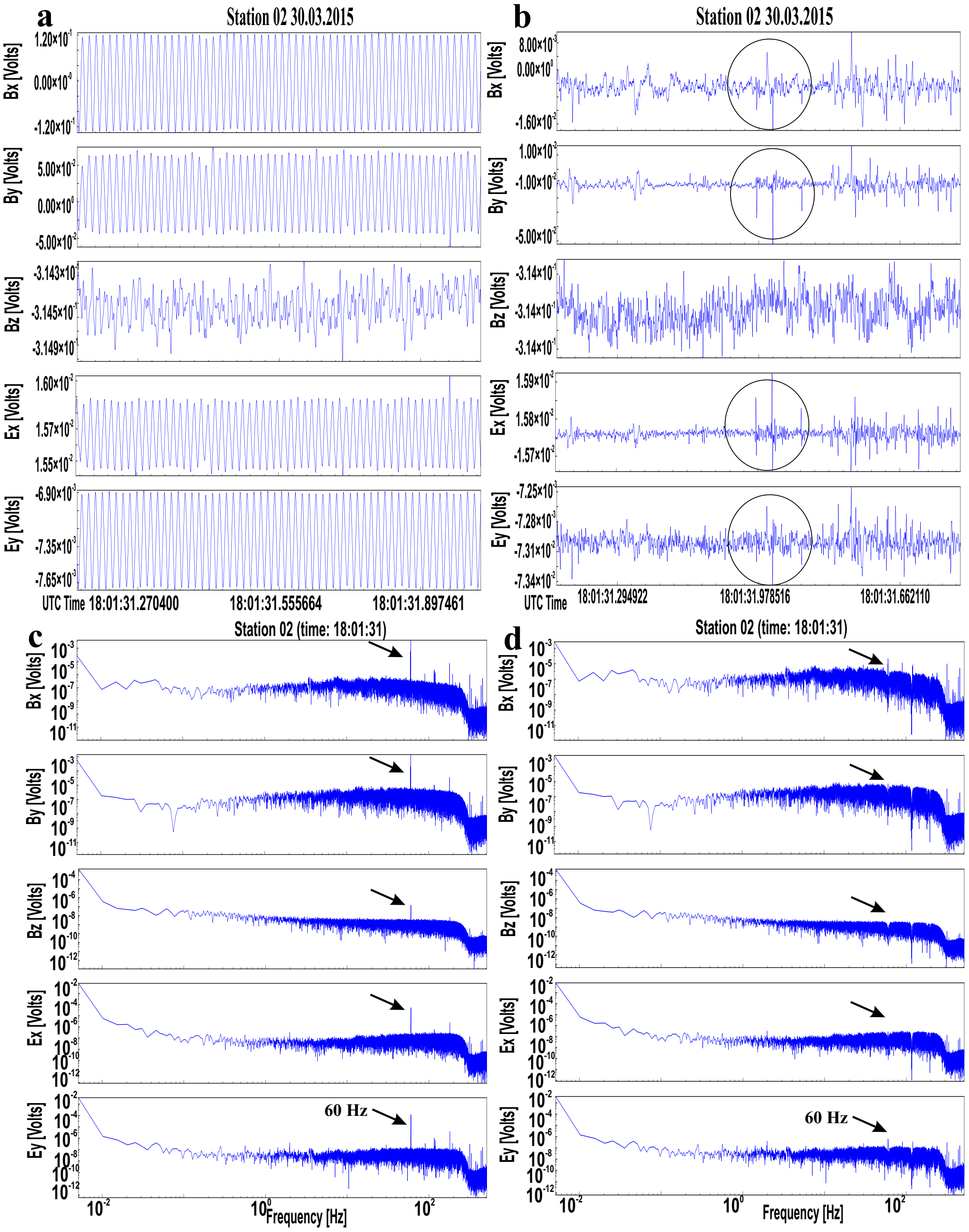

Figure 3.4.: Station 0002 before (a and c) and after (b and d) filtering 60 Hz signal and its harmonics. Top in the time domain and bottom in the frequency domain. The Figure depicts approximately 2 s of signal on 30.03.2015 at 18:00. Black arrows in (c) and (d) indicate the position of the 60 Hz.

3.3. Data Processing

Magnetotelluric transfer functions were estimated within a period range of 10^{-5} s to more than 1000 s, using robust single site and remote reference processing routines of the EMERALD software package (Ritter *et al.*, 1998). Data quality could be further improved by using a frequency domain selection scheme (Weckmann *et al.*, 2005) and a novel statistical approach for data pre-selection employing the concept of the Mahalanobis distance and the magnetic polarization direction to remove outliers and EM noise (Platz & Weckmann, 2019).

After data collection, the recorded fields are converted into the EMERALD format, and processed with the EMERALD package, that comprises the following general steps:

- Time-series of the five components are band-pass filtered into narrow bands (cascade decimation) and subsequently divided into short, adjacent segments of fixed length of 128 samples, which are then cosine tampered (to ensure that the time series vanish at the window's margins) and Fourier transformed. Each one of these segments are known as events.
- Each event is corrected for instrumental response function and divided into sub-bands of periods equally distributed in a logarithmic scale.
- Spectral terms (smoothed auto and cross spectra) between all the components are calculated and stacked over all time windows. These are used to compute the transfer functions (TF) solving equations 2.17 and 2.20 by means of the least square estimator (as shown in section 2.5). At this point data could be further improved using the data pre-selection per frequency (Weckmann *et al.*, 2005). It is also common practice to establish a coherence threshold prior to the statistical analysis. For this dataset a coherency criterion threshold was set between 0.8 and 0.9.
- In order to improve the transfer functions (TF) estimation, particularly in areas with high levels of EM noise, different statistical and physical approaches can be employed. For the Venezuelan dataset the statistical approach to decrease the influence of events outliers included the use the Mahalanobis distance (Platz & Weckmann, 2019) and robust statistics (Ritter *et al.*, 1998). Before the statistical analysis the remote reference processing (Gamble *et al.*, 1979) scheme can also be applied. The physical analysis automatically removes magnetically polarized data based on the criteria described by Platz & Weckmann (2019).

3.3.1. Data pre-selection scheme

To improve data quality a scheme of data pre-selection per frequency was applied using a code developed by Weckmann *et al.* (2005). This data pre-selection relies on a thorough visual inspection of the data set in a variety of statistical parameters such as spectral power densities of input and output channels, data coherences, response functions and their errors distribution, and others. Extreme outliers and particularly noisy data segments are excluded from further data processing by setting threshold values for individual parameters.

Station 40 pre-selection window is shown in Figure 3.5. In this example, we present clearly magnetically polarized events in red. The effect of the polarization can be seen for a larger period in Figure 3.3A. Figure 3.5f shows also that magnetically polarized events are highly coherent, and their effects are even clearer in the response function in the complex plane (Fig. 3.5g). In this window two different clusters of data can be seen, the red marked events are driving the value of the response function, resulting in a incorrect measurement. The events marked in red were subsequently removed from all frequencies and the station could be used for further studies.

Generally for the Venezuelan dataset defining threshold values for statistical errors (Fig. 3.5e), magnetic polarization (Fig. 3.5h) and the response functions in the complex plane (Fig. 3.5d and g) showed the highest improvement of the measured responses. Specially the response functions in the complex plane plot, depending on data and noise distribution the events plotted tend to cluster around a central value. Defining limits around this clustered events can considerably diminish the influence of outliers. This process, however, is time consuming as the events have to be analysed independently per frequency and station. Thus, it was only applied to the stations that needed more improvement after the statistical and physical approaches (stations 0017 to 0020, 0102-0110 and 0038-0042) and to the mid range periods (10^{-2} and 1 s).

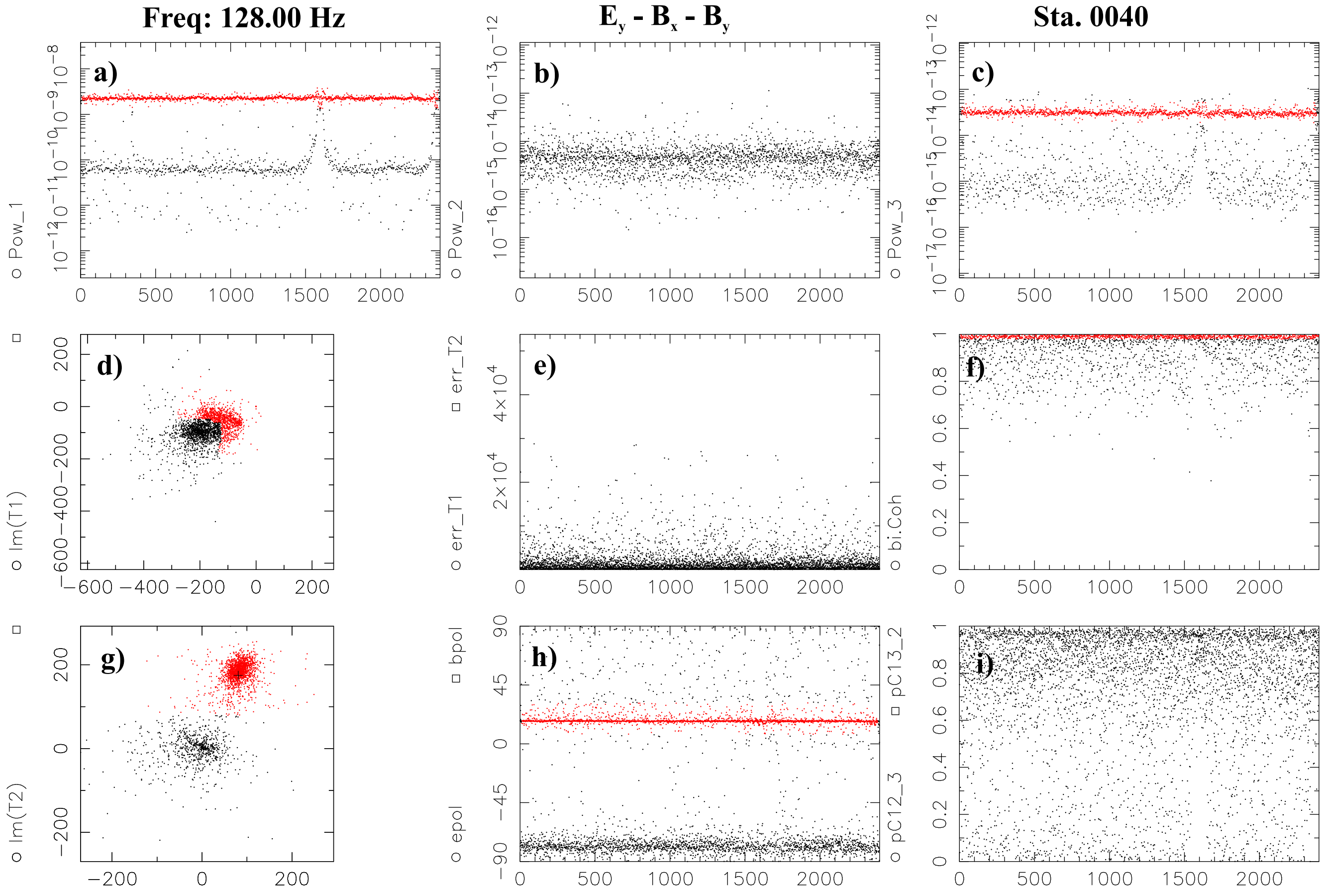

Figure 3.5.: Example of the data pre-selection scheme window (after Weckmann *et al.*, 2005) for station 0040 in the frequency band 128 Hz (0.0078 s). The events in red are magnetically polarized and were not considered in further processing steps (see text).The upper panel represent the spectral power densities (a-c) of the input and output channels in eq. 2.23, the response functions Z1 and Z2 in the complex plane are located on the left (d and g), window (e) presents the statistical errors of both transfer functions, (f) the bivariate coherences, (h) electric and magnetic polarizations and (i) the partial coherences.

3.3.2. Remote referencing

The remote reference (RR) method is based on the idea that magnetic fields recorded at two different sites have only uncorrelated noise components (Gamble *et al.*, 1979). It requires simultaneously recorded EM fields from at least one reference station. In order to apply the RR method the time series of the local and remote stations have to be synchronized. The transfer functions are estimated employing the horizontal magnetic fields of the reference station in equations 2.24 and 2.25. The larger improvement improved in data quality was observed in the TF between 10^{-1} and 10 s.

3.3.3. Mahalanobis distance and automatic removal of Magnetic polarization

The Mahalanobis distance (MD) allows the use of the covariance matrix in addition to the mean value to describe the shape of the data distribution (Platz & Weckmann, 2019). Several values were tested for the MD varying from 1.2 to 2.5, the best results were achieved with a value of 1.5.

A physical criterion based on magnetic polarization was also applied to eliminate outliers in the data. MT data can be electrically polarized due to current channelling of surface structures. However, polarization of the direction of the magnetic wave field is not expected given that the magnetic field is generated by a broad variety of sources (Vozoff, 1991). Hence, magnetically polarized events need to be removed from the dataset. This was achieved employing an automatic selection algorithm developed by Platz & Weckmann (2019) to remove strongly magnetically polarized events which is currently integrated in the EMERALD software package.

Station 0040 (Fig. 3.5h) is a good example of a magnetically polarized station. This effect could be automatically removed of all periods employing the physical criterion.

3.3.4. Iterative robust response estimation

Robust statistics aim to single out data that belongs to an unknown noise distribution of outliers, or outside of a normal distribution. An outlier is usually characterized as a data point that is different from the remaining data, e.g. extreme values.

The robust statistics applied for this project are part of the EMERALD software package as described by Ritter *et al.* (1998). The robust algorithm consists of an iterative weighting scheme which combines two parts, 1) the chi-square (χ^2) criterion and 2) the consistency criterion. Theχ^2 criterion examines whether a single event spectrum fits into the global view of the majority of the data and accordingly the weight of a single event spectrum is increased or decreased (Ritter *et al.*, 1998). The consistency criterion reduces non-stationary contributions in the response functions by interactively replacing a certain amount of bad data (outliers events) with predicted values and therefore reduces non-stationary contributions in the transfer functions (Ritter *et al.*, 1998).

In other words it takes the entire events that define a frequency and iteratively contrast them against a modelled result based on an initial noise-source distribution assumption. It also compares the events to the main trend or dominant distribution. After several iterations clear outliers are discarded and the remaining events should agree with the real and modelled trend of the data.

The best results for the entire dataset were obtained by a combination of all the above explained techniques. MT data processing is an iterative process and stations respond differently to different approaches. In many cases transfer functions obtained by the RR method showed no improvement after the MD statistical analysis. Therefore, final processed responses resulted from the selection of the best sections of the data from the different processing schemes.

Figure 3.6 shows a comparison of the results applying the different methodologies at station 0002. This station was not excessively affected by noise, nonetheless the different statistical analysis in addition to the filtering allowed to appreciate a clearer tendency on the responses. It is particularly noticeable in this sense the improvement in the induction vectors by means of the MD (Figure 3.6 bottom right).

It is important to mention that the effectiveness of any statistical approach depend on the volume of good quality data. As the statistical analysis respond to the data trend, they respond to the majority of the data. To improve the responses of a site with high levels of noise, data must be inspected closely and compared with stations in the vicinity. In this cases a frequency selection scheme would obtain better results than an iterative statistical approach. However, even after taking all processing steps TF showed data points of sections that did not follow the general trend, these clear outliers that could not be corrected by means of processing were manually removed.

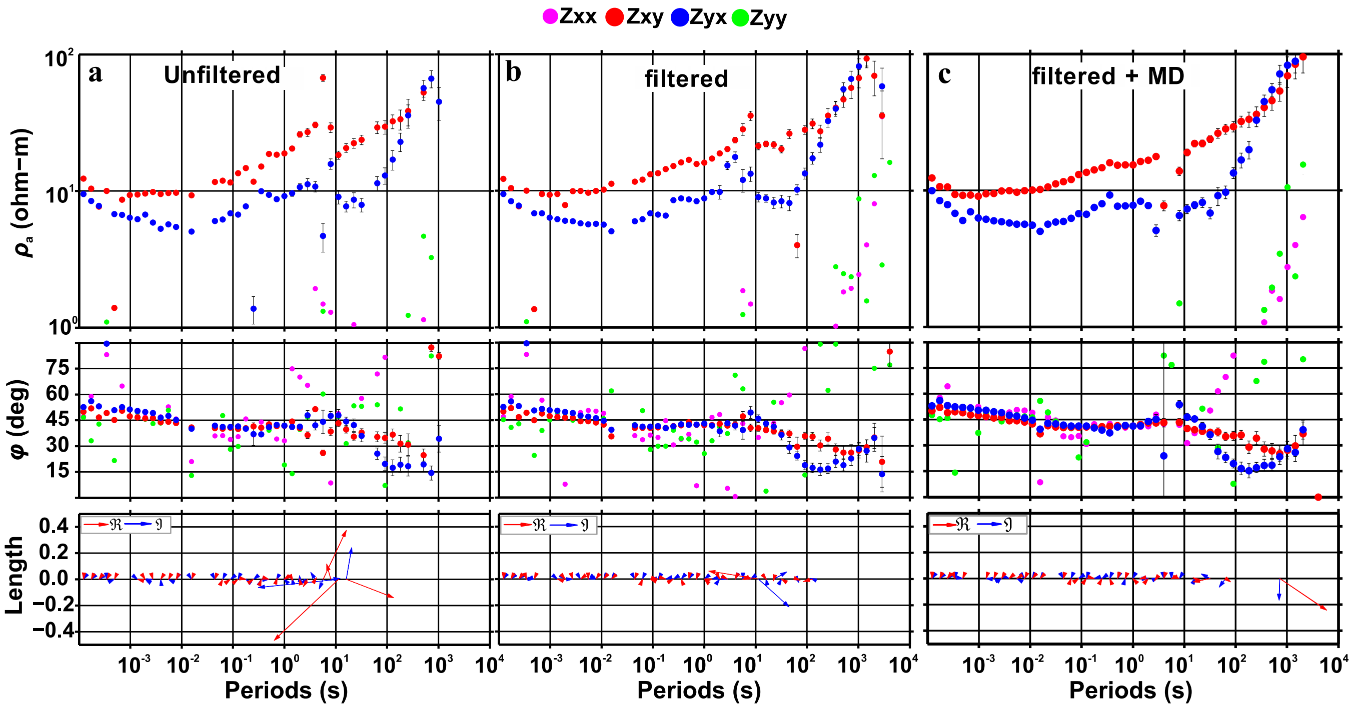

Figure 3.6.: Comparison between robust processing on unfiltered data (a), filtered data with RR method (b) and filtered data with MD approach (c) for the responses in apparent resistivity for all four elements of the impedance matrix (top), phases (middle) and induction vectors (bottom) for station 0002. Clear outliers were masked.

3.4. Dimensionality and directionality analysis

In order to understand the structural complexity in the data, MT responses must be thoroughly studied. Data dimensionality (complexity of the subsurface) and geoelectric strike are strong indicators for conductive structures and data quality control tools. Induction vectors ability to respond to lateral contrast permits in general estimate the direction and even size of anomalous bodies. A regional geoelectrical strike is present in the data when the horizontal dimensions of a conductivity anomaly are comparable with the depth of penetration (Bahr, 1988). The integral study of data responses is basic to understand the data set and its relationship with the geology, particularly in zones without prior information.

In this section, the methodologies applied in this thesis to estimate data dimensionality and geoelectrical strike are explained. However, based on the variations in dimensionality and the different strike directions obtained, stations were subdivided into three groups as presented in Figure 3.7. The northern, central and southern sections coincide roughly with the location of the major superficial geological structures, namely from North to the South the Maracaibo Basin, the Mérida Andes and the Barinas-Apure Basin. Thus, the analysis presented in this section are described using these subdivisions.

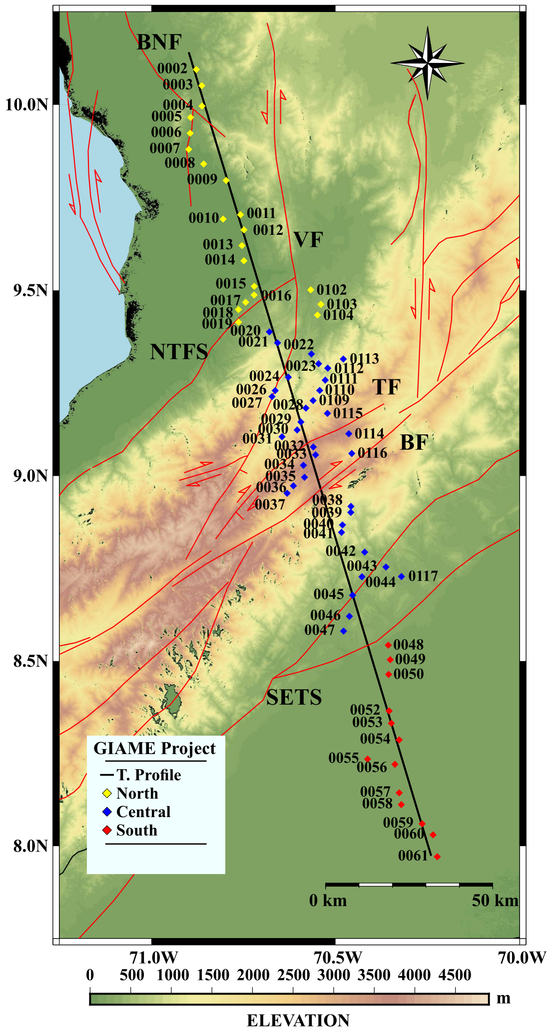

Figure 3.7: MT survey stations final distribution after data acquisition. The yellow, blue and red coloring of the stations represent the Northern, Central and Southern sections, respectively, see text. Red lines indicate Quaternary fault system (from Audemard *et al.* (2006)). Black line indicates the profile where stations are projected in the next figures. Topographic data was taken from the ETOPO1 world reference Amante & Eakins (2009).

3.4.1. Phase tensors and induction vector analyses

Dimensionality analysis describes the complexity of an area or its deviation from simple structures, such as a homogeneous or layered (1D). The analysis of the impedance tensor makes it possible to differentiate if the subsurface is dominated by a (regional 2D) geoelectrical strike or by more complex (3D) structures without a clear geoelectrical strike. Data complexity and dimensionality of the data set was studied with phase tensors (PT, Caldwell *et al.*, 2004) in combination with induction vectors (IV) in the Wiese Convention (Wiese, 1962). Phase tensors are also a tool to investigate data quality, as mentioned by Booker (2013) smooth variations of the phase tensors with period and position are a strong indicator of data consistency.

In practice, the phase tensor, and more specifically the skew angle (β), are used as an indicator of the complexity of the underlying geological structures. Accounting for noise on field data, β values above ±3° are generally considered to be incompatible with 1D/2D assumptions (Caldwell *et al.*, 2004; Booker, 2013).Moreover, the shape of the ellipse is also indicative of the data complexity. For a 1D case, the ellipses assume a circular shape ($\Phi_{max} = \Phi_{min}$). In the 2D case, PT are no longer circular in shape ($\Phi_{max} \neq \Phi_{min}$), with their major or minor axis aligned with the preferred electric current direction, the geoelectrical strike, or its perpendicular. For a 3D case, PT geometry is also elliptical and not necessarily aligned with regional conductive structures.

Figure 3.8 presents pseudo-sections of the PT and IV for short periods (<1 s). Pseudo-sections for periods larger than 1 s are shown in Figure 3.9. In these pseudo-sections, stations were projected into a 17°NW oriented profile (black line in Figure 3.7). The x-axis represent the distance between the station. The y-axis represent period, in MT the sounding range increases with period including larger horizontal and vertical distances. The PT fillings are colour coded to show β values between -3° and 3° in white, whereas values above and below these limits are depicted in blue and red, respectively.

The short period data (Fig. 3.8) showed 1D dimensionality for the PT (circular shape, low β) and no large variations from the north to the south of the profile, this may indicate a homogeneous of vertically layered subsurface with no large structural variation. The IV were small and scattered for the same periods, excepting under the MA, where large variations in magnitude and direction are visible in the vicinity of the fault systems, possibly acting as local conductors. Small IV indicate an absence of lateral conductive variations, further proving the simple dimensionality of the dataset for short periods.

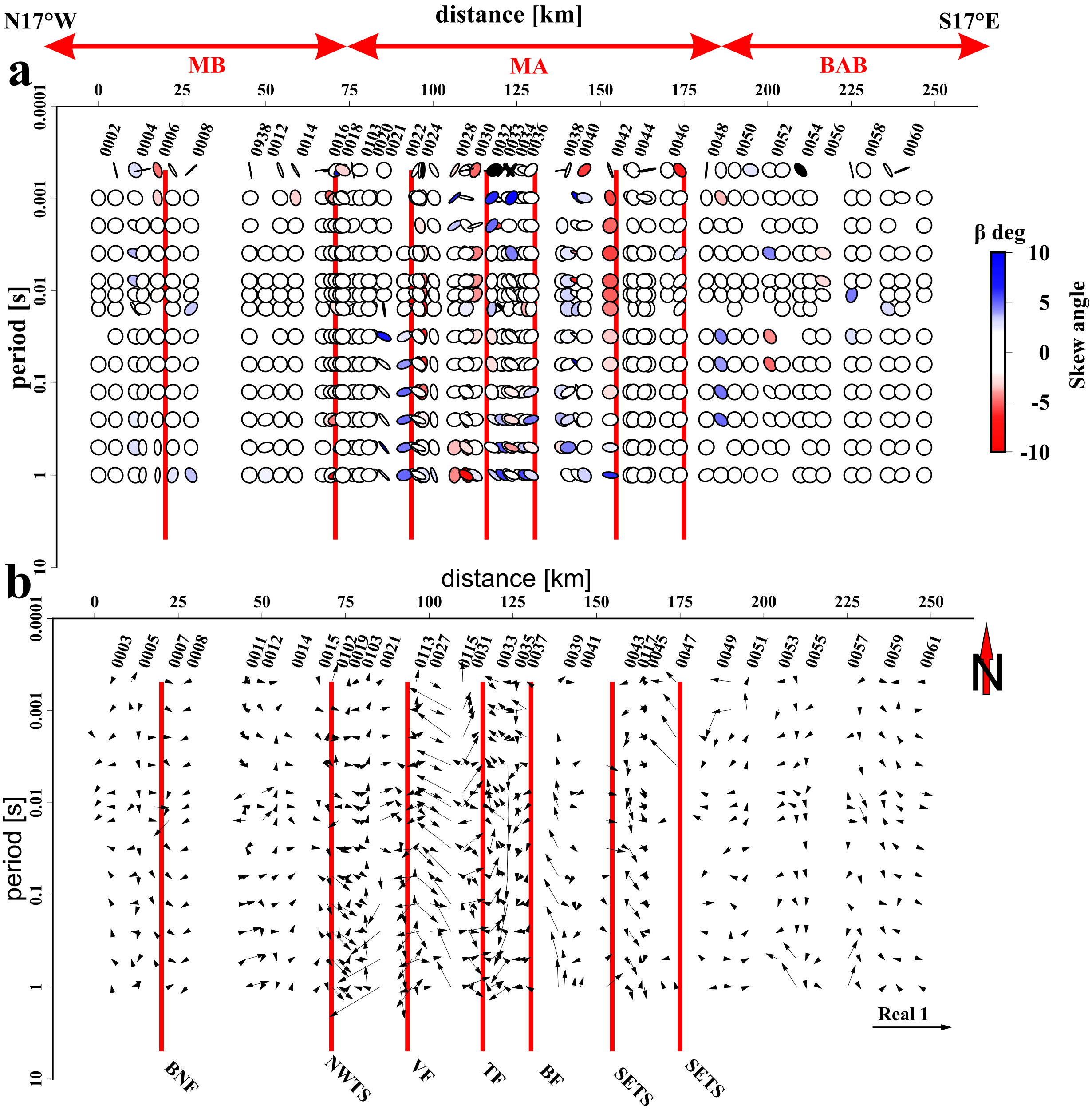

Figure 3.8.: Phase tensors (a) and real induction vectors (b) for the short periods (<1 s). Horizontal red arrows the approximate surface extension of the Maracaibo Basin (MB), Mérida Andes (MA) and Barinas-Apure Basin (BAB). The filling of the ellipses represents the skew angles β, values outside $\pm 10°$ are depicted in black. Ellipses are normalized to Φ_{max}. The vertical red lines represent the surface expression of the fault systems cross-cut by the profile (see red lines in Fig. 3.7).

The long period data (>1 s, Fig. 3.9a) show stations to the north and south of the MA that present

1D/2D dimensionality, low β values and quasi-circular PT above 10 s. However, in the northern section in the vicinity of the Burro Negro fault (BNF), PTs from 1 s show an elliptic shape with the major axis showing a north orientation. Below 10 s, most PT major axis in the northern section rotate to an almost E-W direction, and the β values at 100 s are larger than ±3°. The IAs (Fig. 3.9b) for periods longer than 10 s point to the east, growing in length and rotating southwards with period, highlighting the presence of a conductor of considerable size north-west of the profile.

The central section β values indicate 3D dimensionality for the entire period range, more importantly PT major axis orientations vary between the fault system (red lines in Fig. 3.9). This spatial correlation can also be drawn for the IV (Fig. 3.9b), showing a clear orientation and similar length between those boundaries. From the north to the south, between the North-western thrust system (NWTS) and the Valera fault (VF), PT orientation is almost E-W while the IV S45°W orientation and length may indicate the presence of a considerable conductor NE. Between the VF and Boconó fault (BF), the PT show a NW-SE orientation and IV are west oriented possibly reacting to a conductor to the east. Whereas between the BF and the South-eastern thrust system (SETS), PT major axes are oriented almost N-S and IV rotate to the west, indicating yet another conductive structure to the west. Finally, between the two strands of the SETS, PT are mostly NE-SW oriented while IV seem to be oriented to the NW.

In the southern section, below 30 s most sites PT major axis show a clear orientation S45°W, and β values seem to increase with period Fig. 3.9a). IAs are usually small and scattered showing that there may not be strong lateral resistivity contrasts (Fig. 3.9b), possibly indicating 1D/2D dimensionality.

The low β values and circular shapes of PT show that the northern and southern subsections, could be 2D approximated. The clear NE-SW orientation of the PT at the southern section seems to be related to the BF direction. In contrast, the β values show that the central section is consistent with a 3D dimensionality. The Φ_{max} directions are either parallel or perpendicular to the fault systems, which might point to current channelling along the fault planes. Northern and central sections of the profile show similar variations in terms of direction and magnitude for the IV between stations and periods. Whereas, the IVs in the southern section seem to be more scattered and generally small. Similarly to the PT, the IV seem to be influenced by the fault systems, which appear to act as boundaries for changes in directions. However, below 100 s, most IVs point away from the highly conductive water of the Caribbean sea (roughly 100 km north of station 0002), also describe as the coast effect.

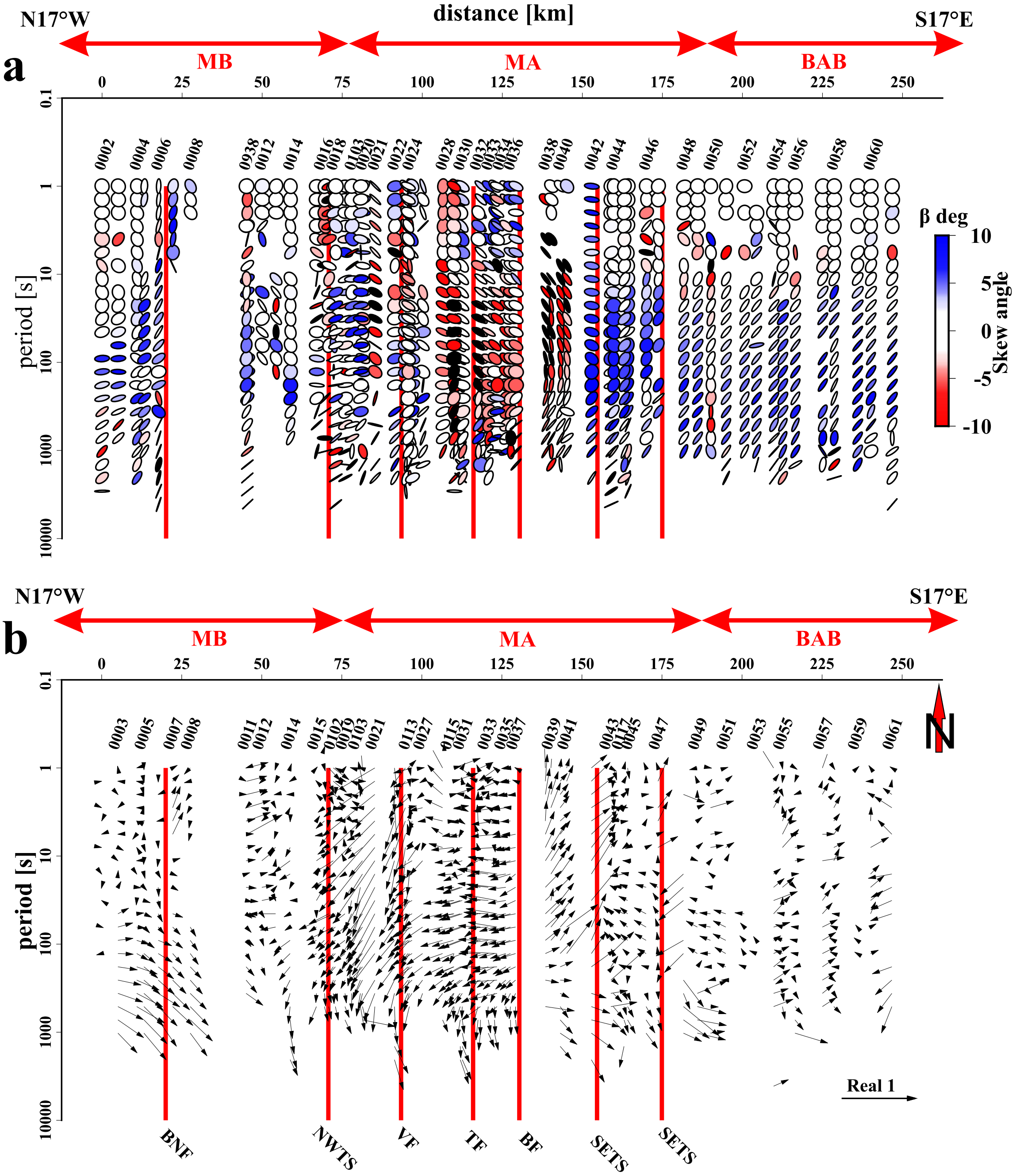

Figure 3.9.: Phase tensors (a) and real induction vectors (b) for the long periods (>1 s). Horizontal red arrows the approximate surface extension of the Maracaibo Basin (MB), Mérida Andes (MA) and Barinas-Apure Basin (BAB). The filling of the ellipses represents the skew angles (β), values outside ±10° are depicted in black. Ellipse sizes are normalized to Φ_{max}. The vertical red lines represent the surface expression of the fault systems cross-cut by the profile.

Further analysis of the data complexity can be made in map view (see Fig. 3.10). The PT fillings are colour coded to show β values between -3° and 3° in white, whereas values above and below these limits are depicted in blue and red, respectively. The black arrows indicate the real component of the IAs.

Figure 3.10a shows PT and IAs for a period of 11 s. In concordance with Figure 3.9, PTs from stations above the sedimentary basins (the northern and southern sections) present mostly 2D dimensionality, as indicated by low β values and IV mostly align with the direction of the main axis of the PT (Φ_{max}). However, in the central section Φ_{max} directions are mostly oriented north-north-west almost perpendicular to the Boconó fault. IAs for the same section point mostly westwards north of the Boconó fault, and to the NE south of it, suggesting the presence of conductors outside the profile to the east and west, respectively. β values indicate a 3D dimensionality for this section.

At 128 s (Fig. 3.10b), skew angle values indicate a 3D electrical conductivity distribution for almost the entire profile. For the northern sub-section, major axes of the PTs rotate in NE-SW direction, with IAs pointing SE. Length of the IV are consistently larger than at 11 s period, indicating a significant conductive structure located north of the stations. In the central section, IAs point consistently to the west and PT Φ_{max} are oriented to the NW. The clear alignment NE-SW of the PTs for the entire southern section is an interesting feature. The corresponding β values of around 5° indicate a 3D dimensionality, however the direction of the PTs are subparallel to the fault systems to the north.

At a period of 524 s (Fig. 3.10c) IAs pointing to the SE suggest a significant influence of a conductor north of the profile, with a slight rotation towards west for the central section. The PT $\mathit{\Phi}_{max}$ are mostly oriented to the NE, and sub-perpendicular to the IAs.

The dimensionality analysis suggests strong 3D effects in the central section of the profile, while the northern and southern subsections seem to be 1D/2D for a wide period range. The 3D effects observed in the central section appear to be the influence by off-profile features to the east and west, with the fault systems serving as boundaries between these anomalies. A coast effect has also a considerable influence on the long periods of the entire dataset and should be addressed during the modelling.

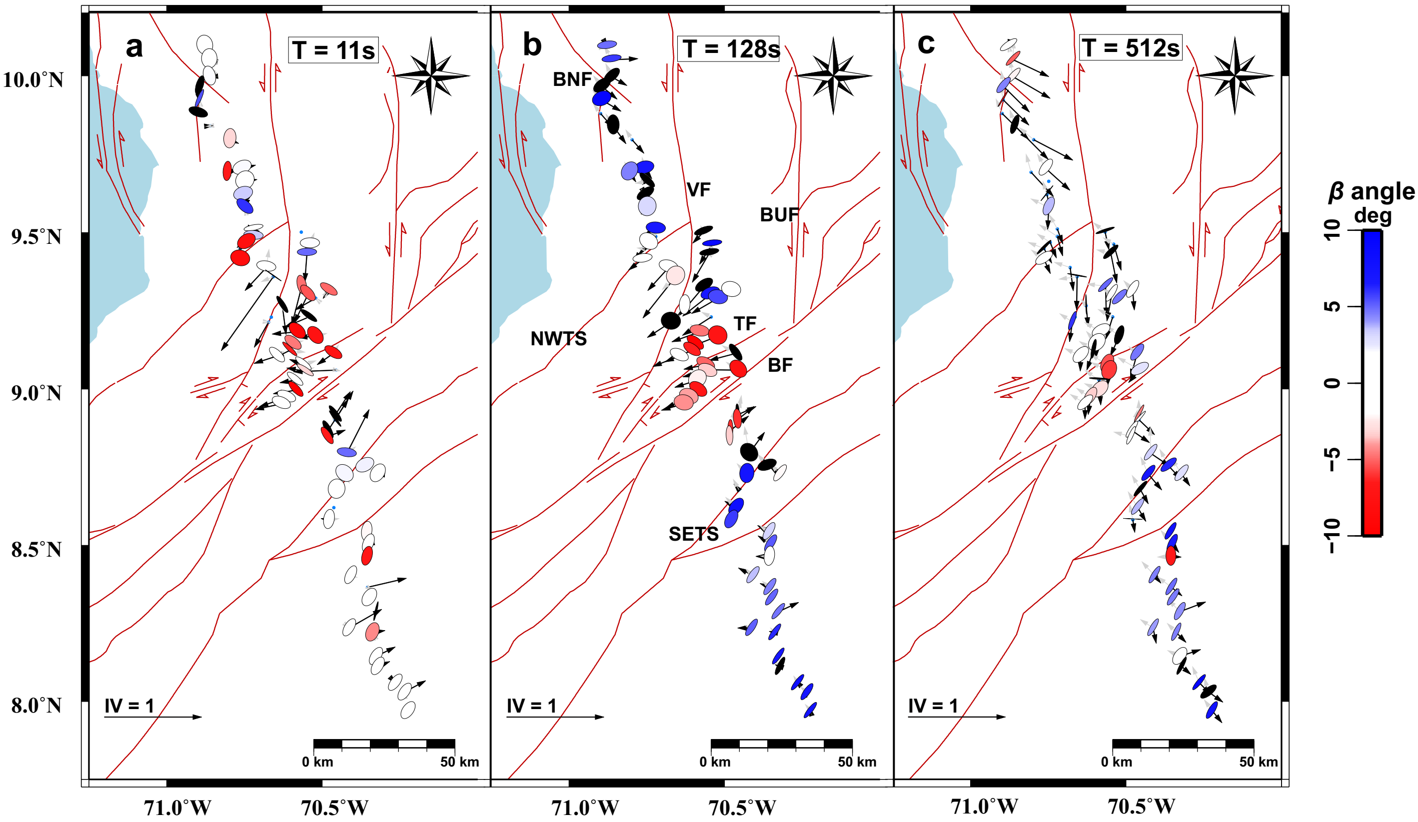

Figure 3.10.: Phase tensors and real induction vectors in map view at periods (a) 11 s, (b) 128 s and (c) 512 s. Red lines indicate Quaternary fault system on the area (from Audemard *et al.*, 2006). The filling of the ellipses represents the skew angle, $|\beta|$ values bigger than 10° are depicted in black. Ellipse sizes are normalized to Φ_{max}.

3.4.2. Estimation of the geoelectrical strike

The tensor decomposition method of Becken & Burkhardt (2004) was employed to calculate a geoelectrical strike direction. This method estimates the geoelectrical strike based on an ellipse parametrization of the columns of Z (equations 2.17) or telluric vectors (Bahr, 1988). The ellipticity of the telluric vectors are rotationally variant and vanish for 2D conditions if data is rotated to the regional strike direction. Therefore, the regional strike direction can be determined by minimizing the sum of squared ellipticity weighted with their variances by rotating the coordinate system (Becken & Burkhardt, 2004). This procedure can be carried out in single and multi-site modes. In single-site mode, each station is analysed individually for a given period range and a regional strike angle is found per site. In the multi-site mode a strike angle is sought that best fits all selected stations in the given period range. The regional geoelectrical strike direction derived by tensor decomposition methods has an inherent 90° ambiguity, which can be solved by considering the IVs.

The investigation on the geoelectrical strike is an important step for 2D modelling approximations and to further evaluate data quality and structural distribution. As noted in the previous section, the northern and southern sections show a 1D/2D dimensionality for a wide period range. In a 3D environment, there is generally no regional geoelectrical strike, but for the central section a dominant strike direction can be identified which is useful for comparison with the regional geology.

Figure 3.11 presents the results of the single mode for the entire profile for different period ranges in a rose diagram, while the multi-site results are depicted by black arrows, real induction vector results are included in the same period range to solve the 90° ambiguity. As IVs in the Wiese convention point away from the conductors and the geoelectrical strike represents the direction of a regional conductivity anomaly. If there is a regional strike direction in the data, it should be perpendicular to the IVs. The strike values for the multi-site analysis are estimated in the range of -90° and 0°. Prior to the analysis, noisy data were masked and IVs with a magnitude smaller than 0.05 were not considered for the plots.

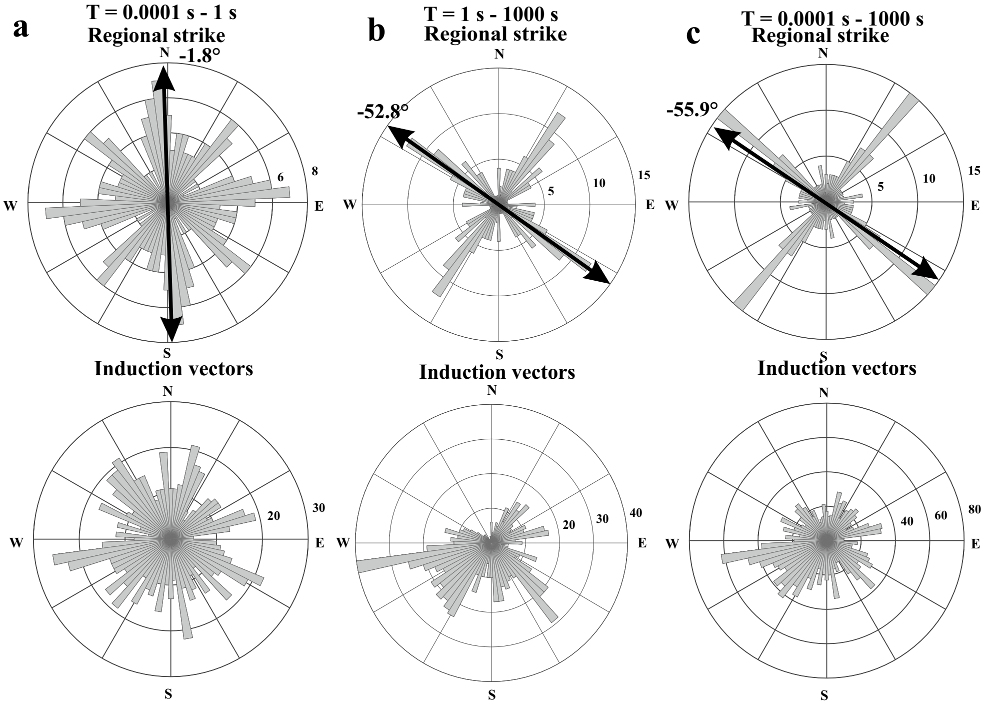

Figure 3.11.: Regional strike (top) and real induction vectors (bottom) for the entire dataset for three different period ranges. (a) T=0.0001 s - 1 s, (b) 1 s - 1000 s and (c) T=0.0001 s - 1000 s. Black arrows indicate the direction of the multi-station analysis for the strike.

Data from periods below 1 s (Fig. 3.11a) showed two main directions for the strike angle 0° and 90°. The multi-site analysis found a geoelectrical strike of -1.8°, that satisfy most of the stations. nonetheless, as homogeneous or layered subsurface (1D) do not have a dominant strike direction, the tensor decomposition results for a strike angle close to zero or 90 degrees may be consistent with no dominant strike. Hence, these strike angles are usually associated with 1D dimensionality, provided that they can not be explained by geological structures. Moreover, the IV are scattered and do not have a clear main tendency. There is, however, a second group of strikes at approximately 50°, which seem to represent the regional trend observed at longer periods (Figs. 3.11b and c).

Figure 3.11b display clearer tendencies for strike and IAs for the period range of 1 s to 1000 s (mid to long periods), the multi-site analysis resulted in -52.8° as IVs point consistently to the west. Figure 3.11c comprises the entire period range of the data set, showing a similar tendency than mid-long periods in the strike but the IV seem more scattered and a strike value resulting of the multi-site analysis of -55.9°. These results showed that the short periods bear little influence on the strike calculations.

The strike analysis (Fig. 3.11a) confirms the 1D dimensionality observed for short periods in the PT (Figure 3.8). Whereas Figure 3.11b, shows a common strike direction for the long period data, however, IV for the same period range (1-1000 s) seem to distinguish at least three main lateral contrast pointing to the west, south-west and the south-east. Furthermore, closer observation of the responses per station showed high error for the ellipticity of several stations for the multi-site calculation between 1-1000 s, indicating that -52.8° may not represent the entire dataset. Thus , the tensor decomposition was repeated splitting the profile into northern, central and southern sections considering only the periods larger than 1 s. These results are shown in Figure 3.11.

The northern section strike analysis (Fig. 3.11a) show two clear tendencies around 0° and -26° with the IV are mostly SE oriented, indicating a dominant geoelectrical strike of 64° (N64°E). The central sub-section (Fig. 3.11b) seems to be in agreement with the general strike (Fig. 3.11b), the multi-site analysis in combination with the east oriented IV show a dominant regional strike of -53.1° (N53.1°W). The southern sub-section presents a clear tendency of -52° or 38°, however, the IV are seemingly scattered (as previously noticed in Fig. 3.9). Nonetheless, in 2D conditions or when these can be assumed, the PT major axis normally aligns with the strike direction (Caldwell *et al.*, 2004), hence from Figure 3.9 it is clear that the PT major axis is consistent with approximately N40°E orientation. Using this value as reference, the regional geoelectrical strike of the southern section is 38° (N38°E) .

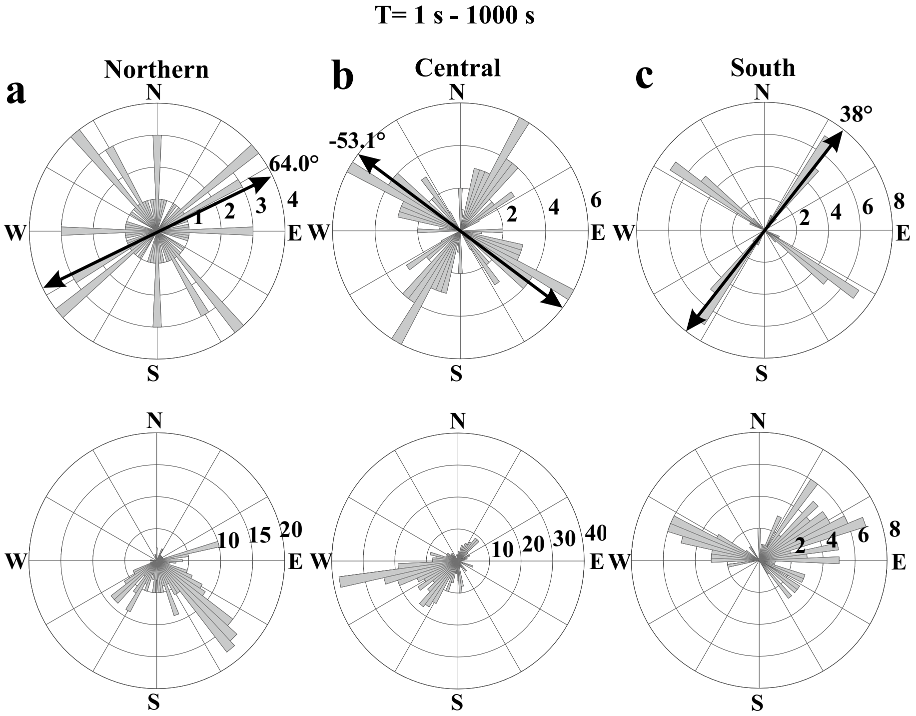

Figure 3.12.: Regional strike for the range of periods from 1 s to 1000 s and the real induction vectors per section. Stations are grouped in (a) northern, (b) central and (c) southern sections (see text).

The combination of the PT and IV in the central section indicate a 3D dimensionality and the influence of an off-profile conductor to the East. The northern and southern sub-sections can be approximate to a 2D case. The IV of the northern section seem to indicate a conductive body to the north, possibly reflecting the coast effect, with another group of IV more SW oriented. The latter could also be related to an off-profile anomaly. The southern section also has a clear strike, which is almost sub-parallel to the fault systems along the MA, possibly indicating that these are the main current channelling structures influencing this sub-section of the dataset.

4. Modelling of the GIAME dataset

The final goal of the magnetotelluric (MT) method is to generate models of the resistivity distribution of the subsurface from the measurement of time-varying electric and magnetic fields at the surface. Forward modelling and inversion tools are applied to obtain a resistivity distribution that can explain the observed data (see section 2.7). Inversion modelling is an iterative process, which searches for a model of resistivity distribution that generates responses closer to some target data (e.g. transfer functions of measured field data). At each iteration, the response of the model is calculated using the forward modelling approach and then compared with the target data.

The analysis of the Venezuelan data set (chapter 3) showed a combination of 2D and 3D dimensionality, as well as varying geoelectric strike angles from north to south of the profile. Furthermore, the distribution of the sites along a profile limits the lateral resolution of the data. Thus, to explain the data set, 2D and 3D inversions were carried out and complimented with synthetic datasets from 3D models to explore the resolution of the inversion models. These synthetic datasets allow a better understanding of the influence of off-profile structures in 2D inversions and their recovery in the 3D inversion.

Another challenge for the interpretation of this dataset was the strong topographic variations. Along with the profile, station elevations vary from 0 m above the sea level to approximately 3600 m, which may have a strong influence on the models (see section 2.6.3). To test the effect of topographic variations required the generation of synthetic datasets from 2D and 3D models, the analysis of the forward responses, and their comparison with field data. The analysis of these models showed significant variations on the apparent resistivity values measured at hills and valleys in areas with similar subsurface resistivity. Topographic effects bear a more considerable influence on short-period data and are more significant at pronounced mountain slopes (>15°). These results are similar to those obtained by other authors (e.g. Jiracek, 1990; Wannamaker *et al.*, 1986; Lin *et al.*, 2018). To account for these effects in the 2D and 3D inversions is necessary: to include smooth variations of the topography in the models; to centre stations at their cells previous to inversion; and to ensure that stations are always under the transition zone between air and land (surface of the models).

The two-dimensional inversion of the data set provided means to test quickly and effectively the effect of the topography along profile. Two-dimensional models are expected to reproduce the sedimentary basins and the structures related tectonic processes that actively deform them. However, these models are susceptible to the influence of off-profile structures that may be recovered with a shift in their location, resistivity or both. To explain the entire dataset is also necessary to employ three-dimensional inversion methods, which can account for off-profile structures that are clearly present in the central part of the dataset. The 3D models are expected to explain not only the mostly 2D sedimentary basins but also account for the effect of the topographic variation along the Mérida Andes and recover the resistive anomalies associated to the oblique fault systems. Comparison of the two modelling approaches proved helpful in identifying the limitations of the obtained models and provided complementary information on the depth and extent of the recovered resistive structures.

Therefore, this chapter presents the 2D and 3D inversion models, the analysis of the obtained conductive structures and their geologic interpretation, geodynamic implications and contribution to the current knowledge of the tectonic evolution of western Venezuela and the Mérida Andes. The arguments presented in this section on the 2D inversions, and 3D synthetic models are part of a peer-reviewed manuscript submitted to the Geophysical Journal International under the title '**Magnetotelluric imaging of the Mérida Andes and surrounding areas in Venezuela**'; by the time of the submission of this thesis, the manuscript was accepted for publication with moderate corrections. The evaluation of the 3D inversion models resolution and limitations as well as the geological interpretations are partially included in a peer-reviewed manuscript submitted to the Journal of South American Earth Sciences titled '**Three-dimensional magnetotelluric imaging of the Mérida Andes, Venezuela**'; by the time of the defence of this thesis the manuscript is submitted.

4.1. Two dimensional inversion

Two-dimensional inversions were conducted employing the code MARE2DEM (Key & Ovall, 2011; Key, 2016), to study the sections of the dataset consistent with 2D dimensionality. MARE2DEM employs an adaptive, unstructured finite element grid and parallel goal-oriented computing. According to Key & Ovall (2011), the model discretization with unstructured triangular grids within MARE2DEM results in accurate resolution of complex subsurface structures. Additionally, the unstructured grid enables an excellent discretization in near-surface areas (Muñoz *et al.*, 2018). To solve the inverse problem MARE2DEM applies an adaptation of the fast Occam inversion technique (Key, 2016). The basis of the Occam approach is the non-linear Gauss-Newton minimisation for solving non-linear least squares problems and is frequently used for geophysical applications (Key, 2016).

4.1.1. MARE2DEM modelling code

In this section, the main elements of the MARE2DEM inversion approach are summarized. The focus is on the parameters that can be defined by the user. For a more detailed explanation of the functionality of the code see Key (2011; 2016).

The inversion approach included in MARE2DEM (Key & Ovall, 2011; Key, 2016) uses a Lagrange multiplier formulation and seeks to minimize an unconstrained functional ($\Psi(m)$) in the form:

$$\Psi(m) = \underbrace{\|Rm\|^2}_{Roughness} + \underbrace{\|P(m-m_*)\|^2}_{Prejudice} + \underbrace{\mu^{-1}\|W(d-F(m)\|^2}_{tradeoff(objfunction)} \tag{4.1}$$

where m is the n-dimensional vector of model parameters. The prejudice P is used to penalize or prioritize sections of the model. The roughness operator matrix R, perform the model regularization (stabilizing functional), and it is defined as:

$$\|Rm\|^2 = \sum_{i=1}^{m} A_i \left[\sum_{j=1}^{N(i)} w_j \left(\frac{\Delta m_{ij}}{\Delta r_{ij}} \right)^2 \right] \tag{4.2}$$

where A_i is the area of parameter i and accounts for the integration over the parameter region and $N(i)$ is the set of all parameters sharing a vertex with parameter i, and:

$$\Delta m_{ij} = m_i - m_j \quad , \quad \Delta r_{ij} = \sqrt{\left(\frac{y_i - y_j}{w_{hv}}\right)^2 + (z_i - z_j)^2} \quad , \quad w_j = \frac{A_j}{\sum_{k=1}^{N(i)} A_k} \tag{4.3}$$

The term in brackets in Δr_{ij} approximates the two-norm of the gradient at parameter i using an area weighted average of differences between all parameters in a ring surrounding parameter i. The horizontal to vertical penalty weight w_{hv} is implemented in the model to bias the inversion towards horizontal or vertical smoothness. When $w_{hv} > 1$, the range is reduced in the horizontal direction, resulting in a larger horizontal gradient; this biases the inversion towards enhanced horizontal smoothness. Conversely, when $w_{hv} < 1$, the horizontal distance is expanded, resulting in less horizontal smoothing and enhanced vertical smoothing (Key, 2016).

Furthermore, data inversion in MARE2DEM is based on the Occam approach (Constable *et al.*, 1987), a variation of the non-linear Gauss-Newton minimization used frequently in geophysical applications (Key, 2016). In this case the model update takes the form:

$$m_{k+1} = \left[\mu(R^T R + P^T P) + (WJ_k)^T WJ_k\right]^{-1} \times \left[(WJ_k)^T W\hat{d} + \mu P^T P m_*\right] \tag{4.4}$$

with the modified data vector ($\hat{d}$)

$$\hat{d} = d - F(m) + J_k m_k \tag{4.5}$$

As explained by Key (2016), the Occam algorithm consists of 2 phases. In phase 1, a line search on (4.4) is performed to find the value of μ that produces a models $m_{k+1}$with the lowest data misfit. The fast Occam approach used in MARE2DEM sets a misfit reduction with respect to the starting model of 15%. If such a minimum value is found, the model is accepted, and the iteration concluded. If not, then the iteration will continue until a minimum is found. On the other hand, if the minimum search fails, a reduced model step is taken, and the line search is carried out again using the model $m'_{k+1} = \alpha m_{k+1} + (1-\alpha)m_k$, with $\alpha = 1$ initially and successively cut in half each time the line search fails to find a better fitting model.

Once a model with a data misfit less than or equal to the target misfit has been found, phase 2 of the Occam algorithm begins, where it seeks the model at the target misfit that has the largest μ, and thus the smallest roughness norm. Data misfit is usually obtained via the normalized Root Mean Squared (RMS), by taking the square root of the squared of the sum of the residuals between the observed data $(d_{obs,k})$ and the modelled responses $(d_{mod,k})$ divided by the number of responses inverted:

$$RMS = \sqrt{\frac{1}{N}\sum_{k=1}^{N}\left(d_{obs,k} - d_{mod,obs}\right)^2} \tag{4.6}$$

Forward computations are carried out in a parallelized way using the data decomposition scheme presented in Key & Ovall (2011), where the model is sliced into smaller subsets that are each modelled in parallel using the goal-oriented adaptive finite element. An additional parallelization is implemented across the data, establishing groups of stations and periods and assigning them to different processors.

To apply the data parallelization and to improve computing times, the user can define the number of MT receiver (N_g) and frequencies (N_f) per group to obtain the number of processors necessary for a given inversion (N_{cpu}) as:

$$N_{cpu} = (N_g * N_f) \tag{4.7}$$

For example, for a dataset of 51 sites and 40 frequencies, a possible combination would be to define 17 station per group (3 groups) ($N_g = 51/17 = 3$), and 2 frequencies per group (20 groups) ($N_f = 40/2 = 20$), thus $N_{cpu} = 60$ processors.

4.1.2. 2D inversion setup

The MARE2DEM code (Key & Ovall, 2011; Key, 2016) official release includes routines to design models and to analyse inversion results. These routines form the MARE2DEM Model Building Assistant (Mamba2D) suite. This suite developed in Matlab® employs a Delaunay triangulation scheme to build an unstructured grid in a defined area. Moreover, inversion parameters can be defined here.

The coordinate system in MARE2DEM is defined with the x-axis perpendicular to the profile and the y-axis parallel to it, and the z-axis positive downwards. However, the user can define the positive direction of the profile, and the data must be rotated accordingly.

The data were rotated to the representative strike of the northern and southern sections, -116° (64°) and -142° (38°), respectively. This rotation effectively assigned the yx- component to the TM- mode and xy- component to the TE- mode, with the y-axis positive to the NW. The rotated sites were projected onto two profiles (blue and red lines in Fig. 4.1). Each profile includes the stations belonging to its section and the sites from the central section for overlap. The profiles were centred on stations 0020 and 0048, respectively. The station distribution and profile location aim are to reduce the effect of station projections and large differences in topography.

Inversions were performed for the each of the subdivisions of the datasets and are presented as northern and southern sections in the following.

The preferred inversion setup was determined after systematically testing different values for the parameters that control the inversion process. Inversion parameters tested included different model grid sizes, a range of values for background resistivity, data error floors, details of topography, the inclusion of the Caribbean Sea to account for the coast effect, regularization and the trade-off. Additionally, to avoid the modelling of unrealistic anomalies to fit the data, minimum and maximum bounds to the resistivity of the elements of the model can be set. This process is time costly and implies several forward calls and comparison of results of inversion of real and synthetic data.

Model grid and coast effect

A model grid has to be designed that can represent small and big scale structures and large enough to accommodate the induction range of the data, to obtain smooth inversion models.

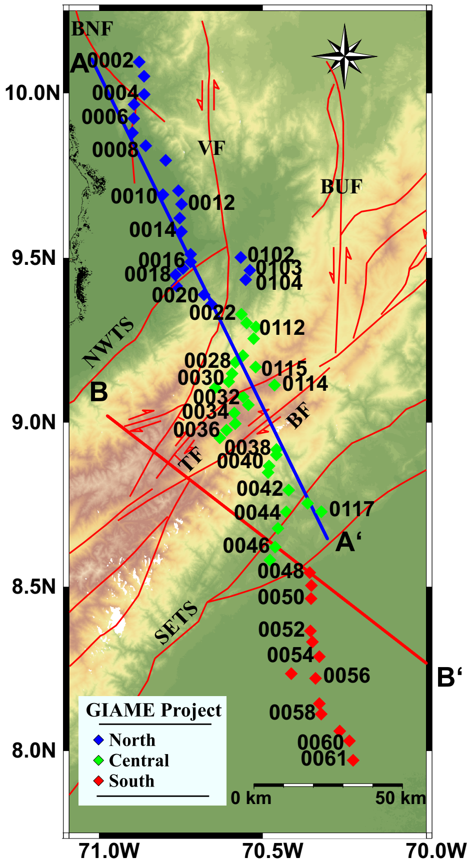

Figure 4.1: Location of the northern and southern sections (blue AA' and red BB' lines) on a topographic map including the Quaternary fault systems. Abbreviations: BNF - Burro Negro Fault, VF - Valera fault, TF - Tuñame Fault, BF - Boconó fault, BUF - Burbusay Fault, NWTS - Northwestern thrust system (also known as Las Virtudes thrust system) and SETS - Southeastern thrust system. See text for descriptions.

Moreover, it must be large enough to include far away structures that may have an influence on the dataset and to avoid border effects.

The maximum extent at both end at the model was tested calculating forward responses for the same period range of the dataset on a homogeneous half-space. The horizontal distances varied from 100 km to 500 km; the vertical distances considered between 100 and 500 km of air and 100 and 1000 km below the surface. The preferred horizontal model extent was defined as 1250 km, with 250 km representing the profile length and 500 km after both ends of the profile. The z-axis comprises 1500 km, with 500 km of air (above the surface) and 1000 km below the surface. The surface was defined by including a smoothed topography and bathymetry taken from the digital elevation model (DEM) generated using the NOAA dataset (Amante & Eakins, 2009). The inclusion of topography allows the modelling of its effects, benefiting the inversion misfit, and the data fit, but this is only possible in the profile direction.

Since the Caribbean Sea is located approximately 200 km north to the profile, its influence on the modelled responses was tested by building resistive homogeneous models (50 to 100 Ωm) with and without the Sea (0.3 Ωm) and comparing the forward responses obtained. Forward responses showed that the Caribbean sea influenced the dataset at large periods (above 100 s), thus it was included in the inversion models.

The air resistivity was fixed at 10^9 Ωm above the surface. The griding of the subsurface includes the introduction of parallel to surface planes located at varying depths from 100 m to 120 km; and cell sizes varied from 50 m to 5 km under the stations. The Mamba2D modelling suite allow for the automatic definition of triangulation outside the scope area (e.g. far from the stations), resulting in a growing cell size from 5 km to 50 km. In total, each model consist of more than 55,000 elements.

Starting model

The starting model is used as a reference to be updated by the inversion process. For an optimal inversion result, it is crucial to find a reasonable resistivity starting model. Therefore, different homogeneous half-spaces with 50 Ωm, 100 Ωm, 300 Ωm and 500 Ωm were tested. The lowest initial misfit (first iteration) with the best relation between sensitivity to structures and fast convergence was observed for the 100 Ωm starting model.

Data input and errors

Input data for 2D inversion are the rotated apparent resistivity (ρ_a) and phase (φ) curves. MT data were inverted in the period range from 0.1381x10^{-2} s to more than 724 s, with seven periods per decade and interpolated to account for masked outliers. Since small scale near-surface heterogeneities can cause distortion and static shift, which affects the apparent resistivity curves but not the phases (see section 2.6.2), they have to be addressed in the inversion. While static shift of TM can be produced by small scale inhomogeneities just beneath or next to a station, 2D models cannot replicate static shift for TE mode data (e.g. Jiracek, 1990; Wannamaker *et al.*, 1984, 1986). Down-weighting of apparent resistivities, in particular of the TE mode, is used in 2D inversion to reduce the influence of static shift on the inverted resistivity structure.

It is common practise to define a averaged error to the input data, to have an even influence of the dataset. Error floors from 5% to 10,000% of the absolute value were tested for the apparent resistivity of the TE- and TE- mode. The phases of both modes were modelled with error floors ranging from 1° to 5°. The influence of the vertical magnetic transfer function was tested employing a range of error floors from 0.001 to 0.1.

Smoothing

As shown in equation 4.3, the model smoothing in MARE2DEM is controlled by the horizontal to vertical penalty weight (w_{hv}). Data fit seemed to be negatively affected by vertically biased smoothing ($w_{hv} < 1$), and better results and data fit were obtained with horizontally biased smoothing ($w_{hv} > 1$). The horizontal to vertical weight was tested in a range of 1 to 4, with the best result obtained with a value of 3 for the smoothing.

Table 4.1 summarizes the main parameters and values used for the 2D inversion in this project.

Table 4.1.: Summary of the 2D inversion set up parameters.

Parameter	preferred value	Tested ranges
Topography and bathymetry	included	with and without topography
triangle size	min = 50 m, max = 5 km	min = 50 - 100 m, max = 2.5 - 10 km
# of elements	~55,000	-
max. length	y = 1250 km, z = 1500 km	y = 500 - 1250 km, z = 200 - 1500 km
starting model	$100\,\Omega m$	50 - $500\,\Omega m$
smoothing	$w_{hv} = 3$	$w_{hv} = 1 - 4$
data error floors	$TE, \rho = 10,000\% \mid \rho \mid, \varphi = 1.5^\circ$	$TE, \rho = 20 - 10,000\% \mid \rho \mid, \varphi = 1^\circ - 3^\circ$
	$TM, \rho = 20\% \mid \rho \mid, \varphi = 1.5^\circ$	$TM, \rho = 10 - 50\% \mid \rho \mid, \varphi = 1^\circ - 3^\circ$

4.1.3. Integrated inversion of TE and TM-modes

The 2D inversion models are presented in Figure. 4.2, black arrows on top of the models mark the surface extent of the basins and the MA; whereas red lines denote the location of the fault systems. The labelling of the structures correspond to C for conductors and R for resistors. The resistivity of the C-labelled structures ranges from 1 to $10\,\Omega m$, whether the R-labelled structures show values higher than $1000\,\Omega m$ (e.g. R1), mostly between the range for sedimentary rocks (0.1 to $10,000\,\Omega m$, see Fig. 2.1). The northern section reduced an initial RMS of 22.98 to 1.25 after 27 iterations (initial RMS of 22.98), and the southern section, in 21 iterations reduced an initial RMS of 41.53 to 1.57, the RMS is analysed in detail in section 4.3.

The 2D models show a variation of conductors and resistors in close to the surface with a more homogeneous and resistive medium below 10 - 15 km, with the exception of the conductor labelled C9 in the northern section (black ellipse in Fig. 4.2a), and in the southern section the conductor located under the BF and the black circle towards the centre of the section (Fig. 4.2b).

Model description

The 2D inversion models from the northern and southern sections (Fig. 4.2) suggest a depth of 5 km to 7 km for the Maracaibo Basin (MB) and 5 km for the Barinas - Apure Basin (BAB). This is consistent with the depths suggested by several authors (e.g. Kohn *et al.*, 1984; Audemard, 1992; De Toni & Kellogg, 1993; Audemard & Audemard, 2002; Duerto *et al.*, 2006). The subsurface MA appears mainly as a resistor intersected by various good conductors. The latter seem to be spatially related to the Boconó and other major fault systems. The position of faults and their associated anomalies may differ as a result of the stations' projection onto the profile.

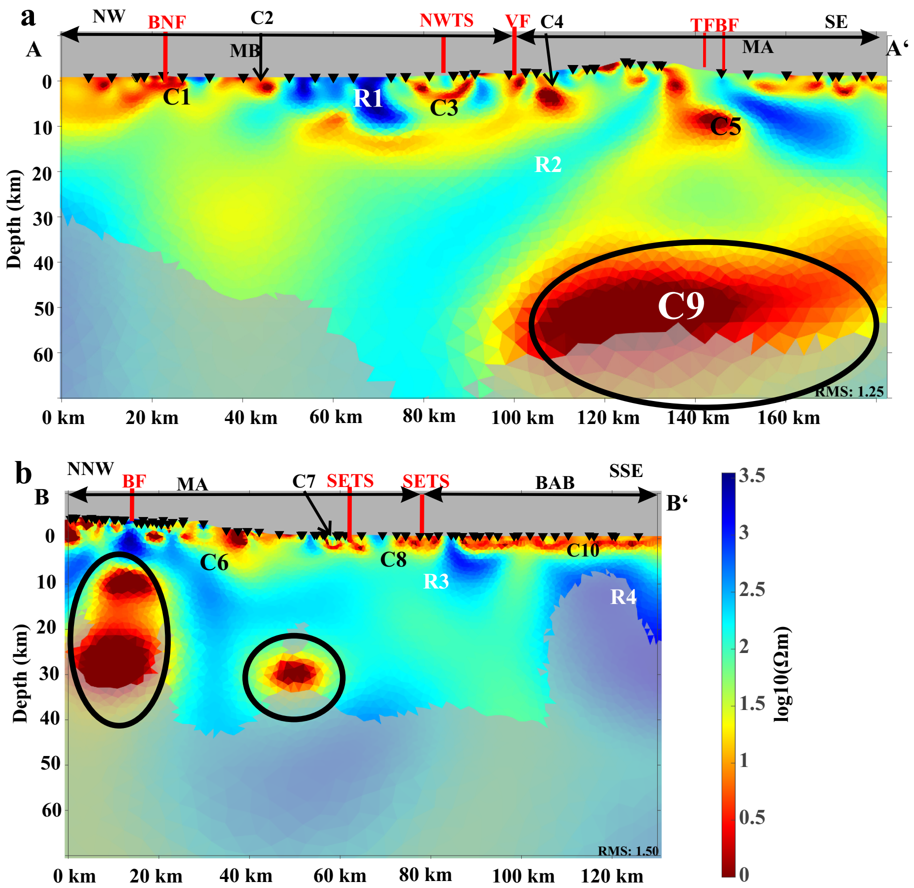

Figure 4.2.: 2D inversion results for (a) the northern subsection and (b) the southern subsection. Surface expressions of fault systems are highlighted with red lines, black arrows depict the surface extensions of the MB, MA and BAB. The grey shaded area represent sections of the model with sensitivities lower than $10^{-6.5}$ and 10^{-6} for the northern and southern sections, respectively (see Fig. 4.10).

In the northern section (Fig. 4.2a), conductors C1 to C4 spatially relate to the MB, and different changes in resistivity possibly related to the tectonic regime to which this basin has been subjected. The centre of the conductors also correlate with location at the surface of the fault systems cross-cutting the profile (see also Fig. 4.1) namely the BNF, NWTS and VF. Between C2 and C3 a considerable resistor (R1, 20 km long, reaching 10 km depth) is placed by the inversion that indicates a lateral variation in structural and rock composition. Conductor C5 may spatially relate to the TF and BF, however it is shifted to the north, possibly as a result of the projected profile position.

The most significant conductive anomaly (C9) is located towards the south (black ellipse, Fig. 4.2a). Such a massive conductive structure at great depth (>45 km) may be the result of an off-profile structure projected onto the 2D plane. Further conclusions on the origins of this structure are accompanied by careful testing with conceptual models.

The southern section (Fig. 4.2b) is also characterized by a series of conductors positionally related to the main fault systems and sedimentary structures. The BF seem to be represented by conductor C6, however it could spatially relate to the central conductor marker by an ellipse. The shift in the location of the conductor and the position of the fault system may be related to the projection of the stations due to the location of the profile and the complex dimensionality of the area. Conductor C7 and C8 are more clearly related to the NWTS, whereas C10 represents the BAB. Conductors C8 and C10 are separated by resistor R3, which is located in an area of uneven station distribution, and could be also the result of poor resolution.

Comparison between the anomalies related to the BF in the northern and southern sections (C5 and C6) (Fig. 4.2) show marked differences, illustrating that the different projection and data rotation have a considerable influence in the modelled anomalies. This effect is further analysed employing synthetic dataset in section 4.5.

4.1.4. Inversion of individual modes

Individual inversions of each mode allows to identify their contributions to the resistivity model of the integrated inversion. Thus, inversions were performed for the TE-, TM-mode and the vertical magnetic transfer function (TP). The error floor settings for these inversion runs were: 20% error floor of the absolute value for the TE- and TM-ρ_a; 1.5° for the phases; and 0.05 for the TP. Figure 4.3 shows the models obtained for the northern section.

The models for TE- and TM-mode (Figs. 4.3a and b) show common features (black ellipses and circles), but differ significantly in the overall appearance and connection between structures. The TE-mode inversion (Fig. 4.3a) reached an RMS of 3.16 after 15 iterations, and the TM-mode reached an RMS 1.8 after 45 iterations. The difference in the RMS is mostly related to the inferior fitting of the TE-mode ρ_a compared to that of the TM mode, while in both cases the phases were tightly fitted. In a 2D inversion, it is more complicated to model variations along strike than along profile. Since the TE-mode represent the former, it is usually poorly fitted in the 2D inversion, whereas the phases can be better fitted in both modes given that they are less affected by galvanic distortions.

The TE-mode inversion shows small conductors close to the surface (black arrows in Fig. 4.3a) and more localized anomalies. The TM-mode inversion model, on the other hand, recovered a more smooth representation of the subsurface, and interconnection of structures along profile. Both inversion models (Fig. 4.3a and b) add elements to the integrated inversion (Fig. 4.2a), however, it is clear that the connection between conductors is part of the TM-mode inversion, particularly the depth extent and overall shape of conductors C1 to C5; whereas the resistive structures and conductor C9 are common feature of both inversion models.

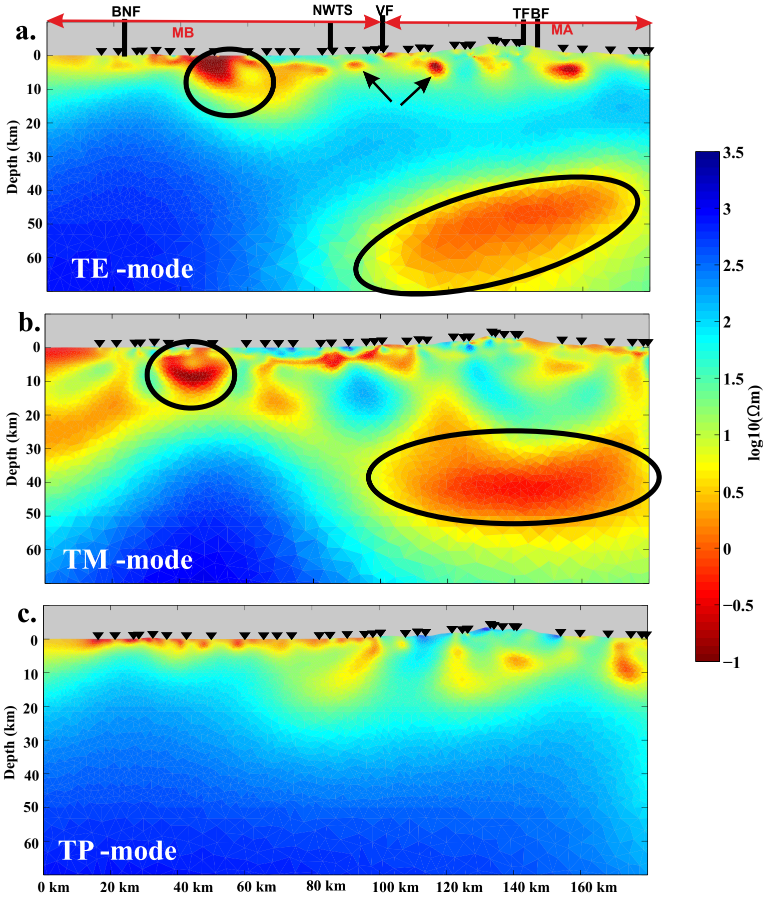

Figure 4.3.: 2D inversion of individual modes for the northern section (blue line in Fig. 4.1). (a) TE-mode, (b) TM-mode and (c) TP-mode. Black circles, ellipses and arrows are described in the text.

The inversion of the TP (Fig. 4.3c) reached a RMS of 1.35 after 69 iterations (from an initial RMS of 2.24). Unlike the TE- and TM- modes, the 2D inversion of the TP- showed infinitesimal variations of the RMS between iterations along with minimal changed in the resulting models. The TP (Figure 4.3c) shows the smoothest results from the individual modes, possibly related to the limited resolution of the vertical magnetic transfer function to horizontal resistivity variations. The modelled structures seem to be focussed mainly on the upper 10 km of the model and do not show the depth conductivity anomaly present in the TE and TM (marked with the black ellipse in Fig 4.3a and b).

The analysis of the individual inversion showed that both modes are needed to recover the structures in the subsurface. Nevertheless, the structures recovered in the inversion of the TE-mode, particularly the small scale conductivity anomalies close to the surface seem to be a result of the tight errors selected for the apparent resistivity. Further confirming the need of down-weighting the apparent resistivities, in particular the TE mode, a approach applied particularly in areas with complicated geological settings and significant topographic variations (e.g. Sass *et al.*, 2014; Kütter *et al.*, 2016; Meqbel *et al.*, 2016; Muñoz *et al.*, 2018).

The model generated with VTF showed only structural variation close to the surface (see Fig. 4.3c). Inclusion of the VTF in the integrated inversion added spurious surface conductors. At longer periods, induction vectors generally became larger than at low periods but were also influenced by off-profile features.

4.2. Three dimensional inversion

The 3D models in this thesis were obtained with the Modular Electromagnetic Inversion system ModEM (Meqbel, 2009; Egbert & Kelbert, 2012; Kelbert *et al.*, 2014). The ModEM package contains programmes and routines for both forward modelling and inversion of frequency-domain EM data with gradient-based search methods. The 3D MT modelling scheme applies a finite difference approach to solve Maxwell's equations numerically. Furthermore, a non-linear conjugate gradients algorithm is used within the inversion process to solve the minimisation problem.

4.2.1. ModEM modelling code

To recover, stably, an M-dimensional Earth's resistivity model parameter vector (m) that can explain the data (d, transfer functions) adequately, ModEM minimizes an objective function (Φ)

with respect to the model parameters.

$$\Phi(m,d) \;=\; \underbrace{(d-F(m))^T C_d^{-1}(d-F(m))}_{data\ misfit} \;+\; \underbrace{\lambda(m-m_0)^T C_m^{-1}(m-m_0)}_{model\ regularization} \tag{4.8}$$

where $F(m)$ is the forward response of the model, C_d is the covariance of data errors, λ is a trade-off parameter, m_0 is the prior model, and C_m is the model covariance. The model regularization term forces the inversion to obtain models that: (i) are smooth (i.e. in which the transition between resistivity structures vary smoothly), and (ii) are as close as possible to the prior model m_0 (but still fitting the data). During the inversion, λ's value decreases controlled by an automatic criterion depending on the evolution of the inversion convergence. In the beginning, model smoothness drives the inversion; towards the end, it is dominated by the data misfit. The model covariance C_m partly depends on the parameter α, which controls the model smoothness in each coordinate direction (the larger the values of α, the smoother the model resulting from the inversion are).

The covariance matrix C_d is a diagonal matrix which contains the inverse of the squared data errors, i.e. the data variances,

$$C_d = diag(1/e_i^2) \tag{4.9}$$

The calculation of the misfit (and consequently the evolution of the inversion process) depend on the magnitude of the data errors considered. Instead of using the statistical errors obtained for each TF estimate during the data processing, it is common practice to use as error floor for the data in the inversion process some arbitrary values which weight the importance of each transfer function component on the target data misfit.

The model covariance C_m is constructed as a sequence of one-dimensional (1D) smoothing and scaling operators (Siripunvaraporn & Egbert, 2000; Egbert & Kelbert, 2012):

$$C_m = c_x c_y c_z c_x^T c_y^T c_z^T \tag{4.10}$$

$C_m = C_m^{1/2}(C_m^{1/2})^T$ is symmetric. The 1D smoothing operators are block-diagonal, e.g. for the x-direction

$$c_x = \begin{pmatrix} c_{11}^x & & & \\ & c_{21}^x & & \\ & & \ddots & \\ & & & c_{N_yN_z}^x \end{pmatrix} \tag{4.11}$$

with one block for each x-yz cell pair of the model mesh with N_y and N_z cells in y- and z-directions, respectively. Each block c^x_{jk} is constructed by an autoregression scheme:

$$c^x_{jk} = \begin{pmatrix} 1 & & & & \\ \alpha_x & 1 & & & \\ \alpha_x^2 & \alpha_x & 1 & & \\ \vdots & & & \ddots & \\ \alpha_x^{N_{x-1}} & & \cdots & & 1 \end{pmatrix} \tag{4.12}$$

The model covariance parameter α_i determines the model smoothness in each direction and it is defined as $0 \leq \alpha_i \leq 1$.

The inversion procedure in ModEM searches for a minimum of the objective function $\Phi(m,d)$ at each iteration employing a non-linear conjugate gradient (NLCG) algorithm, which is performed in two steps. The first step involves the calculation of the gradient of $\Phi(m,d)$ for the variations in m, to determine a search direction in which $\Phi(m,d)$ decreases most quickly. The second step finds a local minimum along the search direction that reduces $\Phi(m,d)$ by an expected value. This procedure is repeated until the inversion reaches one of the following predefined stopping criteria: the maximum data misfit, the minimum λ, or the maximum number of iterations.

From the parameters mentioned above, the user must provide the initial model, the data vector and its error bounds, and the smoothing settings on each direction $(\alpha_x, \alpha_y, \alpha_z)$. Additionally, the initial λ and its update value, the stopping criteria (i.e. the minimum λ, the target data misfit, and the maximum number of iterations) and the initial search step size. The data misfit in ModEM is calculated using a Root Mean Squared (RMS) value in the form:

$$RMS = \sqrt{\frac{1}{N}\sum_{k=1}^{N}\left(\frac{d_{obs,k} - d_{mod,k}}{e_k}\right)^2} \tag{4.13}$$

where N is the number of all data (transfer functions) points, $d_{obs,k}$ is the observed data, $d_{mod;k}$ is the calculated data (model response), and e_k is the data error. The RMS in equation (4.13) is a unit-less measured, normalized by the data errors. In general, the RMS is commonly considered a measurement of data fit, with a value of 1 corresponding to an optimal fit within the given error bounds.

ModEM is parallelized over independent forward problems reducing both memory requirements and run times. The optimal number of processes is $2N_{per} + 1$, where N_{per} is the number of periods, the factor of 2 accounts for polarizations, and one process serves as the master (Meqbel *et al.*, 2014).

4.2.2. 3D inversion setup

Inversion parameters were tested by experimenting with data input and errors, a range of values for background resistivity, grid sizes, detail of topography, the inclusion of the Caribbean Sea to account for the coast effect and smoothing.

Data input and errors

Input data for the 3D inversions were the elements of the impedance tensor (Z) and the vertical magnetic transfer function (VTF) for a period range of 0.01 s to over 1000 s. Data errors are essential parameters in the inversion, as they directly control the influence that a specific component may have over the resulting model. The tested error floors for the VTF ranged from 0.03 - 0.1. Whereas, for the impedance data, fixed errors were computed using values of 3 - 10% of the absolute value ($\mid Z_{ij} \mid$) for the off-diagonal components and 10-100% of a weighted norm ($\sqrt{\mid Z_{ii} \cdot Z_{ij} \mid}$) for the main diagonal elements.

The best results were obtained by setting 5% for the off-diagonal, 50% main diagonal elements and the VTF 0.005 (initial model) and 0.003.

Model grid and coast effect

For all tested grids, the coordinate system was oriented with x- and y-axis pointing towards geographic north and east, respectively. As ModEM utilises a Cartesian, right-hand coordinate system, the z-axis points downwards.

The extensions of the different grids were chosen large enough to cover parts of the Caribbean sea, as modelling tests for the study area confirmed that the ocean has significant influence on the long period data (T > 100 s) of the vertical magnetic transfer functions. Several different model grids were tested with edge lengths from 1800 m to 2600 m in both x- and y-direction. Since station are distributed along a profile more cells are required in x-direction than in y-direction, resulting in a rectangular model. The selected cell size of 2600 m guarantees that only one station lies within a cell. 30 and 26 padding cells were added at x- and y-direction, respectively, with increasing size by a factor of 1.2.

The distribution of cells in z-direction was design to represent smooth topographic variations and the short period data at different elevations. The surface of the model was generated using the NOAA dataset (Amante & Eakins, 2009), starting at an altitude of approximately 4800 m (highest point in the model). To account for those mentioned factors, starting at the highest point in the model 10 layers of 150 m thickness were introduced (3300 m altitude), followed by 45 layers of 75 m (reaching 75 m below the sea level). From this point, the growth factor changed with depth: 1.05 to 3000 m depth, 1.10 to a depth of 13500 m, 1.15 until 25000 m depth and 1.2 for the remaining extent of the model.

The final version of the model grid used for the 3D inversions of measured data presented in this thesis comprises 170, 116 and 116 elements in x-, y- and z-direction, respectively, corresponding to 1495, 894 and 927 km (in each direction).

Starting model

Several initial models with varying resistivities ($10\,\Omega m$, $65\,\Omega m$, $100\,\Omega m$, $300\,\Omega m$ and $500\,\Omega m$) were tested to find the best fit for the data and model representation. In all models, the bathymetry was included from the NOAA dataset (Amante & Eakins, 2009), the resistivity of the sea was fixed to $0.3\,\Omega m$, and 5 km of sea sediments added. The best data fit was obtained with the $65\,\Omega m$ starting model, the averaged apparent resistivity of the measured data.

Further test consisted of constraining the inversion by including the extent and depth of the Maracaibo and Barinas-Apure basins, based on known geological and geophysical information and the 2D inversions results. The resistivity values for each basin were taken from the averaged apparent resistivity of the stations above these structures, resulting in $25\,\Omega m$ and thickness of 10 km for the Maracaibo basin and $15\,\Omega m$ and 5 km thickness for the Barinas-Apure basin. The Mérida Andes and the background resistivity were set to $120\,\Omega m$. The resistivity of the basins from the surface was linearly interpolated in depth to the background resistivity, to avoid sharp contrast in the model.

The best trade between model smoothness and RMS was obtained employing the constrained model in the 3D inversion.

Model smoothing

Different model smoothing parameter combinations were examined with $0.1 \leq \alpha_x, \alpha_y, \alpha_z \leq 0.7$. The best data fit and geologically accurate models were obtained with setting a higher horizontal smoothing than the vertical. However, values over 0.3 showed overly smoothed structures connected at areas with no station coverage. The horizontal smoothness was set to 0.3 with 0.2 for the vertical smoothness.

4.2.3. Integrated inversion of VTF and impedances

The preferred model for the integrated inversion is shown in Figure 4.4. This model shows a clear correlation with surface structures, such as the MB, the BAB and the fault systems, consistent with the geological information available. However, anomalies were recovered, which could not be directly related to described geological structures.

To obtain the preferred model, the integrated inversion was performed in a two staged process. The first stage focussed on fitting the long period (>1 s) data of the VTF, and the second stage added the short period data and the impedances. The aim of this staged inversion was to initially focus the inversion in regional and off-profile structures, that have a more considerable influence over the VTF; to then focus on the more local variations. This inversion scheme guaranteed to recover both close to profile and off-profile structures.

For the first stage the long period data of the VTF was inverted with an error floor of 0.05, the inversion needed eight iterations to reduce an initial misfit of 2.67 to 1.00. The resulting model from this inversion was the initial model of the second stage.

For the second stage, the VTF error floor was reduced to 0.03, and the low period VTF and impedances were included. The error floor for the components of the impedance tensor were 5% of $\mid Z_{ij} \mid$ for Z_{xy} and Z_{yx}, and 50% of $\sqrt{\mid Z_{ii} \cdot Z_{ij} \mid}$ for Z_{xx} and Z_{yy}. Table 4.2 presents summary of the main inversion parameters. After 97 iterations an initial RMS of 10.14 was reduced to 1.40.

Table 4.2.: Summary of the initial parameters for the 3D inversion.

Parameter	value	tested ranges
Topography and bathymetry	included from Amante & Eakins (2009)	-
horizontal cell size	2600 m	1800 m to 2600 m
# of elements	x = 170, y = 116, z = 116	-
max. length	x= 1,495 km, y = 894 km, z = 927 km	-
starting model	constrained with MB and BAB	half-space 65 Ωm to 500 Ωm
smoothing	$\alpha_x = \alpha_y = 0.3$ and $\alpha_z = 0.2$	0.2 to 0.7 for each component
data error floors	$Z_{xx}, Z_{yy} = 50\% \sqrt{\mid Z_{ii} \cdot Z_{ij} \mid}$	10% to 100%
	$Z_{xy}, Z_{yx} = 5\% \mid Z_{ij} \mid$	3% to 20%
	$T_x, T_y = 0.03 - 0.05$	0.03 to 0.1

Model description

The extent, location, depth and resistivity of surface structures recovered in the preferred model (Fig. 4.4) are consistent with the geological data available. The inclusion of simplified sedimentary basins (after Hackley *et al.*, 2006; Urbani, 2017) in the initial model improved modelling considerably, when compared to unconstrained inversions (not shown). The surface expressions of the most active faults are correlated with conductive anomalies, especially in areas with dense station coverage. The lateral resolution of the model allows identifying a sizeable conductor east of the profile (C9). This structure was observed throughout the data analysis and is clearly of high relevance to the data set and 3D inversion models.

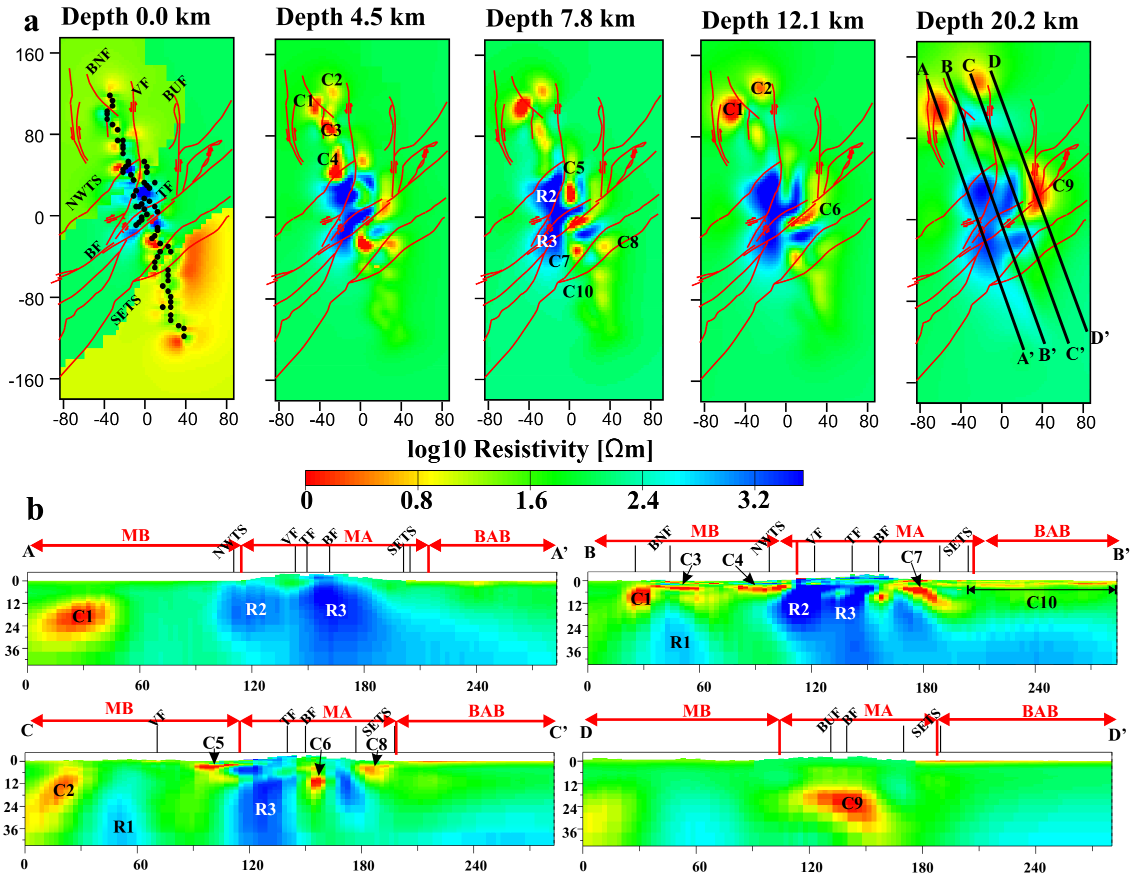

Figure 4.4.: Preferred 3D inversion model showing: (a) Depth slices increasing depth from left to right including the location of main fault systems (Red lines, after Audemard *et al.* (2005)). (b) 2D profiles extracted from the 3D model from East to west. Their location was defined to showcase the main anomalies observed in the model. Black lines show the profile locations.

The northern part of the model shows a series of conductors and resistors labelled C1-4 and R1-2 (Fig. 4.4a and Fig. 4.4b profiles BB' and CC'). Conductors C1 and C2 are recovered as circular anomalies which depth extent, al least in the case of C1 seem to be related to the fault plane of the BNF. The flat conductors C3 and C4 are spatially related to the MB, and could be representing the bottom of the basin. Conductor C4 located at the lateral transition between the

MB and MA seems to also be partially related to the fault plane of NWTS. These conductors present low resistivity ($< 10\,\Omega m$) and are mostly located in areas of contrast between between conductive and resistive mediums. Resistor R1 could represent the transition at depth from the conductive basin to the more resistive upper crust, whereas R2 represents the high resistivity of the MA. The MB is recovered as an inhomogeneous conductive zone, which could be explain by geological processes or the result of an uneven stations distribution fostering the inclusion of resistors in areas of poor station coverage.

Resistors R2 and R3 are located beneath the MA, extending to the west, limited to the east by conductor C5 and split by conductor C6. The conductors C5 and C6 correlate spatially with the VF and BF, and both anomalies dip to the east. Conductor C7, located between the BF and the surface expression of the northern strand of the SETS, dips towards the south (see C7 in Fig. 4.4b, profile BB'), and connects with conductor C8. Based on their location, C7 and C8 seem to be related to both strands of the SETS. However, C7 northern extent and depth (> 10 km) may indicate a connection between the fault systems (BF and SETS), and C8 seem to be limited by the fault strands of the SETS possibly representing an accumulation of sediments between the fault planes.

Conductor C10 (Fig. 4.4b, profile BB') correspond spatially with the BAB. Its depth of 5 km is consistent wit the depths obtained by other methodologies (e.g. González de Juana *et al.*, 1980a; Jácome *et al.*, 1995; Callejón & von der Dick, 2002) and its low resistivity is representative of the typical resistivity of sedimentary rocks (see Figure 2.1).

The off-profile conductor to the east labelled C9 is a necessary feature for the model to fit the dataset, since it was consistently recovered with different inversion test. This structure is also in agreement with induction vectors (see section 2.6) that indicate a conductor to the east. Moreover, this conductor seems to be connected in depth (>12 km) with conductors C6 and partially to C5, as observed in Figure 4.4a (depths 12.1 and 20.2 km).

Most conductive anomalies recovered seem to have an off-profile extent, since stations are distributed along a single profile, their off-profile extent is not well constrained (e.g. Tietze & Ritter, 2013; Kiyan *et al.*, 2013; Wannamaker *et al.*, 2014, among others). This is further investigated in section 4.3 employing resolution tests and synthetic data from conceptual models.

4.2.4. Inversion of individual transfer functions

Further understanding of the recovered structures in the integrated inversion (Fig. 4.4) requires to estimate the influence of the impedances and vertical magnetic transfer function on the 3D inversion model. In the following independent 3D inversion of the impedances and vertical magnetic transfer function; the labelling of anomalies is set to coincide with that of the integrated inversion.

Impedance tensor inversion

Inversion of the impedance tensor included all the elements of the tensor with an error floor of 5% of $\mid Z_{ij} \mid$ for Z_{xy} and Z_{yx}, and 50% of $\sqrt{\mid Z_{ii} \cdot Z_{ij} \mid}$ for Z_{xx} and Z_{yy}. After 61 iterations the RMS was reduced from 19.25 to 1.27. The short periods (< 1 s) showed a lower RMS than the long periods, 1.4 and 1.9, respectively. This difference can be explained by the vertical discretization of the model that accumulated a large percentage of the cells in the upper 10 km, allowing for higher variability of the modelled structures closer to the surface.

The inversion results shown in Figure 4.5 display excellent correspondence with surface structures, sedimentary basins and fault systems. At great depths (>15 km) a north-south resistor was placed under the stations at the centre of the model (R3). Conductors C3 and C4 are recovered aligned with the stations located between the BNF and the NWTS from a depth of approximately 3 km, where they form a 30 km long 8 km wide conductor reaching up to 10 km in depth, corresponding with the location of the MB (Fig. 4.5a, depth 4.5 km). South to the BF, conductor C6 and C7 represent the BF and possibly the northern strand of the SETS, however, conductor C6 is hardly visible at the centre of the profile but seem to limit the southern extent of R3 (see Fig. 4.5b, profile AA'). Conductor C10, on the southern section of the profile, seems to represent the BAB with a maximum depth of 4 km and a length of 60 km.

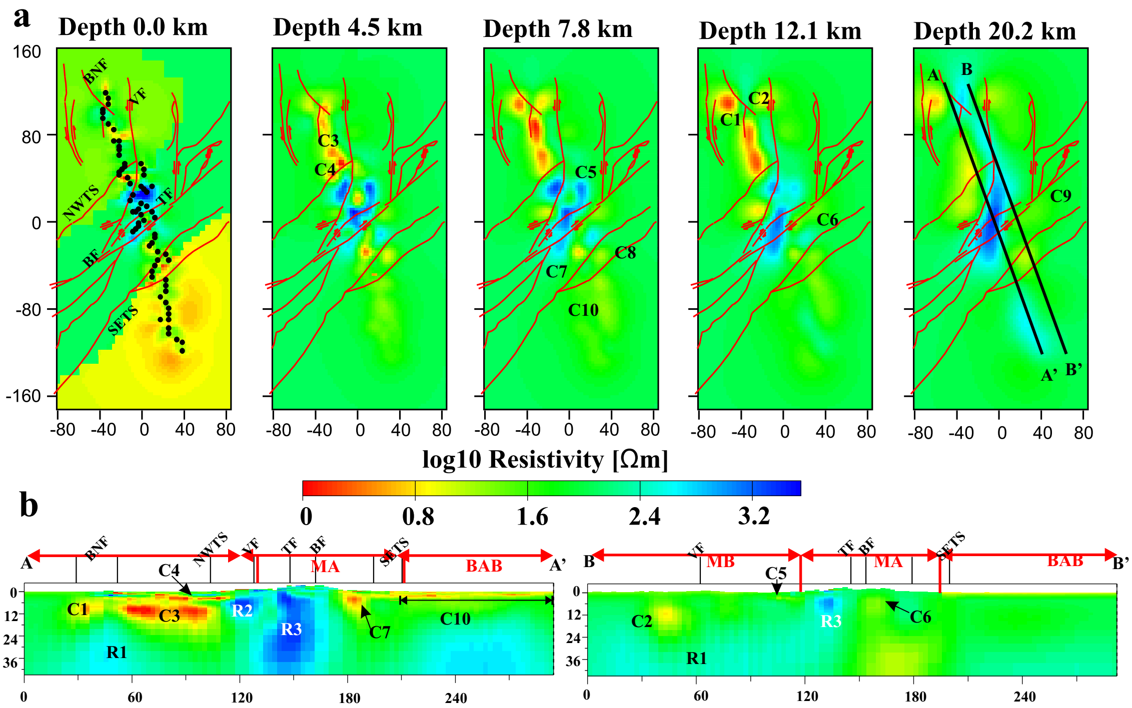

Figure 4.5.: 3D inversion model of the impedance tensor showing (a) Horizontal slices at increasing depths including the location of main fault systems. Red lines indicate the location of the quaternary fault systems after Audemard *et al.* (2005). (b) Two selected profiles showcasing the main structures. Black lines in (a) indicate the profile locations. Labelling of structures was set to coincide with the preferred model from the integrated inversion (see Fig. 4.4).

The structural distribution of the model agrees with the geology and also show the limitations of three-dimensional inversion of profile distributed datasets with oblique conductors (BF, MB and BAB). In general, this structural and stations setting show a limited lateral resolution and reproduced localized resistors under the stations in the resulting inversion models, as observed in similarly distributed models (e.g. Tietze & Ritter, 2013; Kiyan *et al.*, 2013).

Vertical magnetic transfer function inversion

The inversion of the VTF included both components (T_x and T_y) with an error floor of 0.05, after 12 iterations it converged to an RMS of 1.04 (from an initial 2.84).

The VTF are mostly sensitive to lateral conductivity variations; thus, conductive anomalies are recovered in the inversion model (Fig. 4.6) that correspond with the location of the fault systems and off-profile conductive features. On the other hand, the sedimentary basins (MB and BAB) are hardly observable.

Conductor C1 is visible between 8 km and 30 km depth located under the BNF, west from the station 0002 to 0007 (see Fig. 4.6a, depth 7.8 km to 20.2 km). Conductors C4 and C5 seem to be related with the NWTS and the VF, respectively. C4 is placed by the inversion from 1.4 km to 7 km depth under a resistor that extends from the surface, more specifically under stations 0015 and 0016 gradually migrating north until it vanishes (see Fig 4.6b, profile AA'). C5 is practically visible from the surface up to 8.5 km depth where it connects with conductor C6 and C9 (see Fig 4.6a, depth 7.8 km).

At the centre of the profile, conductors C6 and C7 is visible from 1 km depth. As C7 deepens, it appears to be separating two resistors, eventually connecting with C6 at depths between 4 and 8 km. These conductors (C7 and C6) seem to be related to the SETS and BF, respectively and possibly hint at a deep connection of the two fault systems. Remarkably, these conductors are more sizeable and present a lower resistivity than in the impedance inversion (4.5).

Conductor C8, located between the strands of the SETS (Fig 4.6a, depth 7.8 km), could represent the fault plane recovered between 3.8 km and 8 km. East of the profile, C9 seems to connect C5 and C6, as the former migrates to the south and later to the north-east. C9 has a thickness of 8 km (from 8 km to 16 km depth), and forms a 35 km long, 15 km wide anomaly that hints at a deep connection between the most prominent tectonic structures in the MA. The induction vector analysis already observed the effect of this conductor on the dataset shown in section 3.4.1.

Resistor R3 with a westward extension represents the MA, which is intersected by the north-south oriented conductor C7 between depths of 2.5 to 12 km and then by conductor C6 from 3.5 km downwards.

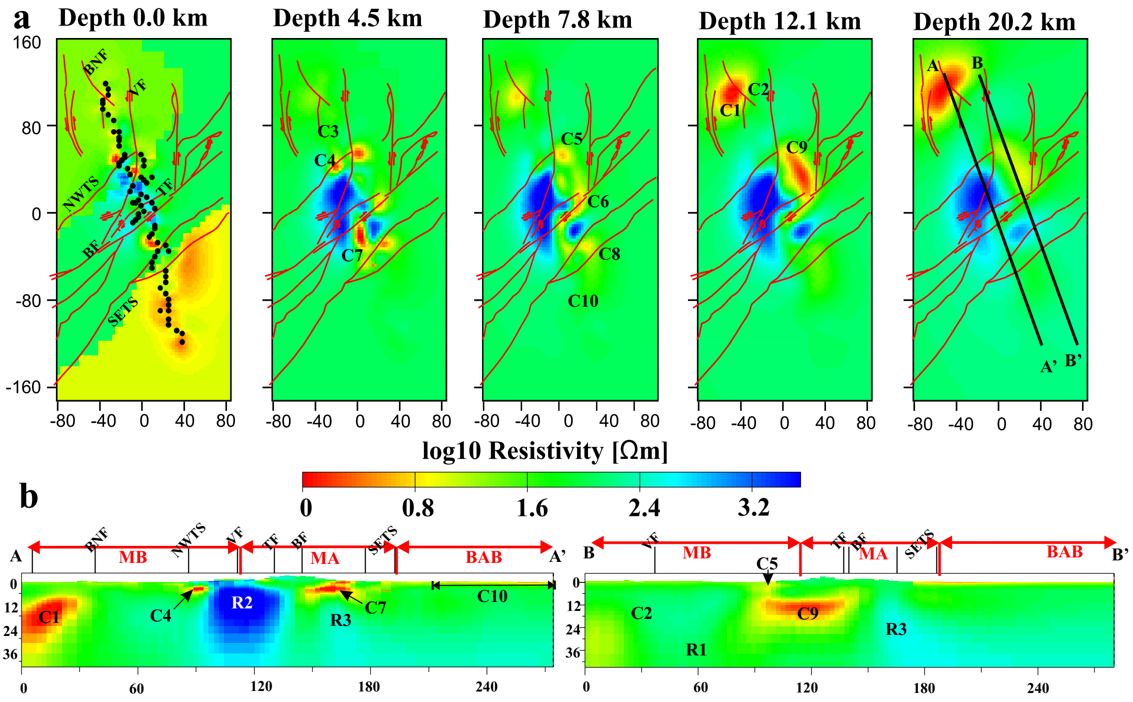

Figure 4.6.: 3D inversion model of vertical magnetic transfer function showing: (a) Horizontal slices at increasing depths slices from left to right including the location of main fault systems (red lines, after Audemard *et al.* (2005)). (b) Two selected profiles showcasing the main structures. Black lines in (a.) indicate the profile locations. Labelling of structures was set to coincide with the preferred model from the integrated inversion (see Fig. 4.4).

The separated inversion of the transfer functions shows that along profile structures are more consistently recovered and contained in the impedance inversion, C3, C4, C7, C8 and C10. Whereas off-profile structures, like C9 ,seem to be mostly related to the VTF in the integrated inversion (Figs. 4.4 and 4.6). Conductor C1 more shallow recovery seem to be related to the impedances, while their deepest and off-profile extent and C2 are part of the VTF. The recovery of the structures shows that both responses (Z and VTF) are necessary to model the complex structures in the study area.

4.3. Sensitivity analysis of the inversion models

In this section, the 2D and 3D models (Figs. 4.2 and 4.4) are subjected to a sensitivity analysis, to explore the relevance or robustness of recovered resistivity structures. In this study to perform a sensitivity analysis, the first step is the comparison of the misfit between the measured and the modelled responses. The sensitivity analysis is complemented by the study of the model resolution, which in general can be performed by substituting structures in the inversion models, generating responses to these modified models and comparing them to the original model responses.

4.3.1. Two-dimensional inversion models sensitivity

Misfit analysis

The global target model misfit was 1.05. The RMS for the northern section (Fig. 4.2a) reached 1.25 after 27 iterations (initial RMS of 22.98). For the southern section (Fig. 4.2b), the RMS value was 1.57 after 21 iterations (initial RMS of 41.53). In both cases the target misfit was modified closer to the final RMS, the inversions were restarted and allowed to converge after 5 and 8 iterations for the northern and southern sections, respectively. The misfit per mode and section is presented in Table 4.3. The RMS for the apparent resistivity of the TE mode is lower than 0.2, and it is a result of the large error floor settings.

Table 4.3.: Misfit of the 2D inversions of field data for the northern (Fig. 4.2a) and southern (Fig. 4.2b) section, for the TE and TM mode apparent resistivity (ρ_a) and phases (φ).

	Northern	Southern
TEφ	2.02	2.28
TMρ_a	0.79	1.40
TMφ	1.22	1.38

The RMS represents an averaged fit for the entire model. Figure 4.7 shows detailed RMS values of the northern and southern sections per station and period colour coded for each mode and response. In both cases (Fig. 4.7a and b), the TM-mode responses (yellow and red for resistivity and phases, respectively) show RMS values similar throughout both sections and generally lower than the average (see Table 4.3), particularly above the basins. The phases of the TE-mode (light blue) show their largest RMS above the MA, and below average RMS over the MB and BAB. Larger RMS values were expected over the MA as both PTs and IV indicated 3D dimensionality for this area (see Fig. 3.10). However, the notably high RMS values for the TE-mode phases stress the difficulties to model topographic and structural variation along strike in a 2D inversion.

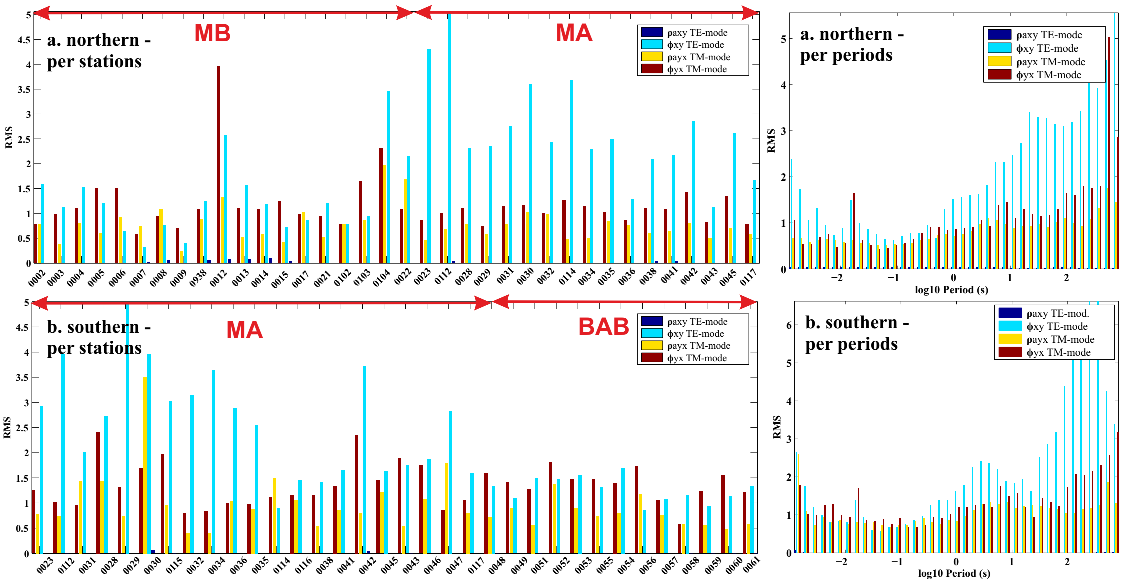

Figure 4.7.: Misfit breakdown for (a) the northern (Fig. 4.2a) and (b) southern (Fig. 4.2b) sections, showing the RMS per station (left) and per period (right). The red arrows mark the surface extensions of the MB, MA and BAB.

In the period plots (right side), the most significant RMS values are found towards the longest periods (>10 s). In MT, the sounding range widens with period and includes larger horizontal distances, hence the large misfit at long periods are the result of the influence of off-profile structures. In general, sections of the data set that are consistent with 2D assumptions showed the lower RMS values, whereas higher RMS values are related to the 3D-influenced sections of the data.

Figure 4.8 shows pseudo-sections of the normalized residuals between measured and modelled data in apparent resistivity and phases of the TE and TM mode for each section. Similarly to the previous RMS analyses, the phases (φ) of both modes and the TMρ_a show the largest variation at long periods (>1 s) and in the transition between the basins and the MA, for both sections. The TEρ_a show little variation, this was expected since the residuals are normalized by the error floor of the inversion (10.000%). Nevertheless, in general Figure 4.8 shows a really good fit between the measured and modelled data in both 2D inversion sections, with the exceptions of a few outliers the difference between responses was quite small, about ±0.5 for most of the apparent resistivity and ±1 for the phases. Pseudo-sections of the measured and modelled data are included in the annexes (Fig. A.1).

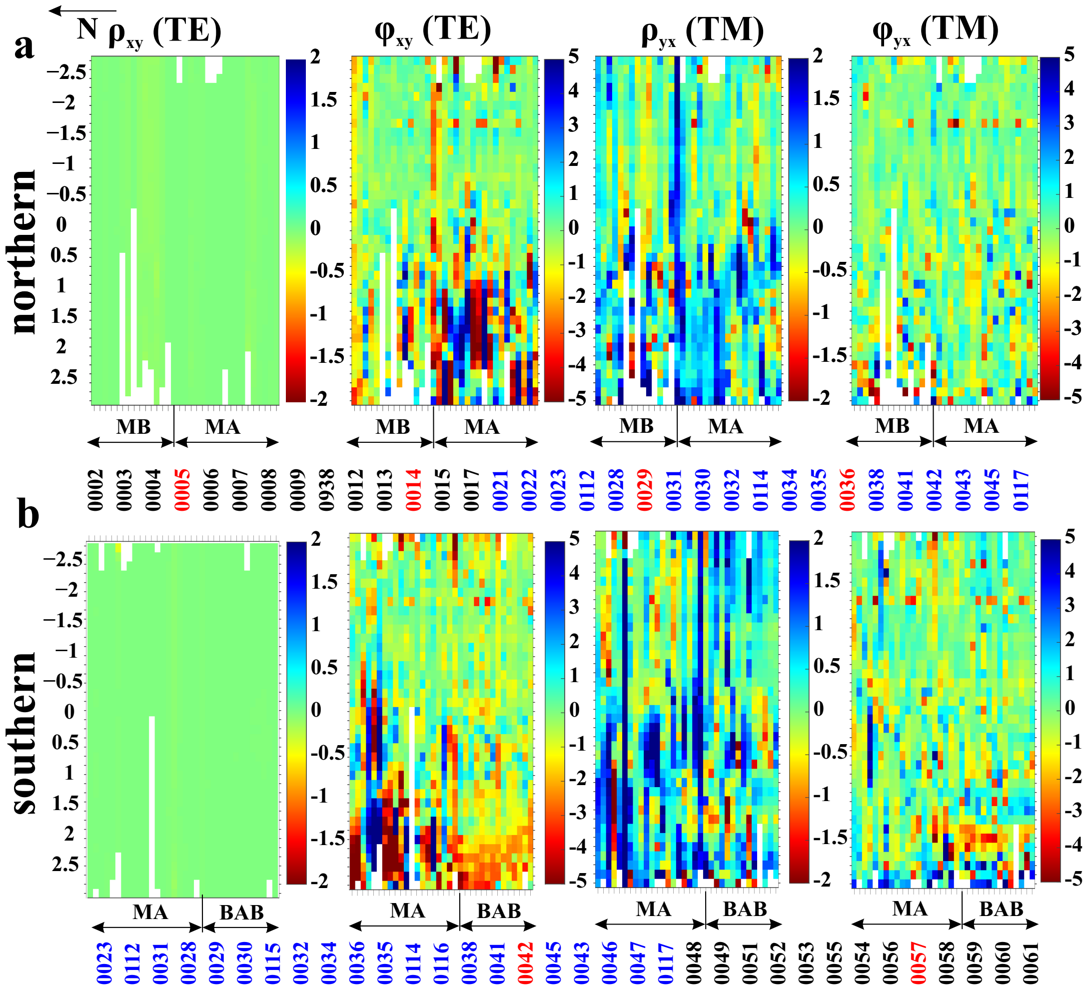

Figure 4.8.: Pseudo-sections of normalized residuals of the decoupled TE and TE apparent resistivity (ρ_a) and phases (φ) for (a) the northern (Fig. 4.2a) and (b) the southern (Fig. 4.2b) sections. Blue coloured station numbers are located above the MA. Red coloured stations indicate the location in profile of the stations in Figure 4.9.

Figure 4.9 shows the MT responses for six selected sites (marked in red in Fig. 4.8), four are from the northern and two from the southern sections. These stations represent the dataset at different locations and elevations. Sites 0005 and 0014 are located in the MB; sites 0029, 0036, and 0042 in the MA; site 0057 is from the BAB.

Due to the tight error floor settings, the phases of both TM and TE mode are generally well fitted. Also, TM resistivities are well matched throughout the data set. TE apparent resistivity responses reproduce the shapes of the measured data, but may be shifted in parallel (e.g. 0042, 0036 and 0014 in Fig. 4.9). The results at these stations demonstrate that our chosen inversion setting can handle static shift in the TE mode apparent resistivity.

The stations above the MB (0005 and 0014) and BAB (0057) show responses in agreement with the 1D/2D dimensionality observed from the PT. The apparent resistivity and phase curves similarly show little variation for periods between 10^{-3} s and 1 s. The split of TE and TM modes at longer periods is likely associated with a change from sedimentary rocks to bedrock formations.

Sites 0036 and 0029 are located in the central section, the PT analysis suggested strong 3D effects (Fig. 3.8) and this section shows the strongest topographic variations (Fig. 4.1). Nevertheless, data at both stations are well fitted (Fig. 4.9a). A strong resistivity contrast nearby causes the splitting of TE and TM mode responses of station 0029.

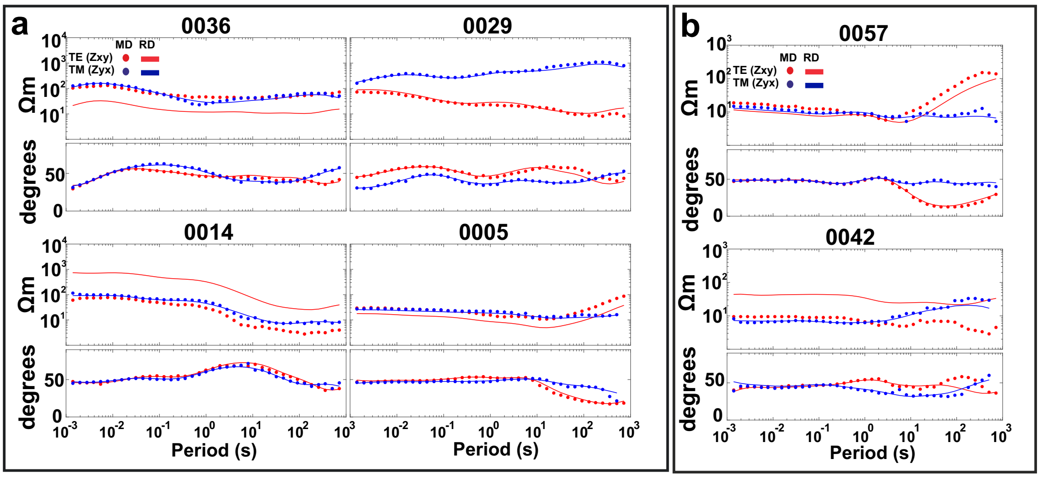

Figure 4.9.: Responses of 2D inversions for selected stations from (a) the northern (Fig. 4.2a) section (sites 0036, 0029, 0014 and 0005) and (b) the southern (Fig. 4.2b) section (sites 0057 and 0042). Dots represent measured data and lines show inversion results. Red and blue indicate TE and TM mode, respectively.

The analysis of the RMS and data responses show that the modelled responses closely reproduced the observed results, showing that the error floor settings are effective in spite of the large error floor set on the TEρ_a. These analyses also indicate that the basins subsurface could be more accurately reproduced that the structures under the MA.

Model resolution

The model resolution was evaluated in two steps. The first step involved the calculation of the model sensitivities and a threshold for defining the sections of the model that influenced the data responses significantly. The second step focused on studying the effect of particular structures or anomalies.

In non-linear inversion methods, the partial derivatives of the electric and magnetic fields at each receiver concerning the model parameters are known as field sensitivities (Schwalenberg *et al.*, 2002). These sensitivities may indicate model parameters that are less resolved by the data, which indicates both well and poorly resolved structures.

To define this threshold in the model sensitivities large sections of the model were modified by including a structure with the initial resistivity at different depths. Forward responses from these modified models were then compared to the responses of the original models. The comparison shows that structures located in areas with model sensitivities above $10^{-6.5}$and 10^{-6}, for the northern and southern sections, respectively, (blue bars in Figure 4.10) have a significantly higher influence on the forward responses of the models than the ones bellow these thresholds. Roughly 88% of the grid elements of the 2D inversion model in the northern section (Fig. 4.10a.) and 67% of the grid elements in the southern section (Fig. 4.10b.) are above these thresholds. Regions with lower sensitivities are grey-shaded in Figure 4.2.

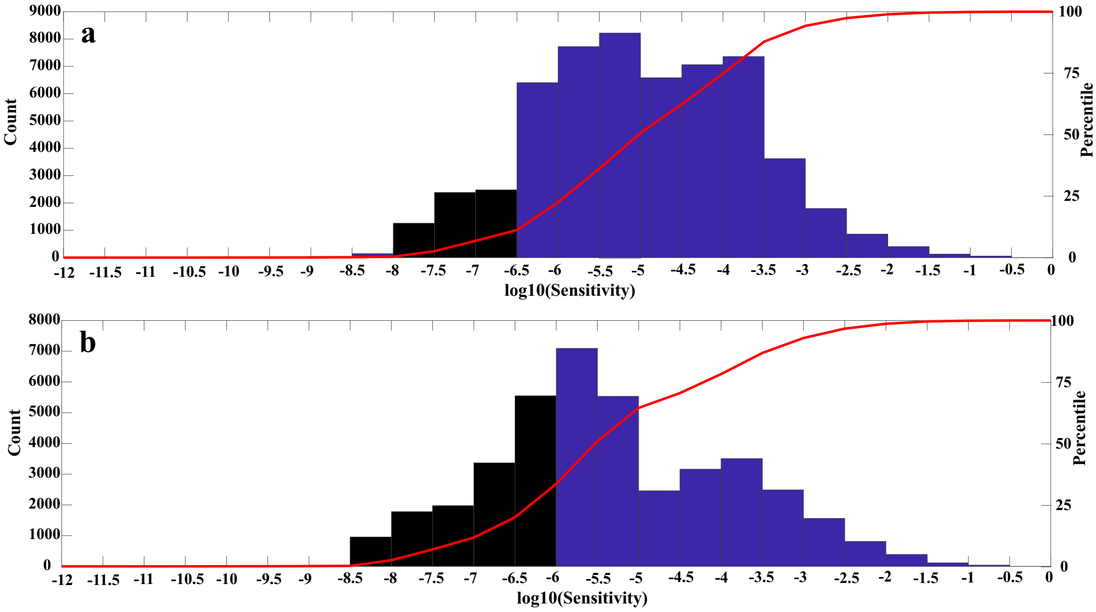

Figure 4.10.: Bar chart and cumulative percentage of the model sensitivities of the 2D inversion models presented in Figure 4.2 for the (a) northern (Fig. 4.2a) and (b) southern (Fig. 4.2b) sections. The x-axis represent the model sensitivities weighted by the size of the grid elements in logarithmic scale. Blue bars represent those elements whose sensitivities are higher than (a) $10^{-6.5}$and (b) 10^{-6}(see text for explanations).

Posteriorly, features labelled with C for conductors and R for resistors in the 2D inversions models (Fig. 4.2) were independently substituted by their average and background resistivity, further testing included substitution by more resistive and more conductive bodies. Forward responses of these modified models were calculated, and new inversions started to confirm the modelling of the structures (resulting models not shown).

A summary of the RMS variation after the resistivity of the structures were modified is shown in Table 4.4. The results shown include only the substitution for the background resistivity and for a more conductive medium. To consider the variation per station in the obtained responses for the modified models and to support the results shown in Table 4.4, a comparison of the measured and modelled responses with the modified responses, similar to that shown in Figure 4.9, was also performed, due to their length these comparison is not shown.

Table 4.4 clearly shows that for the northern section any variation on the structures translates in a considerable difference between the model responses (minimum difference = 0.13 in RMS, ~10%), even for the deepest structure (C9 in Fig. 4.2), showing their strong influence on the data. Conductor C4 bears the least variation in comparison with the other labelled anomalies, possibly due to its location between stations and its rather small size. The southern section shows similar results than the northern, with considerable variations resulting from the substitution of conductors, either by a conductive or resistive medium. From all conductors in the southern section, the data responses showed the smallest variation to the substitution of C6, the model clearly requires a conductor at this location, but as in the case of C4, its location between stations and close to the surface minimize its impact on the data responses.

Table 4.4.: Comparison of the misfit between the 2D preferred inversion model and the modified models for the tested structures for the northern (left, Fig. 4.2a) and southern (right, Fig. 4.2a) sections.

section	**RMS**	**replacement**	**section**	**RMS**	**replacement**
Northern	1.25	-	Southern	1.58	-
C1	1.62	$10\,\Omega m$	C6	1.70	$1\,\Omega m$
	13.73	$100\,\Omega m$		1.88	$100\,\Omega m$
C2	1.62	$10\,\Omega m$	C7	2.65	$1\,\Omega m$
	13.73	$100\,\Omega m$		16.90	$100\,\Omega m$
C3	1.53	$10\,\Omega m$	C8	2.22	$1\,\Omega m$
	4.11	$100\,\Omega m$		9.33	$100\,\Omega m$
C4	1.39	$10\,\Omega m$	C10	2.67	$1\,\Omega m$
	1.46	$100\,\Omega m$		24.97	$100\,\Omega m$
C5	1.96	$0.1\,\Omega m$			
	1.62	$100\,\Omega m$			
C9	1.50	$10\,\Omega m$			
	1.38	$100\,\Omega m$			

In summary, the modified models showed that the station misfits in the vicinity of the modified structures increased considerably. Most labelled structures are required by the data particularly when these structures are located above the threshold set for the model sensitivity. Anomalies recovered in areas with poor or uneven station coverage, e.g. between stations, bare a smaller influence in the resulting RMS and by extension in the modelled responses (C4 and C6). After repeating the inversions, the substituted features reappeared roughly with the same extents, depths and resistivity, further indicating that all the labelled features are supported by the data.

4.3.2. Three-dimensional inversion models sensitivity

Misfit analysis

The analysis of the misfit per station and per period (Fig. 4.11) permits to assess the adjustment of the model. The RMS distribution shows a generally good fitting for the entire dataset and for all inverted elements, showing that the error floor and staged inversion could recover responses closely resembling the measured data.

The best fitting per station (Fig. 4.11a and b) is found on the stations above the MB and BAB, whereas towards the MA, especially in the transition between basins and the mountain, the RMS is larger, for both Z and T. This increase in RMS is probably related to the lateral geological changes, the transition from conductive to resistive areas, and the changes in the elevation. The higher RMS in the vicinity of most fault systems (marked with red lines in Fig. 4.11a) indicates the sensitivity of the data to these active structures, and the generally low RMS of T, the capacity of the staged inversion to fit the VTF data.

Figures 4.11c and d, show the distribution of the RMS by periods. The RMS of Z (Fig. 4.11c) shows a good misfit for periods between 0.01 - 1 s and 10 - 1000 s, with the longer periods (>1000 s) and Zyx (yellow bars) between 1 and 10 s showing the largest RMS. Since the sensitivity of the MT data deepen and widen with increasing periods, long-period measurements are more influenced by faraway structures, which are more complicated to model due to the lack of station coverage.

The VTF shows generally low RMS values and a variable response with increasing period (T, Fig. 4.11d). Due to the staged inversion scheme, the long periods were tightly modelled whereas short periods, show a larger misfit, mainly between 10^{-2} and 1 seconds. In the second stage of the inversion, the short period VTF data (<1 s) had to be modelled in agreement with the impedance responses, the finer discretization in the vertical direction and the effect of the topography, further explaining the larger misfit compared to the long periods.

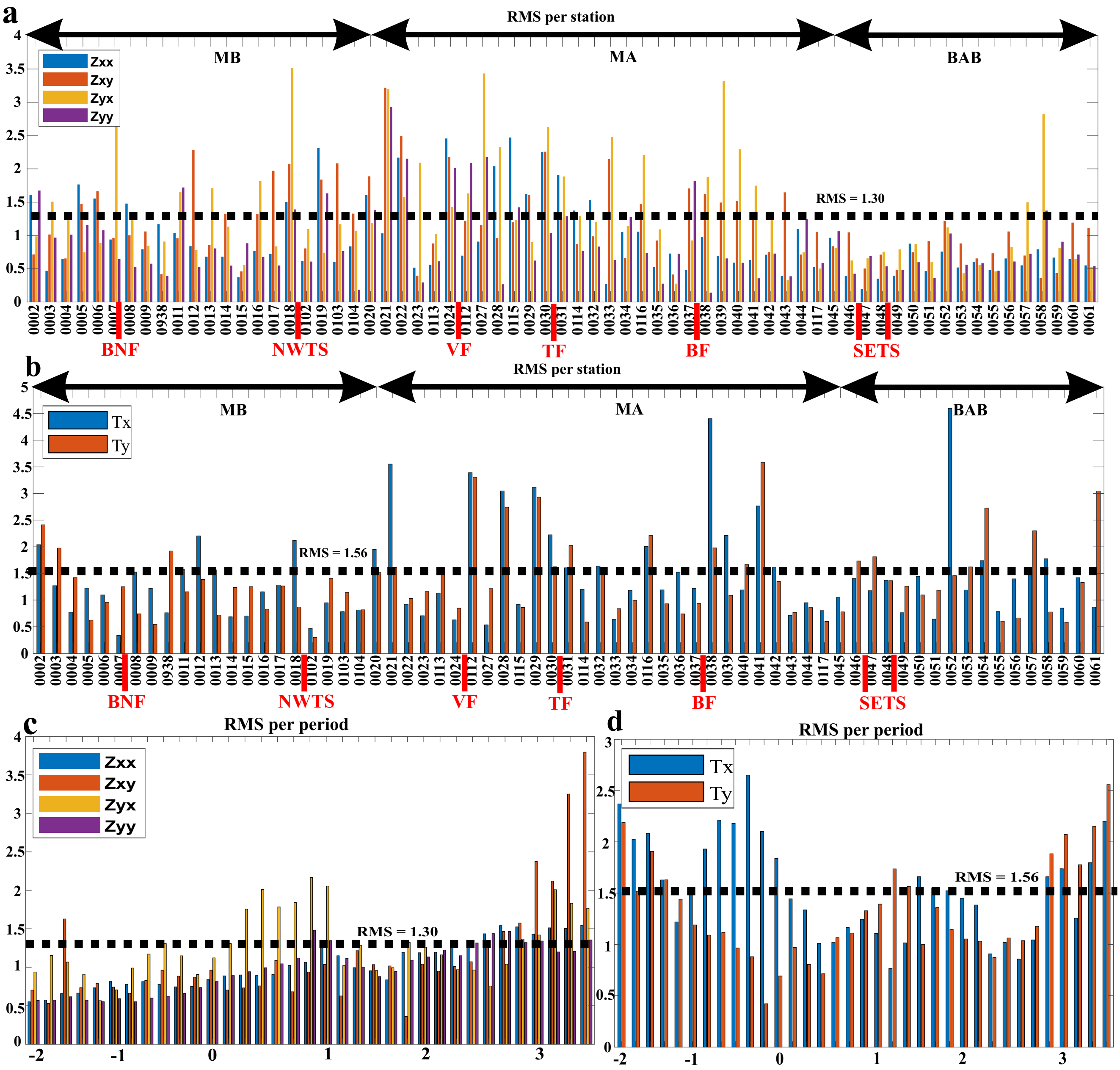

Figure 4.11.: Misfit breakdown showed at impedances (Z) (a) per station; (c) per period; and vertical magnetic transfer function (T) (b) per station; and (d) per periods. The black arrows mark the surface extensions of the MB, MA and BAB, and red lines the location of the fault systems.

The analysis of pseudo-section of normalized residuals allows for the comparison of the measured and the modelled responses. Figure 4.12 presents the pseudo-sections of the impedance tensor elements expressed in terms of apparent resistivity (ρ_a) and phases (φ) for all elements of the impedance tensor (see section 2.5). The pseudo-sections show each station from north (left) to south (right) in the x-axis and the period in logarithmic scale in the y-axis.

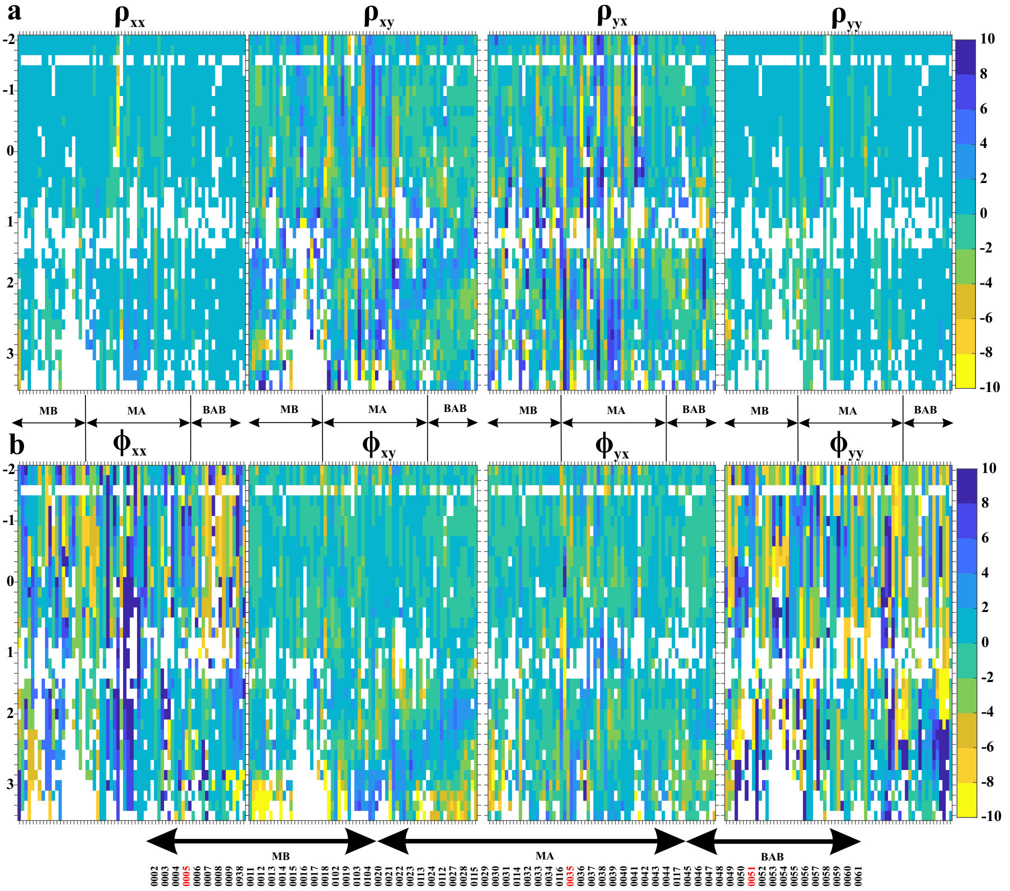

Figure 4.12.: Pseudo-sections of the normalized residual for the preferred model (Fig. 4.4) of each component of the impedance tensor presented as (a) apparent resistivity (ρ_a) and (b) phases (φ) . The y-axis represent periods in logarithmic scale and the x-axis the stations locations, as presented below the sections in relation to the main structures. Responses of the station marked red in the bottom are presented in Fig. 4.14.

Figure 4.12a shows ρ_a per component of Z. Since the responses are normalized by their error floor, the main diagonals elements (ρ_{xx} and ρ_{yy}) seem to show the least variation, with an averaged difference of 2 Ωm. Given the tight error settings, the residual from the responses of ρ_{xy} and ρ_{yx} show larger variation, with generally low values over the basins (about 2 Ωm) and higher differences over the MA (4 Ωm), particularly the long periods. In contrast to the apparent resistivity, the phases (Fig. 4.12b) show a good correlation for the off-diagonal elements but larger differences for the main-diagonal components of Z, illustrating the difficulties of reproducing the main-diagonal elements. Pseudo-sections of the measured and modelled components of Z are included in the annexes (Fig. A.2).

Comparison of the induction vectors of the measured (black arrows) and modelled (red arrows) data (Fig. 4.13) shows a generally good fit throughout the period range and the stations, with only slight differences in the short period data above the MA.

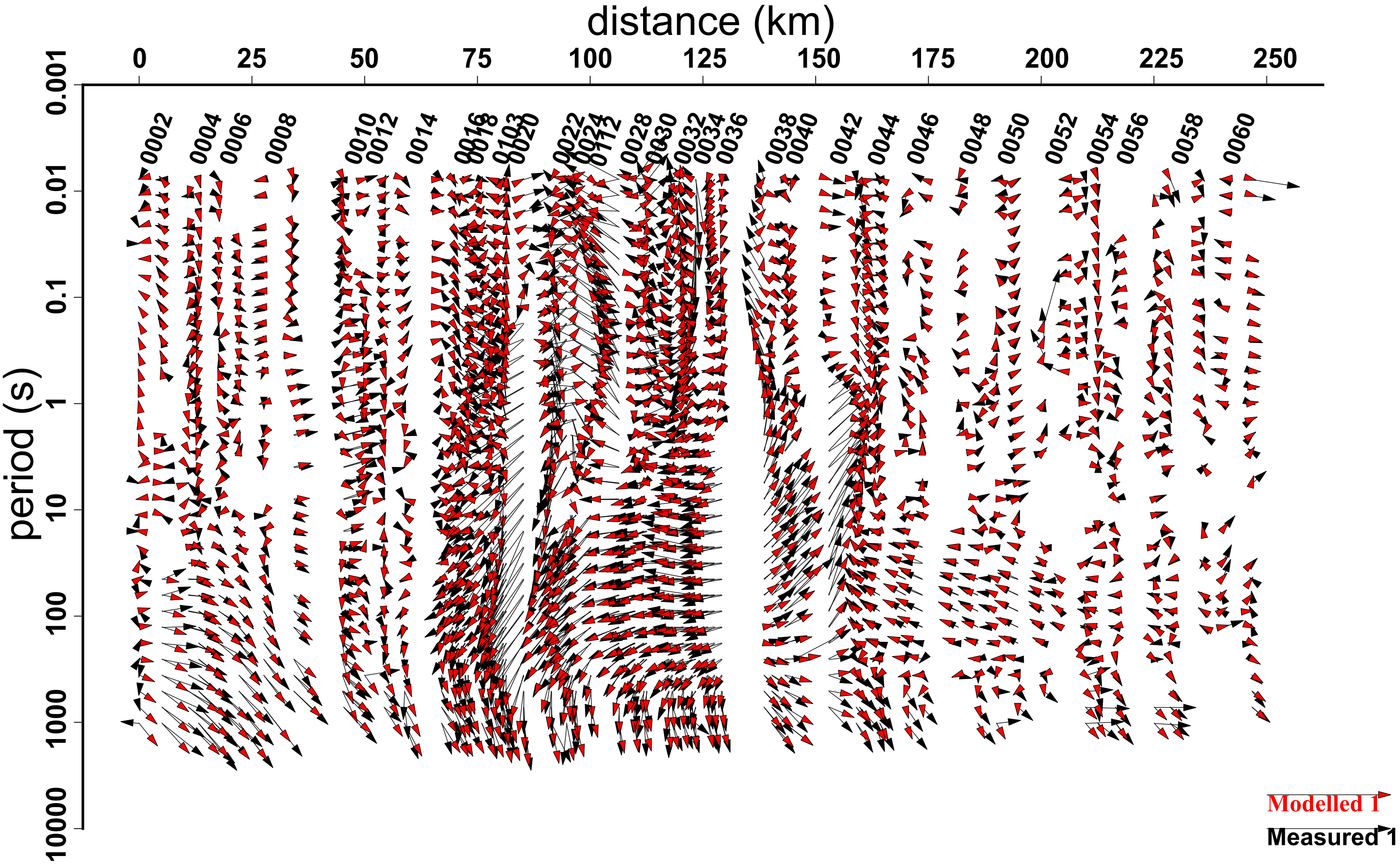

Figure 4.13.: Comparison of induction vector of observed (Fig. 3.9b) and modelled data (Fig. 4.4). Black arrows represent the observed data and red arrows the modelled data. The surface expression of the main structures is included on top of the figure.

Figure 4.14 shows a comparison of the measured (dots) and modelled (lines) responses for selected stations along the profile, for simplicity only the off-diagonal components of Z are shown. Station 0005 (Fig. 4.14a) is located over the MB and in the vicinity of the BNF strand (see

Fig. 4.1). This stations clearly shows a divergence between the Zyx and Zxy modes, with the later indicating a almost constant resistivity (~50 Ωm) up to 100 s and Zyx showing a clear decrease in resistivity, possibly related to a conductive subsurface structure (BNF). The VTF show as well no variations up to 10 s, for larger periods both modes split indicating a lateral resistivity contrast. Figure 4.13 also reflect a change in the IV length and direction below 10 s. Nevertheless, the modelled responses for station 0005 (Fig. 4.14a) follow closely the measured data indicating a good fit.

Station 0035 (Fig. 4.14b), over the MA, show a high resistivity at low periods and the apparent resistivity split at ~0.1 s. Due to the location of the BF to the south of the station, Zxy shows a low resistivity (below 100 Ωm) for periods over 0.1 s, compared to Zyx. The VTF, particularly Ty, show more variation than in station 0005, indicating lateral contrasts related to the complex subsurface of the MA. The modelled responses fit quite well the measured data, however, between 0.1 s and 10 s the apparent resistivity fail to reproduce the split of the responses observed in the measured data, exemplifying the difficulty to model the structural complexity of the MA.

Station 0051 (Fig. 4.14c) shows the structural simplicity of the MB. The measured apparent resistivity responses show a conductive (~20 Ωm) and homogeneous subsurface up to 10 s period, where the resistivity increases, possibly related to the transition from the basin to the upper crust. These responses are in agreement with the PT analysis (Fig. 3.8) that described the southern section of the dataset as clearly 1D/2D. Similar to the apparent resistivity responses, the VTF show close to zero (0) responses and a clear split at 10 s periods, an indication of lack of strong lateral resistivity contrast. However, for larger periods the amplitude of the VTF increases agreeing with the IV (Fig. 4.13) in this area. The modelled responses followed closely the measured data, which was expected since this section has a simple dimensionality.

The stations shown in Figure 4.14 are considered representative of the entire dataset. The generally low RMS values (Fig. 4.11) and the good correlation between measured and modelled data (see Figs. A.2 and 4.13) indicate an overall a good fit between the observed and modelled data for the entire period range. This misfit illustrates the efficacy of the staged inversion.

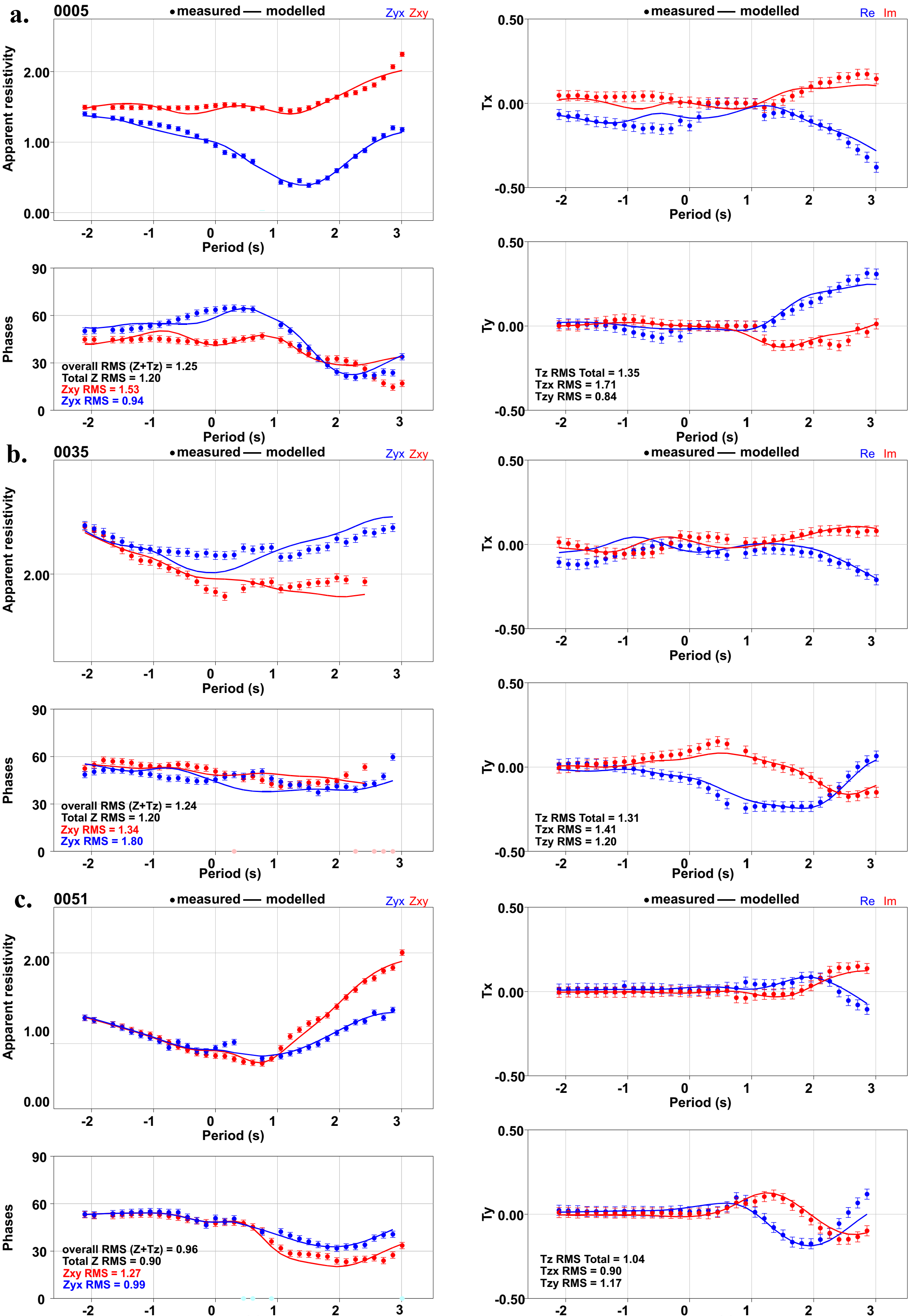

Figure 4.14.: Selected stations along the profile showing the measured and modelled data for the preferred 3D model. (a.) Station 0005 on the MB. (b.) Station 0035 over the MA. (c.) Station 0051 on the BAB.

Model resolution

Squeeze test

To test the depth resolution of the preferred model (Fig. 4.4), the 'squeeze test' as described in Meqbel *et al.* (2014) was used. For this test, the resistivity below a specific depth was set to 120 Ωm and fixed. The inversion was started with the modified model to examine the impact of the constrain on the data fit and the recovered structures. Depths from 5 to 45 km were tested as shown in Table 4.5.

The resulting total RMS of the fixed depths models are consistently larger than the RMS of the preferred model (Table 4.5). Interestingly, increases in the RMS are especially significant in the responses of the VTF (T). This RMS variations show that Z is less sensitive to structures deeper than 20 km, given that the RMS variation are smaller below this limit than above it. In contrast, the VTF is still presenting considerable variations in RMS (>0.1) up to 45 km.

In general, the squeeze test affects the misfit of all stations, but when distributed per station (not shown), the central and southern sections are particularly affected. The resulting models with fixed resistivity seem to show that the structures are better redistributed north of the NWTS, by expanding small scale conductive structures in the vicinity of the stations close to the surface. While the central and southern sections tend to be more dependent on large scale and deeper structures. This difference between inversion models seem to indicate that the sensitivity of the model vary in different regions. The variability of the sensitivity could be related to the surface structures, both to the north and south of the MA the geology is characterized by sedimentary basins, normally associated with low resistivity. The MB is twice as thick as the BAB ((e.g. Callejón & von der Dick, 2002; Escalona & Mann, 2003)), which according to the skin depth (eq. 2.15) would further limit the resolution in these areas.

Table 4.5.: Squeeze test results comparing the RMS of the different controlled depths and the preferred model. Showed as the normalized RMS (nRMS), the RMS of the impedance tensor (Z RMS) and the vertical magnetic transfer function RMS (T RMS).

model	**nRMS**	**Z RMS**	**T RMS**
original	1.40	1.30	1.56
5 km	1.77	1.47	2.22
15.4 km	1.59	1.36	1.94
23.5 km	1.50	1.33	1.76
45 km	1.45	1.33	1.64

Sensitivity test

The preferred 3D model (Fig. 4.4) was subjected to a sensitivity test to explore the relevance of each recovered structure independently. In this case, labelled conductors in the preferred model were substituted by more resistive and conductive ones. Forward responses of these modified models were calculated, and the models re-inverted, to evaluate the effect of the modification and to test the recovery of the structures. The influence of each structure over the calculated responses of the modified models were analysed in terms of the variation of the misfit of the responses for the entire dataset, and also comparing the misfit per station (as shown for the preferred model in Fig. 4.14). Table 4.6 presents a summary of the RMS variations, whereas a condensed version of individual analysis grouped by section and period is included in the annexes (Fig. A.3).

Table 4.6 shows a comparison of the averaged RMS of the responses of Z and T for the preferred 3D model with the modified models for each conductive structure. The conductive structures of the northern section (C1 to C4), excepting C2, show a considerable variation in Z when replaced for both a conductive ($10\,\Omega m$, > 0.61) and a resistive ($100\,\Omega m$, > 2.56) material, though their influence in T is quite limited. As noticed in the 3D inversion of Z (Fig. 4.5), C1, C3 and C4 are included in the inversion models mostly by the impedances explaining their relevance in the RMS variation of Z and confirming that they are required by the model. The smaller variation in T shows that when replaced by a homogeneous conductor the lateral contrast is kept. The low variation also agrees with the recovered structures in the inversion of T (Fig. 4.6), particularly in the case of C3 and C4. Conductor C2 seem to show only marginal influence over the misfit of the model, however, the observation of the modelled responses per stations (not shown) showed that the misfit at long periods (>10 s) of the northernmost stations (0002 to 0005) was affected, indicating that this conductor could a projection or inversion artefact from an unconstrained structure to the north.

Conductors C5 to C8, located at the centre of the profile, show the largest variation on the RMS in Z and T for the modified models. This variation confirms the relevance of these structures in the modelled responses. The higher variation is also the result of their location and extent, since the stations distribution design allocated more stations above the MA than over the basins, any change in the model in this area is reflected over a large volume of stations. The analysis of the independent responses and the grouped sections (Fig. A.3) indicate that these conductors have influence over the entire period range in stations belonging to the central and southern sections.

Conductor C9, located off-profile, seem to have influence over the long periods (>10 s) of all stations in the central section. Interestingly, the modified models responses showed a larger variation when the modified structure was resistive oppose to the minimal difference with a

Table 4.6.: Comparison of the misfit between the 3D preferred inversion model (Fig. 4.4) and the modified models for the tested structures. Listed as the RMS for the impedance tensor (Z) and the vertical magnetic transfer function (T).

preferred	Z_{RMS} = Z = 1.30					T_{RMS} = T = 1.56			
modified	$10\,\Omega m$		$100\,\Omega m$		modified	$10\,\Omega m$		$100\,\Omega m$	
response	Z	T	Z	T	response	Z	T	Z	T
C1	2.17	1.61	6.63	1.76	C6	1.43	1.60	3.88	1.93
C2	1.32	1.56	1.66	1.59	C7	2.49	1.64	7.83	2.31
C3	3.0	1.59	8.32	1.72	C8	1.79	1.59	6.26	1.96
C4	1.91	1.57	3.89	1.61	C9	1.37	1.58	3.42	1.80
C5	2.42	1.62	10.00	2.01	C10	1.51	1.57	19.13	1.91

conductive medium. This limited variation indicates that while a low resistivity structure ($< 20\,\Omega m$) is needed in this area to generate modelled responses close to the measured ones, due to its location the true resistivity of this structure cannot be accurately recovered. Conductor C10, due to its size (60 km long, 5 km depth, ~5 km wide) and location, has an influence over the entire southern section and period range.

In summary, all C-labelled structures located at depths where the model resolution is high (see Table 4.5) and are necessary to fit the data. The inversion of the modified model recovered structures with a similar extent, resistivity and location, further showing their robustness. However, off-profile features, in particular C2, may actually represent a far away structures or projected artefacts due to the low station coverage.

4.4. Inversion test with conceptual models

To investigate the consistency and reliability of inversion models, synthetic complimentary datasets were inverted. Testing of different geological settings and resistivity of the structures served to measure the model resolution. For the Venezuelan dataset, which was collected along a profile, examination of 3D off-profile features on 2D and 3D inversion models is of particular importance.

The synthetic datasets were generated using ModEM (Meqbel, 2009; Egbert & Kelbert, 2012). The 3D conceptual models included simplified regional geological and tectonic structures, as shown in Fig. 1.1 and Fig. 1.8, such as regional sedimentary basins from western Venezuela, northern Colombia and the South American craton (Fig. 4.15a). Their resistivity values, lateral and depth extents were taken from literature and regional studies (Telford *et al.*, 1977; La Marca, 1997; Escalona & Mann, 2003; Chacín *et al.*, 2005; Duerto *et al.*, 2006; Urbani, 2017).

4.4.1. The synthetic datasets

Several levels of complexity in the conceptual models were tested to generate the synthetic datasets. Figure 4.15 present two depth slices of the main models used in this thesis. Model variants included different fault systems and interconnections, as well as, variations of the resistivity and extent of the sedimentary basins. Following the analysis of PT and IVs (see Fig.3.8), a conductor was added east of the profile. Thickness and extent of this conductor were defined from forward modelling of a range of scenarios.

The 3D modelling grid consists of 152, 92, 132 cells in x-, y- and z- directions (1789, 1633, 885 km). In the innermost part of the grid, horizontal cell sizes are 2.6 x 2.6 km^2 while cell sizes increase gradually to 225 km in the outer parts of the grid. For the top 5000 m, vertical cells have fixed values between 25 m and 100 m. At 5000 m depth (below the sea level), the vertical dimension of the cells increase gradually by a factor of 1.2. Topographic and bathymetric data were taken from the NOAA open database (Amante & Eakins, 2009). The Caribbean Sea is included with a resistivity of 0.3 Ωm and 5 km of sea sediments with gradually increasing resistivity in the vertical direction.

Depending on the level of complexity of the conceptual model different structures were added. All conceptual models shown in Figure 4.15 included sedimentary basins, their thicknesses and resistivity are 10 km and 20 Ωm for the Maracaibo, 5 km and 25 Ωm for the Barinas-Apure, 3.5 km and 40 Ωm for the Falcón, and 15 km and 50 Ωm for the Los Llanos basins. The background resistivity is 500 Ωm outside of the described structures and for the MA. Faults were considered generally conductive and attributed with an average value of 5 Ωm, they were modelled following their position at the surface after Audemard *et al.* (2000) with their wide determined by the horizontal cell size crossed by the faults (from 2.6 x 2.6 km^2 to 7.4 x 2.6 km^2). Only the more significant fault strands were considered (BNF, VF, BUF and BF in Figs. 4.15b-c, and BNF, VF, BUF, BF, NWTS and SETS in Fig. 4.16d), reaching maximum depths of ~15 km. A 1 Ωm conductor (OPC) was added to the east of the profile limited by the BF and VF fault systems. In Figure 4.15b, the OPC was included at 11 km depth with 15 km thickness disconnected from the fault systems, whereas in Figure 4.15c and d, the OPC was added at 15 km depth with 1.5 km thickness connected to the VF and BF.

Synthetic datasets were produced for all conceptual 3D models shown in Figure 4.15 for a period range of 10^{-3} s to 1000 s, and 5 % of random Gaussian noise was added before inversion. These synthetic datasets were subjected to the same analysis applied to the measured data presented in chapter 3.

Directionality and dimensionality analyses of the synthetic responses of the flat OPC models (Figs. 4.15c and d) showed considerable similarity to the measured data. 2D and 3D inversion

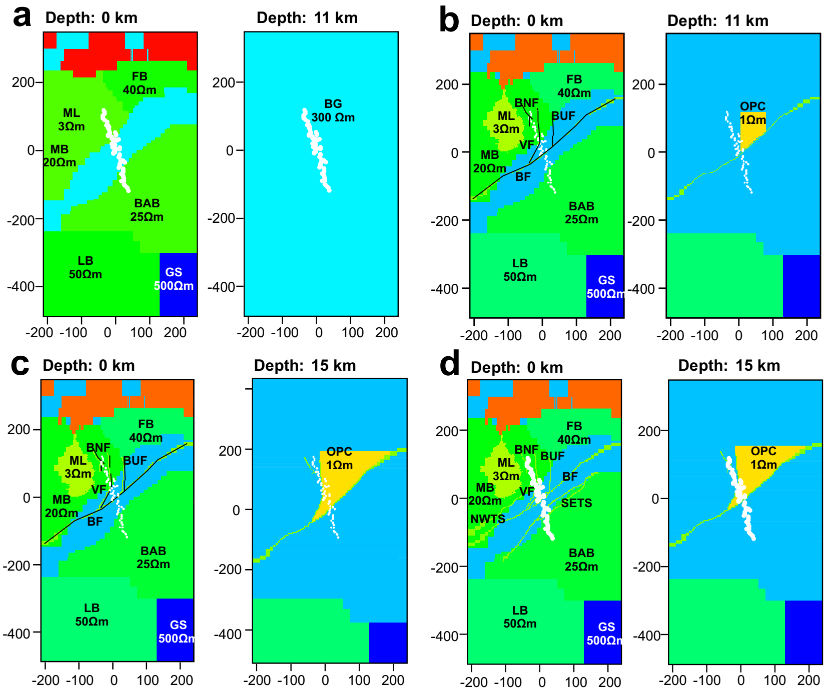

Figure 4.15.: Different conceptual models used to generate synthetic datasets. (a) Sedimentary basins only. (b) Sedimentary basins, main fault systems and a rectangular off-profile conductor (OPC). (c) Sedimentary basins, main fault systems and a flat and extended OPC, limited by the BF and VF. (d) Same as (c) also including the SETS and the NWTS and the TF. Abbreviations: MB - Maracaibo Basin, ML - Maracaibo Lake, FB - Falcón Basin, BAB - Barinas-Apure Basin, LB - Llanos Basin, GS - Guyana Shield, OPC - Off profile conductor, BNF - Burro Negro Fault, VF - Valera Fault and BF - Boconó Fault, NWTS - North-western trust system, SETS - South-eastern trust system and TF - Tuñame fault.

models were generated for all synthetic datasets, comparison between them and the measured data models revealed important information that is discussed in the following sections. The synthetic dataset generated from the flat OPC model of Figure 4.15c was selected as the preferred conceptual dataset, as it presented the best fit in term of data complexity and resemblance to the measured responses (see Figs. 3.10, 3.11b and 4.16a-b).

Figure 4.16 show a summary of the main aspects of the preferred conceptual model (flat OPC, Fig. 4.15c). The regional geoelectrical strike obtained between 10 s to 1000 s period was -36.5° (Fig. 4.16b), subparallel to profile. When divided in sections (see Fig. 4.1), the northern, central and southern sections show strikes of -1.8°, -36.2° and 23.3°, respectively. Compared to the 64°, -53.1° and 38° strike of the measured data (Fig. 3.12), the central and southern sections show similar results whereas the northern section differ considerably. The PT β values mainly indicate a 2D subsurface which is the result of the simplified and only regional structure of the conceptual model (Figs. 4.16c and e). The IVs are particularly influenced by the fault systems and the OPC pointing away from these structures (see Fig. 4.16a).

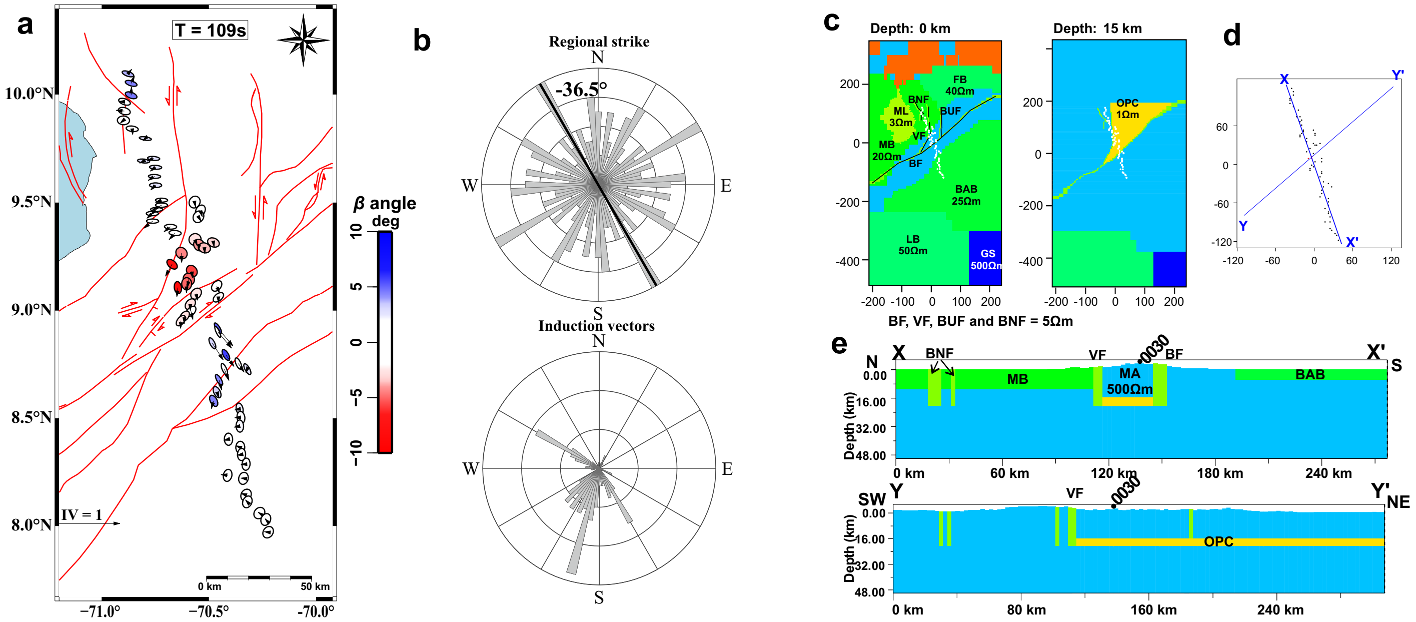

Figure 4.16.: 3D model with a flat off-profile conductor (OPC) showing (a) Phase tensors (coloured ellipses) and induction vectors (black arrows; real part) for a period of 109 s; (b) regional strike and induction vector analyses results for the period range 10-1000 s; (c) two depth slices at 0 km and at 15 km, the modelled fault systems are showed in black; (d) Location of the N-S and SW-NE sections presented in (e) For abbreviations see Fig. 4.15.

4.4.2. 2D inversions

To allow the comparison of the synthetic and measured data 2D inversion models, the synthetic datasets were projected onto the northern and southern sections of the profile (see blue AA' and red BB' in Fig. 4.1) and rotated to the strike of the measured data (see Fig. 3.11a). Most inversion setting are analogous with those of the measured data inversion (see table 4.1). However, since only 5% of Gaussian noise was added to the synthetic data, error floors had to be tighter than those for the field data in order to resolve all known resistivity contrasts. Therefore the error floor for the apparent resistivities of TM was set 10% and 1° for the phases of both modes, TE-mode apparent resistivity error floor was kept at 10,000%.

The resulting 2D inversion models for the synthetic data sets are shown together with the surface expression of structures from the original 3D models. Labelling and numbering of the recovered structures are set to coincide with the 2D inversions of measured data models shown in section 4.1.

In the upper 20 km, the 2D inversion models presented in Figure 4.17 mainly resemble the structures of the true models. In particular, the sedimentary basins were successfully recovered. Conductors C1-C3 and C10 represent the MB and BAB, respectively. Conductor C3 seems to also be related to a strand of the VF that runs parallel to the profile. This structure seems to be smeared out by the projection of the stations onto a profile.

Conductors C4 and C5 represent the VF and BF. Since these faults cross-cut the profile, their position coincides with the surface expression of the faults included in the 3D models. 2D inversion of synthetic datasets without the fault system (Fig. 4.15a) did not model these structures, confirming that these anomalies correspond to fault systems included in the 3D true model (Fig. 4.15c).

Interestingly, due to its size and interconnection with other structures the OPC can be related to three different conductive anomalies labelled C9 projected onto the profiles at different depths. Between C4 and C5 (Fig. 4.17a), the OPC is recovered 5 km shallower than in the original 3D model. However, 2D inversions of synthetic datasets without an explicit connection between the OPC, the BF and the VF (Fig. 4.15b) recovered a similar connection between the faults with a higher resistivity. This shows that, the oblique extent of the modelled faults (BF and VF) in the conceptual model can be partially responsible for the recovered conductive anomaly, whereas the connection between conductive structures generates a more conductive anomaly.

The black ellipse in Figure 4.17a marks the location of the other two anomalies associated with the eastward extent of the OPC, as projected under the stations mostly influenced by it (black ellipses in Fig. 4.19b).

Conductor C6 (Fig. 4.17b) is also related to the BF. The large rotation angle applied to the dataset for the southern section (52°) resulted in a horizontal shift in the position of the modelled anomaly compared to the surface expression of the fault. This rotation angle has also a considerable influence on the OPC recovery (C9, black circles in Fig. 4.17b).

Another effect in the 2D inversion models is the inclusion of small conductors in areas of lateral transition between a resistive medium and a conductive one. A spurious conductor (C8) is modelled close to the surface in the transition between the MA and the BAB. This effect is further exaggerated by an uneven stations distribution, which is the case of the conductive anomaly marked with the black ellipse (Fig. 4.17b) recovered in an area with no similar structures in the true model. In the case of an homogeneous conductive structure like the BAB, the station distribution foster the inclusion of resistors in otherwise conductive areas (i.e. red circles in Figure 4.17b).

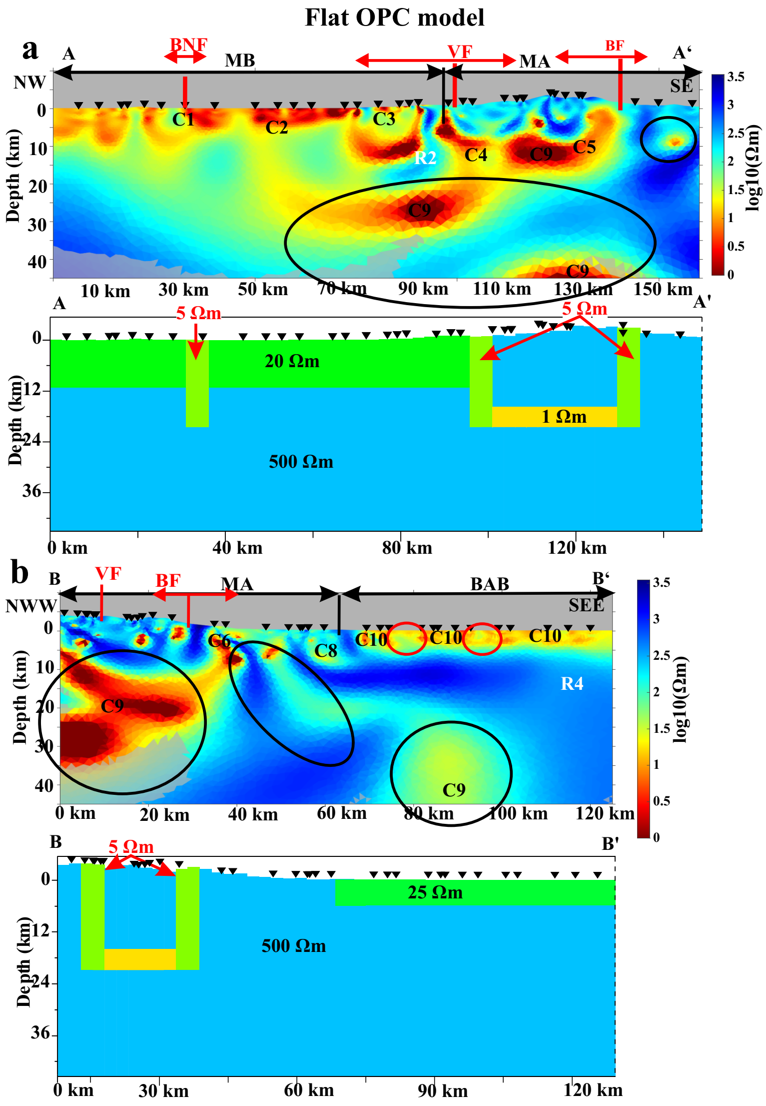

Figure 4.17.: 2D inversion models from synthetic data sets with their corresponding sections of the true 3D models. (a) northern, and (b) southern sections (Fig. 4.1). The black triangles represent the projected sites. Red bars mark the surface expressions of the faults and double headed arrows for their regions of influence. Black arrows indicate the extent of the sedimentary basins and the MA. Black circles and ellipses are described in the text. The grey shaded areas represent sections of the 2D models with sensitivities lower than $10^{-6.5}$ for the northern and 10^{-6} for the southern sections.

4.4.3. 3D inversion

The 3D inversion of the synthetic dataset (Fig. 4.18) employed the same initial model and inversion settings as the measured data inversion (see Table 4.2).

In general, conductive anomalies recovered reproduce the location, extent and resistivity of the conductive structures included in the true model (e.g. C5, C6 and C9 in Fig. 4.18a). The 3D inversion also recovered the modelled deep connection of the VF, BF and the OPC (C9), particularly the profile view (Fig. 4.18b) shows that such a conductor in depth can be recovered when embedded in a strong resistivity contrast. The 3D inversion also recovered successfully the most 2D parts of the model, namely the MB and BAB represented by conductors C1-C3 and C10, respectively. Interestingly, since the BAB is modelled almost like a 1D structure, it is better recovered than the MB, which is cross-cut by conductive structures (BNF and VF).

Notably, the surface expression of the conductive structures associated to the modelled fault systems are not recovered, showing low-resolution zones close to the surface possibly due to poor station coverage and the inverted period range (>0.01 s).

In summary, the 2D and 3D inversions (Figs. 4.17 and 4.18) of the synthetic dataset recovered the modelled structures and also resembled the measured data inversions (Figs. 4.2 and 4.4), further confirming that the simplified model served as a rough representation of the geology of the study area. Nevertheless, a series of artefacts were observed in the inversion models that highlighted the limitations of the data distribution and inversion approaches and need to investigated in-depth.

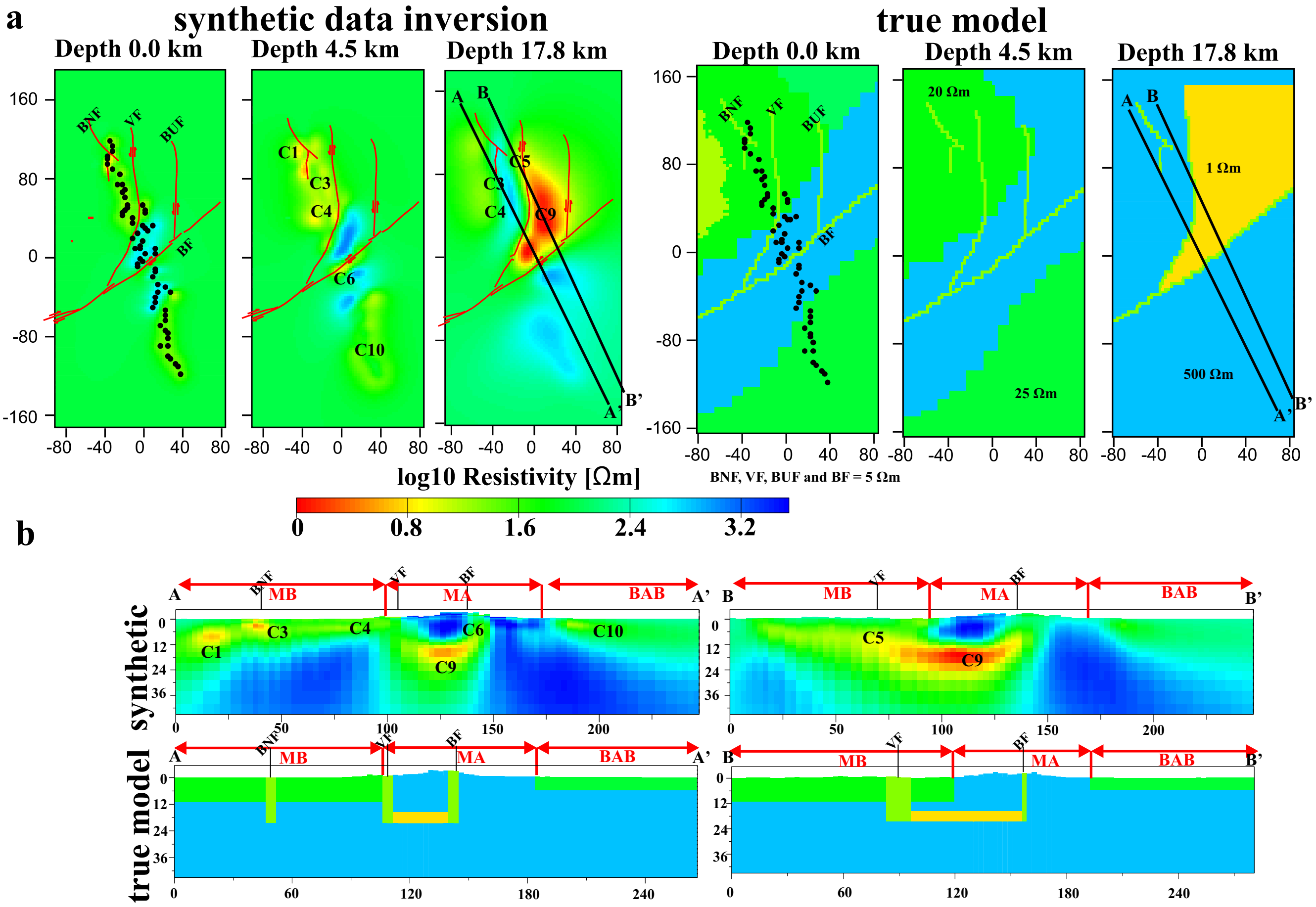

Figure 4.18.: 3D inversion of synthetic data generated from the flat OPC model (Fig. 4.16). (a) horizontal slices at selected depths from the inversion model (left) and true model (right) (b) East to west profiles. In (a): red lines represent the fault systems included in the true model, black dots the location of the stations and black lines location of profiles in (b). In (b.) black lines the surface expressions of the fault systems, red arrows show the extent of the sedimentary basins and the Mérida Andes.

4.5. Influence of off-profile structures and data distribution

Comparison between the 2D inversion of different synthetic datasets (not shown) with varying levels of complexity (Fig. 4.15) allowed to correlate the recovered anomalies with the structures in the true models (e.g. C1 - BNF, C3/C4 - VF, C5/C6 - BF, C9 - OPC in Figs. 4.17 and 4.18). However, in some cases the origin of the recovered anomalies was unclear, or they differed considerably from the structures included in the true model.

Inversion models may contain anomalies which do not have an obvious correlation with the subsurface structures. These structures are considered artefacts, possibly caused by the limited resolution of the dataset, poor fitting of the data or a modelling approach with lower dimensionality than the investigation target (e.g. 2D inversion of a 3D data set). For a profile distributed dataset, off-profile structures appear as such artefacts, for example, as a deep projection, in 2D inversions, and as a spurious structure with unconstrained lateral extent, in 3D inversions.

The main objective of this section is to identify areas of the synthetic data inversion models (Figs. 4.17 and 4.15) where distorting effects can be expected and to find ways to improve the resulting models of measured data (Figs. 4.2 and 4.4) and the interpretations of the recovered structures.

4.5.1. Effects in 2D inversion

When attempting to interpret 3D structures in 2D inversions, the distance of the anomalous structures from the profile must be considered. Figure 4.19 shows horizontal slices of the flat OPC model (Fig. 4.16), illustrating the lateral geometries of the fault systems and the OPC together with the location of the profiles.

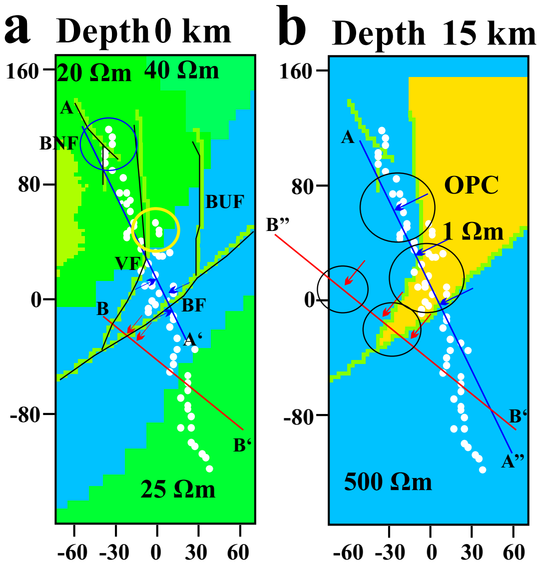

Figure 4.19.: Zoomed view of the 3D conceptual model highlighting the influence of off-profile structures on the stations. Presented in horizontal slices at (a) 0 km and (b) 15 km depth. The blue and red arrows mark the lateral influence of the fault systems and the OPC in the northern (blue) and southern (red) profiles. Coloured circles mark areas of poor coverage or 3D effects (see text).

The arrow heads indicate the position of observed resistivity anomalies in the 2D models that do not directly correlate with on-profile features (cf. black circles and C8 in Figs 4.17). The arrows are approximately 10-15 km long and perpendicular to the profiles; the length of the arrows is equivalent to the skin depth at periods of around 10 s with a 100 Ωm resistivity.

The arrows illustrate the sensitivity radius around these anomalies and identify the possible regions along the profile that are affected by off-profile, oblique or perpendicular structures mapped into the 2D inversion model (Fig. 4.17).

Lateral off-profile projections in 2D inversions

Off-profile structures can have a considerable effect in shaping the resulting structures of 2D inversion models, particularly the projection of oblique structures in a 2D plane adds artefacts to the inversion models that should not be interpreted. To further study this effects stations prone to be influenced by off-profile features were excluded from the inversion of synthetic data. The resulting models after the exclusion were compared to the previous models and to the corresponding section of the true model (Fig. 4.16) to evaluate the improvement on the recovery of the original structures. The 2D inversions presented in this section employed the same inversion settings of the 2D inversion of synthetic data in section 4.4.2.

Assuming that sites 0102, 0103 and 0104 are highly influenced by the N-S trace of the VF east of the profile (yellow circle Fig. 4.19a). The projection of these stations onto the 2D plane is responsible for the resulting U-shape of conductor C3 (Fig. 4.17a) that does not correlate with the location of the VF in the true model.

Figure 4.20 shows a comparison of the 2D inversion of synthetic data of the northern section (a) before and (b) after the exclusion of sites 0102, 0103 and 0104 with (c) the true model. This exclusion revealed a different shape of C3 and resulted in a more prominent resistor R2 located at the transition from a conductive to a resistive medium. Though R2 is not included in the original model (Fig. 4.20c), this resistor is possibly the result of the gap between the stations. Additionally, conductor C4 is larger and more clearly related to the VF, as included in the true model. The dip to the south of this conductor might be related to the south-western component of the VF (see blue arrows in Fig. 4.19a).

The results shown in Figure 4.20 confirmed the influence of the projection of the stations 0102 - 0104 over conductor C3. Thus, a 2D inversion of the measured data for the northern section was repeated excluding these stations. The 2D inversion model (Fig. 4.21) converged after 39 iterations, and reduced an initial RMS of 22.46 to 1.23 (TEφ: 1.92, TMρ_a: 0.76, TMφ: 1.34). The slight reduction in the RMS after the exclusion compared to the previous inversion (Table 4.3) shows that the 3D effect removed was local and had no major impact over the entire model.

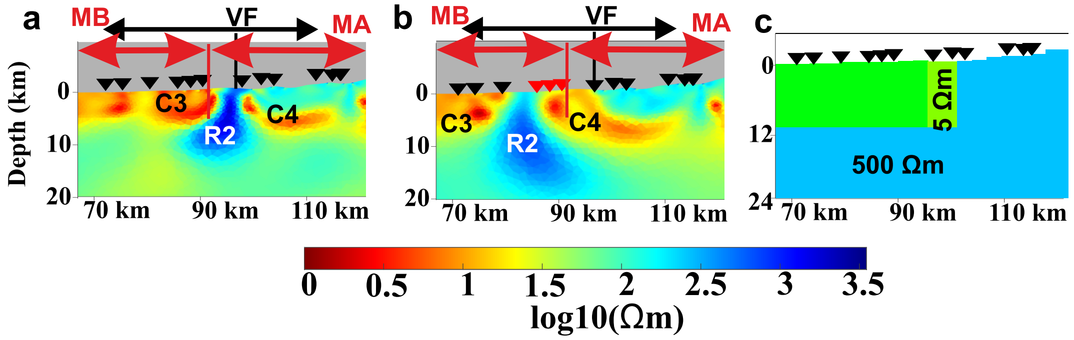

Figure 4.20.: Excerpt from 2D inversion of synthetic data (Fig. 4.16) showing the effect of the exclusion of stations 0102-0104. Showing the 2D inversions (a) before exclusion, (b) after exclusion and (c) true 3D model (Fig. 4.16). Red arrows indicate the surface expression of the MB and MA. Black arrows mark the possible area of influence of the VF (see yellow circle in Fig. 4.19). Black triangles are the location of the stations and red triangles the excluded ones.

After the exclusion, conductor C3 appears as a thin sub-vertical structure, reflecting the expectations of a fault separating the MA from the MB, and has a depth of approximately 10 km. Maximum depth of resistor R1 is now imaged at 9 km.

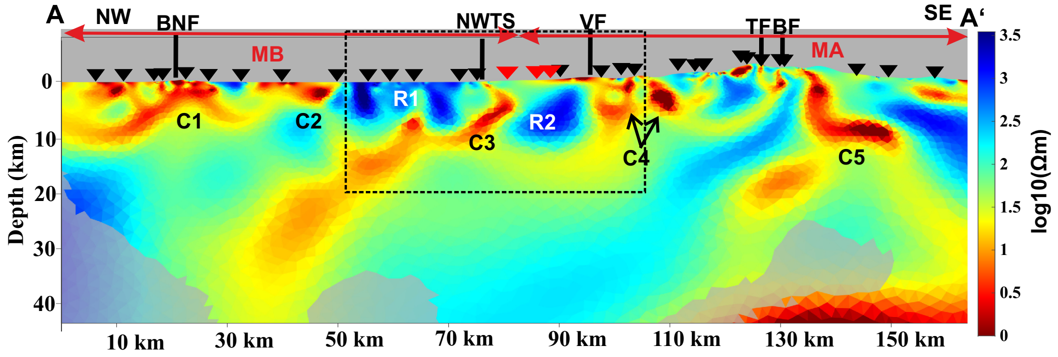

Figure 4.21.: 2D inversion results of the Northern section after excluding stations deemed influenced by an off-profile NS trace of the VF. Red triangles mark the excluded stations. Conductive and resistive structures are labelled as in Figure 4.2a. The grey shaded area represent sections of the model with sensitivities lower than $10^{-6.5}$. Surface locations of fault systems are indicated by black lines; the extents of the MA and MB are depicted by red arrows.

Excluding stations influenced by off-profile structures allowed for better mapping of the MA's northern front, represented by the north-western thrust system (NWTS) and the VF. This improvement in the modelling of the NWTS confirms that parallel and subparallel to profile conductive structures can be projected onto the 2D plane and influence considerably the modelling of the real structures. Nevertheless, the exclusion of station could also lead to inadequate site

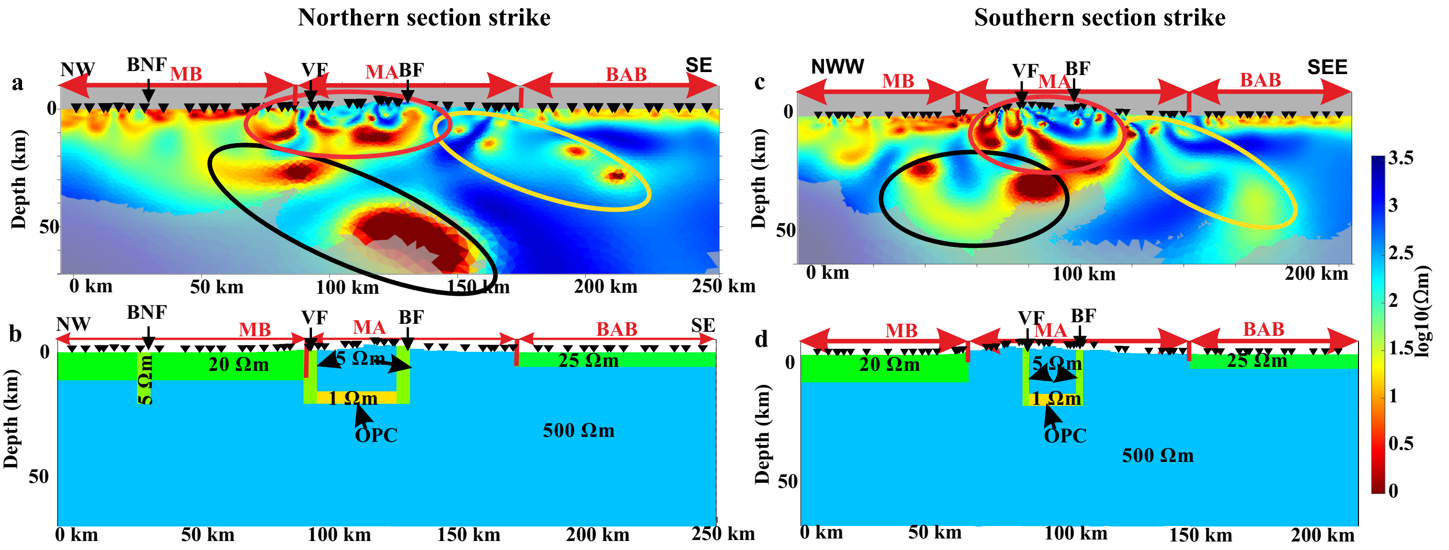

Figure 4.22.: 2D inversion of synthetic data from the flat OPC model (Fig. 4.16) for the entire data set rotated to the strike of the northern (left) and southern (right) sections and their corresponding section from the true model. The coloured ellipses marked the location of conductivity anomalies discussed in text.

coverage (i.e. above R2). As seen with synthetic data (i.e. yellow circles in C10 in Fig. 4.17 and R2 in Fig. 4.20) uneven spatial distribution of stations can place resistors in conductive areas, or exaggerate them.

The influence of data rotation and profile orientation

Data rotation and profile orientation have a considerable effect in the recovered structures in a 2D inversion. In the following, the influence of the profile orientation was tested performing inversions for the entire synthetic dataset (Fig. 4.16). Figure 4.22 shows the results of the 2D inversion of the preferred synthetic dataset rotated to the geoelectric strike of the northern and southern sections and projected onto the profiles AA" and BB" (Fig. 4.19b). These models were obtained employing the same inversion settings of the 2D inversion of synthetic data in section 4.4.2.

There are evident differences between the 2D inversion of the northern (Fig. 4.22a) and southern (Fig. 4.22c) strike profiles. The northern profile reproduction of the true model is superior to the southern, based on the location, depth and extent of the sedimentary basins, fault systems and the OPC. The area marked with the red ellipses shows good correspondence with the true model (Figs. 4.22b and d), as well as, the MB and BAB.

The black and red ellipses show the anomalies recovered for the OPC in both profiles. A possible reason for the two separate structures is that the northernmost anomaly is related to the stations north of the VF, and the deeper anomaly is associated with the stations located south of it (black circles in Fig. 4.19b). The different shape of the ellipse marked anomalies between profiles is a result of the stations' projection. This projection promotes the grouping of stations and their responses, shifting the modelled structures. For example, the southern profile rotation angle and projection fostered uneven station and a cluster of station above the MA (red ellipsis in Fig. 4.22c) that resulted in circular near-surface anomalies and a southwards dipping conductive zone for the OPC that cannot be related to the true model (Fig. 4.22d).

Another effect fostered by the relocation of stations is the skewing of the modelled anomalies. Stations north of the BF when projected onto the northern section stay north of the surface expression of the fault (Fig. 4.19a), explaining the northwards extension of the BF (Fig. 4.17a). Whereas, when the same stations are projected to the southern section, they are relocated south of the surface expression of the fault; hence the BF appears smeared out southwards (Fig. 4.17b).

Moreover, the rotation angle seems to add artefacts with larger strikes, due to data rotation and projection onto profiles. The yellow ellipses in Figures 4.22a and 4.22c mark the location of conductive anomalies that are not part of the true model (Figs. 4.22b and d). In the case of the northern section, the artefacts are small localized conductors; whereas, in the southern section, the artefact is a deepening conductor connected to surface.

In summary, modelling approaches with lower dimensionality than the investigation target are deemed to be affected by several effects ranging from the influence of off-profile and oblique extending structures to the skewing of recovered anomalies due to stations projection. Nevertheless, the inversion models can still be useful provided that this effects are considered. The exclusion of stations affected by off-profile oblique extent of structures showed a considerable improvement in the recovery of the in-profile structures (Fig. 4.21). Considering the rotation angle and the projection of the stations can limit the skew of the recovered anomalies.

4.5.2. Effects in 3D inversions

Three-dimensional inversion of single profile data can provide a more meaningful picture of the subsurface geometry beneath the profile, mainly when using the full complete impedance tensor (e.g. Siripunvaraporn *et al.*, 2005; Kiyan *et al.*, 2013) than that obtained from 2D inversions alone, particularly in areas characterized by complicated geologic settings and off-profile structures. However, the information recovered about off-profile structures is also limited, more so along strike (Siripunvaraporn *et al.*, 2005). Comparison of the 3D inversion of measured and synthetic data with the true model allows studying the limitations of the resolution of the 3D inversion and helps to identify structures that must be interpreted with caution.

Spurious conductors along profile

The sensitivity test showed that the labelled structures in the 3D preferred model (Fig. 4.4) are needed for the model to fit the data. Due to the limited lateral resolution of profile data in a 3D inversion, anomalies may still be misplaced or shifted. Figure 4.23 show an example of this comparing excerpts from the measured (Fig. 4.4) and synthetic (Fig. 4.18) data 3D inversions. In this case, conductors C1 and C2, that are confirmed by the sensitivity test (Table 4.6), may be the result of unconstrained structures to the north or simply artefacts of the inversion.

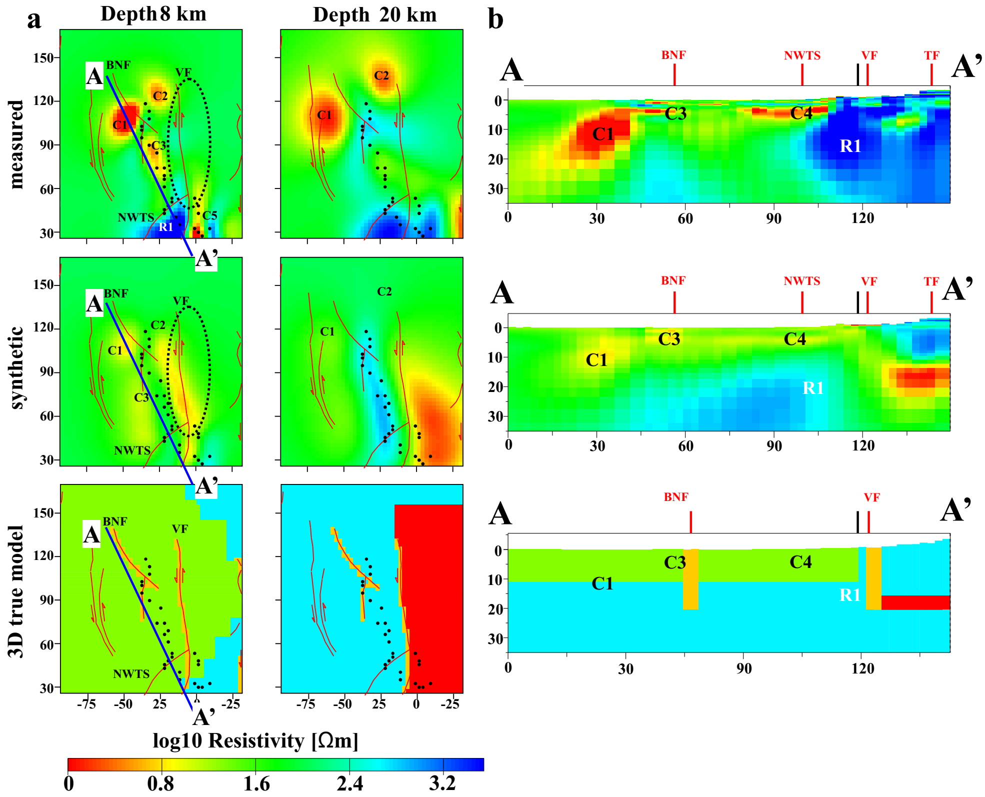

Figure 4.23.: Zoomed image of Conductor C1 and C2 in (a) horizontal slices at 8 km and 20 km comparing the preferred 3D inversion models of measured and synthetic data with the true 3D model, and (b) profile AA' (black line in (a).

Conductors C1 and C2 are located at the northernmost section of the profile and illustrate the model's lateral resolution limitations. These structures were recovered in both the measured data 3D inversion of the impedance tensor (Fig. 4.5) and the vertical magnetic transfer function

(Fig. 4.6); though, in the later, both anomalies are merged with a deep extent similar to that of the integrated inversion. Comparison between the inversion of measured and synthetic data with the true model (Fig. 4.23) shows that at 8 km depth this C1 could be related to the north-western strand of the BNF. At 20 km, neither C1 nor C2 are present in the synthetic data inversion, even when the BNF was modelled up to 20 km in the true model (see Figs. 4.23a and b, bottom).

The comparison suggests that the shallow section of C1 (>10 km) is a combination of the influence of the Maracaibo Basin and the BNF, supported by both impedance and vertical magnetic transfer function responses. In the 3D preferred model, conductor C2 migrates to the north with depth eventually merging with a far away conductor about 60 km to the north of the profile at 40 km depth. Whereas, in the synthetic data inversion C2 is not recovered at all, indicating that the conceptual model lacks structural complexity to the north of the profile. Therefore, C2 and the deeper extent of C1 are possibly artefacts, resulting from unconstrained conductors to the north contained in the long periods of the VTF, and should not be considered for interpretation since they also lay on the limits of the model resolution.

Lateral resolution and limitations of the 3D model

Comparison between the 3D inversion of synthetic datasets and their true model (e.g. Fig. 4.16) permits to determine the lateral resolution of the inversion models/datasets and to understand the different factors that can influence it. Furthermore, this comparison shows how the station distribution affects the recovery of anomalies in - and off-profile.

Figure 4.24 shows that the conductive anomaly associated with the OPC is sub-horizontal up to 15 km away from the profile, dipping eastwards until 30 to 35 km away from the stations. The dipping shows a maximum shift in depth of 10 to 20 km (see Figs. 4.24c and d).

In actuality, model's resolution depends on several factors such as the resistivity of the medium, structural homogeneity, and the period range of the dataset. MT data and inversion models are particularly sensitive to vertically integrated conductivity or conductance (the conductivity-thickness product). When conductance of a structure significantly exceeds the integrated conductance of the entire overlying layers, this structure is more detectable by the MT data.

Figure 4.24(c-e) show an excellent recovery of the OPC, since this conductive structure is constrained in a resistive medium, both depth and resistivity of the anomaly correlate with the true model. However, the fault planes and the connection of the VF and, BUF and BF with the surface is hardly recovered in profiles BB' and CC' (see red circles Fig. 4.24d and e), and mixed with anomaly associated with the MB in profile AA' (Fig. 4.24c).

In profile AA' (Fig. 4.24c), the low resistivity ($< 20\,\Omega m$) of the MB limits the depth of investigation (see eq. 2.15). Hence below stations 0103 and 0104, there is a vertical and lateral shift in the location of the VF and the OPC, and the model can hardly recover the lateral variation from the basin to the background resistivity (500 Ω*m*). In profile BB' (Fig. 4.24d), the OPC is modelled at the same depth and resistivity than in the true model up to 10 km to the east of station 0113, located above a more resistive medium. Yet, the lack of station coverage (no station close enough to the faults) limits considerably the resolution of the inversion to these conductive structures (BUF and BF, 20 km and 32 km away from station 0113, respectively).

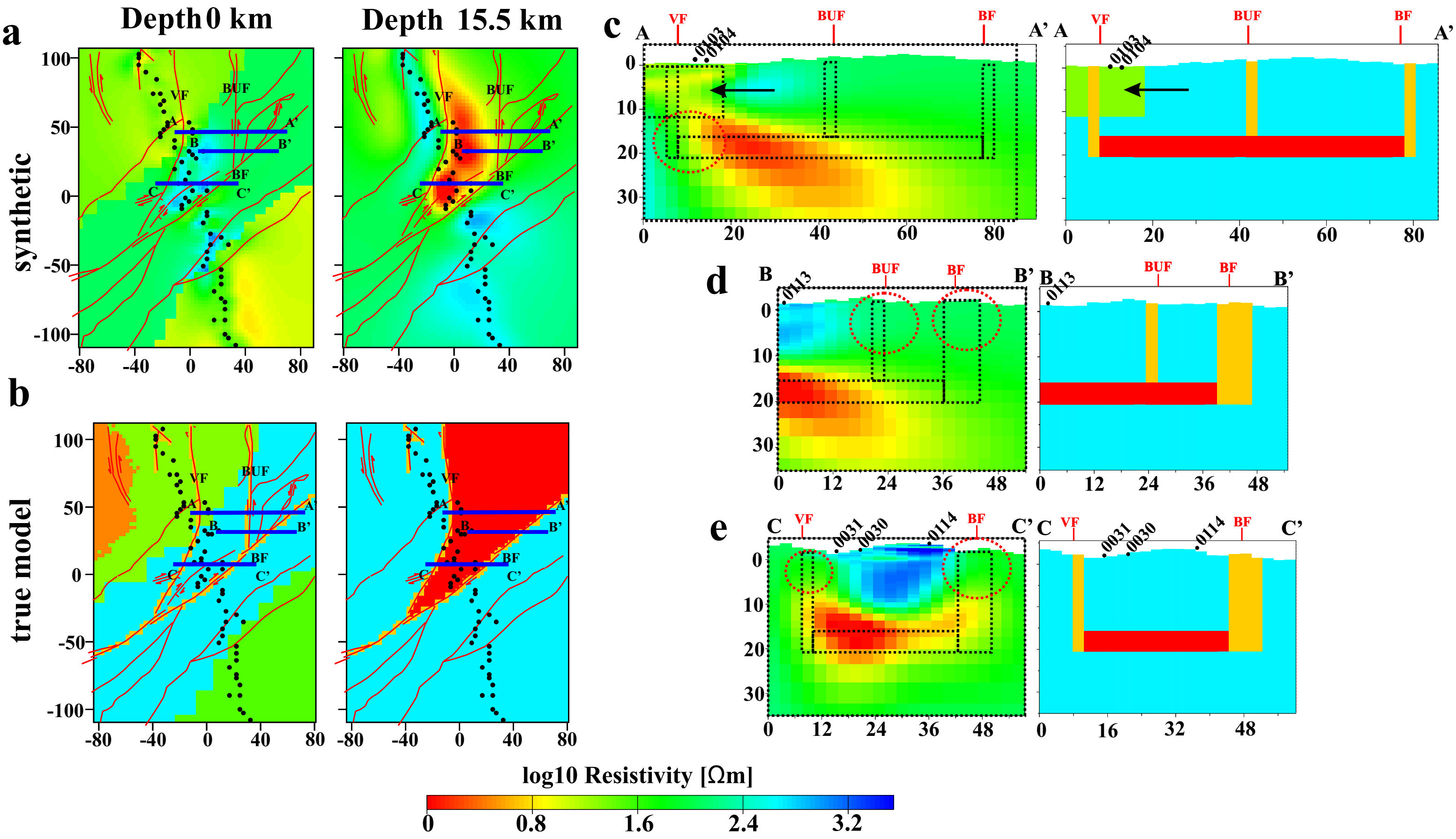

Figure 4.24.: Comparison between the 3D inversion of the synthetic dataset produced from the flat OPC 3D model (Fig. 4.16) and the true model (Fig. 4.16). Horizontal slices of the models at depth of 0 km and 15 km below the sea level are shown for (a) the synthetic 3D inversion and (b) true model (c), (d) and (e) show east to west parallel profiles superimposing the true model over the 3D inversion. Location of the profiles is indicated with blue lines in (a) and (b). Red circles in (c), (d) and (e) are discussed in the text.

Profile CC' (Fig. 4.24e) is located in the central part of the MT profile and has a higher volume of stations in the vicinity of the modelled structures, which ensure good station coverage. Thus, this profile shows a resistor between the surface location of the faults and recovers a conductor that can represent both the OPC and the fault systems, depth and shape of the OPC towards the VF (below stations 0031 and 0030) than towards the BF (below station 0114), compared to the true model. Profile CC' (Fig. 4.24e) further illustrate the limits of the 3D inversion to model a fault plane above ~4 km (red circles), also showing that the high resistivity at the surface foster better modelling of the deep connection of the fault systems and the OPC, in contrast to profiles AA' and BB' (Figs. 4.24c and d).

The 3D inversion of the synthetic dataset discussed in this section shows that the interpretations of the 3D inversions model of the measured data should be limited to a maximum of 15 km away from the profile for the deep structures (e.g. conductor C9 in Fig. 4.4). As recovered anomalies consistently showed that away from the stations off-profile structures tend to deepen and their resistivity decreases, the deeper extent of off-profile structures should be interpreted with caution, particularly those structures are located in areas of poor station coverage (e.g. C2). The connection of the fault systems with the surface, even if present in the true model, may not be recovered by the inversion of the data due to poor station coverage, the resistivity of the surface and the period range of the data.

4.6. Geologic interpretation

The analysis of the inversion models sensitivity and resolution allowed to limit the geological interpretation to highly reliable recovered structures. These analyses showed that off-profile structures greatly influenced the outcome of the 2D and 3D inversions, particularly the 2D inversions recovery of the oblique conductive structures (e.g. faults) proved inadequate due to lateral projection onto the 2D plane (C3 in Fig. 4.2a). The recovery of the same structures in the 3D inversion was superior to the 2D inversion, with the off-profile resolution of the 3D inversion models limited to 15 km away from the stations.

Although, the 2D inversion preferred models (Fig. 4.21 and Fig. 4.2b for the northern and southern sections respectively) consistently recovered the mostly 2D structures in the study area (e.g. MB and BAB), the preferred 3D inversion model (Fig. 4.4) shows a more clear recovery of dimensionally complex structures. Therefore, the geologic interpretation presented in this section is conducted mostly in extracts of the preferred 3D inversion model.

The geological interpretation of the model is divided into three main groups based on the surface geology. This division outlines the relationship of the observed anomalies with the Maracaibo basin (MB), the Barinas - Apure basin (BAB) and the Mérida Andes (MA).

4.6.1. The Maracaibo basin

As described in the section 1.4, the MB is a hydrocarbon rich foreland sedimentary basin that consists of Eocene to Quaternary sediments with a maximum depth at its depocenter of 10 km. The MT profile crosses this basin from its south-western boundary to its eastern part (see Figs. 1.8 and 4.25). The MB is subjected to an active deformation process due to the interplay between the eastward movement of the Caribbean Plate and the north-westward tectonic escape of the Maracaibo and Trujillo Blocks. This ongoing tectonic process causes folding and normal faulting towards the eastern boundary of the basin. Conductive anomalies associated with these processes are characterized and described in this section.

Conductors C1 to C4 (see Fig. 4.25a depths 1.5 km and 4.5 km and profiles BB' and CC') are spatially related to the MB with a resistivity ranging from 1 to 20 Ωm and a maximum depth of 10 km slightly larger than those reported in the literature (e.g. Duerto *et al.*, 2006). However, there are clear divisions between these conductors. Conductors C1 could be partly related to the BNF; this normal fault is oblique to the section of the profile between stations 0002 and 0009 (the northernmost stations of the profile, blue circle in Fig. 4.19). Profile BB' (Fig. 4.25) presents a maximum depth of 12 km for conductor C1, in agreement with the known depth of the BNF. Conductor C2 and the deeper extent of C1 (below 12 km) were shown to be artefacts resulting from unconstrained structures north of the profile.

Between conductors C1, C3 and C4 there are resistive areas (60 Ωm up to 500 Ωm, black arrows in Fig. 4.25a, depth 1.5 km) from shallow to deep depths. This juxtaposition of anomalies could be related to the north to south compression resulting from the convergence of the MTB with the MA, which creates a series of anticline and synclinal structures putting together Eocene compact sediments, exposed at the surface by erosion, with Quaternary ones (Escalona & Mann, 2003, 2006a). Although, an uneven station distribution may foster such an effect in the inversion models, synthetic data inversion models do not show a marked differentiation in the MB (Fig. 4.18), confirming these resistors to be the result of the modelling. 2D models also recover resistive structures between the conductors (e.g. R1 in Fig. 4.21), however, their depth and resistivity are exaggerated due to 3D effects.

Conductor C4 extents from the surface expression of the NWTS to the north about 20 km. Below 5 km depth, C4 and C3 merge toward the bottom of the MB (see black line in profiles AA' and BB' in Fig. 4.25b). The variation in resistivity from surface to bottom may indicate different rock composition, with older and consolidated structures at depths. The lower resistivity closer to the surface may also indicate fluids path from the surface through the faults (BNF and NWTS), or combination of both fluid content and rock composition.

The westward extent of conductor C4 along the surface expression of the NWTS (black arrow in Fig. 4.25a, depth 4.5 km) represents the fault system, as confirmed by 3D inversion models of synthetic datasets with and without the NWTS up to 5 km depth (Fig. 4.15c and d). Below C4, the NWTS is interpreted as the northern limit of the MA root followed to a depth of 30 km (red dotted line under NWTS in profiles AA' to CC' in Fig. 4.25b).

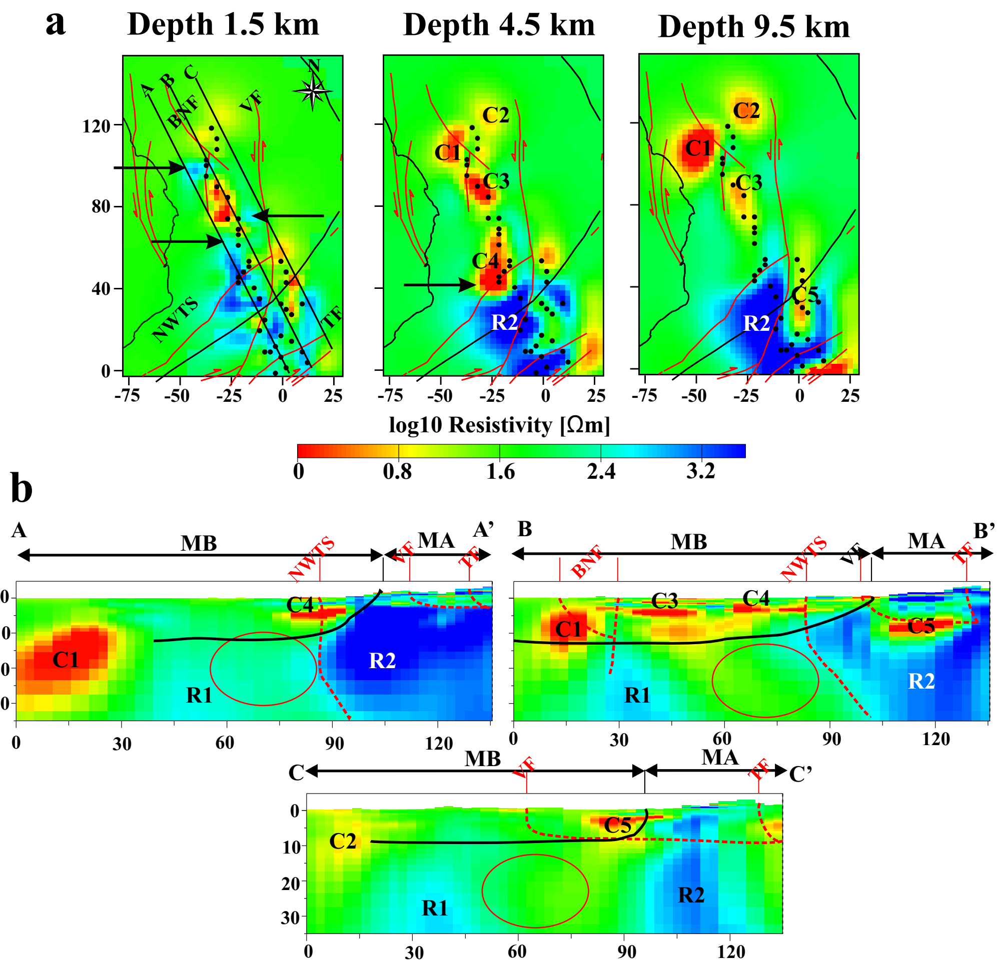

Figure 4.25.: Extract of the 3D inversion preferred model (Fig. 4.4) over the Maracaibo basin. (a) Three selected horizontal slices at 1.5 km, 4.5 km and 9.5 km below the sea level depth. The black lines in the depth slice at 1.5 km indicate the profiles location in (b). Red lines indicate the location of the Quaternary fault systems (after Audemard *et al.*, 2005) and black lines indicate the limits of the MB (Urbani, 2017). (b) Three selected profiles up to 35 km depth. Red lines indicate interpreted fault planes and detachment surfaces; solid black lines interpreted basin depth. Labelled features are discussed in the text.

The evident separation between the deep (>20 km) resistive structures possibly representing the upper crust (R1) and the root of the MA (R2) (red circle in Fig. 4.25) coincides with a gravimetric low (Bouger and free anomaly), reported in several studies (e.g. Hospers & VanWijnen, 1959; Rod, 1960; Kellogg & Bonini, 1982). This anomaly has been attributed to the thickness of the Maracaibo basin (e.g. Rod, 1960). The separation between these two resistors (R1 and R2) may indicate a SE tilt of the Maracaibo Block due to the large subsidence of the lithosphere caused by the MA (Arnaiz-Rodríguez & Audemard, 2014) with the NWTS functioning as a detachment surface.

4.6.2. The Barinas Apure basin

The BAB is Venezuela's third-largest oil-producing basin. This foreland basin south to the MA is characterized by Cretaceous to Pleistocene sediments (sandstone, limestone and shale) that rest disconformably over a pre-Paleozoic basement of igneous and metamorphic rocks. The central part of the BAB reaches a maximum depth of 5 km; grabens present in this area are considered as evidence of the opening of the Proto-Caribe associated with the separation of the Americas (Yoris & Ostos, 1997).

The southernmost conductor of the models (C10) correlates with the location at the surface of the BAB (Fig. 4.26). This conductor reaches a maximum depth between 4 and 5 km towards the MA and 3 to 4 km to the south end of the models (black lines in Fig. 4.26b). These depths agree with those reported by flexural modelling (Chacín *et al.*, 2005). The resistivity obtained from the 3D inversion model between $5\,\Omega m$ and $25\,\Omega m$ is in the range of known values of sedimentary rocks (see Fig. 2.1), especially for the reported stratigraphic column contents of Tertiary molassic sequences of sandstone, shale, and conglomerates (Callejón & von der Dick, 2002).

Interestingly, the resistivity anomalies associated with the BAB could be successfully modelled and are highly similar independently of the inversion scheme (2D and 3D see Fig. 4.26). Dimensionality and directionality analyses (see section 3.4) show 1D/2D settings for the BAB, indicating that most of the deformation resulting from the tectonic settings in western Venezuela are focussed north to the BF (northern flank of the MA and MB).

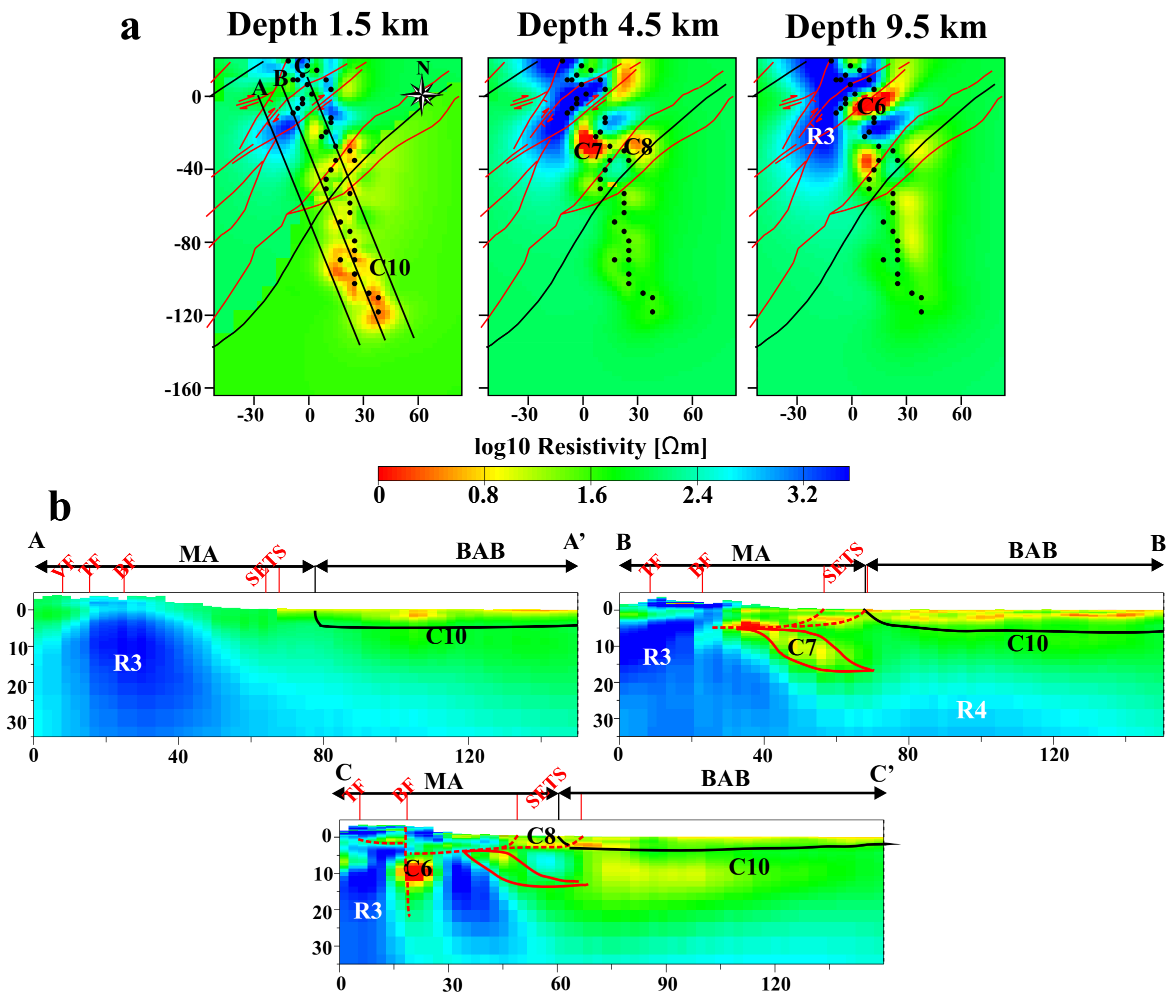

Figure 4.26.: Extract of the 3D inversion preferred model (Fig. 4.4) over the Barinas-Apure Basin. (a) Three selected horizontal slices at 1.5 km, 4.5 km and 9.5 km below the sea level depth. The black lines in the depth slice at 1.5 km indicate the profiles in (b). Red lines indicate the location of the Quaternary fault systems (after Audemard *et al.*, 2005) and black lines indicate the limits of the MB (Urbani, 2017). (b) Three selected profiles up to 35 km depth. Red lines indicate interpreted fault planes and detachment surfaces; solid black lines interpreted basin depth. Labelled features are discussed in the text.

4.6.3. The Mérida Andes

The central part of the MA consists of Cenozoic and Mesozoic igneous-metamorphic rocks, which are considered generally a resistive material. The most relevant fault systems of the area, the Boconó (BF) and Valera (VF) Faults, cross-cut the MA in NE-SW direction along its strike on a length of 400 km and in N-S direction at its centre on a length of 60 km, respectively.

However, there are also several smaller fault systems with normal and inverse components that further juxtaposed Precambrian and Paleozoic rocks of the MA core (Audemard *et al.*, 2000). The uplift of the MA also caused the formation of thrust systems to the north and south known as the north-western and south-eastern thrust systems (NWTS and SETS in Fig. 1.8). These thrust systems fostered the formation of piggyback basins and brought Precambrian and Paleozoic metamorphic rocks in contact with Tertiary rocks at the mountain fronts (Audemard & Audemard, 2002).

The VF is represented by conductor C5 (Fig. 4.27). Its resistivity ranges between 1 and 50 Ωm and reaches a maximum depth of 12 km (Fig. 4.27, the bottom of the anomaly in profile CC'). The anomaly is recovered with a shift to the south-west when compared to its position at the surface (Fig. 4.27 depth 9.5 km). At its lowest resistivity (~1 Ωm), it forms a north-south 40 km long anomaly under stations 0022 to 0028 (Fig. 4.27, depth 9.5 km).

The MA nucleus, which consists of Precambrian and Jurassic igneous-metamorphic rocks, widens to the west of the profile (Fig. 1.8). This nucleus is represented by resistors R2 and R3 with resistivity above 300 Ωm up to more than 35 km depth, depicting the cortical root of the MA. Interestingly, Figure 4.27 shows a south-westward extension of these resistors, yet north-east of the profile they seem to be limited by the VF and BF. These lateral changes of resistivity may indicate that these fault systems are a structural boundary between different geological structures.

Resistors R2 and R3 are split by conductor C6 (between 5 and 10 km deep, see Fig. 4.27 depth 9.5 km and profiles BB' to DD'). This conductor spatially related to the BF, with a maximum depth of 35 km, unlike other conductive anomalies (e.g. C5), C6 is not constrained by the resistors representing MA. However, R2 and R3 do merge at great depth, below the limits of the model resolution (>40 km). This splitting indicates that the BF carries deformation at least to the upper crust. Similar depths were reported by wide-angle seismic and seismic anisotropic analysis (Niu *et al.*, 2007; Masy *et al.*, 2011).

Conductor C7 with a maximum depth of 12 km represents a depth connection between the BF and the SETS. This connection may be related to back-thrust in the southern flank of the MA, which foments the formation of tectonic wedges basinwards. Conductor C8 related to the SETS may also represents the Tertiary and Quaternary alluvial terraces that form the southern foothills, with a depth of 3-4 km at the centre of the anomaly and dipping to the north under the northern strand of SETS. To the east, C8 reaches a maximum depth of 8 km (see C8 in Fig. 4.27 profile DD'), this east-dipping extension of C8 is not cover by stations and it is most likely the result limited lateral resolution (see Fig. 4.24).

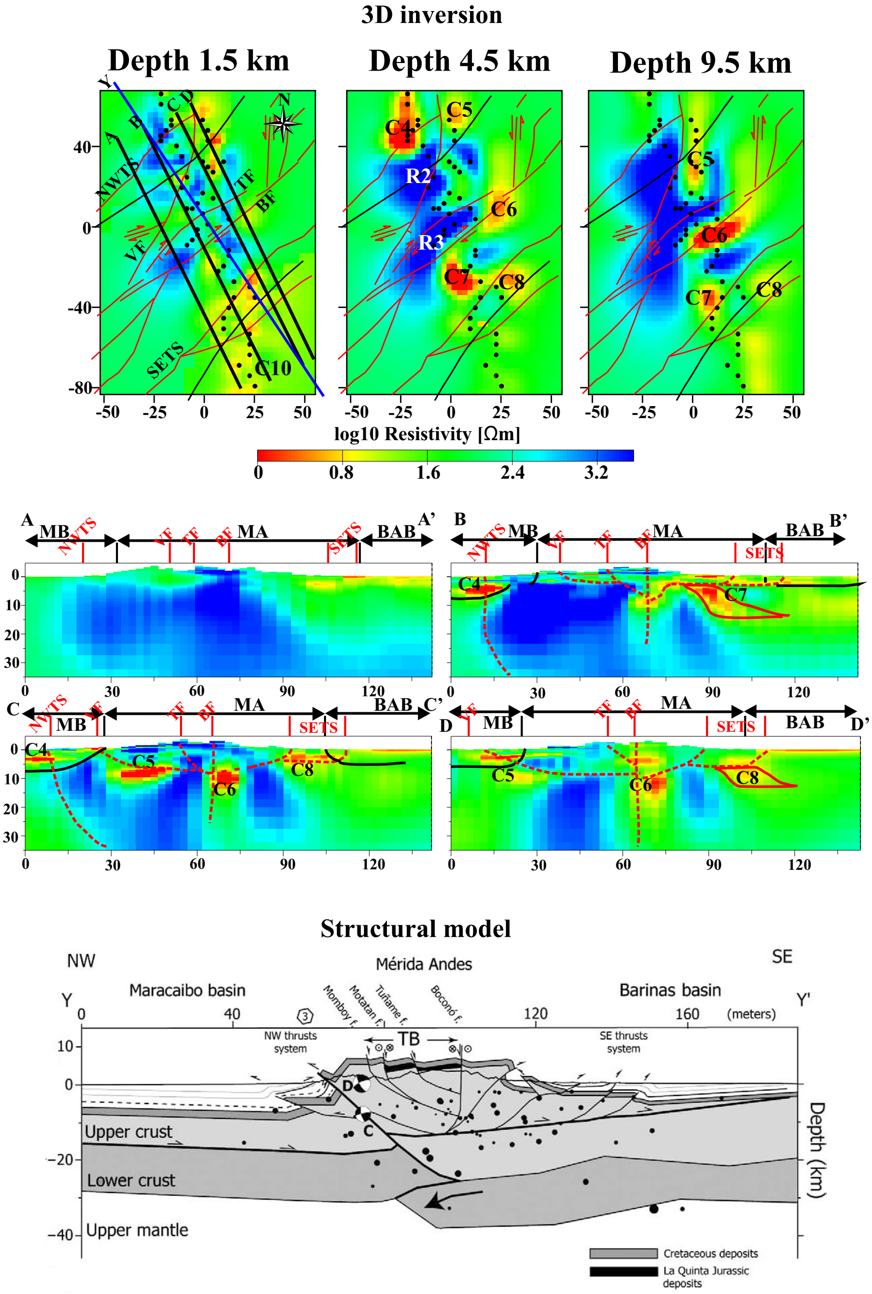

Figure 4.27.: Extract of the 3D inversion preferred model (Fig. 4.4) over the Mérida Andes (top) and a structural model of the central part of the mountain chain (taken from Monod *et al.*, 2010, bottom). The 3D inversion depicts 3 selected horizontal slices at 1.5 km, 4.5 km and 9.5 km below the sea level depth. Location of profiles AA' to CC' are marked with black lines in the depth slice at 1.5 km. Blue line indicate the location of the structural section YY'. In depth slices: red lines indicate the location of the Quaternary fault systems (after Audemard *et al.*, 2005) and black lines indicate the limits of the MB (Urbani, 2017) and the Maracaibo lake. In 2D and 3D profiles: dotted red lines indicate interpreted fault planes, red lines detachment surfaces and solid black lines interpreted basin depth. Labelled features are discussed in the text.

The central section of the 3D model and interpreted profiles show increasing complexity and interconnection of the conductive anomalies from west to east (Fig. 4.27, profiles AA' to DD') consistent with crustal scale cross-sections across the Mérida Andes (e.g. Monod *et al.*, 2010). Particularly, profiles BB' to DD' image a deep connection between the fault systems of the MA in agreement with known structural models (red dotted lines in Fig. 4.27). The resolution of the model is limited to the upper 40 km (see table 4.5), thus a deep connection (below 40 km depth) between the NWTS and the BF can only be assumed, however the preferred 3D inversion model (Fig. 4.27) strongly suggest that both structures carry deformation to the lower crust.

The generally low resistivity of these near-surface and crustal structures (<10 Ωm) may be associated with fluids circulation, fracturing, fault systems interconnection, and remineralization processes.

Possible presence of fluids under the Mérida Andes imaged with MT data

The redistribution of fluids in seismic fault zones can trigger shallow earthquakes (e.g. Jiracek *et al.*, 2007, and references therein) and these seismogenic zones are often characterized by interconnected pore fluid (e.g. Fialko, 2004). Particularly zones of high electrical conductivity are often associated with major fault zones or detachment zones in the mid- and lower-crust (e.g. Unsworth & Bedrosian, 2004; Ritter *et al.*, 2005; Becken & Ritter, 2011; Meqbel *et al.*, 2014).

Furthermore, high conductivity in active tectonic regimes is often explained with fluids in fault systems and fluids derived from remineralization reactions of hydrous minerals, or both (Jones, 1993; Boerner *et al.*, 1998; Ritter *et al.*, 2005; Becken & Ritter, 2011; Meqbel *et al.*, 2016). The seismicity in western Venezuela is related to the eastward movement of the Caribbean plate and the tectonic escape of the North Andean block to the NE, distributed along a series of dextral strike-slip fault systems, i.e. the Ocá-Acón, Boconó and El Pilar fault systems.

The fault systems and active deformation structures recovered in the preferred 2D and 3D inversion models are characterized by their low electrical resistivity (>10 Ωm). The focus of this section is the explore the possible relationship of the obtained conductive anomalies with fluids, enhanced seismicity and conductive anomalies interconnection.

Figure 4.28 show a superposition of historical seismicity over the 3D preferred resistivity model (Fig. 4.4), to identify a possible relation with the recovered resistivity structures. In general, for shallow earthquakes (Fig. 4.28a) there is no clustering or absence of events. Actually, seismicity is evenly distributed along the surface expression of fault panes. Only a few events of the deep earthquakes (Fig. 4.28b) show two possible cluster. Towards the centre of Figure 4.28b, a black ellipse marks a series of events related to the surface expression of the VF, but not to conductor C5 located to the east of this cluster. Another cluster of earthquakes to the north-east of C9 (black circle), could be related to the escape front of the Trujillo block (e.g. Dhont *et al.*, 2012), yet there is no resolution so far east from the profile. Although, these events do not seem to be directly related to the recovered anomalies (black ellipse) or are simply too far away from the profile (black circle), they indicate areas of interest for future studies.

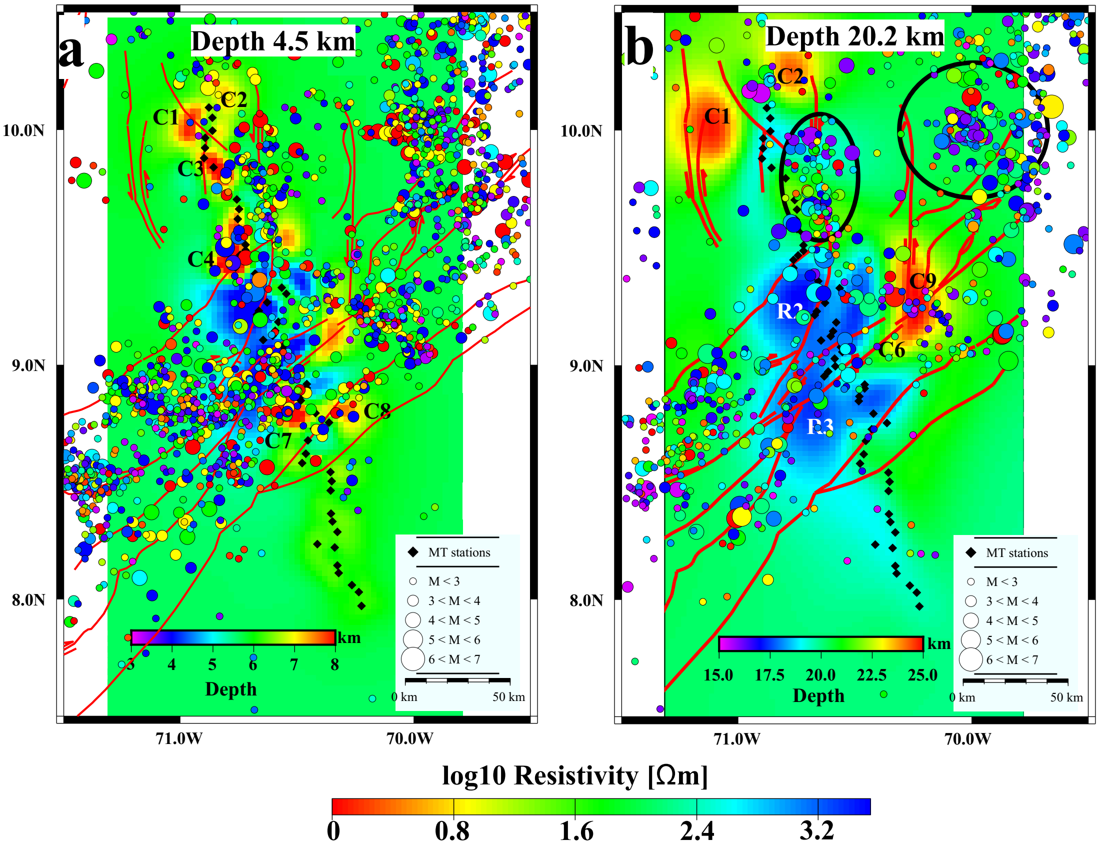

Figure 4.28.: Horizontal slices of the 3D preferred inversion model (Fig. 4.4) and historical earthquakes hypocenters. (a) Depth slice 4.5 km and seismicity between 3 - 8 km. (b) Depth slice 20.2 km and seismicity between 15 - 25 km. Seismological information compiled from Audemard *et al.* (2005); ISC (2003); U.S. Geological Survey (2020); and FUNVISIS historical database (pers. comm.). Quaternary fault systems (red lines, after Audemard *et al.*, 2000).

Shallow conductive structures related to tectonic processes, conductors C4 and C7

In the geological description of the structures, conductors C4 and C7 were related to the NWT-S/MB and partially the BF, respectively. However, these conductive anomalies may also represent a connection between the faults systems in the MA (Fig. 4.27 dotted red lines profile CC') and their extension basinward and shape also indicate more complicated tectonic structures. The connection between fault planes may also function as pathways for fluids. The origin of the fluids possibly are shallow re-mineralization processes of clay minerals. Since clay sediments have been reported along strike in the faults systems in the Mérida Andes (e.g. Audemard *et al.*, 1999, 2008), and the accumulation of clay sediments in fault gauges is also associated with low resistivities (e.g. Unsworth *et al.*, 1997).

Audemard (2003) explains that one type of active deformation occurring in the MA linked to strain partitioning is axial dextral strike-slip along with the BF and related transtensional basins or deep erosional valleys sitting on heavily fractured bedrock. Fracturing is often related to higher porosity and permeability in rocks, which also explains low resistivities at depth (see section 2.1).

Despite the differences between the MB and BAB, the structures formed by the NW- and SE-thrust systems in the MA show marked similarities. These similarities could explain the recovered anomalies as presented in Figure 4.29. Audemard (2003) summarizes these features in both mountain fronts as:

1. intracutaneous wedges verge basinward,
2. Tertiary sequences decoupled from the basement by a basinward detachment,
3. the intracutaneous wedges containing thrust sheets of basement rocks overridden by the Tertiary sequence above chainward passive roof back-thrusts,
4. small triangular zones (frontal edge of a thrust and fold belt bounded by a foreland-directed basal detachment and a hinterland-directed upper detachment) within the Tertiary sequence,
5. foreland verging ramps,
6. piggy-back basins decoupled from the underlying sequences, and
7. synorogenic molassic sequences.

Short profiles over the observed conductive anomalies and a simplified structural model of the central part of the MA are shown in Figure 4.29. Profile AA' above conductor C4 (Fig. 4.29b) shows that this structure is related to the detachment surface of the MB, and the NWTS possibly enhances its conductivity. The later contributes to the fracturing of the sedimentary structure, fostering the formation of triangle zones. In the 3D inversion models, the NWTS fault plane is interpreted as a vertical to sub-vertical structure (red dotted line in AA' Fig. 4.29b) while the not scaled structural model (Fig. 4.29c) shows a sub-horizontal plane.

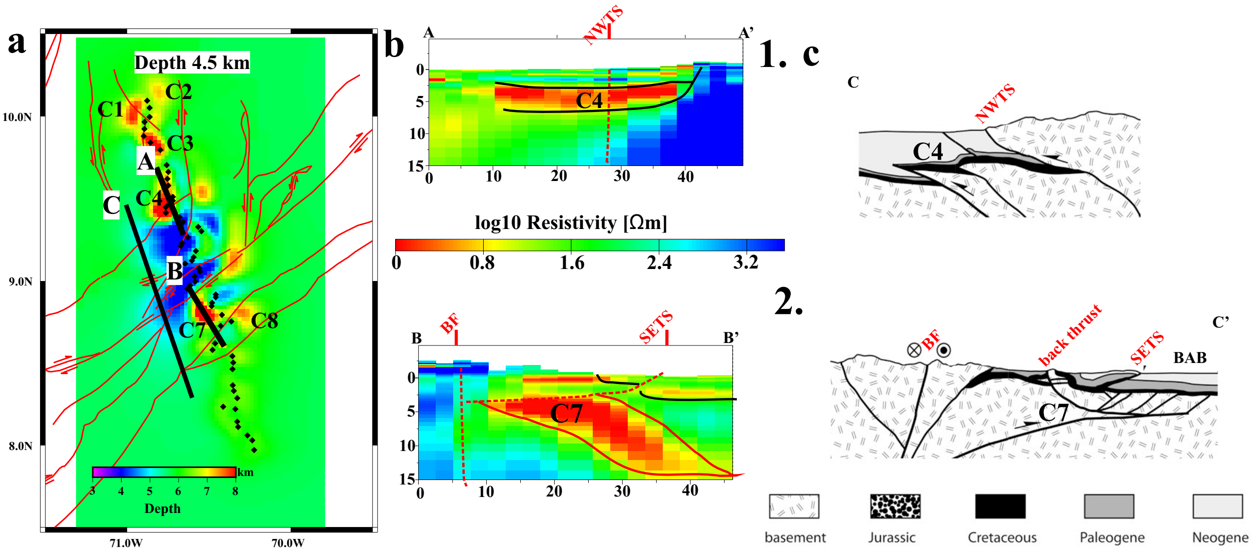

Figure 4.29.: (a) Horizontal slice of the 3D preferred model (Fig. 4.4) at 4.5 km depth, (b) 2 profile sections depicting conductive anomalies C4 and C7, and (c) structural model of the central part of the MA (not to scale) (modified from Erikson *et al.*, 2012). In 3D profiles: dotted red lines indicate interpreted fault planes, red lines detachment surfaces and solid black lines interpreted basin depth.

Conductor C7 may represent the imaging of a tectonic wedge along with a back-thrust surface. Tectonic or intracutaneous wedges have been identified by several authors (e.g. Audemard & Audemard, 2002; Duerto *et al.*, 2006; Erikson *et al.*, 2012) as a deformation structure resulting from the oblique convergence of the Caribbean Plate with the South American Plate. The back-thrust extent along the axial part of the MA south to the BF, thus, a similar conductive structure is observed to the east of C7 in Figures 4.27 and 4.26 (C8 in profiles DD' and CC', respectively); however, the eastern extent is located in an area of low resolution.

Analysis of the shallow structures shows that their shape, extent and low resistivity resulted from an interplay between different factors. The active tectonic processes in the MA fostered the formation of several structures associated with the stress regimes. Heavy fracturing and re-mineralization processes along fault planes and detachment surfaces contribute to the formation of low resistivity anomalies. Particularly, C7 is a compelling case of a sizeable conductor that may be functioning as a pathway for surface fluids.

The amount of shortening and wrenching at the MA necessitate that the majority of strike-slip offset may be distribute internally and along its flanks (Erikson *et al.*, 2012). The structural complexity of the near-surface structures in the 3D model may partially support this theory. However, there are clear differences between the 3D inversion models and the structural model (e.g. NWTS in Fig. 4.29). Although the structural models are not drawn to scale, the observed differences indicate that an inversion with increased resolution to the near-surface structure (i.e. inversion of lower periods, smaller horizontal and vertical cell size) may be needed.

Deep and off-profile conductors related to the Valera fault, the Boconó fault systems and the Trujillo block, conductors C5, C6 and C9

Possibly the most relevant structure resulting from the modelling of the Venezuelan MT data set is the conductor labelled C9. This conductor is the most sizeable anomaly recovered, its location at great depth in the 2D inversion models and to the east of the profile in the 3D inversion models required an in-depth analysis of its influence in the MT station and its interconnection with other structures.

The sensitivity test showed that conductor C9 influences approximately 30 sites (0014 - 0045) mostly at long periods (>100 s) in both 2D and 3D inversion models. MT theory explains that the induction range widens with increasing period. This widening means that the conductive structure must be located at greater depth, at a lateral distance from the stations, or a combination of both. The location at a lateral distance is supported by the IVs, which indicate a conductive feature east to the profile particularly for periods larger than 10 s. However, its exact position is poorly resolved as there is no station coverage. Conductor C9 is partially responsible for geoelectrical strike of the central section, subparallel to profile (Fig. 3.12b), and the complex dimensionality of the central section.

To further test the effect of conductor C9 in the dataset, several synthetic datasets from 3D models were generated (e.g. Fig. 4.15b, c and d) including a conductive structure to the east of the profile testing different conductivities, depths, thickness and extents, and using different fault systems as limits for the structure.

Comparison of the preferred 2D and 3D inversion models of measured and synthetic data (Figs. 4.21, 4.2b, 4.4, and Figs. 4.17, 4.18, respectively) shows that a simplified model including a flat off-profile conductive anomaly ($\rho = 1\,\Omega m$) limited by the VF and BF (see Fig. 4.16) could simulate the results obtained for the inversion of the measured data. Moreover, they indicate that C9 is unequivocally related to this off-profile structure, modelled after the NE displacement of the Trujillo Block, more specifically to its detachment surface. According to Dhont *et al.* (2012), this block is limited by the BF and the VF, and has a detachment surface at about 15 km depth.

The motion of the Trujillo block is accompanied with widespread extension towards the NE accommodated by normal faults (Dhont *et al.*, 2012). These normal faults (e.g. the Tuñame fault - TF) cause the Trujillo Block to split into smaller micro blocks at its south-western termination

(Fig. 1.6b). Listric faulting and fracturing in the south-western part of the block (at the connection at surface between the BF and VF) may decrease the resistivity of the subsurface, further limiting the resolution of the model to deep conductive structures in this area.

The Trujillo block is also divided into two major structures in N-S direction by the Burbusay Fault (BUF), which was an active structure during the Plio-Quaternary (Backé *et al.*, 2006). Conspicuously, under the surface expression of the BUF and BF, C9 reaches its lowest resistivity and widest extent (Fig. 4.30a), showing that C9 not only partially represent the BUF but also the connection between the fault planes of the BUF and BF.

To further study the deep connection between conductive anomalies under the MA, Figure 4.30 presents a series of interpreted sections from the preferred 3D model across the VF, BF and the detachment surface of the Trujillo Block, namely conductors C5, C6 and C9.

In section AA' (Fig. 4.30b), conductor C6 splits the deep root of the MA (R2 and R3). Conductors C5 and C6 show their lowest resistivity at 10-12 km depth. Section BB' (Fig. 4.30c), that cross-cuts the conductor C9 at its centre, shows a path of low resistivity at 10 km depth approximately (black ellipse), where C6 meet with conductor C9.

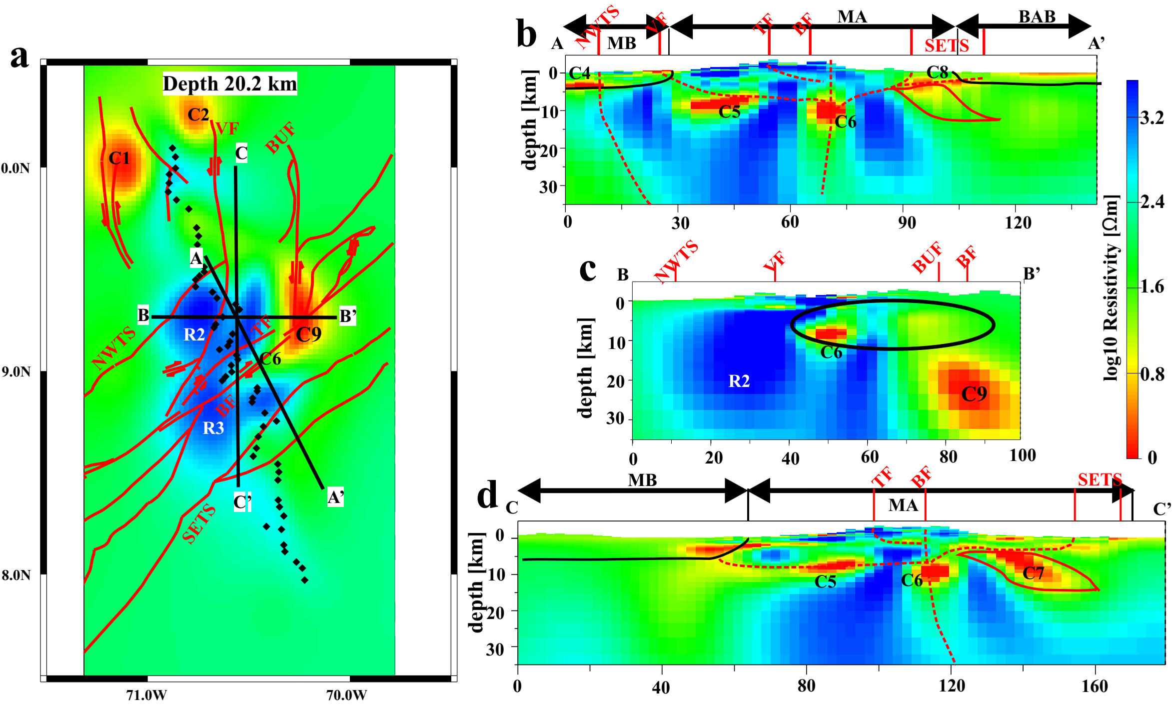

Figure 4.30.: Comparison of interpreted conductive anomalies with historical seismicity. Showing (a) horizontal slice of the 3D preferred model (Fig. 4.4) at 20.2 km depth and (b) to (e) interpreted profiles across the MA. Black lines in (a) depicts the location of the profiles. Black dots represent projected earthquakes 5 km wide. Marked features are described in text.

Although the preferred 3D inversion model show no explicit connection between C5 and C9, the 3D inversion models of synthetic data (Fig. 4.24) demonstrated that the structures connection is also characterized by low resistivity. Thus, the lowest resistivities in the north-south section CC' of C5 and C6 (Fig. 4.30e) must indicate the connection between the fault systems and the detachment surface, in an interconnected system (red dotted line). Mazuera *et al.* (2019) using wide-angle seismic 150 km to the north-east of the study area also map the BF to 40 km depth and identify a shallow low-angle subduction (~10–12°) of the Caribbean slab under the South American Plate.

Based on the interpretation of the connection between conductors C5, C6 and C9, one could speculate that the BF (C6) is a pathway for fluids to reach the detachment surface of the Trujillo Block (C9) and the VF (C5).

High conductivity crustal anomalies are often associated to the presence of fluids. Compressional tectonic settings, may favour laterally extensive fluid reservoirs formed by the arrest of upward propagating porosity waves at permeability or strength discontinuities (Connolly, 1997). Furthermore, greater fluid interconnection and reduction of resistivity in the strike-slip direction is expected in highly transpressional orogens (Wannamaker *et al.*, 2004).

The tectonic settings of western Venezuela seem to promote the formation of fluid reservoirs and fluid interconnection. In this sense, the detachment of the Trujillo block could provide a pathway for fluids, which may originate from re-mineralization processes associated with the shallow subduction of the Caribbean plate in north-western Venezuela. The tectonic escape of the Trujillo Block may function as a local crustal extension process, allowing the formation of a low resistivity zone. This zone signals the link between the main fault systems (BF and VF) in the MA and the detachment surface of the Trujillo Block, showing that deep-reaching fault systems of the area (e.g. the NWTS, the VF and the BF) may even provide pathways for fluids towards the surface. A combination of these factors could explain the observed anomalies alignment along with the fault planes of the BF (C6 E-W), VF (C5 N-S) and BUF (partially C9?) at several depths.

The MT inversion models seem to agree mostly with floating orogen model (Monod *et al.*, 2010) for the formation of and tectonic evolution of the MA. The MT data and inversion models put a strong emphasis on the relevance of the tectonic escape of the Trujillo block and fluids flow, possibly from the subducting Caribbean slab, in the structural evolution and tectonic processes in western Venezuela.

5. General conclusions and outlook

The MT profile acquired across the Mérida Andes (MA), from the central part of the Barinas - Apure (BAB) and into the Maracaibo (MB) basins, resulted in the first images of the deep electrical conductivity structure of the subsurface of western Venezuela. The dataset was strongly affected by several sources of EM noise that could not be avoided. Therefore, a combination of data improving techniques and processing approaches, including data filtering, data pre-selection per frequency, single site, remote processing and robust statistics were applied to obtain smooth response curves that could be analysed and inverted.

The dimensionality and directionality analyses of the MT data suggested that the northern and southern parts of the dataset are generally consistent with 1D/2D assumptions. However, 3D structures are present in the MA section. Since MT stations were distributed along a single profile line, 2D and 3D inversion schemes were applied. Consequently, thorough investigation of the effects and influence of off-profile and 3D structures on both 2D and 3D resistivity profiles was a key component of the interpretation workflow.

The finite elements code MARE2DEM (Key, 2016; Key & Ovall, 2011) was used to solve the 2D inverse problem, whose unstructured grid scheme can represent well the topography in profile direction. The 2D inversion models emphasize the TE- and TM- modes' phases as they are not affected by galvanic distortion. While the apparent resistivities, particularly for the TE mode, were down-weighted. Other authors (e.g. Meqbel, 2009; Sass *et al.*, 2014; Muñoz *et al.*, 2018) used similar approaches in complicated topographic and geological settings. The induction vectors (IV) are generally small and poorly resolved for the basins, becoming larger and strongly influenced by off-profile structures in the MA. The IVs' behaviour resulted in over smoothed near-surface structures and generally larger misfit of the other responses in the 2D inversion models. Therefore, the IVs were excluded from the 2D inversion.

The 3D inverse problem was solved employing the finite difference 3D inversion code ModEM (Meqbel, 2009; Egbert & Kelbert, 2012). The inversion's main focus was the fitting of the vertical magnetic transfer functions, the off-diagonal elements of the impedance tensor, and the long period data of the diagonal elements of the impedance tensor.

The 2D inversion of the measured data could recover the BAB, and MB sedimentary basins largely considered the most 2D sections of the study area. However, 3D effects resulting from the projection of off-profile structures distorted and exaggerated the recovered anomalies. The limitations of the 2D inversion models stressed the need to generate 3D inversion models.

In general, the 3D inversion models reproduced the area's structural complexity better than the 2D models, recovering similar structures for the BAB and MB sedimentary basins and showing superior modelling of the structures under the MA the off-profile features. The modelled conductive anomalies labelled in the 2D and 3D inversion models were subjected to a sensitivity test, that confirmed that these conductive anomalies are necessary to generate model responses that closely resemble the measured data.

Nevertheless, the 2D inversion of a 3D influenced dataset, and the 3D inversion of a dataset distribute along a single profile present serious limitations to the resulting models' resolution. Thus, the 2D and 3D inversion models' depth and lateral resolution were tested using 3D conceptual models, containing simplified regional geological and tectonic structures. These included all regional sedimentary basins, the Caribbean Sea, main fault systems, and eventually a significant off-profile conductor associated with the Trujillo Block.

The analysis of the 2D and 3D inversion of synthetic data from conceptual models is a fundamental part of this thesis. The obtained models and responses highlighted the limitations of the inversion approaches and the resolution of the measured data inversions and greatly improved the recovered structures' interpretation.

In the case of the 2D inversions, synthetic data inversions found that obliquely striking fault systems can also appear as artefacts or strongly distorted. Horizontally elongated structures obliquely crossing the profile can generally appear with a vertical and/or horizontal offset in the 2D sections. Due to its limited resolution to these structures, 2D inversion tends to overestimate their conductivity to reproduce its lateral extension, partially explaining the fault systems' generally low resistivity values in our 2D inversions. The uneven station coverage combined with the regularization (smoothing) can foster separate bodies within originally contiguous layers (e.g. the BAB). These results clearly emphasize the importance of off-profile structures on MT data, particularly when 2D interpretation tools are used.

The 3D inversions of synthetic data confirmed that inversion of single profile data could provide a meaningful picture of the subsurface geometry beneath the profile. However, the resolution to off-profile features is rather limited. The lateral resolution was limited to 15 km away from the stations, from this threshold recovered anomalies tend to dip or shift in depth. The synthetic data inversion showed that unconstrained off-profile features, particularly towards the end of the profile, can result in artefacts in the 3D models. The structure's connection to the surface cannot be recovered due to an interplay of the inverted period range, uneven stations distribution, and the subsurface's resistivity.

The 2D inversion models supported by synthetic data inversion provided a clear image of the dataset's 2D sections. They helped to draw definitive conclusions on the nature of the off-profile features. The 3D inversion confirmed the results obtained on the 2D models and truly showed the structural complexity of the study area. The use of both methodologies in this thesis complemented the geological interpretations and shed light over the limitations and strengths of the MT Venezuelan dataset, which could be applied to similar datasets in other areas.

Shallow resistivity structures

The basins' depths along the profile (5 km for the BAB and 10 km for the MB) are consistent with results from seismic studies (Callejón & von der Dick, 2002; Chacín *et al.*, 2005; Escalona & Mann, 2006b,a). Conductive anomalies were related to the main fault systems. The lateral transition of conductors and resistors in the MB represents deformation (folding of sedimentary sequences) caused by the NE tectonic escape of the North Andean Block (NAB).

The MA's central part consists of Cenozoic and Mesozoic igneous-metamorphic rocks, recovered in the models as generally resistive material. Zones of high conductivity in the MA often correlate with major fault systems, forming an interconnected system of sub-vertical to sub-horizontal fault planes. The north-western thrust system (NWTS), located at the transition between the conductive MB and the resistive MA, can be interpreted from the surface to a depth larger than 30 km, representing the MA's northern limit. The centre of the anomalies related to the Valera (VF) and Boconó (BF) faults at 12 km depth represent a detachment plane at mid-crustal levels, consistent with existing geodynamic models (e.g. Audemard & Audemard, 2002; Duerto *et al.*, 2006; Dhont *et al.*, 2012; Monod *et al.*, 2010).

To the south of the BF, a southward deepening conductor (C7) is correlated with a tectonic wedge and a back-thrust surface extending to the east. The prominence of this structure in the 3D models indicates its relevance to explaining the formation and current distribution of the MA's fault systems.

The shallow conductors (>5 km depth) related to the fault systems indicates a pathway for groundwater circulation and the accumulation of clay sediments in fault gauges.

Deep and crustal structures and their tectonic implications

The 3D preferred models show under the MB (>20 km) deep resistive structures (R1 and R2) split by a conductive zone. This zone correlates spatially with the location of a gravimetric low to the north of the MA (e.g. Hospers & VanWijnen, 1959; Folinsbee, 1972). Bouguer gravity anomalies of -160 mGal and -150 mGal in the Maracaibo trough adjacent to the MA front (Bonini, 1978) indicate 25 km of shortening on this flank along a low-angle, south-east dipping thrust (Kellogg & Bonini, 1982). Arnaiz-Rodríguez & Audemard (2014) suggest a SE tilt of the Maracaibo Triangular Block (MTB) under the MA which is partially responsible for the MA's ongoing uplift. Assuming that the aforementioned conductive zone represents the MTB, its apparent subduction under R2 is consistent with the SE tilt of the MTB due to the significant subsidence of the lithosphere caused by the MA. The strong contrast between the resistive MA ($>500\Omega m$) and the conductive zone ($<100\Omega m$) is interpreted as the NWTS, which functions as a detachment surface for the uplift of the MA carrying deformation to lower crust.

A significant finding in the preferred 2D models was a conductive zone 60 km long and 20 km thick below 40 km depth. This conductive zone is a projection of an off-profile feature to the east, confirmed by the IVs and conceptual models' inversion. The 3D inversion model recovered an off-profile conductor to the east limited and connected to conductive anomalies interpreted as the BF and VF.

Nevertheless, the models included in this thesis show that it is reasonable to link the associated off-profile conductivity anomaly with the Trujillo Block, more specifically with a detachment surface resulting from the north-eastward tectonic escape of this block. The Trujillo block is bounded laterally by both the BF and VF systems and is assumed to have a detachment level at mid-crustal depth (15 km) (Dhont *et al.*, 2012). This detachment surface is then related to the recovered conductor C9, and its connection with the fault system represented C5 and C6 at 12 km depth in the 3D preferred model.

The Trujillo block plays a crucial role in recent geodynamic models developed for north-western Venezuela (e.g. Audemard & Audemard, 2002; Monod *et al.*, 2010), as it could be absorbing one-quarter of the deformation related to the oblique convergence in the MA (e.g. Backé *et al.*, 2006; Dhont *et al.*, 2005; Monod *et al.*, 2010). High conductivities in active tectonic zones is often associated with fluids and hydrous minerals (e.g. Unsworth, 2010; Ritter *et al.*, 2005; Meqbel *et al.*, 2014). The low resistivity associated with the Trujillo Block detachment surface could originate from mineralized shear-planes or fluids, possibly from the Caribbean plate's subduction. However, more MT data with better aerial coverage would be required to confirm this speculation.

Far more resolved are the zones of high conductivity associated with the fault systems of the MA. The MA's most prominent tectonic features are the 500 km long BF and the 240 km long left-lateral strike-slip VF. These fault systems likely provide pathways for meteoric water or fluids generated at depth since drainage and alluvial deposits are reported along the strike of the

BF (Audemard & Audemard, 2002). Clay minerals in fault gauges may also contribute to the strike-slip faults' high conductivity (Unsworth *et al.*, 1997).

Based on the 3D inversion models, the BF is interpreted to a depth of 35 km, similar to the 40 km interpreted from seismic refraction and shear wave splitting studies on the northern section of the MA (Masy *et al.*, 2011; Mazuera *et al.*, 2019). This interpretation of the BF is considerably deeper than presented in structural models (e.g. Rod, 1956; Jácome *et al.*, 1995; Audemard & Audemard, 2002; Monod *et al.*, 2010; Arnaiz-Rodríguez *et al.*, 2011). Nevertheless, the deformation related to the BF could extend deeper than the lower crust, or much deeper than the crust-mantle boundary, estimated to be approximately 50 km deep (Niu *et al.*, 2007). This result indicates that tectonic models attempting to explain the formation and current geodynamics of the MA needs to be adapted to include a deeper BF and to give a larger relevance to the block interaction in north-western Venezuela, particularly the role play by the escape of the Trujillo Block in the ongoing deformation.

Although the asymmetrical structural models, particularly the NW continental subduction model, are consistent with the deformation structures revealed by the 2D and 3D preferred models, the depth of the Trujillo block's BF and relevance in the inversion models are only consistent with the orogenic float model (Monod *et al.*, 2010).

The orogenic float model for the MA (Monod *et al.*, 2010) based on the orogenic float concept for transpressional orogens (Oldow *et al.*, 1990) describes western Venezuela's current settings as floating blocks or orogens, whose current deformations are controlled by the relative movement of the Caribbean and South American plates. The BF is considered an upper crustal fault that connects to a mid-crustal detachment level, which allows the orogen to float within the lithosphere. Balanced sections crossing the MA suggest 40 km of shortening in the southern part of the belt and 30 km in the northern part. The difference of 10km of shortening between both cross-sections is attributed to the Trujillo block's escape.

Outlook of the MT Venezuelan dataset

In the framework of the Geosciences of the Mérida Andes (GIAME) project, the integration of different geophysical methods is envisioned. Datasets of gravimetric, magnetic, seismic and other geophysical methods measured along profiles roughly at the same location than the magnetotelluric profile presented in this thesis are available for integration. The integrated interpretation or inversion could constrain structures in- and off-profile, resulting in more accurate models.

The apparent limitation of the 3D inversion models to effectively recover near-surface structures could be overcome by employing different inversion parameters, including lower periods from the data and decreasing the vertical and horizontal cell size of the starting models. Detailed modelling of the near-surface structures is out of the scope of this study. Nonetheless, it could benefit the integration with other geophysical datasets.

Since the data distribution along a single profile line greatly limits the resolution of the 3D inversion models, two steps could be taken to increase the current model results' confidence. On the one hand, the 3D inversion of the dataset employing an inversion code with a different approach (e.g. a finite elements 3D inversion) would allow for comparing the recovered structures. On the other hand, the acquisition of more MT data with a more areal distribution could complement the current dataset, particularly to the profile's east. Better station coverage above the Trujillo Block would result in better resolution to this structure.

Appendix A.

Annexes

A.1. Two-dimensional inversion

Figure A.1 shows the apparent resistivity and phases of the TE and TM mode for the rotated to strike dataset and the resulting modelled data as pseudo-sections. The phases (φ) of both modes and the TMρ_a are quite similar between observed and modelled data in terms of variations of magnitudes, as expected from the low RMS values. The modelled TEρ_a of the northern section, however, shows a higher resistivity to the north from short to medium periods (Fig A.1a) and lower resistivity in general for the long periods. Similarly, on the southern section (Fig A.1b) the modelled responses are generally less resistive than the observed ones. This result is expected given the large error floor set on the TEρ_a and the tight error on the other transfer functions.

The analysis of the RMS and data responses show that the modelled responses closely reproduced the observed results, showing that the error floor settings are effective in spite of the large error floor set on the TEρ_a.

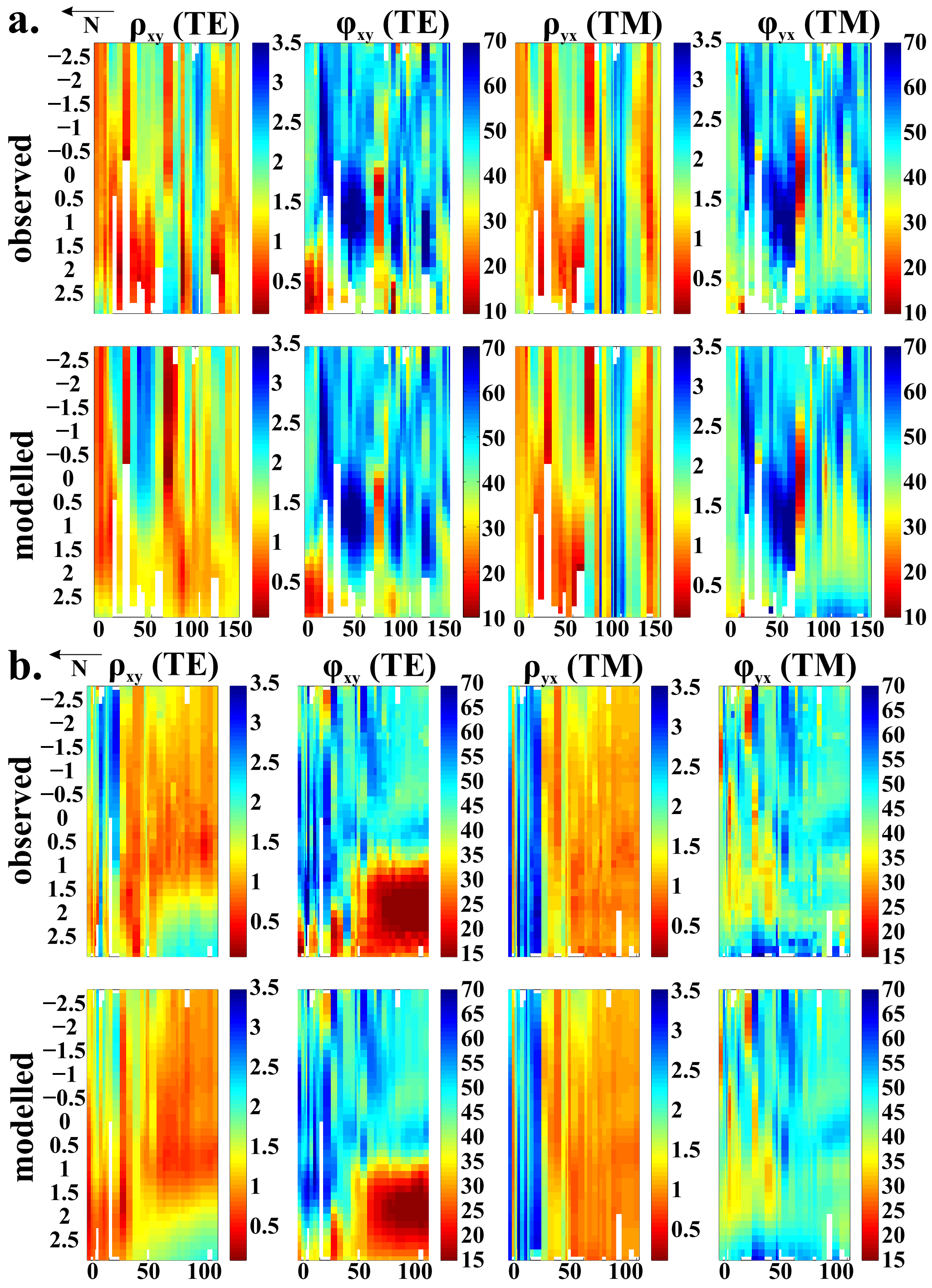

Figure A.1.: Pseudo-sections of the decoupled TE and TE apparent resistivity (ρ_a) and phases (φ) for (a.) the northern (Fig. 4.2a) and (b.) the southern (Fig. 4.2b) sections.

A.2. Three-dimensional inversion

Pseudo-sections of the measured and modelled data

Figure A.2a shows the ρ_a per component of Z. As expected given the tight error settings, the modelled responses from ρ_{xy} and ρ_{yx} closely resemble the observed data in magnitude and size of the anomalies. Both presenting a conductive anomaly at long periods to the north, followed by a more resistive one towards the centre of the profile, where the stations above the MA are located, to finally present another conductive anomaly towards the south. These major anomalies are possibly related to the geological structures at the surface namely the MB, MA and BAB, respectively (see the bottom of Fig. A.2 for a spatial relation with surface structures). However, the main diagonal elements ρ_{xx} and ρ_{yy} seem to show a similar trend but differ on more than two orders of magnitude for the short periods, and less than 2 for the long ones. This is also related to the error floor scheme, which tend to be looser at short periods and tighter at long ones. The rationale behind it is that the main diagonal components contain more information when their magnitude is closer to the off diagonal components, this occurred generally at long periods, thus the tighter error.

The phases (Fig. A.2b) show a good correlation between observed and modelled data, particularly for the off-diagonal elements, with similar anomalies en in term of extension and phase. Moreover, they also show a good match with Figure A.2a. In general, a more resistive medium should show phases below 45°, and conductive ones above.

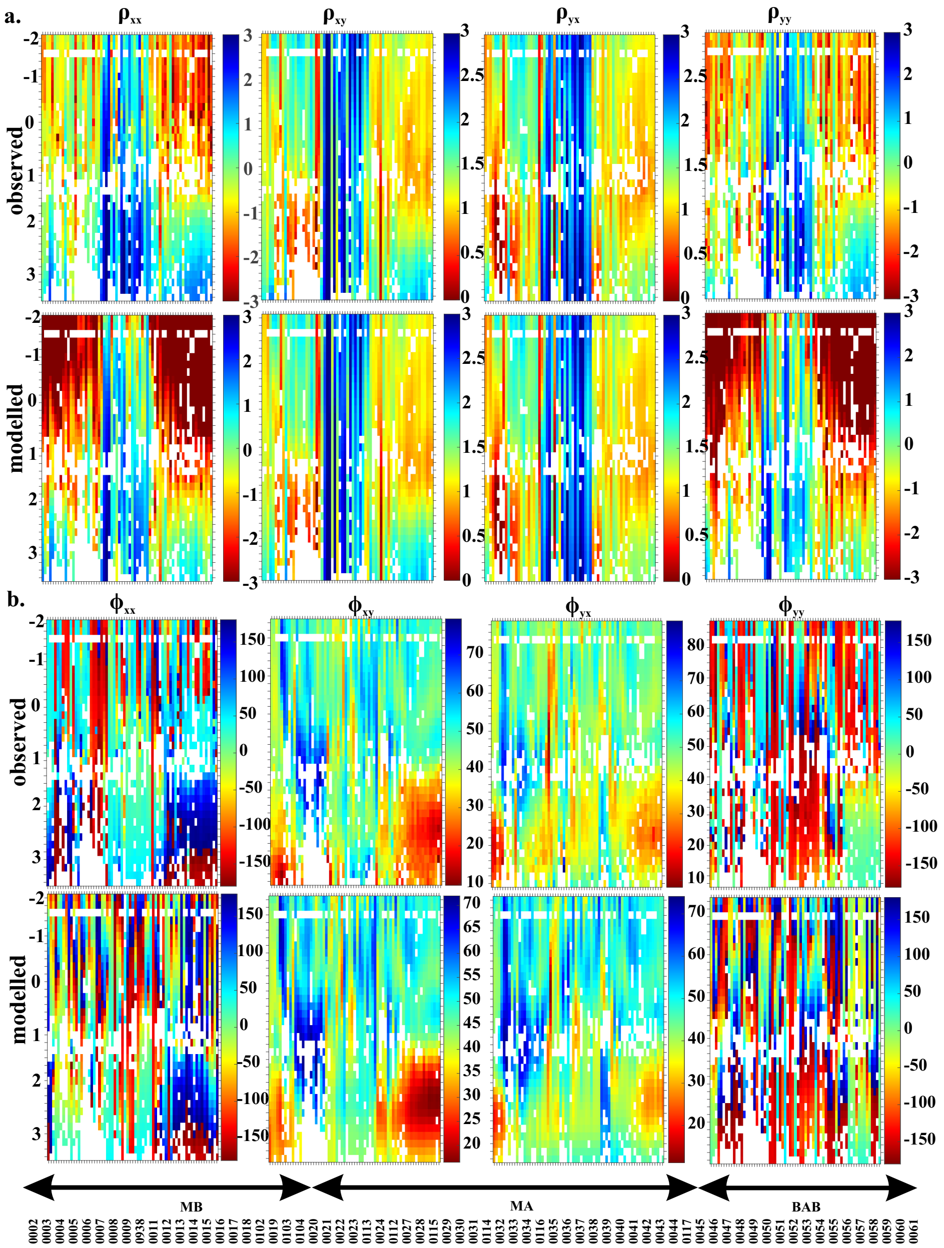

Figure A.2.: Pseudo-sections of each component of the impedance tensor presented as (a) apparent resistivity (ρ_a) and (b) phases (φ) for observed data (top) and modelled data (bottom), for the preferred model (Fig. 4.4). The y-axis represent periods in logarithmic scale and the x-axis the stations locations, as presented below the sections in relation to the main structures.

Resolution test results for all labelled structures

Figures A.3 show the normalized by the error floor residual between the preferred model and the modified models responses RMS as a percentage of variation colour coded on a logarithmic scale. The blue colours indicate high variation between the models, showing that the modified structure is necessary for the model misfit. In contrast, red colours indicate low variations; thus, the structure may not have a considerable influence on the model at large. The plots are divided into six different response types, the four components of the impedance tensor (Z_{xx}, Z_{xy}, Z_{yx} and Z_{yy}) and the two elements of the vertical magnetic transfer function (T_x and T_y) and between high frequency (HF <1 Hz) and long periods (LP > 1 s). The responses are also grouped in northern (N), central (C) and southern (S) sections, red, green and blue coloured in Fig. 4.1, respectively.

The independent analysis of structures (Fig. A.3) shows that even slight variations in the bulk resistivity of the structures affect the modelled responses. Structures labelled C1 to C4 show a quite local influence, focused on the northern section and in the entire period of Z_{xy} and Z_{yx}, excepting C2 that does not show a considerable variation. Conductor C5 seems to have a considerable effect in the northern and central section overall responses, but a limited influence on the southern section. Whereas, conductors C6 to C8 have a considerable influence on the off-diagonal components of Z mostly for the central and southern section. Conductor C9 shows its lager variation on the off-diagonal components of Z and the long periods of Ty in the central section, while C10 influences all responses on the souther section.

Conductors C1 to C5 showed variation regardless of the modified model, whereas C6 to C9 only when substituted by a more resistive structure, indicating in all cases that a conductor is needed in the area.

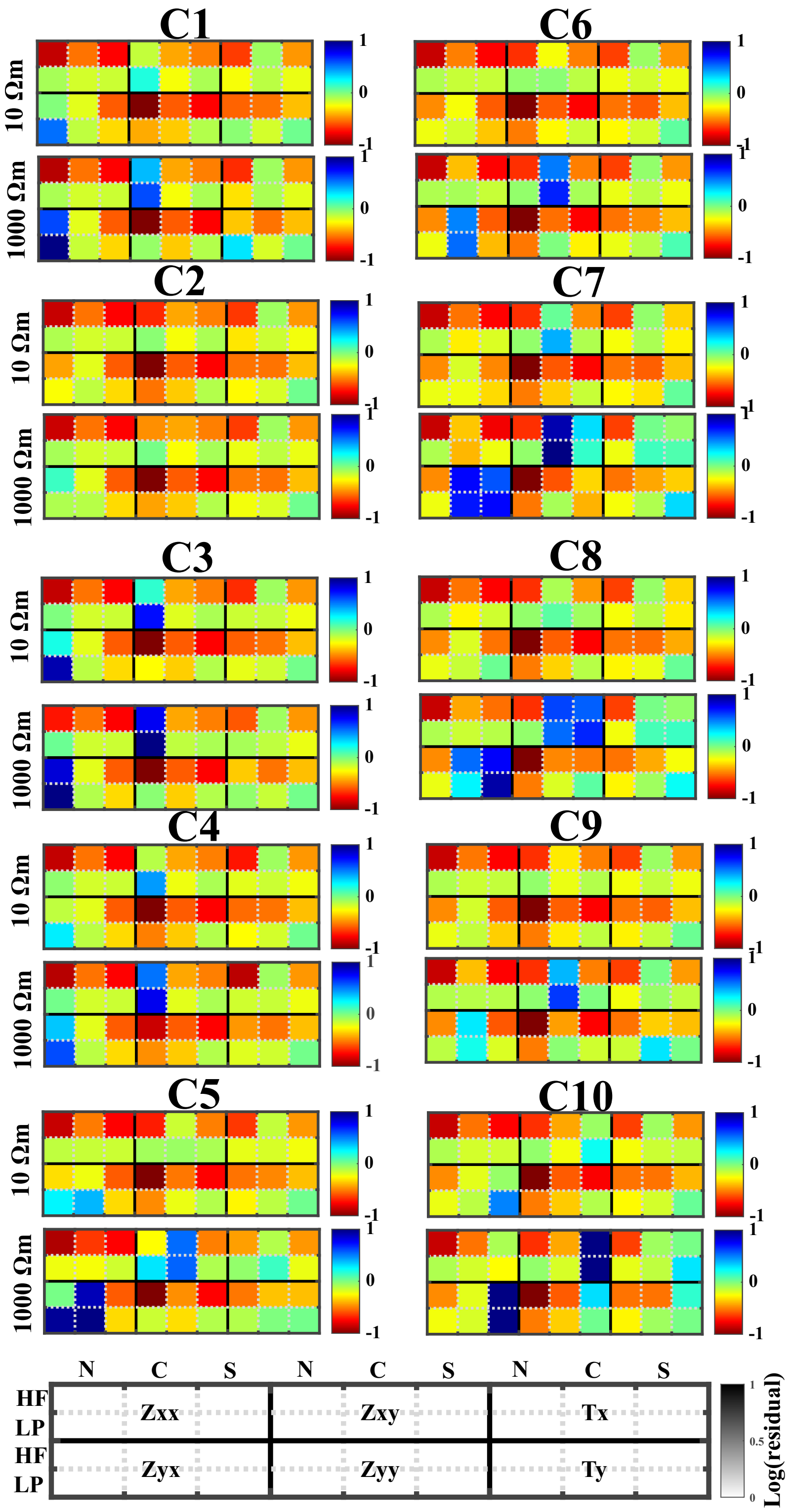

Figure A.3.: Analysis of the RMS normalized residuals between the preferred model and the modified models for each labelled conductive structure (see Fig. 4.4). The blue colours represent large variations between models. The lower inset show the distribution of the data. See text for explanations.

Bibliography

Adao, F. 2015. *The electrical resistivity of the Posidonia black shale - from magnetotelluric exploration to rock samples*. Ph.D. thesis, Free University Berlin.

Amante, C., & Eakins, B.W. 2009. *ETOPO1 1 Arc-Minute Global Relief Model: Procedures, Data Sources and Analysis*.

Arnaiz-Rodríguez, M. S., & Audemard, F. 2014. Variations in elastic thickness and flexure of the Maracaibo block. *Journal of South American Earth Sciences*, **56**(dec), 251–264.

Arnaiz-Rodríguez, M. S., Rodríguez-Millán, I., & Audemard, F. 2011. Análisis gravimétrico y flexural del occidente de Venezuela. *Revista mexicana de ciencias geológicas*, **28**(3), 420–438.

Audemard, F., Singer, A., Acosta, L., & González, R. 2007a. La falla de Burbusay (bloque de Maracaibo, Venezuela occidental): accidente activo sinestral submeridiano. *Page 87 of: Memorias del IX CONGRESO GEOLÓGICO VENEZOLANO*.

Audemard, F, Ollarves, R., Bechtold, M., Díaz, G., Beck, C., Carrillo, E., Pantosti, D, & Diederix, H. 2008. Trench investigation on the main strand of the Boconó fault in its central section, at Mesa del Caballo, Mérida Andes, Venezuela. *Tectonophysics*, **459**(1-4), 38–53.

Audemard, F. A. 1999. Morpho-structural expression of active thrust fault systems in humid tropical foothills of Colombia and Venezuela. *Zeitschrift fuer Geomorphologie*, **118**(1), 18.

Audemard, F. A. 2003. Geomorphic and geologic evidence of ongoing uplift and deformation in the Merida Andes, Venezuela. *Quaternary International*, **101-102**(jan), 43–65.

Audemard, F. A. 2014. Active block tectonics in and around the Caribbean: A review. *Chap. 2, pages 29–77 of:* Schmitz, M., Audemard, F., & Urbani, F. (eds), *El Límite Noreste de la Placa Sudamericana - estructuras litosféricas de la superficie al manto*. Fac. Ing. UCV, ComitÃ© Editor Libros y MonografÃas.

Audemard, F. A., Singer, A., Rodrıguez, J. A., & Beltrán, C. 1994. Definición de la traza activa del sistema de fallas de Oca–Ancón, Noroccidente de Venezuela. *VII Congr. Venezolano Geofısica, Caracas, Venezuela*, 43–51.

Audemard, F. A., Pantosti, D., Machette, M., Costa, C., Okumura, K., Cowan, H., Diederix, H.,

& Ferrer, C. 1999. Trench investigation along the Mérida section of the Boconó fault (central Venezuelan Andes), Venezuela. *Tectonophysics*, **308**(1-2), 1–21.

Audemard, F. A., Machette, M. N., Cox, J. W., Dart, R. L., & Haller, K. M. 2000. *Map and database of Quaternary faults in Venezuela and its offshore regions*.

Audemard, F. A., Romero, G., Rendon, H., & Cano, V. 2005. Quaternary fault kinematics and stress tensors along the southern Caribbean from fault-slip data and focal mechanism solutions. *Earth-Science Reviews*, **69**(3-4), 181–233.

Audemard, F. A., Carrillo, E., & Beck, C. 2007b. Fieldtrip Guidebook. *Page 77 of: International Workshop on "Blind dip-slip faulting and strain partitioning in an active orogen: The Mérida Andes case, Venezuela"*.

Audemard, F. E. 1992. *Tectonics of western Venezuela*. Ph.D. thesis, Rice University, Houston, Texas. USA.

Audemard, F. E., & Audemard, F. A. 2002. Structure of the Mérida Andes, Venezuela: relations with the South America–Caribbean geodynamic interaction. *Tectonophysics*, **345**(1-4), 1–26.

Audemard, F.A., Singer, P. A., Soulas, J-P., & FUNVISIS Earth Sciences Deparment, Neotectonics Section. 2006. Quaternary Faults and Stress Regime of Venezuela. *Rev. Asoc. Geol. Argent.*, **61**(4).

Backé, G., Dhont, D., & Hervouët, Y. 2006. Spatial and temporal relationships between compression, strike-slip and extension in the Central Venezuelan Andes: Clues for Plio-Quaternary tectonic escape. *Tectonophysics*, **425**(1-4), 25–53.

Bahr, K. 1988. Interpretadon of the magnetotelluric impedance tensor: regional induction and local telluric distortion. *Journal of Geophysics*, **62**, 119–127.

Becken, M., & Burkhardt, H. 2004. An ellipticity criterion in magnetotelluric tensor analysis. *Geophysical Journal International*, **159**(1), 69–82.

Becken, M., & Ritter, O. 2011. Magnetotelluric Studies at the San Andreas Fault Zone: Implications for the Role of Fluids. *Surveys in Geophysics*, **33**(1), 65–105.

Bezada, M. J., Levander, A., & Schmandt, B. 2010. Subduction in the southern Caribbean: Images from finite-frequency P wave tomography. *Journal of Geophysical Research*, **115**(B12).

Bibby, H. M. 1986. Analysis of multiple-source bipole-quadripole resistivity surveys using the apparent resistivity tensor. *Geophysics*, **51**(4), 972–983.

Boerner, D. E., Craven, J. A., Kurtz, R. D., Ross, G. M., & Jones, F. W. 1998. The Great Falls Tectonic Zone: suture or intracontinental shear zone? *Canadian Journal of Earth Sciences*, **35**(2), 175–183.

Bonini, W. E. 1978. Anomalous crust in the eastern Venezuela Basin and the Bouguer gravity anomaly field of northern Venezuela and the Caribbean borderland. *Geol. Mijnbouw*, **57**(2), 117–122.

Booker, J. R. 2013. The Magnetotelluric Phase Tensor: A Critical Review. *Surveys in Geophysics*, **35**(1), 7–40.

Bouysse, P. 1988. Opening of the Grenada back-arc Basin and evolution of the Caribbean plate during the Mesozoic and early Paleogene. *Tectonophysics*, **149**, 121–143.

Brasse, H. 2011. Electromagnetic Images of the South and Central American Subduction Zones. *Pages 43–81 of:* PetrovskÃ½, E., Ivers, D., Harinarayana, T., & Herrero-Bervera, E. (eds), *The Earth's Magnetic Interior*. IAGA Special Sopron Book Series, vol. 1. Springer.

Burke, K. 1988. Tectonic Evolution Of The Caribbean. *Ann. Rev. Earth Planet. Sci.*, **16**, 201–230.

Burke, K., Fox, P. J., & Şengör, A. M. C. 1978. Buoyant ocean floor and the evolution of the Caribbean. *Journal of Geophysical Research: Solid Earth*, **83**(B8), 3949–3954.

Byrne, D. B., Suarez, G., & McCann, W. R. 1985. Muertos Trough subduction-microplate tectonics in the northern Caribbean? *Letter to Nature*, **317**, 420–421.

Cagniard, L. 1953. Basic theory of the magnetotelluric method of geophysical prospecting. *Geophysics*, **1**(18), 605–635.

Caine, J. S., & Forster, C. B. 1999. Fault zone architecture and fluid flow: Insights from field data and numerical modeling. *Pages 101–127 of:* Haneberg, W. C., Mozley, P. S., Moore, J. C., & Goodwin, L. B. (eds), *Faults and Subsurface Fluid Flow in the Shallow Crust*. Whshington, DC: American Geophysical Union.

Calais, E., & Mann, P. 2009. A combined GPS velocity field for the Caribbean plate and its margins: AGU Fall Meeting. *In: Eos Trans. AGU*, vol. 90.

Caldwell, T. G., Bibby, H. M., & Brown, C. 2004. The magnetotelluric phase tensor. *Geophysical Journal International*, **158**(2), 457–469.

Callejón, A. F., & von der Dick, H. H. 2002. *Numerical identification of microseeps in surface soil gases of western Venezuela, and its significance for hydrocarbon exploration, in Surface exploration case histories: pplications of geochemistry, magnetics, and remote sensing*. AAPG Studies in Geology No. 48 and SEG Geophysical References Series No. 11. Chap. 15, pages 381–392.

Chacín, L., Jácome, M., & Izarra, C. 2005. Flexural and gravity modelling of the Mérida Andes and Barinas-Apure Basin, Western Venezuela. *Tectonophysics*, **405**(1-4), 155–167.

Chave, A. D., & Jones, A. G. (eds). 2012. *The Magnetotelluric Method*. Cambridge University Press.

Colletta, B., Roure, F., De Toni, B., Loureiro, D., Passalacqua, H., & Gou, Y. 1997. Tectonic inheritance, crustal architecture, and contrasting structural styles in the Venezuela Andes. *Tectonics*, **16**, 777–794.

Connolly, J. A. D. 1997. Devolatilization-generated fluid pressure and deformation-propagated fluid flow during prograde regional metamorphism. *Journal of Geophysical Research: Solid Earth*, **102**(B8), 18149–18173.

Constable, S. C., Parker, R. L., & Constable, C. G. 1987. Occam's inversion: A practical algorithm for generating smooth models from electromagnetic sounding data. *GEOPHYSICS*, **52**(3), 289–300.

Cruces-Zabala, J., Ritter, O., Weckmann, U., Tietze, K., & Schmitz, M. 2020. Magnetotelluric imaging of the Mérida Andes and surrounding areas in Venezuela. *Geophysical Journal International*, **222**(3), 1570–1589.

De Toni, B., & Kellogg, J. 1993. Seismic evidence for blind thrusting of the northwestern flank of the Venezuelan Andes. *Tectonics*, **12**(6), 1393–1409.

Dewey, J. W. 1972. Seismicity and tectonics of western Venezuela. *Bulletin of the Seismological Society of America*, **62**(6), 1711–1751.

Dhont, D., Backé, G., & Hervouët, Y. 2005. Plio-Quaternary extension in the Venezuelan Andes: Mapping from SAR JERS imagery. *Tectonophysics*, **399**(1-4), 293–312.

Dhont, D., Monod, B., Hervouët, Y., Backé, G., Klarica, S., & Choy, J. E. 2012. 3D geological modeling of the Trujillo block: Insights for crustal escape models of the Venezuelan Andes. *Journal of South American Earth Sciences*, **39**(nov), 245–251.

Duerto, L. 1998. *Principales zonas triangulares del Occidente de Venezuela*. M.Phil. thesis, School of Geology and Mines, Universidad Central de Venezuela.

Duerto, L., Escalona, A., & Mann, P. 2006. Deep structure of the Mérida Andes and Sierra de Perijá mountain fronts, Maracaibo Basin, Venezuela. *AAPG Bulletin*, **90**(4), 505–528.

Duncan, R. A., & Hargraves, R. B. 1984. Plate tectonic evolution of the Caribbean region in the mantle reference frame. *Geological Society of America Memoir*, **162**, 81–94.

Egbert, G. D., & Booker, J. R. 1986. Robust estimation of geomagnetic transfer functions. *Geophysical Journal International*, **87**(1), 173–194.

Egbert, G. D., & Kelbert, A. 2012. Computational recipes for electromagnetic inverse problems. *Geophysical Journal International*, **189**, 251–267.

Egbue, O., & Kellogg, J. 2010. Pleistocene to present North Andean "escape". *Tectonophysics*, **489**(1-4), 248–257.

Ego, F., Sébrier, M., Lavenu, A., Yepes, H., & Egues, A. 1996. Quaternary state of stress in the Northern Andes and the restraining bend model for the Ecuadorian Andes. *Tectonophysics*, **259**, 101–116.

Erikson, J. P., Kelley, S. A., Osmolovsky, P., & Verosub, K. L. 2012. Linked basin sedimentation and orogenic uplift: The Neogene Barinas basin sediments derived from the Venezuelan Andes. *Journal of South American Earth Sciences*, **39**(nov), 138–156.

Escalona, A., & Mann, P. 2003. Three-dimensional structural architecture and evolution of the Eocene pull-apart basin, central Maracaibo basin, Venezuela. *Marine and Petroleum Geology*, **20**(2), 141–161.

Escalona, A., & Mann, P. 2006a. An overview of the petroleum system of Maracaibo Basin. *AAPG Bulletin*, **90**(4), 657–678.

Escalona, A., & Mann, P. 2006b. Tectonic controls of the right-lateral Burro Negro tear fault on Paleogene structure and stratigraphy, northeastern Maracaibo Basin. *AAPG Bulletin*, **90**(4), 479–504.

Fialko, Y. 2004. Evidence of fluid-filled upper crust from observations of postseismic deformation due to the 1992Mw7.3 Landers earthquake. *Journal of Geophysical Research: Solid Earth*, **109**(B8).

Folinsbee, R. 1972. *The gravity field and plate boundaries in Venezuela*. Massachusetts Institute of Technology and Woods Hole Oceanographic Institution.

Freymueller, J. T., Kellogg, J. N., & Vega, V. 1993. Plate Motions in the north Andean region. *Journal of Geophysical Research: Solid Earth*, **98**(B12), 21853–21863.

Gamble, T. D., Goubau, W. M., & Clarke, J. 1979. Magnetotellurics with a remote magnetic reference. *Geophysics*, **44**(1), 53–68.

Garcia, R., & Campos, C. 1977. Evolución tectónica e historia geológica de la región de Valera-Escuqeu, Estados Trujillo y Zulia. *Pages 1825–1836 of: II Cong. Latino-Americano Geol., Caracas (1973)*, vol. 7. Bol. Geol. Publ. Espec.

Giraldo, C. 1985. Neotectónica y sismotectónica de la región de El Tocuyo-San Felipe (Venezuela centro-occidental). *Pages 2415–2451 of: VI Congreso Geológico Venezolano*, vol. 4. Sociedad Venezolana de Geólogos Caracas, Caracas.

González de Juana, C. 1972. *Introducción al estudio de la geología de Venezuela*. Caracas Tall. Gráf. del Congreso de la Repuública 1972.

González de Juana, C., Iturralde, J. M., & Picard, X. 1980a. *Geología de Venezuela y sus cuencas petrolíferas*. Vol. 1-2. Ediciones Foninves.

González de Juana, C., Iturralde, J. M., & Picard, X. 1980b. *Geología de Venezuela y sus cuencas petrolíferas*. Vol. 1-2. Ediciones Foninves.

Govers, R., & Wortel, M. J. R. 2005. Lithosphere tearing at STEP faults: response to edges of subduction zones. *Earth and Planetary Science Letters*, **236**(1-2), 505–523.

Gutscher, M. A., Malavieille, J., Lallemand, S., & Collot, J. Y. 1999. Tectonic segmentation of the North Andean margin: impact of the Carnegie Ridge collision. *Earth and Planetary Science Letters*, **168**, 255–270.

Hackley, P. C., Urbani, F., Karlsen, A., & Garrity, C. 2006. *Geological shaded relief map of Venezuela*. Tech. rept. U.S. Geological Survey.

Hall, S. A., Ghosh, N., Casey, J. F., & Burke, K. C. 1995. Age and formation of oceanic basement beneath the Colombian and Venezuela basins, magnetic anomaly evidence. *Pages 30–31 of: 3rd Geological Conference of the Geological Society of Trinidad and Tobago and 14th Caribbean Geological Conference, Abstracts*.

Hanstein, T., Eilenz, E., & Strack, K. M. 1986. Einige Aspekte der Aufbereitung von LOTEM Daten. *In: EMTF colloquium*.

Heise, W., Caldwell, T. G., Bertrand, E. A., Hill, G. J., Bennie, S. L., & Ogawa, Y. 2013. Changes in electrical resistivity track changes in tectonic plate coupling. *Geophysical Research Letters*, **40**(19), 5029–5033.

Hervouët, Y., Castrillo-Delgado, J. T., & Odreman, O. 2001. Interaction entre un chevauchement imbrique et une zone transcurrente; le flanc nord-ouest de Andes venezueliennes. *Bulletin de la Societe Geologique de France*, **172**(2), 159–175.

Hospers, J., & VanWijnen, J. 1959. The gravity field of the Venezuelan Andes and adjacent basins. *Verslag van de Gewone Vergadering van de Afdeling Natuurkunde, Koninklijke Nederlandse Akademie van Wetenschappen*, **23**(1), 1–95.

ISC. 2003. *ISC Seismological Dataset Repository*.

Jácome, M., Audemard, F. E., & Graterol, V. 1995. A seismic, gravimetric and geologic interpretation of a transandean profile across the Venezuelan Andes. *I Latinoamerican Geophysical Congress, Rio de J, Baneiro, Brazil*, 15–18.

James, K. H. 2005a. A simple synthesis of Caribbean geology. *Caribbean Journal of Earth Science*, **39**, 68–82.

James, K. H. 2005b. Arguments for and against the Pacific origin of the Caribbean Plate and arguments for an in situ origin. *Caribbean Journal of Earth Science*, **39**, 47–67.

James, K. H., Lorente, M. A., & Pindell, J. L. 2009. *The Origin and Evolution of the Caribbean Plate*.

Jansma, P., Mattioli, G., Lopez, A., DeMets, C., Dixon, T., Mann, P., & Calais, E. 2000. Neotectonics of Puerto Rico and the Virgin Islands, northeastern Caribbean, from GPS geodesy. *Tectonics*, **19**(6), 1021–1037.

Jiracek, G. R. 1990. Near-surface and topographic distortions in electromagnetic induction. *Surveys in Geophysics*, **11**(2-3), 163–203.

Jiracek, G. R., Gonzalez, V. M., Caldwell, T. G., Wannamaker, P. E., & Kilb, D. 2007. Seismogenic, electrically conductive, and fluid zones at continental plate boundaries in New Zealand, Himalaya, and California, USA. *Pages 347–369 of:* Okaya, D., Stern, T., & Davey, F. (eds), *A continental plate boundary: tectonics at South Island, New Zealand*, vol. 153. AGU AMERICAN GEOPHYSICAL UNION.

Jones, A. G. 1993. Electromagnetic images of modern and ancient subduction zones. *Tectonophysics*, **219**(1-3), 29–45.

Kelbert, A., Meqbel, N., Egbert, G. D., & Tandon, K. 2014. ModEM: A modular system for inversion of electromagnetic geophysical data. *Computers & Geosciences*, **66**, 40–53.

Kellogg, J. N., & Bonini, W. E. 1982. Subduction of the Caribbean Plate and basement uplifts in the overriding South American Plate. *Tectonics*, **1**(3), 251–276.

Kellogg, J. N., & Vega, V. 1995. Tectonic development of Panama, Costa Rica, and the Colombian Andes: Constraints from Global Positioning System geodetic studies and gravity. *Pages 75–90 of:* Mann, P. (ed), *Geologic and Tectonic Development of the Caribbean Plate Boundary in Southern Central America*, vol. 295. Geological Society of America.

Kerher, L. 1925. *Geological exploration of the Northern Trujillo mountains range foothills in the southern corner of Maracaibo basin*. Tech. rept. Maraven.

Kerr, A. C., Tarney, J., Marriner, G. F., Nivia, A., & Saunders, A. D. 1997. The Caribbean-Colombian Cretaceous Igneous Province: The Internal Anatomy of an Oceanic Plateau. *Pages 123–144 of:* Mahoney, J. J., & Coffin, M. F. (eds), *Large Igneous Provinces, Continental, Oceanic, and Planetary Flood Volcanism. American Geophysical Union, Geophysical Monograph*, vol. 100.

Key, K. 2016. MARE2DEM: a 2-D inversion code for controlled-source electromagnetic and magnetotelluric data. *Geophysical Journal International*, **207**(1), 571–588.

Key, K., & Ovall, J. 2011. A parallel goal-oriented adaptive finite element method for 2.5-D electromagnetic modelling. *Geophysical Journal International*, **186**(1), 137–154.

Kiyan, D., Jones, A. G., & Vozar. 2013. The inability of magnetotelluric off-diagonal impedance tensor elements to sense oblique conductors in three-dimensional inversion. *Geophysical Journal International*, **196**(3), 1351–1364.

Kohn, B. P., Shagam, R., Banks, P. O., & Burkley, L. A. 1984. Mesozoic-Pleistocene fission-track ages on rocks of the Venezuelan Andes and their tectonic implications. *Pages 365–384 of: Geological Society of America Memoirs*. Geological Society of America.

Kütter, S., Weckmann, U., & de Wit, M. J. 2016. A deep electrical conductivity structure of the southern Barberton Greenstone Belt, South Africa, derived from magnetotelluric measurements. *South African Journal of Geology*, **119**(1), 273–290.

La Marca, E. 1997. *Origen y evolución geológica de la Cordillera de Mérida (Andes de Venezuela)*. Facultad de Ciencias Forestales y Ambientales, ULA.

Levander, A., Bezada, M. J., Niu, F., Humphreys, E. D., Palomeras, I., Thurner, S. M., Masy, J., Schmitz, M., Gallart, J., Carbonell, R., & Miller, M. S. 2014. Subduction-driven recycling of continental margin lithosphere. *Nature*, **515**(7526), 253–256.

Lin, C., Zhong, S., Auken, E., Cai, H., Tan, H., Peng, M., & Kong, W. 2018. The effects of 3D topography on controlled-source audio-frequency magnetotelluric responses. *GEOPHYSICS*, **83**(2), WB97–WB108.

Lonsdale, P. 1978. The Ecuadorian Subduction System. *AAPG Bulletin*, **62**, 2454–2477.

Lugo, J., & Mann, P. 1995. *Jurassic-Eocene tectonic evolution of Maracaibo basin, Venezuela. In A. Tankard, S. Suarez, and H. Welsink (Eds.), Petroleum basins of South America*. Vol. 62. The American Association of Petroleum Geologists, Memoir. Pages 699–725.

Malavé, G., & Suárez, G. 1995. Intermediate-depth seismicity in northern Colombia and western Venezuela and its relationship to Caribbean plate subduction. *Tectonics*, **14**(3), 617–628.

Mann, P., & Burke, K. 1984. Neotectonics of the Caribbean. *Reviews of Geophysics*, **22**(4), 309–362.

Mann, P., Schubert, C., & Burke, K. 1990. The Caribbean Region. *Pages 307–338 of:* Dengo, J. E. (ed), *Review of Caribbean neotectonics*. Boulder, CO: The Geological Society of America.

Mann, P., Escalona, A., & Castillo, M. V. 2006. Regional geologic and tectonic setting of the Maracaibo supergiant basin, western Venezuela. *AAPG Bulletin*, **90**(4), 445–477.

Masy, J., Niu, F., Levander, A., & Schmitz, M. 2011. Mantle flow beneath northwestern Venezuela: Seismic evidence for a deep origin of the Mérida Andes. *Earth and Planetary Science Letters*, **305**(3-4), 396–404.

Mazuera, F., Schmitz, M., Escalona, A., Zelt, C., & Levander, A. 2019. Lithospheric Structure of Northwestern Venezuela From Wide-Angle Seismic Data: Implications for the Understanding of Continental Margin Evolution. *Journal of Geophysical Research: Solid Earth*, **124**(12), 13124–13149.

Meissner, R., & Mooney, W. 1998. Weakness of the lower continental crust: a condition for delamination, uplift, and escape. *Tectonophysics*, **296**, 47–60.

Meqbel, N. 2009. *The electrical conductivity structure of the Dead Sea Basin derived from 2D and 3D inversion of magnetotelluric data*. PhD Thesis, Free University Berlin.

Meqbel, N., Weckmann, U., Muñoz, G., & Ritter, O. 2016. Crustal metamorphic fluid flux beneath the Dead Sea Basin: constraints from 2-D and 3-D magnetotelluric modelling. *Geophysical Journal International*, **207**(3), 1609–1629.

Meqbel, N. M., Egbert, G. D., Wannamaker, P. E., Kelbert, A., & Schultz, A. 2014. Deep electrical resistivity structure of the northwestern U.S. derived from 3-D inversion of USArray magnetotelluric data. *Earth and Planetary Science Letters*, **402**(sep), 290–304.

Meschede, M., & Frisch, W. 1998. A plate-tectonic model for the Mesozoic and Early Cenozoic history of the Caribbean plate. *Tectonophysics*, **296**(3-4), 269–291.

Minster, J., & Jordan, T. 1978. Present-day plate motions. *Journal of Geophysical Research*, **83**(B11), 5331.

Molnar, P., & Sykes, L. 1969. Tectonics of the Caribbean and Middle America Regions from Focal Mechanisms and Seismicity. *Geological Society of America Bulletin*, **80**(9), 1639.

Monod, B., Dhont, D., & Hervouët, Y. 2010. Orogenic float of the Venezuelan Andes. *Tectonophysics*, **490**(1-2), 123–135.

Mora, J. A., Oncken, O., Le Breton, E., Ibánez-Mejia, M., Faccenna, C., Veloza, G., Vélez, V., de Freitas, M., & Mesa, A. 2017. Linking Late Cretaceous to Eocene Tectonostratigraphy of the San Jacinto Fold Belt of NW Colombia With Caribbean Plateau Collision and Flat Subduction. *Tectonics*, **36**(11), 2599–2629.

Muñoz, G., Weckmann, U., Pek, J., Kováčiková, S., & Klanica, R. 2018. Regional two-dimensional magnetotelluric profile in West Bohemia/Vogtland reveals deep conductive channel into the earthquake swarm region. *Tectonophysics*, **727**(mar), 1–11.

Newman, G. A., & Alumbaugh, D. L. 1997. Three-dimensional massively parallel electromagnetic inversion-I. Theory. *Geophysical Journal International*, **128**(2), 345–354.

Niu, F., Bravo, T., Pavlis, G., Vernon, F., Rendon, H., Bezada, M., & Levander, A. 2007. Receiver function study of the crustal structure of the southeastern Caribbean plate boundary and Venezuela. *Journal of Geophysical Research*, **112**(B11).

Oldow, J., Bally, A., & Avé Lallemant, H. 1990. Transpression, orogenic float, and lithospheric balance. *Geology*, **18**(10), 991.

Orihuela Guevara, N., García, A., & Arnaiz, M. 2012. Magnetic anomalies in the Eastern Caribbean. *International Journal of Earth Sciences*, **102**(3), 591–604.

Padrón, C., & Izarra, C. 1996. Modelo de velocidad 1D para el occidente de Venezuela. *Pages 401–408 of: VIII Congreso Venezolano de Geofísica.*

Palacky, G. J. 1988. 3. Resistivity Characteristics of Geologic Targets. *Pages 52–129 of: Electromagnetic Methods in Applied Geophysics.* Society of Exploration Geophysicists.

Palme de Osechas, C., Choy, J. E., & Morandi, M. T. 2001. Mecanismos focales sísmicos y esfuerzos tectónicos en la región norte de los Andes Merideños, Venezuela. *Interciencia*, **26**(5), 201–209.

Pennington, W. D. 1981. Subduction of the Eastern Panama Basin and seismotectonics of northwestern South America. *Journal of Geophysical Research*, **86**, 10753–10770.

Pérez, O. J., Wesnousky, S. G., De La Rosa, R., Márquez, J., Uzcátegui, R., Quintero, C., Liberal, L., Mora-Páez, H., & Szeliga, W. 2018. On the interaction of the North Andes plate with the Caribbean and South American plates in northwestern South America from GPS geodesy and seismic data. *Geophysical Journal International*, **214**(3), 1986–2001.

Pérez, O. P., Jaimes, M. A., & Garciacaro, E. 1997. Microseismicity evidence for subduction of the Caribbean plate beneath the South American Plate in northwestern Venezuela. *Journal of Geophysical Research: Solid Earth*, **102**(B8), 17875–17881.

Pindell, J., Kennan, L., Maresch, W. V., Stanek, K.-P., Draper, G., & Higgs, R. 2005. Plate-kinematics and crustal dynamics of circum-Caribbean arc-continent interactions: Tectonic controls on basin development in Proto-Caribbean margins. *Pages 7–52 of:* Avé Lallement, H. G., & Sisson, V. B. (eds), *Caribbean-South American plate interactions, Venezuela*, vol. 394. Geological Society of America Special Paper.

Pindell, J. L., & Barrett, S. F. 1990. Geologic evolution of the Caribbean region; A plate-tectonic perspective. *Chap. The geology of North America, pages 405–432 of:* Dengo, G., & Case, J. E. (eds), *The Caribbean region*. Geological Society of America.

Platz, A., & Weckmann, U. 2019. An automated new pre-selection tool for noisy Magnetotelluric data using the Mahalanobis distance and magnetic field constraints. *Geophysical Journal International*, apr.

Ritter, O., Junge, A., & Dawes, G. 1998. New equipment and processing for magnetotelluric remote reference observations. *Geophysical Journal International*, **132**(3), 535–548.

Ritter, O., Hoffmann-Rothe, A., Bedrosian, P. A., Weckmann, U., & Haak, V. 2005. Electrical conductivity images of active and fossil fault zones. *Geological Society, London, Special Publications*, **245**(1), 165–186.

Rod, E. 1956. Strike-Slip Faults of Northern Venezuela. *American Association of Petroleum Geologists Bulletin*, **40**, 457–476.

Rod, E. 1960. Comments on the gravity field of the Venezuelan Andes and adjacents basins. *Pages 170–175 of:* Hospers, J., & Vanwijner, J. C. (eds), *Boletin Inf. Asociación Venezolana de Geología Minería y Petroleo*, vol. 3. Asociación Venezolana de Geología Minería y Petroleo.

Russo, R. M., Speed, R. C., Okal, E. A., Shepherd, J. B., & Rowley, K. C. 1993. Seismicity and tectonics of the southeastern Caribbean. *Journal of Geophysical Research: Solid Earth*, **98**(B8), 14299–14319.

Sánchez, M., Audemard, F. E., Giraldo, C., & Ruiz, F. 1994. Interpretación sísmica y gravimétrica de un perfil a través de los Andes venezolanos. *Pages 251–258 of: Mem. VII Congr. Venez. GeofÃsica.*

Sass, P., Ritter, O., Ratschbacher, L., Tympel, J., Matiukov, V. E., Rybin, A. K., & Batalev, V. Yu. 2014. Resistivity structure underneath the Pamir and Southern Tian Shan. *Geophysical Journal International*, **198**(1), 564–579.

Schmitz, M., Chalbaud, D., Castillo, J., & Izarra, C. 2002. The crustal structure of the Guayana Shield, Venezuela, from seismic refraction and gravity data. *Tectonophysics*, **345**(1-4), 103–118.

Schmitz, M., Avila, J., Bezada, M., Vieira, E., Yáñez, M., Levander, A., Zelt, C. A., Jácome, M. I., & Magnani, M. B. 2008. Crustal thickness variations in Venezuela from deep seismic observations. *Tectonophysics*, **459**(1-4), 14–26.

Schmucker, U. 1987. Substitute conductors for electromagnetic response estimates. *Pure and Applied Geophysics*, **125**(2-3), 341–367.

Schubert, C. 1980a. Late-Cenozoic pull-apart basins, Bocono fault zone, Venezuelan Andes. *Journal of Structural Geology*, **2**(4), 463–468.

Schubert, C. 1980b. Morfología neotectónica de una falla rumbo deslizante e informe preliminar sobre la falla de Boconó , Andes merideños. *Acta Cientifica Venezolana*, **31**, 98–111.

Schubert, C. 1982. Neotectonics of Boconó fault, Western Venezuela. *Tectonophysics*, **85**(3-4), 205–220.

Schubert, C. 1993. The Bocono Fault Zone, Western Venezuela. *Page 347 of: AAPG/SVG Int. Congr.*, vol. 77.

Schubert, C., & Vivas, L. 1993. *El cuaternario de la Cordillera de Mérida, Andes Venezolanos*. Fundacion Polar.

Schwalenberg, K., Rath, V., & Haak, V. 2002. Sensitivity studies applied to a two-dimensional resistivity model from the Central Andes. *Geophysical Journal International*, **150**(3), 673–686.

Schwarz, G. 1990. Electrical conductivity of the earth's crust and upper mantle. *Surveys in Geophysics*, **11**(2-3), 133–161.

Shankland, T. J., & Waff, H. S. 1977. Partial melting and electrical conductivity anomalies in the upper mantle. *Journal of Geophysical Research*, **82**(33), 5409–5417.

Simpson, F., & Bahr, K. 2005. *Practical Magnetotellurics*. Cambridge University Press.

Singer, A., & Beltrán, C. 1996. Active faulting in the Southern Venezuelan Andes and Colombian borderland. *Pages 243–246 of: 3rd International Symposium on Andean Geodynamics*. Saint-Malo, France: Orstom éditions, Paris.

Siripunvaraporn, W., & Egbert, G. D. 2000. An efficient data-subspace inversion method for 2-D magnetotelluric data. *GEOPHYSICS*, **65**(3), 791–803.

Siripunvaraporn, W., Egbert, G., & Uyeshima, M. 2005. Interpretation of two-dimensional magnetotelluric profile data with three-dimensional inversion: synthetic examples. *Geophysical Journal International*, **160**(3), 804–814.

Soulas, J. P. 1986. Neotectónica y tectónica activa en Venezuela y regiones vecinas. *Pages 6639–6656 of: VI Congreso Geológico Venezolano, Caracas 1985*, vol. 10. Sociedad venezolana de geológos, Caracas.

Soulas, J. P., & Giraldo, C. 1994. Características sismogénicas de las fallas de Oca-Ancón, Mene Grande y Valera (Región noroccidental de Venezuela). *Pages 35–42 of: Memorias VII Congreso Venezolano de Geofísica*.

Soulas, J. P., Rojas, C., & Schubert, Y. C. 1985. Excursion no. 4, Neotectonica de las fallas de Boconǿ, Valera. Tuname y Mene Grande. *Pages 6961–6999 of: VI Congresso Venezolano*.

Stephan, J. F. 1982. *Evolution géodinamique du domaine Caraïbe, Andes et chaîne Caraibe sur la transversale de Barquisimeto (Vénézuéla)*. Ph.D. thesis, Université Pierre et Marie Curie, Paris, France.

Szarka, L. 1988. Geophysical aspects of man-made electromagnetic noise in the earth—A review. *Surveys in Geophysics*, **9**(3-4), 287–318.

Taboada, A., Rivera, L. A., Fuenzalida, A., Cisternas, A., Philip, H., Bijwaard, H., Olaya, J., & Rivera, C. 2000. Geodynamics of the northern Andes: Subductions and intracontinental deformation (Colombia). *Tectonics*, **19**(5), 787–813.

Telford, W. M., Geldart, L. P., Sheriff, R. E., & Keys, D. A. 1977. *Applied Geophysics*. Cambridge University Press.

Tietze, K., & Ritter, O. 2013. Three-dimensional magnetotelluric inversion in practice—the electrical conductivity structure of the San Andreas Fault in Central California. *Geophysical Journal International*, **195**(1), 130–147.

Tikhonov, A. N. 1950. On determining electrical characteristics of the deep layers of the Earth's crust. *Dokl. Akad. Nauk. SSSR*, **1**(73), 295–297.

Unsworth, M. 2010. Magnetotelluric Studies of Active Continent–Continent Collisions. *Surveys in Geophysics*, **31**(2), 137–161.

Unsworth, M., & Bedrosian, P. A. 2004. On the geoelectric structure of major strike-slip faults and shear zones. *Earth, Planets and Space*, **56**(12), 1177–1184.

Unsworth, M., Malin, P., Egbert, G. D., & Booker, J. R. 1997. Internal structure of the San Andreas fault at Parkfield, California. *Geology*, **25**(4), 359.

Urbani, F. 2017. *Distribución de los terrenos geológicos del Sistema Montañoso del Caribe, norte de Venezuela: Síntesis actualizada*. Boletín de la Academia Nacional de Ciencias Físicas, Matemáticas y Naturales.

U.S. Geological Survey. 2020. *API Documentation - Earthquake Catalog*. webpage. accessed January 31, 2020.

van der Hilst, R., & Mann, P. 1994. Tectonic implications of tomographic images of subducted lithosphere beneath northwestern South America. *Geology*, **22**(5), 451–454.

Vozoff, K. 1991. *The magnetotelluric method*. Society of Exploration Geophysicists. Chap. 8, pages 641–712.

Wannamaker, P. E., Hohmann, G. W., & Ward, S. H. 1984. Magnetotelluric responses of three-dimensional bodies in layered earths. *GEOPHYSICS*, **49**(9), 1517–1533.

Wannamaker, P. E., Stodt, J. A., & Rijo, L. 1986. Two-dimensional topographic responses in magnetotellurics modeled using finite elements. *GEOPHYSICS*, **51**(11), 2131–2144.

Wannamaker, P. E., Caldwell, T. G., Doerner, W. M., & Jiracek, G. R. 2004. Fault zone fluids and seismicity in compressional and extensional environmen inferred from electrical conductivity: the New Zealand Southern Alps and U. S. Great Basin. *Earth, Planets and Space*, **56**(12), 1171–1176.

Wannamaker, P. E., Evans, R. L., Bedrosian, P. A., Unsworth, M. J., Maris, V., & McGary, R. S. 2014. Segmentation of plate coupling, fate of subduction fluids, and modes of arc magmatism in Cascadia, inferred from magnetotelluric resistivity. *Geochemistry, Geophysics, Geosystems*, **15**(11), 4230–4253.

Weckmann, U., Magunia, A., & Ritter, O. 2005. Effective noise separation for magnetotelluric single site data processing using a frequency domain selection scheme. *Geophysical Journal International*, **161**(3), 635–652.

Wiese, H. 1962. Geomagnetische Tiefentellurik Teil II: Die Streichrichtung der untergrundstrukturen des elektrischen Widerstandes, erschlossen aus geomagnetischen Variationen. *Geofisica Pura e Applicata*, **52**(1), 83–103.

Yoris, F., & Ostos, M. 1997. Geology of Venezuela: General Geology and Oil Basins. *Pages 1–17 of:* Singer, J. (ed), *WEC 1997 Well Evaluation Conference. Schlumberger-Surenco, CA*, vol. 1.

Yrigoyen, M., & Urien, C. M. 1988. *Geología de la América del Sur*. Vol. 1. Univ. Nac. Tucumán, Argentina. Chap. Cuadro Geostructural de la América del Sur, pages 17–106.

Curriculum vitae

The curriculum vitae is not included in the online version for data protection reasons.

The curriculum vitae is not included in the online version for data protection reasons.